frontiers | Research Topics

Nanomaterial-based biosensors, diagnosis, and applications

Edited by
Kang Cui, Yizhong Huang and
Li Wang

Published in
Frontiers in Bioengineering and Biotechnology

ISSN 1664-8714
ISBN 978-2-8325-4860-8
DOI 10.3389/978-2-8325-4860-8

About Frontiers

Frontiers is more than just an open access publisher of scholarly articles: it is a pioneering approach to the world of academia, radically improving the way scholarly research is managed. The grand vision of Frontiers is a world where all people have an equal opportunity to seek, share and generate knowledge. Frontiers provides immediate and permanent online open access to all its publications, but this alone is not enough to realize our grand goals.

Frontiers journal series

The Frontiers journal series is a multi-tier and interdisciplinary set of open-access, online journals, promising a paradigm shift from the current review, selection and dissemination processes in academic publishing. All Frontiers journals are driven by researchers for researchers; therefore, they constitute a service to the scholarly community. At the same time, the *Frontiers journal series* operates on a revolutionary invention, the tiered publishing system, initially addressing specific communities of scholars, and gradually climbing up to broader public understanding, thus serving the interests of the lay society, too.

Dedication to quality

Each Frontiers article is a landmark of the highest quality, thanks to genuinely collaborative interactions between authors and review editors, who include some of the world's best academicians. Research must be certified by peers before entering a stream of knowledge that may eventually reach the public - and shape society; therefore, Frontiers only applies the most rigorous and unbiased reviews. Frontiers revolutionizes research publishing by freely delivering the most outstanding research, evaluated with no bias from both the academic and social point of view. By applying the most advanced information technologies, Frontiers is catapulting scholarly publishing into a new generation.

What are Frontiers Research Topics?

Frontiers Research Topics are very popular trademarks of the *Frontiers journals series*: they are collections of at least ten articles, all centered on a particular subject. With their unique mix of varied contributions from Original Research to Review Articles, Frontiers Research Topics unify the most influential researchers, the latest key findings and historical advances in a hot research area.

Find out more on how to host your own Frontiers Research Topic or contribute to one as an author by contacting the Frontiers editorial office: frontiersin.org/about/contact

Nanomaterial-based biosensors, diagnosis, and applications

Topic editors

Kang Cui — University of Jinan, China

Yizhong Huang — Nanyang Technological University, Singapore

Li Wang — Jiangxi Normal University, China

Citation

Cui, K., Huang, Y., Wang, L., eds. (2024). *Nanomaterial-based biosensors, diagnosis, and applications*. Lausanne: Frontiers Media SA. doi: 10.3389/978-2-8325-4860-8

Table of contents

frontiers | Frontiers in Bioengineering and Biotechnology

TYPE Editorial
PUBLISHED 24 April 2024
DOI 10.3389/fbioe.2024.1414746

OPEN ACCESS

EDITED AND REVIEWED BY
Gianni Ciofani,
Italian Institute of Technology (IIT), Italy

*CORRESPONDENCE
Yizhong Huang,
yzhuang@ntu.edu.sg

RECEIVED 09 April 2024
ACCEPTED 11 April 2024
PUBLISHED 24 April 2024

CITATION
Cui K, Wang L and Huang Y (2024), Editorial: Nanomaterial-based biosensors, diagnosis, and applications.
Front. Bioeng. Biotechnol. 12:1414746.
doi: 10.3389/fbioe.2024.1414746

Editorial: Nanomaterial-based biosensors, diagnosis, and applications

Kang Cui[1], Li Wang[2] and Yizhong Huang[3]*

[1]School of Chemistry and Chemical Engineering, University of Jinan, Jinan, China, [2]College of Chemistry and Chemical Engineering, Jiangxi Normal University, Nanchang, China, [3]School of Materials Science and Engineering, Nanyang Technological University, Singapore, Singapore

KEYWORDS

nanomaterials, biosensors, diagnosis, health monitoring, biotechnology

Editorial on the Research Topic
Nanomaterial-based biosensors, diagnosis, and applications

Owing to their distinctive chemical compositions and diverse biological functionalities, numerous nanomaterials derived from organic, inorganic, and hybrid compounds have garnered significant attention from the scientific community and have played a pivotal role in advancing biosensors, diagnostics, and related applications over recent decades. These varieties of nanomaterials serve as valuable platforms for immobilization, optical interrogation, and (photo)electrochemical labeling, thereby enhancing the sensitivity, stability, and selectivity of biosensing devices, which undoubtedly reshapes conventional approaches to health monitoring, food safety, and environmental research. Accordingly, in anticipation of forthcoming advancements in this research area, we have curated this Research Topic to present the latest developments and perspectives concerning nanomaterial-based biosensors, diagnosis, and applications. Encompassing two reviews and eight original research articles, this collection spans fundamental nanomaterial physics, manufacturing techniques, and biosensing applications.

As nanomaterials play a significant role in enhancing the performance of electrochemical biosensors due to their unique physical and chemical properties, such as large surface area, high catalytic activity, and superior electron transfer kinetics. Shahid et al. highlights the application of carbon-based nanomaterials, metallic nanoparticles, quantum dots, and nanowires in biosensors. In this review article, they summarized a range of fabrication strategies utilizing diverse nanocomposites which enhance the limit of detection for different miRNAs and advance the miniaturization process of electrochemical biosensors. This review article offers researchers a comprehensive perspective on the advancements in electrochemical biosensors, particularly focusing on the latest strategies for improving detection limits and biosensor miniaturization. As the synergy between nanomaterials with biomolecules is also a key part to improve the performance of biosensors, Reaño et al. review the synergistic systems of antibodies, aptamers, and nanomaterials for amplified electrochemical signaling. The review discusses how antibodies, aptamers, or target antigens can be immobilized on the electrode, and the importance of proper immobilization techniques to support the formation of bioreceptor-biomarker complex and induce signal generation.

In the original work, Toyos-Rodríguez et al. emphasize the significance of electrochemical techniques in the development of highly sensitive biosensors by

optimizing the thickness of nanoporous alumina membranes which are integral to the electrochemical sensing platform for the detection of catalase, a key biomarker in wound infection. The study successfully applies this optimization to construct a label-free immunosensor that effectively detects catalase with high precision, showcasing the potential of electrochemical methods for rapid and accurate diagnostics in clinical settings. The research article by Cheng et al. focuses on the development of a photoelectrochemical (PEC) biosensor based on SiW_{12}@CdS quantum dots and colloidal gold nanoparticles, providing a low background signal and good sensitivity, for the detection of HPV 16 DNA, a significant biomarker for cervical cancer. The study highlights the importance of the PEC technique in advancing cancer diagnostics and the potential for early detection, which is critical for improving treatment outcomes. In the original work by Kan et al. the importance of the fluorescent technique is highlighted by its ability to enable real-time monitoring and selective detection of SO_3^{2-} at low concentrations within complex biological environments, allowing for the rapid, sensitive, and selective detection of sulfate ions, which is crucial for understanding cellular processes, diagnosing diseases, and guiding drug development. The research highlights the importance of fluorescent probes in advancing biomedical studies and emphasizes their potential practical application in clinical settings. In the research article, Nishan et al. present the development of a colorimetric biosensor for detecting H_2O_2 using zinc oxide nanoparticles deposited on Morus nigra sawdust. This colorimetric technique allows for the visual detection of H_2O_2 through a change in color facilitated by the presence of 3,3′,5,5′-tetramethylbenzidine. The advantages of the colorimetric technique render it a valuable tool in biotechnology, medical diagnostics, and environmental monitoring. The original research by Cheng et al. concentrates on the design and fabrication of a surface-enhanced Raman scattering (SERS) sensor based on functionalized Au/Si cap-cone arrays and Au nanocubes modified with 5-carboxyfluorescein as a probe tailored for the highly sensitive detection of Vimentin, a protein linked to gastric cancer. The study elucidates the utility of SERS as a valuable technique for the early detection of cancer and for monitoring therapeutic responses. Besides, the research article by Lv et al. focuses on the development of a highly sensitive flexible capacitive pressure sensor that utilizes a hierarchical pyramid micro-structured polydimethylsiloxane dielectric layer. The research demonstrates the potential of flexible sensors in advancing technology for electronic skin, intelligent robotics, and personalized health monitoring.

A multiplex detection biosensor, which is capable of detecting or measuring biological analytes through multiple modes or strategies simultaneously or sequentially, can enhance the versatility, sensitivity, and reliability of the biosensor. The original works from Xiao and Wang focused on the multiplex detection techniques. Xiao et al. combines the graphene oxide-assisted multiplex recombinase polymerase amplification assay, targeting two conserved insertion sequences (IS6110 and IS1081) within *mycobacterium tuberculosis* complex (MTBC), with a CRISPR–Cas12a-based trans-cleavage assay for a comprehensive diagnostic approach. The combined approach with a CRISPR–Cas12a-based multiplex detection aims to provide a straightforward, expeditious, highly sensitive, and precisely targeted diagnostic tool for MTBC. Besides, Wang et al. explores a cellulase protected fluorescent gold nanoclusters which serve as dual-functional nanoclusters, demonstrating their potential as fluorescent bioprobes for ascorbic acid detection and bacterial labeling, thereby facilitating medical diagnosis and human health maintenance.

In conclusion, from the reviews and research works included in this Research Topic, it is revealed that a multitude of nanomaterial-based methodologies utilizing electrochemistry, PEC, fluorescence, SRES, and colorimetric analysis have been devised. These techniques combined with functional nanomaterials form the basis for the fabrication of different types of nanomaterial-based biosensors and diagnosis applications. However, meeting the increasing demand for application platforms characterized by high sensitivity, cost-effectiveness, and ease of operation remains a significant challenge, particularly in the rigorous fabrication standards demanded by industry. To further promote the development of biosensors, more bio-compatible nanomaterials and assembly techniques are in great demand. We believe further research in the nanomaterial-based biosensors and diagnosis will have a significant impact on future personalized healthcare, food safety and environmental analysis.

Author contributions

KC: Writing–original draft, Writing–review and editing. LW: Writing–review and editing. YH: Writing–review and editing.

Funding

The author(s) declare that no financial support was received for the research, authorship, and/or publication of this article.

Conflict of interest

The authors declare that the research was conducted in the absence of any commercial or financial relationships that could be construed as a potential conflict of interest.

Publisher's note

frontiers | Frontiers in Bioengineering and Biotechnology

TYPE Original Research
PUBLISHED 14 June 2023
DOI 10.3389/fbioe.2023.1193052

OPEN ACCESS

EDITED BY
Li Wang,
Jiangxi Normal University, China

REVIEWED BY
Yue Cao,
Nanjing University of Posts and Telecommunications, China
Cheng Ma,
Yangzhou University, China

*CORRESPONDENCE
Xiao Li,
lix163@163.com
Liang Sun,
sunliang@sdfmu.edu.cn
Dejin Zang,
zangdejin_lm@163.com

RECEIVED 24 March 2023
ACCEPTED 02 June 2023
PUBLISHED 14 June 2023

CITATION
Cheng Y, Sun C, Chang Y, Wu J, Zhang Z, Liu Y, Ge S, Li Z, Li X, Sun L and Zang D (2023), Photoelectrochemical biosensor based on SiW_{12}@CdS quantum dots for the highly sensitive detection of HPV 16 DNA.
Front. Bioeng. Biotechnol. 11:1193052.
doi: 10.3389/fbioe.2023.1193052

Photoelectrochemical biosensor based on SiW_{12}@CdS quantum dots for the highly sensitive detection of HPV 16 DNA

Yao Cheng[1], Chaoyue Sun[1,2], Yuhua Chang[3], Jiayin Wu[1], Zhihao Zhang[1], Yunqing Liu[2], Shenguang Ge[2], Zhao Li[4], Xiao Li[5,6]*, Liang Sun[1]* and Dejin Zang[1]*

[1]National Key Laboratory of Advanced Drug Delivery and Release System, NHC Key Laboratory of Biotechnology Drugs (Shandong Academy of Medical Sciences), Key Lab for Rare and Uncommon Diseases of Shandong Province, School of Pharmacy and Pharmaceutical Sciences, Institute of Materia Medica, Shandong First Medical University and Shandong Academy of Medical Sciences, Jinan, China, [2]Institute for Advanced Interdisciplinary Research (iAIR), School of Chemistry and Chemical Engineering, University of Jinan, Jinan, China, [3]Shandong Provincial Maternal and Child Healthcare Hospital, Jinan, China, [4]Suzhou KunTao Intelligent Manufacturing Technology Co., Ltd., Suzhou, China, [5]NMPA Key Laboratory for Quality Evaluation of Medical Materials and Biological Protective Devices, Jinan, China, [6]Shandong Institute of Medical Device and Pharmaceutical Packaging Inspection, Jinan, China

A highly sensitive biosensor for detecting HPV 16 DNA was prepared based on Keggin-type polyoxometalate (SiW_{12})-grafted CdS quantum dots (SiW_{12}@CdS QDs) and colloidal gold nanoparticles (Au NPs), which exhibited remarkable selectivity and sensitivity upon target DNA detection because of its excellent photoelectrochemical (PEC) response. Here, an enhanced photoelectronic response ability was achieved with the strong association of SiW_{12}@CdS QDs by polyoxometalate modification, which was developed through a convenient hydrothermal process. Furthermore, on Au NP-modified indium tin oxide slides, a multiple-site tripodal DNA walker sensing platform coupled with T7 exonuclease was successfully fabricated with SiW_{12}@CdS QDs/NP DNA as a probe for detecting HPV 16 DNA. Due to the remarkable conductivity of Au NPs, the photosensitivity of the as-prepared biosensor was improved in an I_3^-/I^- solution and avoided the use of other regents toxic to living organisms. Finally, under optimized conditions, the as-prepared biosensor protocol demonstrated wide linear ranges (15–130 nM), with a limit of detection of 0.8 nM and high selectivity, stability, and reproducibility. Moreover, the proposed PEC biosensor platform offers a reliable pathway for detecting other biological molecules with nano-functional materials.

KEYWORDS

biosensor, polyoxometalates, quantum dots, HPV 16 DNA, photoelectrochemistry

1 Introduction

Cancer has always been the most malignant disease affecting human health, with high morbidity and mortality rates. The development of targeted diagnosis and personalized treatment has never stopped; thus, early diagnosis with precise cancer biomarker recognition that will offer valuable opportunities for more effective treatment is of great significance to specific therapy of cancer patients (Garland, 1953; Helmink et al., 2019). Nowadays, various therapeutic modalities based on chemotherapy regimens have been exploited for mid–late stage cancer patients despite a lack of research into earlier diagnosis and more effective

treatments. Thus, the exploration of highly effective diagnoses with remarkable sensitivity, high selectivity, and reliability remains challenging and is urgently required (Xiao et al., 2022).

Among various cancers, cervical cancer is the second most common cancer in women; moreover, cervix cancer caused by infection with high-risk human papillomavirus (HPV) accounts for more than 99% of cervical cancers. Although stage-specific survival has been improved since the 1960s, along with the development of multi-modality treatment, the 5-year survival rate of women with advanced non-metastatic cervical carcinomas is still low at ~40%. However, the cure rate could reach 70%–85%, which would occur in cervical cancer patients with stage I and II_a lesions, indicating the very significance of early diagnosis (Kay et al., 2005). Two high-risk sexually transmittable human HPV types of 16 and 18 can cause cervical cancers. Importantly, this cancer shows no symptoms until the advanced stages of the disease. Therefore, finding a new diagnostic methodology that can detect the presence of HPV or cervical cancer at the earliest stage is a real challenge, which also stimulates the development of new biosensors for cancer early diagnosis (Jampasa et al., 2018).

Photoelectrochemical (PEC) biosensors based on photocurrent conversion functional materials are an ideal pathway to detect biomolecules owing to their low background signal and excellent sensitivity (Kay et al., 2005; Jampasa et al., 2018; Wang F. et al., 2022; Wang L. et al., 2022; Huang et al., 2022; Nanocubes et al., 2023). However, the unfavorable biocompatibility, belated photocurrent response, and low stability of these functional materials have limited the development of PEC biosensors. Compared with the electrochemiluminescence immunoassay strategy, which depends on the concentration of $^{\bullet}OH$ induced by H_2O_2 conversion, PEC biosensors require no auxiliary additives and exhibit lower toxicity and higher sensitivity but rely heavily on outstanding photochromic properties (Nie et al., 2020; Wang L. et al., 2022). Quantum dots (QDs) are extensively used in the fields of energy catalysis (Liu et al., 2014; Weiss, 2017; Kong et al., 2018; Shi et al., 2019; Zheng et al., 2020; Zhang M. et al., 2022), imaging (Nguyen et al., 2017; Park et al., 2017; Mallick et al., 2019; Min et al., 2019; Zheng et al., 2020; Xu et al., 2021; Liu et al., 2017), and chemical sensors (Wang F. et al., 2022; Zhang J. et al., 2022; Huang et al., 2022) due to their remarkable photoelectric response properties. Cadmium sulfide quantum dots (CdS QDs) have attracted broad and interdisciplinary attention for a long time because of their excellent properties in that their band gap (2.3 eV) corresponds well with the spectrum of sunlight, qualifying their superior visible light photosensitiveness and proposing remarkable compatibility with other functional materials (Ahamad et al., 2016). More importantly, the photoelectric properties of CdS QDs can be significantly tuned by introducing heteroatoms or dopants into their lattice or matrix. Modified CdS QDs are regarded as promising photocurrent conversion materials and have been widely used in solar cells and biological sensors (Jeong et al., 2017; Smith et al., 2017; Lee et al., 2018; Morgan and Kelley, 2018; Sui et al., 2018; Zhang et al., 2019). Multiple synthetic strategies, such as growth doping, nucleation doping, diffusion doping, and single-source precursor strategy have been reported for the synthesis of modified CdS QDs (Sui et al., 2018; Yu et al., 2021). In parallel, polyoxometalates (POMs) have emerged as a new class of materials due to their unique electronic, optical, magnetic, and catalytic properties (Luo et al., 2013; Ueda, 2018; Kong et al., 2020; Liu et al., 2020; Misra et al., 2020; Gu et al., 2021; Fabre et al., 2022; Kruse et al., 2022). According to some recent reports, when CdS QDs and POMs are successfully composited to have a hierarchical nanostructure under certain conditions, a unique phenomenon of interaction involving electron and energy transfer will occur (Xing et al., 2013; Dong et al., 2021). Such as-prepared POM@CdS QD composites demonstrate a novel strategy toward advanced photoelectric functional materials.

POMs are a class of negatively charged molecular metal oxides with well-defined structures, beautiful geometries, and nanoscale sizes (Luo et al., 2013; Xing et al., 2013; Kong et al., 2020; Kondinski, 2021) and have been successfully used in a wide domain of industrial catalysis of functional materials (Ji et al., 2015; He et al., 2016; Tourneur et al., 2019; Zang et al., 2019; Wang et al., 2020; Gul et al., 2022; Shi et al., 2022), environmental science (Girardi et al., 2015; Chen et al., 2018; Guo et al., 2018; Cao et al., 2019; Huang et al., 2019; Li C. et al., 2020; Yu H. et al., 2020; Li N. et al., 2020; Yu F. Y. et al., 2020; Lang et al., 2020; Zang et al., 2021; Fabre et al., 2022; Zang and Wang, 2022), life science (Bijelic et al., 2019; Li N. et al., 2020; Shi et al., 2020; Alizadeh and Yadollahi, 2022; Su Y. et al., 2022; Fabre et al., 2022; Xiao et al., 2022), pharmacology (Sarver et al., 2021; Su Y. et al., 2022; Liu et al., 2022), and other disciplines (Boulmier et al., 2018; Mitchell et al., 2022). As additives in the modification of CdS QDs, POMs with rich charges and excellent electron transfer ability can rationally adjust their band gaps through the synergistic effect to eliminate the intrinsic limits of their rapid recombination of photogenerated carriers and severe photocorrosion, improving the PEC performance of POM@CdS QD composites (Dong et al., 2021). Meanwhile, POM@CdS QDs are rarely applied in PEC biosensor fabrication for biomolecule detection such as protein, DNA, or RNA.

In this study, a highly sensitive biosensor for detecting HPV 16 DNA fabricated with Keggin-type POM (SiW_{12})-grafted CdS QDs (SiW_{12}@CdS QDs) and colloidal gold nanoparticles (Au NPs) is reported for the first time. These SiW_{12}@CdS QDs exhibited enhanced photocurrent response and high stability after being combined with NP DNA; with chitosan (CS)/Au NPs as the first layer on indium tin oxide (ITO) slides, a series of biochemical DNA primers were incubated to fabricate a multi-site tripodal DNA walker sensing platform coupled with T7 exonuclease. Due to the remarkable conductivity of Au NPs, the photosensitivity of the as-prepared biosensor was further improved in an I_3^-/I^- solution and avoided the use of other regents toxic to living organisms. Finally, under optimized conditions, the as-prepared biosensor protocol demonstrated wide linear ranges (15–130 nM), with a limit of detection (LOD) of 0.8 nmol/L and high selectivity, stability, and reproducibility. Furthermore, the proposed PEC biosensor platform offers a reliable and promising pathway for detecting biological molecules.

2 Experiments

2.1 Materials and methods

All chemical reagents in this experiment were of analytical grade. $Na_2S{\cdot}9H_2O$, $CdCl_2{\cdot}2.5H_2O$, I_2, KI, and $HAuCl_4{\cdot}4H_2O$ were purchased from Sinopharm Chemical Reagent Co., Ltd. (Shanghai, China). NaOH and trisodium citrate dihydrate ($Na_3C_6H_5O_7{\cdot}2H_2O$) were obtained from Shanghai Aladdin biochemical technology Co., Ltd.

TABLE 1 The nucleotide sequences of oligonucleotides.

Name	Sequence (5′ to 3′)
ArmDNA	TTTTTGCTGGAGGT TTTTTTTTTTTTTTTTTTTTTTT TTTTTTTTTTTTTTTTT-$(CH_2)_3$-SH
cDNA	CATACACCTCCAGC
pDNA	SH--$(CH_2)_6$-GCCGGACTAG
NP DNA	COOH-TCCAGCGGGCTAGTC
HPV 16 DNA	GCTGGAGGTGTATG
HPV 18 DNA	GGATGCTGCACCGG
HPV 33 DNA	CACATCCACCCGCA

(Shanghai, China). $H_4[Si(W_3O_{10})_4]\cdot xH_2O$, CS was obtained from Shanghai Maclin Biochemical Technology Co., Ltd. Synthetic oligodeoxy-nucleotides corresponding to partial sequences of the gene of HPV type 16 and TE buffer were received from Sangon Biotech (Shanghai) Co., Ltd. T7 Exo and NE buffer were received from New England Biotechnology (Beijing) Co., Ltd. HPV samples of vaginal swab scraping with different infection subtypes (HPV 16, 18, 33 DNA) were supplied by Suzhou KunTao Intelligent Manufacturing Technology Co., Ltd. All reagent solutions were prepared using ultrapure water (resistivity as 18 MΩ·cm at 25°C). The nucleotide sequences of the oligonucleotides are listed in Table 1.

2.2 Synthesis of SiW_{12}@CdS QDs

First, CdS QDs were synthesized according to our previously published literature (Wang F. et al., 2022). Afterward, a post-modification procedure of CdS QDs with SiW_{12} proceeded. $H_4[Si(W_3O_{10})_4]\cdot xH_2O$ (0.1435 g) were dissolved in a CdS QD solution (15 mL), and the obtained mixed solution was vigorously stirred at 40°C for 12 h to obtain the final products, a homogeneous yellow solution. The product solution was stored at 4°C for the next step.

2.3 Preparation of Au particle-based CS hydrogel

Au NPs were synthesized according to the previously published literature (Wang F. et al., 2022). First, 1-mg CS and a 20-mL gold solution were added to 30-mL ultrapure water. After that, the obtained solution was stirred at room temperature (25°C) for 24 h to achieve a CS hydrogel. The obtained Au NP-based CS hydrogel was stored at 4°C (Suginta et al., 2013; Liu et al., 2018; Feyziazar et al., 2020; Vesel, 2023).

2.4 Construction of PEC biosensor

5 mL of a 9-μM armDNA solution and 5 mL of a 9-μM cDNA solution were mixed and heated at 95°C for 5 min. After cooling down to room temperature, arm-cDNA was received. For the fabrication of the PEC biosensor, 40 μL of the Au NP-based CS hydrogel (Au NP/CS gel) was embellished on the ITO slide surface, and then, 2 μL of the arm-cDNA solution and 3 μL of 3-μM pDNA were sequentially modified on the electrode. When they were successfully connected to the electrode, 3 μL of the SiW_{12}@CdS QD/NP DNA solution was successively modified and incubated for 2 h, and unstable residues on the electrode surface were washed with buffer. Finally, the prepared electrode was incubated with a series of concentrations of HPV 16 DNA for 2 h. Then, the electrode was dropped in 50-U mL^{-1} T7 exonuclease and incubated for 2 h. The electrode was rinsed with buffer and dried under nitrogen atmosphere for PEC measurements in a 5-mM I_3^-/I^- working solution. Here, an HPV 16 DNA-detecting biosensor was successfully fabricated.

2.5 PEC measurement procedure

The detection performance and reliability of the as-prepared PEC biosensor were investigated with the samples from vaginal swab scraping. Different specimens of the as-prepared biosensor were incubated with different patients' samples of HPV 16 DNA for 2 h. Then, the electrode was washed and dropped in 50-U mL^{-1} T7 exonuclease. Finally, the electrode was rinsed with buffer and dried under nitrogen atmosphere for PEC measurements in 5-mmol L^{-1} of I_3^- and 0.5-mol L^{-1} of an I^- working solution, and each sample was detected three times. Similarly, to detect the samples of HPV 18 DNA and HPV 33 DNA to evaluate the selectivity and stability of the as-prepared biosensor, the same PEC measurement procedure was performed with different HPV DNA subtypes.

2.6 Material characterization

Transmission electron microscopy (TEM) images of the NPs were obtained using an HT7800 transmission electron microscope at 200-kV acceleration voltages. The Zeta potentials and particle size distribution of the SiW_{12}@CdS QDs were obtained by Malvern nano-ZS NP size and Zeta potential analyses, and UV–vis absorption spectra were recorded with a UV-26001 UV–vis spectrophotometer. Electrochemical data were obtained with a three-electrode-system CHI 660E electrochemical workstation. PEC signals were obtained from a PL-X500D Simulated solar xenon lamp source and electrochemical word station (CHI 660e). A single-sided glass electrode (1 cm × 3 cm) was coated with ITO as the working electrode. A platinum wire and a saturated calomel electrode were used as the counter and reference electrodes, respectively; PEC measurements were performed in a 5-mM I_3^-/I^- working solution.

3 Results and discussion

The synthesis of key photochromic materials such as SiW_{12}@CdS NPs, the fabrication of the as-prepared PEC biosensor, and the comprehensive detection process of HPV DNA were performed according to the procedure shown in Scheme 1.

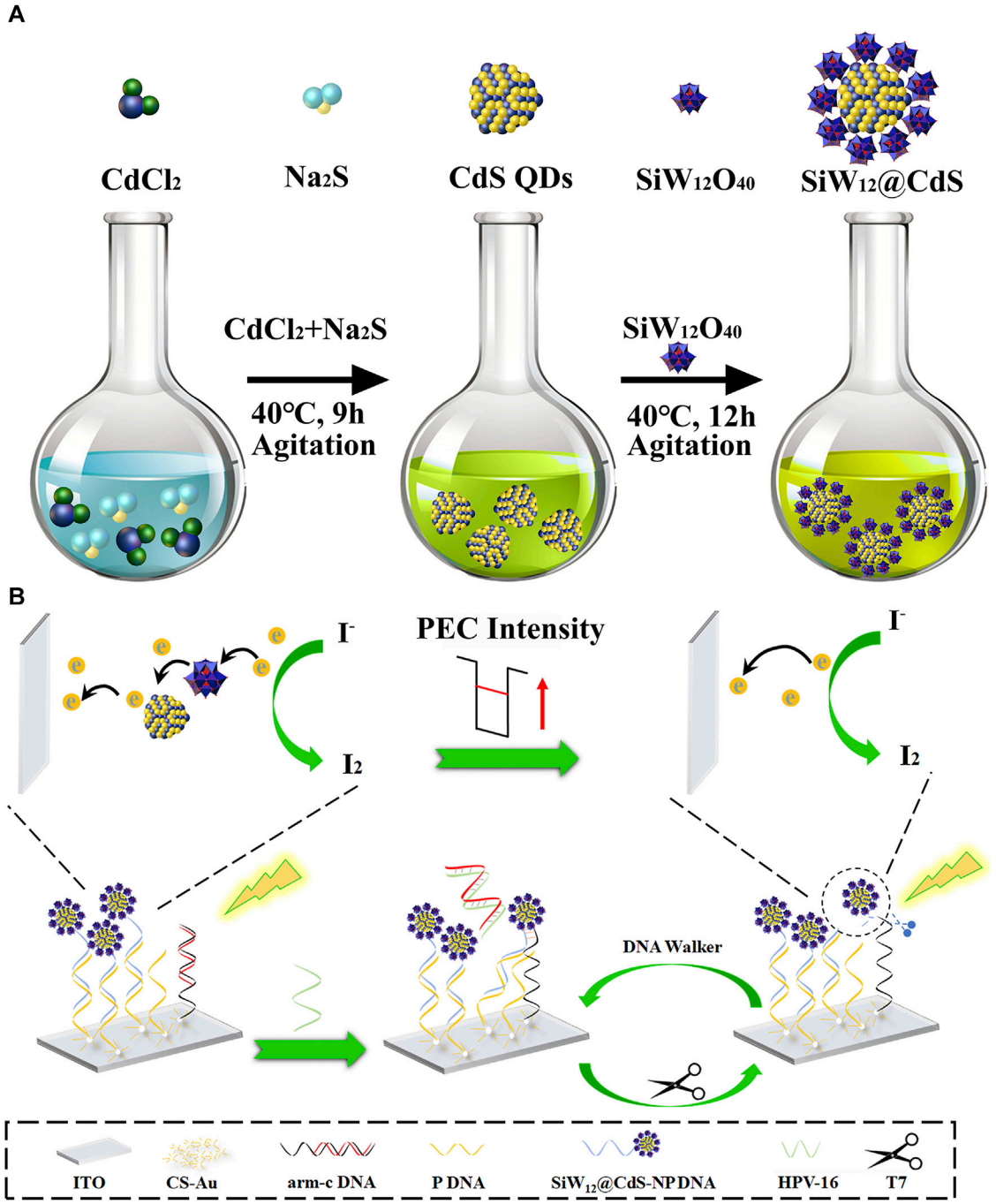

SCHEME 1
Schematic illustration of **(A)** the synthesis of POM@CdS QD composites and **(B)** PEC sensor for detecting HPV 16 DNA.

3.1 Characterization of SiW_{12}@CdS QDs

The morphology and size distribution of the as-prepared CdS QDs and SiW_{12}@CdS NPs were characterized via TEM and Malvern nano-ZS NP size analysis. As shown in Figures 1A, C black curve, uniform CdS QDs were obtained using the solvothermal method and observed as a yellow solution (insert photograph on Figure 1A), and the average particle size of the obtained CdS QDs was ~10 nm; note that the size of the as-prepared SiW_{12}@CdS NPs has increased to ~100 nm, making the color brighter yellow, as shown in Figures 1B, C red curve. The larger size resulted from the aggregation of the SiW_{12}-modified CdS QDs, as shown in Figure 1B (Liu et al., 2018; Feyziazar et al., 2020; Zhang J. et al., 2022; Vesel, 2023). Here, the SiW_{12}@CdS NPs were successfully synthesized. The photographs of the as-prepared CdS QDs and SiW_{12}@CdS NPs under UV light irradiation are shown in Supplementary Figure S1.

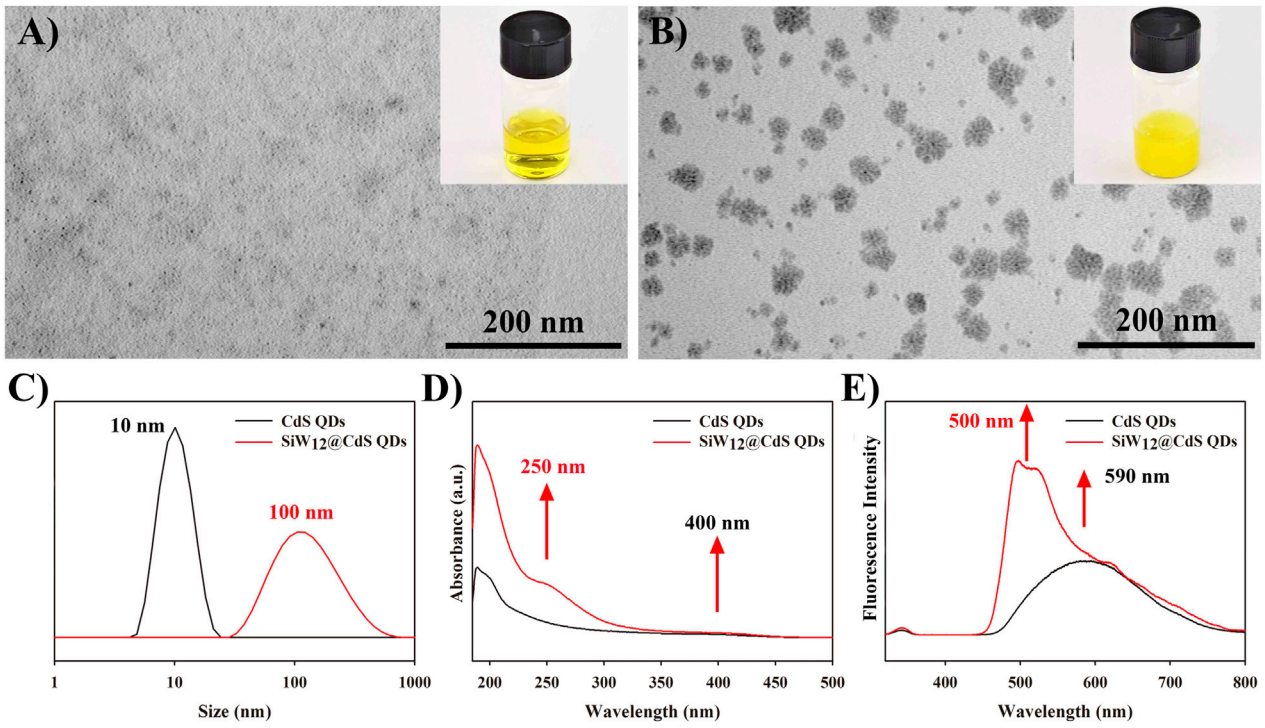

FIGURE 1
TEM images of **(A)** CdS QDs and **(B)** SiW_{12}@CdS QDs. **(C)** Size distribution diagram of CdS QDs and SiW_{12}@CdS QDs. **(D)** UV–vis absorption spectra of CdS QDs and SiW_{12}@CdS QDs. **(E)** Fluorescence emission spectra of CdS QDs and SiW_{12}@CdS QDs, excitation wavelength: 340 nm.

After the modification of SiW_{12} to CdS QDs, a new absorption wave appeared at ~250 nm on the UV–vis absorption spectrum of the SiW_{12}@CdS NPs (Figure 1D, red curve) compared with that of the CdS QDs (Figure 1D, black curve), and both underwent absorption at ~400 nm. Thus, improved light absorption was achieved according to this phenomenon. Otherwise, from Figure 1E of the fluorescence emission spectrograms of the CdS QDs and SiW_{12}@CdS QDs, an enhanced emission spectrum and a 90-nm blue shift were observed from ~590 nm of the CdS QDs to ~500 nm of SiW_{12}@CdS QDs under the same excitation light at 340 nm, indicating a strong interaction between SiW_{12} and CdS QDs with a broader band gap (Guo et al., 2016; Ji et al., 2017; Zang et al., 2022; Nie et al., 2020). To summarize the UV–vis absorption and fluorescence emission spectroscopic studies, the improved light response ability was successfully achieved by the strong association between SiW_{12} and CdS QDs, indicating remarkable photoelectric properties.

3.2 Characterization of Au NPs

As an important role of the first layer in the construction of the as-prepared PEC biosensor, Au NPs were synthesized using the solvothermal method, as shown in Figure 2A, with a size of ~24 nm in Figure 2C. Notably, during the preparation of the Au NP/CS gel (Au NP/CS gel), the Zeta potential of the Au NPs decreased by 20 mV from −45 to −25 mV (Figure 2B), indicating a strong accumulating capacity, which would endow it with good adhesive ability as the first layer on the ITO slide to fabricate the PEC biosensor, while the visible light absorption ability of the Au NPs was well maintained without any changes in the UV–vis absorption spectrum at 524 nm (as shown in Figure 2D), high conductivity and visible light absorption for the PEC biosensor.

3.3 PEC characterization of PEC biosensor

Electrochemical impedance spectroscopy (EIS) changes associated with the modification of the ITO slide and the PEC response of the as-prepared PEC biosensor were measured for each modification layer. As shown in Figure 3A, the first layer of the Au NP/CS gel on the ITO slide showed the largest R_{et} value (Figure 3A; a: red curve) because the poor conductivity of the CS gel obstructed electron transfer to the ITO electrode. Au NP addition not only increases conductivity but also PEC response via the LSPR effect, emphasizing its importance (Aiken and Finke, 1999; Lee et al., 2013; Chou et al., 2017; Wen et al., 2017; Domingues et al., 2018; Shi et al., 2019; Figueiredo et al., 2021). After the successive modification with arm-c DNA and pDNA (Figure 3A, b: green curve), the obtained R_{et} value decreased because of the association between Au NPs and the primers, offering an electron transfer pathway with reasonable steric hindrance to the ITO electrode. The smallest R_{et} value appeared after the NP DNA–SiW_{12}@CdS NP modification (Figure 3A, c: dark blue curve), for the reason that the remarkable conductivity of the SiW_{12}@CdS NPs significantly improved electron transfer. The R_{et}

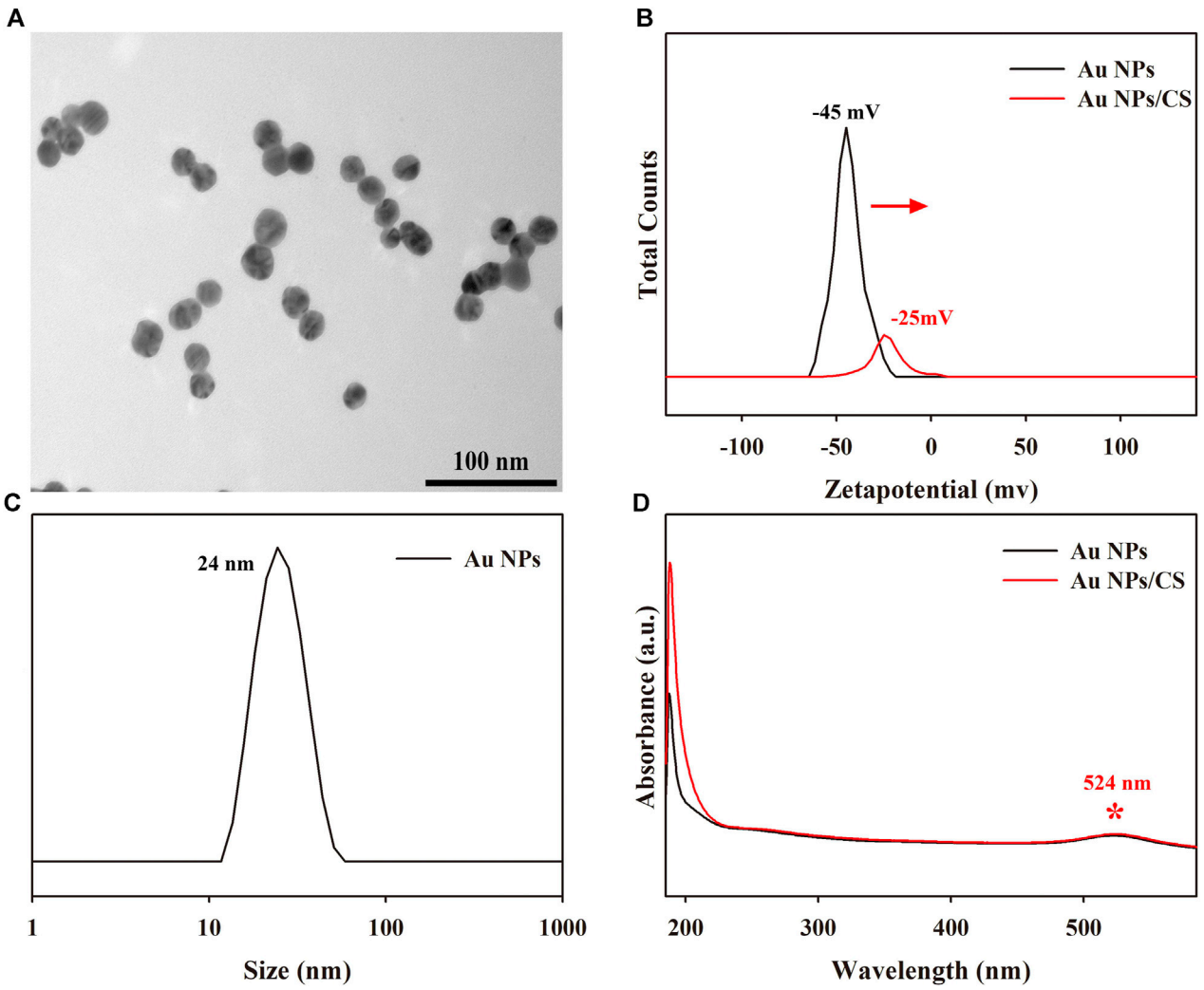

FIGURE 2
(A) TEM images of Au NPs. **(B)** Zeta potential distribution curves of Au NPs and Au NP/CS gel. **(C)** Size distribution diagram of Au NPs. **(D)** UV–vis absorption spectra of Au NPs and Au NP/CS gel.

value was increased when the HPV 16 DNA was added, as shown in Figure 3A, d: light blue curve, owing to the high steric hindrance of HPV DNA. The photocurrent response (PEC) was consistent with the EIS investigation, as shown in Figure 3. The ITO/Au NP/CS sample exhibited the smallest photocurrent (Figure 3B, a: red curve), and the photocurrent increased when the primers were continuously anchored onto the modified ITO slide (Figure 3B, b: green curve). The largest photocurrent was achieved by the NP DNA–SiW_{12}@CdS NP modification (Figure 3B, c: dark blue curve) because of the strong synergistic effect on the photoelectronic phenomenon that occurred within the association of SiW_{12}@CdS NPs. Here, the photocurrent response of the as-prepared PEC biosensor with the outmost layer of NP DNA–SiW_{12}@CdS NPs established the maximum photocurrent monitoring range.

From the spectrum analysis in Figures 1D, E and photocurrent response analysis in Figure 3B, the intense PEC response occurrence mechanism for the largest photocurrent with SiW_{12}@CdS QDs can be illustrated, as shown in Figure 3C. The SiW_{12}@CdS QDs were stimulated under Xe light irradiation, in detail. The highest occupied molecular orbital (HOMO) of both the SiW_{12} and CdS QDs were stimulated to generate photo-electrons (e^-) and photo-holes (h^+) simultaneously; I_3^-/I^- electrolytes donating electrons via I^- to I^0 occurred on the excited HOMO of SiW_{12} through the generated photo-holes (h^+). The photo-electrons naturally transfer to the lowest unoccupied molecular orbital (LUMO) of SiW_{12} and then to the LUMO of CdS QDs due to the close contact between them, with a matched energy level (0.4 eV difference between 5.87 and 5.47 eV). Successfully, the photo-electrons finally moved to the ITO external circuit to generate photocurrent, and the generated photo-holes (h^+) from the HOMO of CdS QDs are transferred to the HOMO of SiW_{12} to complete the PEC procedure (Liang et al., 2015; Kokal et al., 2016; Li et al., 2016; Shi et al., 2018; Su S. et al., 2022; Kar et al., 2023). The enhanced PEC response of SiW_{12}@CdS QDs to bare CdS QDs is attributed to the increased photogenerated electron

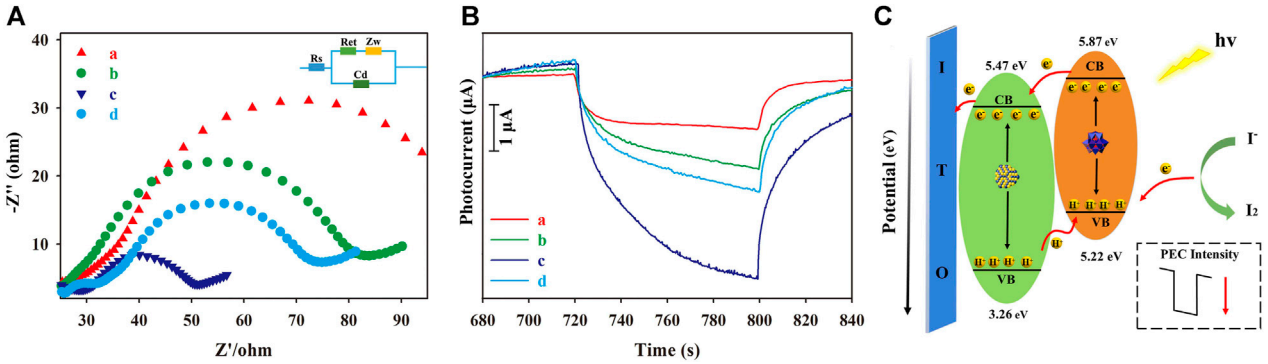

FIGURE 3
(A) EIS spectra of each modification of the ITO slide; **(B)** Photocurrent response of each modification of the PEC biosensor; **(C)** Schematic of the PEC mechanism of the as-prepared biosensor. (a) ITO/Au NP–CS; (b) ITO/Au NP–CS/arm-cDNA, pDNA; (c) ITO/Au NP–CS/arm-cDNA, pDNA/NP DNA–SiW_{12}@CdS QDs; (d) ITO/Au NP–CS/arm-cDNA, pDNA/NP DNA–SiW_{12}@CdS QDs/15-nM HPV 16. The measurements were performed under working conditions of 5 mmol L^{-1} of I_3^- and 0.5 mol L^{-1} of I^- solution.

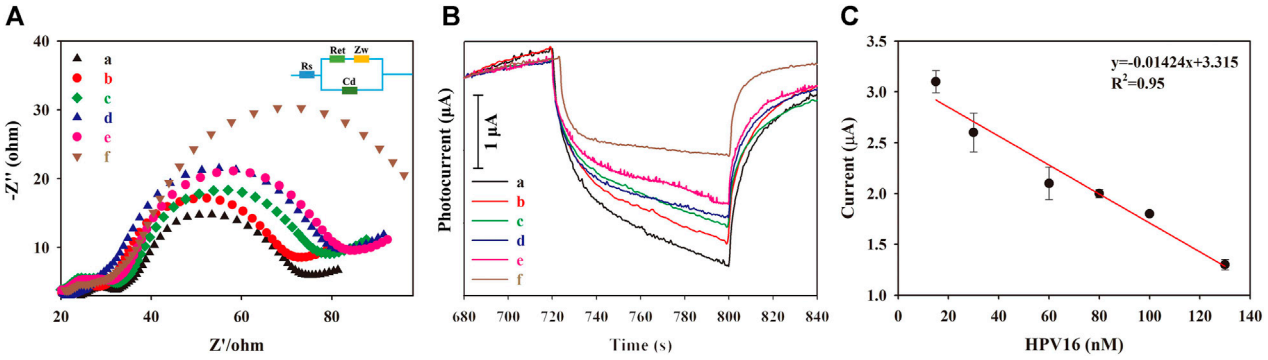

FIGURE 4
(A) EIS spectra of (a) 15 nM, (b) 30 nM, (c) 60 nM, (d) 80 nM, (e) 100 nM, and (f) 130 nM. **(B)** Photocurrent responses of (a) 15 nM, (b) 30 nM, (c) 60 nM, (d) 80 nM, (e) 100 nM, and (f) 130 nM. **(C)** PEC linear relationship of HPV 16 DNA detection.

energy of 0.4 eV from the strong synergistic effect resulting from the association of SiW_{12}@CdS NPs realizing the outstretched band gap from a HOMO of 3.26 eV to LUMO of 5.87 eV.

3.4 Detection of HPV 16 DNA

For the detection of HPV 16 DNA, a series of target DNA samples of different concentrations were incubated in the PEC biosensor, and PEC detection was performed accordingly. EIS spectra after this target DNA incubation were also investigated, as depicted in Figure 4 A, and the observed R_{et} value increased gradually with increasing HPV 16 DNA concentrations (15–130 nm), which was predictable because of the increasing steric hindrance. Conversely, the measured PEC response of the biosensor gradually decreased (Figure 4B), exhibiting a PEC quenching phenomenon caused by the addition of T7 exonuclease in the DNA walker cycle process (Scheme 1B) to release the corresponding associated SiW_{12}@CdS NPs from the PEC biosensor. Finally, the detection of HPV 16 DNA achieved the expected performance of linear quantitative determination, as shown in Figure 4C. The PEC response had a linear relationship with the concentration of the target DNA, ranging from 15 to 130 nM, with an LOD of 0.8 nM, according to Eq. 1:

$$C_L = \frac{K \cdot S_b}{m}; \quad (1)$$

C_L: LOD;S_b: Blank standard deviation;m: The slope of the calibration curve in the low concentration range that was analyzed;K: Confidence coefficient; the value is 3.

All required photocurrent values are listed in Supplementary Table S1.

3.5 Specificity, repeatability, and stability of as-prepared biosensor

Specificity is critical to verify the accuracy and sensitivity of PEC biosensors, indicating their anti-jamming capability. Different HPV

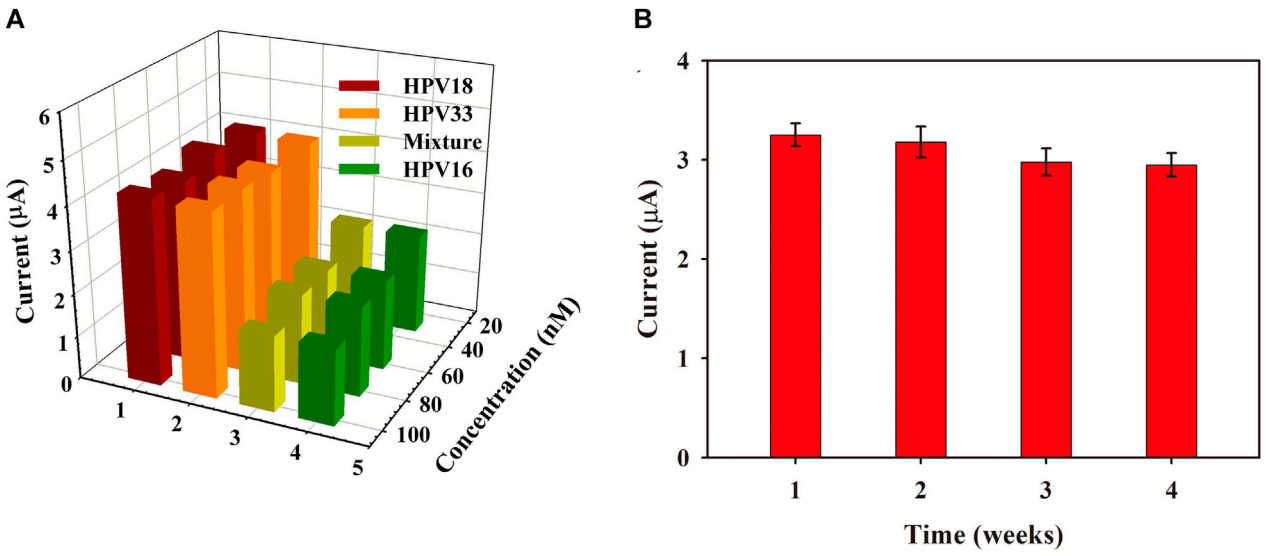

FIGURE 5
(A) Specificity of PEC biosensor against HPV 18 DNA, HPV 33 DNA, HPV16 DNA, and a mixture of all solutions mentioned above (30, 60, 80, and 100 nmol). **(B)** The photocurrent response of the biosensor stored at different times (error bars show S.D., n = 3).

subtypes of HPV 18 DNA and HPV 33 DNA were selected as potential disruptors for specific studies of the as-prepared PEC biosensor. As shown in Figure 5 A, the presence of the target HPV 16 DNA (Figure 5A, green column) or target DNA-containing mixture (Figure 5A, yellow-green column) showed an obvious decrease in the PEC response, whereas the highly homologous interference of HPV 18 DNA and HPV 33 DNA would not promote the biological DNA walker cycle process to decrease the photocurrent, indicating the remarkable specificity of the proposed PEC biosensor. For the stability test of the as-prepared PEC biosensor, the fabricated ITO electrodes were preserved at 4°C for 1–4 weeks, and three parallel experiments were conducted every week. As shown in Figure 5B, the PEC response was 90.77% of the initial value after 4 weeks of storage, indicating the significant stability of the as-prepared PEC biosensor. Moreover, within one PEC measurement process, 7 times consecutive light "on/off" cycles were performed to evaluate its repeatability. As shown in Supplementary Figure S2, the photocurrent response exhibited a steady signal with an incredibly small variation, and the relative standard deviation was 6.37%, indicating the distinguished reproducibility of the as-prepared PEC biosensor.

4 Conclusion

In summary, a highly sensitive PEC biosensor for detecting HPV 16 DNA, fabricated using SiW_{12}@CdS QDs and Au NP/CS gel, was successfully prepared for the first time. The as-prepared SiW_{12}@CdS QDs showed an enhanced photoelectric response and high stability after being combined with NP DNA; with the Au NP/CS gel as the first layer on the ITO slides, a series of biochemical DNA primers were incubated to fabricate a multi-site tripodal DNA walker sensing platform coupled with T7 exonuclease. Due to the remarkable conductivity and LSPR of Au NPs, the photosensitivity of the as-prepared biosensor was further improved under I_3^-/I^- electrolytes and avoided the use of other regents toxic to living organisms, and a photocurrent quenching mechanism within the detection process of the as-prepared PEC biosensor was perfectly executed. Finally, under optimized conditions, the as-prepared biosensor protocol demonstrated wide linear ranges (15–130 nM), with an LOD of 0.8 nM and high selectivity, stability, and reproducibility. Furthermore, the proposed PEC biosensor platform offers a reliable and promising pathway for detecting other biological molecules.

Data availability statement

The datasets presented in this study can be found in online repositories. The names of the repository/repositories and accession number(s) can be found in the article/Supplementary Material.

Author contributions

YaC: conceptualization, methodology, investigation, visualization, writing—original draft preparation, and funding acquisition. CS: data curation, visualization, software, and validation. YuC: conceptualization, data curation, visualization, software, and validation. JW: data curation, visualization, software, and validation. ZZ: data curation, visualization, software, and validation. YL: data curation, visualization, software, and validation. SG: visualization, software, and validation. ZL: data curation, visualization, and validation. XL: supervision, conceptualization, Writing—reviewing and editing, project administration, and funding acquisition. LS: supervision, conceptualization, writing—reviewing and editing, project administration, and funding acquisition. DZ: supervision, conceptualization, writing—reviewing and editing, project

administration, and funding acquisition. All authors contributed to the article and approved the submitted version.

Funding

This work was supported by the National Natural Science Foundation of China (No. 21801153, 31970636); International (regional) cooperative research and exchange programs (No. 32211530422); Shandong Institute of Medical device and pharmaceutical packaging inspection program (NB202203); Academic promotion program of Shandong First Medical University (No. 2019LJ003) and Wujiang Development Zone Chongben Technology Leading Talent Plan.

Conflict of interest

Author ZL was employed by Suzhou KunTao Intelligent Manufacturing Technology Co., Ltd.

The remaining authors declare that the research was conducted in the absence of any commercial or financial relationships that could be construed as a potential conflict of interest.

Publisher's note

All claims expressed in this article are solely those of the authors and do not necessarily represent those of their affiliated organizations, or those of the publisher, the editors and the reviewers. Any product that may be evaluated in this article, or claim that may be made by its manufacturer, is not guaranteed or endorsed by the publisher.

Supplementary material

The Supplementary Material for this article can be found online at: https://www.frontiersin.org/articles/10.3389/fbioe.2023.1193052/full#supplementary-material

References

Ahamad, T., Majeed Khan, M. A., Kumar, S., Ahamed, M., Shahabuddin, M., and Alhazaa, A. N. (2016). CdS quantum dots: Growth, microstructural, optical and electrical characteristics. *Appl. Phys. B Lasers Opt.* 122, 179. doi:10.1007/s00340-016-6455-3

Aiken, J. D., and Finke, R. G. (1999). A review of modern transition-metal nanoclusters: Their synthesis, characterization, and applications in catalysis. *J. Mol. Catal. A Chem.* 145, 1–44. doi:10.1016/s1381-1169(99)00098-9

Alizadeh, M., and Yadollahi, B. (2022). A niobium polyoxometalate-folic acid conjugate as a hybrid drug for cancer therapeutics. *New J. Chem.* 46, 18199–18206. doi:10.1039/d2nj01766k

Bijelic, A., Aureliano, M., and Rompel, A. (2019). Polyoxometalates as potential next-generation metallodrugs in the combat against cancer. *Angew. Chem. - Int. Ed.* 58, 2980–2999. doi:10.1002/anie.201803868

Boulmier, A., Vacher, A., Zang, D., Yang, S., Saad, A., Marrot, J., et al. (2018). Anderson-type polyoxometalates functionalized by tetrathiafulvalene groups: Synthesis, electrochemical studies, and NLO properties. *Inorg. Chem.* 57, 3742–3752. doi:10.1021/acs.inorgchem.7b02976

Cao, Y., Chen, Q., Shen, C., and He, L. (2019). Polyoxometalate-based catalysts for CO_2 conversion. *Molecules* 24, 2069. doi:10.3390/molecules24112069

Chen, J. J., Symes, M. D., and Cronin, L. (2018). Highly reduced and protonated aqueous solutions of $[P_2W_{18}O_{62}]^{6-}$ for on-demand hydrogen generation and energy storage. *Nat. Chem.* 10, 1042–1047. doi:10.1038/s41557-018-0109-5

Chou, H. T., Huang, W. H., Wu, T. M., Yu, Y. K., and Hsu, H. C. (2017). LSPR effects of Au nanoparticles/ZnO nano-composite films. *Sens. Bio-Sensing Res.* 14, 17–20. doi:10.1016/j.sbsr.2017.04.003

Domingues, R. P., Rodrigues, M. S., Proença, M., Costa, D., Alves, E., Barradas, N. P., et al. (2018). Thin films composed of Au nanoparticles embedded in AlN: Influence of metal concentration and thermal annealing on the LSPR band. *Vacuum* 157, 414–421. doi:10.1016/j.vacuum.2018.09.013

Dong, Y., Han, Q., Hu, Q., Xu, C., Dong, C., Peng, Y., et al. (2021). Carbon quantum dots enriching molecular nickel polyoxometalate over CdS semiconductor for photocatalytic water splitting. *Appl. Catal. B Environ.* 293, 120214. doi:10.1016/j.apcatb.2021.120214

Fabre, B., Falaise, C., and Cadot, E. (2022). Polyoxometalates-functionalized electrodes for (Photo)Electrocatalytic applications: Recent advances and prospects. *ACS Catal.* 12, 12055–12091. doi:10.1021/acscatal.2c01847

Feyziazar, M., Hasanzadeh, M., Farshchi, F., Saadati, A., and Hassanpour, S. (2020). An innovative method to electrochemical branching of chitosan in the presence of copper nanocubics on the surface of glassy carbon and its electrical behaviour study: A new platform for pharmaceutical analysis using electrochemical sensors. *React. Funct. Polym.* 146, 104402. doi:10.1016/j.reactfunctpolym.2019.104402

Figueiredo, N. M., Serra, R., and Cavaleiro, A. (2021). Robust lspr sensing using thermally embedded Au nanoparticles in glass substrates. *Nanomaterials* 11, 1592. doi:10.3390/nano11061592

Garland, L. H. (1953). Cancer diagnosis. *J. Am. Med. Assoc.* 152, 75. doi:10.1001/jama.1953.03690010081027

Girardi, M., Blanchard, S., Griveau, S., Simon, P., Fontecave, M., Bedioui, F., et al. (2015). Electro-assisted reduction of CO_2 to CO and formaldehyde by $(TOA)_6[\alpha\text{-}SiW_{11}O_{39}Co(\_)]$ polyoxometalate. *Eur. J. Inorg. Chem.* 2015, 3642–3648. doi:10.1002/ejic.201500389

Gu, J., Chen, W., Shan, G. G., Li, G., Sun, C., Wang, X. L., et al. (2021). The roles of polyoxometalates in photocatalytic reduction of carbon dioxide. *Mat. Today Energy.* 21, 100760. doi:10.1016/j.mtener.2021.100760

Gul, E., Rahman, G., Wu, Y., Bokhari, T. H., Rahman, A., Zafar, A., et al. (2022). An amphiphilic polyoxometalate-CNT nanohybrid as a highly efficient enzyme-free electrocatalyst for H_2O_2 sensing. *New J. Chem.* 46, 16280–16288. doi:10.1039/d2nj03112d

Guo, S. X., Li, F., Chen, L., Macfarlane, D. R., and Zhang, J. (2018). Polyoxometalate-promoted electrocatalytic CO_2 reduction at nanostructured silver in dimethylformamide. *ACS Appl. Mat. Interfaces.* 10, 12690–12697. doi:10.1021/acsami.8b01042

Guo, W., Lv, H., Chen, Z., Sullivan, K. P., Lauinger, S. M., Chi, Y., et al. (2016). Self-assembly of polyoxometalates, Pt nanoparticles and metal-organic frameworks into a hybrid material for synergistic hydrogen evolution. *J. Mat. Chem. A* 4, 5952–5957. doi:10.1039/c6ta00011h

He, P., Xu, B., Xu, X., Song, L., and Wang, X. (2016). Surfactant encapsulated palladium-polyoxometalates: Controlled assembly and their application as single-atom catalysts. *Chem. Sci.* 7, 1011–1015. doi:10.1039/c5sc03554f

Helmink, B. A., Khan, M. A. W., Hermann, A., Gopalakrishnan, V., and Wargo, J. A. (2019). The microbiome, cancer and cancer therapy. *Nat. Med.* 25, 377–388. doi:10.1038/s41591-019-0377-7

Huang, C., Wang, X., Zhang, Z., Zhang, L., Zang, D., Ge, S., et al. (2022). Photoelectrochemical platform with tailorable anode-cathode activities based on semiconductors coupling DNA walker for detection of MiRNA. *Sensors Actuators B Chem.* 365, 131969. doi:10.1016/j.snb.2022.131969

Huang, Y., Sun, Y., Zheng, X., Aoki, T., Pattengale, B., Huang, J., et al. (2019). Atomically engineering activation sites onto metallic 1T-MoS_2 catalysts for enhanced electrochemical hydrogen evolution. *Nat. Commun.* 10, 982. doi:10.1038/s41467-019-08877-9

Jampasa, S., Siangproh, W., Laocharoensuk, R., Yanatatsaneejit, P., Vilaivan, T., and Chailapakul, O. (2018). A new DNA sensor design for the simultaneous detection of HPV type 16 and 18 DNA. *Sensors Actuators, B Chem.* 265, 514–521. doi:10.1016/j.snb.2018.03.045

Jeong, W., Hui, K. S., Hui, K. N., Cho, Y. R., and Cho, K. M. (2017). Tunable emission properties of CdSe/CdS quantum dots by Ce doping. *J. Mat. Sci. Mat. Electron.* 28, 17331–17337. doi:10.1007/s10854-017-7665-0

Ji, Y., Hu, J., Biskupek, J., Kaiser, U., Song, Y. F., and Streb, C. (2017). Polyoxometalate-based bottom-up fabrication of graphene quantum dot/manganese vanadate composites as lithium ion battery anodes. *Chem. - A Eur. J.* 23, 16637–16643. doi:10.1002/chem.201703851

Ji, Y., Huang, L., Hu, J., Streb, C., and Song, Y. F. (2015). Polyoxometalate-functionalized nanocarbon materials for energy conversion, energy storage and sensor systems. *Energy Environ. Sci.* 8, 776–789. doi:10.1039/c4ee03749a

Kar, A., Dagar, P., Kumar, S., Singh Deo, I., Vijaya Prakash, G., and Ganguli, A. K. (2023). Photoluminescence and lifetime studies of C-dot decorated CdS/$ZnFe_2O_4$ composite designed for photoelectrochemical applications. *J. Photochem. Photobiol. A Chem.* 439, 114612. doi:10.1016/j.jphotochem.2023.114612

Kay, P., Allan, B., Denny, L., Hoffman, M., and Williamson, A. L. (2005). Detection of HPV 16 and HPV 18 DNA in the blood of patients with cervical cancer. *J. Med. Virol.* 75, 435–439. doi:10.1002/jmv.20294

Kokal, R. K., Deepa, M., Ghosal, P., and Srivastava, A. K. (2016). $CuInS_2$/CdS quantum dots and poly(3,4-ethylenedioxythiophene)/carbon-fabric based solar cells. *Electrochim. Acta.* 219, 107–120. doi:10.1016/j.electacta.2016.09.134

Kondinski, A. (2021). Metal-metal bonds in polyoxometalate Chemistry. *Nanoscale* 13, 13574–13592. doi:10.1039/d1nr02357h

Kong, X., Wan, G., Li, B., and Wu, L. (2020). Recent advances of polyoxometalates in multi-functional imaging and photothermal therapy. *J. Mat. Chem. B* 8, 8189–8206. doi:10.1039/d0tb01375g

Kong, Z. C., Liao, J. F., Dong, Y. J., Xu, Y. F., Chen, H. Y., Kuang, D. B., et al. (2018). Core@shell Cspbbr3@zeolitic imidazolate framework nanocomposite for efficient photocatalytic Co_2 reduction. *ACS Energy Lett.* 3, 2656–2662. doi:10.1021/acsenergylett.8b01658

Kruse, J. H., Langer, M., Romanenko, I., Trentin, I., Hernández-Castillo, D., González, L., et al. (2022). Polyoxometalate-soft matter composite materials: Design strategies, applications, and future directions. *Adv. Funct. Mat.* 2022, 2208428. doi:10.1002/adfm.202208428

Lang, Z., Miao, J., Lan, Y., Cheng, J., Xu, X., and Cheng, C. (2020). Polyoxometalates as electron and proton reservoir assist electrochemical CO_2 reduction. *Apl. Mater* 8, 120702. doi:10.1063/5.0031374

Lee, S., Lee, M. H., Shin, H. J., and Choi, D. (2013). Control of density and LSPR of Au nanoparticles on graphene. *Nanotechnology* 24, 275702. doi:10.1088/0957-4484/24/27/275702

Lee, T., Shimura, K., and Kim, D. (2018). Surface modification effects on defect-related photoluminescence in colloidal CdS quantum dots. *Phys. Chem. Chem. Phys.* 20, 11954–11958. doi:10.1039/c7cp07812a

Li, C., Zha, B., and Li, J. (2020a). A SiW_{11}Mn-assisted indium electrocatalyst for carbon dioxide reduction into formate and acetate. *J. CO_2 Util.* 38, 299–305. doi:10.1016/j.jcou.2020.02.008

Li, N., Fang, S., Sun, Z., Liu, R., and Xu, L. (2016). Investigation on the photoconductivity of polyoxometalates. *RSC Adv.* 6, 81466–81470. doi:10.1039/c6ra15544h

Li, N., Liu, J., Dong, B. X., and Lan, Y. Q. (2020b). Polyoxometalate-based compounds for photo- and electrocatalytic applications. *Angew. Chem. - Int. Ed.* 59, 20779–20793. doi:10.1002/anie.202008054

Liang, R., Chen, R., Jing, F., Qin, N., and Wu, L. (2015). Multifunctional polyoxometalates encapsulated in MIL-100(Fe): Highly efficient photocatalysts for selective transformation under visible light. *Dalt. Trans.* 44, 18227–18236. doi:10.1039/c5dt02986d

Liu, G., Ma, C., Jin, B. K., Chen, Z., and Zhu, J. J. (2018). Direct electrochemiluminescence imaging of a single cell on a chitosan film modified electrode. *Anal. Chem.* 90, 4801–4806. doi:10.1021/acs.analchem.8b00194

Liu, J., Huang, M., Zhang, X., Hua, Z., Feng, Z., Dong, Y., et al. (2022). Polyoxometalate nanomaterials for enhanced reactive oxygen species theranostics. *Coord. Chem. Rev.* 472, 214785. doi:10.1016/j.ccr.2022.214785

Liu, J. X., Zhang, X. B., Li, Y. L., Huang, S. L., and Yang, G. Y. (2020). Polyoxometalate functionalized architectures. *Coord. Chem. Rev.* 414, 213260. doi:10.1016/j.ccr.2020.213260

Liu, J., Zhang, H., Tang, D., Zhang, X., Yan, L., Han, Y., et al. (2014). Carbon quantum dot/silver nanoparticle/polyoxometalate composites as photocatalysts for overall water splitting in visible light. *ChemCatChem* 6, 2634–2641. doi:10.1002/cctc.201402227

Liu, X., Braun, G. B., Qin, M., Ruoslahti, E., and Sugahara, K. N. (2017). *In vivo* cation exchange in quantum dots for tumor-specific imaging. *Nat. Commun.* 8, 343. doi:10.1038/s41467-017-00153-y

Luo, Z., Musaev, D. G., Lian, T., Hill, C. L., Zhang, N., Zhang, L., et al. (2013). Electron transfer dynamics in semiconductor-chromophore-polyoxometalate catalyst photoanodes. *J. Phys. Chem. C* 117, 918–926. doi:10.1021/jp312092u

Mallick, S., Kumar, P., and Koner, A. L. (2019). Freeze-resistant cadmium-free quantum dots for live-cell imaging. *ACS Appl. Nano Mat.* 2, 661–666. doi:10.1021/acsanm.8b02231

Min, H., Qi, Y., Chen, Y., Zhang, Y., Han, X., Xu, Y., et al. (2019). Synthesis and imaging of biocompatible graphdiyne quantum dots. *ACS Appl. Mat. Interfaces* 11, 32798–32807. doi:10.1021/acsami.9b12801

Misra, A., Kozma, K., Streb, C., and Nyman, M. (2020). Beyond charge balance: Counter-cations in polyoxometalate Chemistry. *Angew. Chem. - Int. Ed.* 59, 596–612. doi:10.1002/anie.201905600

Mitchell, S. G., Mart, R., and Martín-Rapún, R. (2022). Polyoxometalate-peptide hybrid materials: From structure-property relationships to applications. *Chem. Sci.* 14, 10–28. doi:10.1039/d2sc05105b

Morgan, D., and Kelley, D. F. (2018). Role of surface states in silver-doped CdSe and CdSe/CdS quantum dots. *J. Phys. Chem. C* 122, 10627–10636. doi:10.1021/acs.jpcc.8b02776

Nanocubes, C. O. C., Shi, H., Che, Y., Rong, Y., Wang, J., Wang, Y., et al. (2023). Visual/photoelectrochemical off-on sensor based on Cu/Mn double-doped CeO_2 and branched sheet embedded. *Biosensors* 13, 227. doi:10.3390/bios13020227

Nguyen, D., Nguyen, H. A., Lyding, J. W., and Gruebele, M. (2017). Imaging and manipulating energy transfer among quantum dots at individual dot resolution. *ACS Nano* 11, 6328–6335. doi:10.1021/acsnano.7b02649

Nie, Y., Zhang, X., Zhang, Q., Liang, Z., Ma, Q., and Su, X. (2020). A novel high efficient electrochemiluminescence sensor based on reductive Cu(I) particles catalyzed Zn-doped MoS_2 QDs for HPV 16 DNA determination. *Biosens. Bioelectron.* 160, 112217. doi:10.1016/j.bios.2020.112217

Park, Y., Jeong, S., and Kim, S. (2017). Medically translatable quantum dots for biosensing and imaging. *J. Photochem. Photobiol. C Photochem. Rev.* 30, 51–70. doi:10.1016/j.jphotochemrev.2017.01.002

Sarver, P. J., Bissonnette, N. B., and Macmillan, D. W. C. (2021). Decatungstate-catalyzed C(Sp^3)-H sulfinylation: Rapid access to diverse organosulfur functionality. *J. Am. Chem. Soc.* 143, 9737–9743. doi:10.1021/jacs.1c04722

Shi, H., Li, N., Sun, Z., Wang, T., and Xu, L. (2018). Interface modification of titanium dioxide nanoparticles by titanium-substituted polyoxometalate doping for improvement of photoconductivity and gas sensing applications. *J. Phys. Chem. Solids.* 120, 57–63. doi:10.1016/j.jpcs.2018.04.014

Shi, P., Wang, X., Zhang, H., Sun, Q., Li, A., Miao, Y., et al. (2022). Boosting simultaneous uranium decorporation and reactive oxygen species scavenging efficiency by lacunary polyoxometalates. *ACS Appl. Mat. Interfaces* 14, 54423–54430. doi:10.1021/acsami.2c11226

Shi, Q., Li, Z., Chen, L., Zhang, X., Han, W., Xie, M., et al. (2019). Synthesis of SPR Au/$BiVO_4$ quantum dot/rutile-TiO_2 nanorod array composites as efficient visible-light photocatalysts to convert CO_2 and mechanism insight. *Appl. Catal. B Environ.* 244, 641–649. doi:10.1016/j.apcatb.2018.11.089

Shi, Y., Zhang, J., Huang, H., Cao, C., Yin, J., Xu, W., et al. (2020). Fe-doped polyoxometalate as acid-aggregated nanoplatform for NIR-II photothermal-enhanced chemodynamic therapy. *Adv. Healthc. Mat.* 9, 2000005–2000010. doi:10.1002/adhm.202000005

Smith, C. T., Leontiadou, M. A., Clark, P. C. J., Lydon, C., Savjani, N., Spencer, B. F., et al. (2017). Multiple exciton generation and dynamics in InP/CdS colloidal quantum dots. *J. Phys. Chem. C* 121, 2099–2107. doi:10.1021/acs.jpcc.6b11744

Su, S., Li, X., Zhang, X., Zhu, J., Liu, G., Tan, M., et al. (2022b). Keggin-type SiW_{12} encapsulated in MIL-101(Cr) as efficient heterogeneous photocatalysts for nitrogen fixation reaction. *J. Colloid Interface Sci.* 621, 406–415. doi:10.1016/j.jcis.2022.04.006

Su, Y., Ma, C., Chen, W., Xu, X., and Tang, Q. (2022a). Flexible and transparent triboelectric nanogenerators based on polyoxometalate-modified polydimethylsiloxane composite films for harvesting biomechanical energy. *ACS Appl. Nano Mat.* 5, 15369–15377. doi:10.1021/acsanm.2c03407

Suginta, W., Khunkaewla, P., and Schulte, A. (2013). Electrochemical biosensor applications of polysaccharides chitin and chitosan. *Chem. Rev.* 113, 5458–5479. doi:10.1021/cr300325r

Sui, C., Liu, F., Tang, L., Li, X., Zhou, Y., Yin, H., et al. (2018). Photoelectrochemical determination of the activity of protein kinase A by using G-C_3N_4 and CdS quantum dots. *Microchim. Acta.* 185, 541. doi:10.1007/s00604-018-3076-z

Tourneur, J., Fabre, B., Loget, G., Vacher, A., Mériadec, C., Ababou-Girard, S., et al. (2019). Molecular and material engineering of photocathodes derivatized with polyoxometalate-supported {Mo_3S_4} HER catalysts. *J. Am. Chem. Soc.* 141, 11954–11962. doi:10.1021/jacs.9b03950

Ueda, T. (2018). Electrochemistry of polyoxometalates: From fundamental aspects to applications. *ChemElectroChem* 5, 823–838. doi:10.1002/celc.201701170

Vesel, A. (2023). Deposition of chitosan on plasma-treated polymers-A review. *Polymers* 15, 1109. doi:10.3390/polym15051109

Wang, F., Liu, Y., Zhang, L., Zhang, Z., Huang, C., Zang, D., et al. (2022a). Photoelectrochemical biosensor based on CdS quantum dots anchored H-bn nanosheets and tripodal DNA walker for sensitive detection of MiRNA-141. *Anal. Chim. Acta* 1226, 340265. doi:10.1016/j.aca.2022.340265

Wang, L., Nie, Y., Zhang, X., Liang, Z., Wang, P., Ma, Q., et al. (2022b). A novel Eu^{3+} doped polydopamine nano particles/reductive copper particle hydrogel-based ECL sensor for HPV 16 DNA detection. *Microchem. J.* 181, 107818. doi:10.1016/j.microc.2022.107818

Wang, Y., Wu, Z., Yu, H., Han, S., and Wei, Y. (2020). Highly efficient oxidation of alcohols to carboxylic acids using a polyoxometalate-supported chromium(III) catalyst and CO_2. *Green Chem.* 22, 3150–3154. doi:10.1039/d0gc00388c

Weiss, E. A. (2017). Designing the surfaces of semiconductor quantum dots for colloidal photocatalysis. *ACS Energy Lett.* 2, 1005–1013. doi:10.1021/acsenergylett.7b00061

Wen, M., Mori, K., Kuwahara, Y., and Yamashita, H. (2017). Plasmonic Au@Pd nanoparticles supported on a basic metal-organic framework: Synergic boosting of H_2 production from formic acid. *ACS Energy Lett.* 2, 1–7. doi:10.1021/acsenergylett.6b00558

Xiao, H. P., Hao, Y. S., Li, X. X., Xu, P., Huang, M. D., and Zheng, S. T. (2022). A water-soluble antimony-rich polyoxometalate with broad-spectrum antitumor activities. *Angew. Chem. Int. Ed.* 61, e202210019. doi:10.1002/anie.202210019

Xing, X., Liu, R., Yu, X., Zhang, G., Cao, H., Yao, J., et al. (2013). Self-assembly of CdS quantum dots with polyoxometalate encapsulated gold nanoparticles: Enhanced photocatalytic activities. *J. Mat. Chem. A* 1, 1488–1494. doi:10.1039/c2ta00624c

Xu, Q., Gao, J., Wang, S., Wang, Y., Liu, D., and Wang, J. (2021). Quantum dots in cell imaging and their safety issues. *J. Mat. Chem. B* 9, 5765–5779. doi:10.1039/d1tb00729g

Yu, F. Y., Lang, Z. L., Yin, L. Y., Feng, K., Xia, Y. J., Tan, H. Q., et al. (2020b). Pt-O bond as an active site superior to Pt^0 in hydrogen evolution reaction. *Nat. Commun.* 11, 490. doi:10.1038/s41467-019-14274-z

Yu, H., Haviv, E., and Neumann, R. (2020a). Visible-light photochemical reduction of CO_2 to CO coupled to hydrocarbon dehydrogenation. *Angew. Chem.* 132, 6278–6282. doi:10.1002/ange.201915733

Yu, J., Zhang, H., Xu, W., Liu, G., Tang, Y., and Zhao, D. (2021). Quantized doping of CdS quantum dots with twelve gold atoms. *Chem. Commun.* 57, 6448–6451. doi:10.1039/d1cc02460d

Zang, D., Huang, Y., Li, Q., Tang, Y., and Wei, Y. (2019). Cu dendrites induced by the anderson-type polyoxometalate $NiMo_6O_{24}$ as a promising electrocatalyst for enhanced hydrogen evolution. *Appl. Catal. B Environ.* 249, 163–171. doi:10.1016/j.apcatb.2019.02.039

Zang, D., Huo, Z., Yang, S., Li, Q., Dai, G., Zeng, M., et al. (2022). Layer by layer self-assembled hybrid thin films of porphyrin/polyoxometalates@Pt nanoparticles for photo & electrochemical application. *Mat. Today Commun.* 31, 103811. doi:10.1016/j.mtcomm.2022.103811

Zang, D., Li, Q., Dai, G., Zeng, M., Huang, Y., and Wei, Y. (2021). Interface engineering of Mo_8/Cu heterostructures toward highly selective electrochemical reduction of carbon dioxide into acetate. *Appl. Catal. B Environ.* 281, 119426. doi:10.1016/j.apcatb.2020.119426

Zang, D., and Wang, H. (2022). Polyoxometalate-based nanostructures for electrocatalytic and photocatalytic CO_2 reduction. *Polyoxometalates* 1, 9140006. doi:10.26599/pom.2022.9140006

Zhang, J., Zhang, M., Dong, Y., Bai, C., Feng, Y., Jiao, L., et al. (2022b). CdTe/CdSe-Sensitized photocathode coupling with Ni-substituted polyoxometalate catalyst for photoelectrochemical generation of hydrogen. *Nano Res.* 15, 1347–1354. doi:10.1007/s12274-021-3663-x

Zhang, L., Lv, B., Yang, H., Xu, R., Wang, X., Xiao, M., et al. (2019). Quantum-confined Stark effect in the ensemble of phase-pure CdSe/CdS quantum dots. *Nanoscale* 11, 12619–12625. doi:10.1039/c9nr03061a

Zhang, M., Xin, X., Feng, Y., Zhang, J., Lv, H., and Yang, G. Y. (2022a). Coupling Ni-substituted polyoxometalate catalysts with water-soluble CdSe quantum dots for ultraefficient photogeneration of hydrogen under visible light. *Appl. Catal. B Environ.* 303, 120893. doi:10.1016/j.apcatb.2021.120893

Zheng, L., Teng, F., Ye, X., Zheng, H., and Fang, X. (2020). Photo/electrochemical applications of metal sulfide/TiO_2 heterostructures. *Adv. Energy Mat.* 10, 1902355. doi:10.1002/aenm.201902355

frontiers | Frontiers in Bioengineering and Biotechnology

TYPE Original Research
PUBLISHED 25 August 2023
DOI 10.3389/fbioe.2023.1233353

OPEN ACCESS

EDITED BY
Kang Cui,
University of Jinan, China

REVIEWED BY
Xin-Jun Du,
Tianjin University of Science and Technology, China
Xiaonan Yang,
Zhengzhou University, China

*CORRESPONDENCE
Yi Wang,
wildwolf0101@163.com
Hairong Huang,
huanghairong@tb123.org
Weiwei Jiao,
jiaowei310@163.com
Adong Shen,
shenad18@126.com

RECEIVED 02 June 2023
ACCEPTED 15 August 2023
PUBLISHED 25 August 2023

CITATION
Xiao J, Li J, Quan S, Wang Y, Jiang G, Wang Y, Huang H, Jiao W and Shen A (2023), Development and preliminary assessment of a CRISPR–Cas12a-based multiplex detection of *Mycobacterium tuberculosis* complex.
Front. Bioeng. Biotechnol. 11:1233353.
doi: 10.3389/fbioe.2023.1233353

Development and preliminary assessment of a CRISPR–Cas12a-based multiplex detection of *Mycobacterium tuberculosis* complex

Jing Xiao[1], Jieqiong Li[2], Shuting Quan[1], Yacui Wang[1], Guanglu Jiang[3], Yi Wang[4]*, Hairong Huang[3]*, Weiwei Jiao[1]* and Adong Shen[1]*

[1]Laboratory of Respiratory Diseases, Beijing Key Laboratory of Pediatric Respiratory Infection Diseases, Key Laboratory of Major Diseases in Children, National Center for Children's Health, National Clinical Research Center for Respiratory Diseases, National Key Discipline of Pediatrics (Capital Medical University), Beijing Pediatric Research Institute, Ministry of Education, Beijing Children's Hospital, Capital Medical University, Beijing, China, [2]Medical Research Center, Beijing Institute of Respiratory Medicine, Beijing Chao-Yang Hospital, Capital Medical University, Beijing, China, [3]National Tuberculosis Clinical Laboratory, Beijing Key Laboratory for Drug Resistance Tuberculosis Research, Beijing Tuberculosis and Thoracic Tumor Research Institute, Beijing Chest Hospital, Capital Medical University, Beijing, China, [4]Experimental Research Center, Capital Institute of Pediatrics, Beijing, China

Since the onset of the COVID-19 pandemic in 2020, global efforts towards tuberculosis (TB) control have encountered unprecedented challenges. There is an urgent demand for efficient and cost-effective diagnostic technologies for TB. Recent advancements in CRISPR–Cas technologies have improved our capacity to detect pathogens. The present study established a CRISPR–Cas12a-based multiplex detection (designated as MCMD) that simultaneously targets two conserved insertion sequences (IS*6110* and IS*1081*) to detect *Mycobacterium tuberculosis* complex (MTBC). The MCMD integrated a graphene oxide-assisted multiplex recombinase polymerase amplification (RPA) assay with a Cas12a-based trans-cleavage assay identified with fluorescent or lateral flow biosensor (LFB). The process can be performed at a constant temperature of around 37°C and completed within 1 h. The limit of detection (LoD) was 4 copies μL^{-1}, and no cross-reaction was observed with non-MTBC bacteria strains. This MCMD showed 74.8% sensitivity and 100% specificity in clinical samples from 107 patients with pulmonary TB and 40 non-TB patients compared to Xpert MTB/RIF assay (63.6%, 100%). In this study, we have developed a straightforward, rapid, highly sensitive, specific, and cost-effective assay for the multiplex detection of MTBC. Our assay showed superior diagnostic performance when compared to the widely used Xpert assay. The novel approach employed in this study makes a substantial contribution to the detection of strains with low or no copies of IS6110 and facilitates point-of-care (POC) testing for MTBC in resource-limited countries.

KEYWORDS

***Mycobacterium tuberculosis* complex, CRISPR-Cas12a, multiplex detection, fluorescent biosensor, lateral flow biosensor, point-of-care testing**

1 Introduction

Before the outbreak of the coronavirus disease 2019 (COVID-19) pandemic in December 2019, tuberculosis (TB) caused by the *Mycobacterium tuberculosis* complex (MTBC) was the leading cause of death from a single infectious agent worldwide, surpassing the human immunodeficiency virus (HIV) infection (World-Health-Organization, 2020). In 2019, an estimated 10 million people developed TB worldwide, of which 29.0% went undiagnosed and unreported due to the lack of rapid screening and accurate diagnostic techniques (World-Health-Organization, 2020). However, as a result of the COVID-19 pandemic, the proportion of undiagnosed TB among the estimated incident TB worldwide increased to 42.6% (2020) and 39.6% (2021) (World-Health-Organization, 2021; World-Health-Organization, 2022). In China, this proportion increased from 12.6% in 2019 to 25.8% in 2020 and 25.0% in 2021 (World-Health-Organization, 2020; World-Health-Organization, 2021; World-Health-Organization, 2022).

The TB diagnostic tests currently available have certain limitations (MacLean et al., 2020). For example, the bacilli culture, known as the gold standard for laboratory diagnosis of TB, is laborious and time-consuming with moderate accuracy. Immunological tests such as the interferon-gamma release assay (IGRA) cannot differentiate active TB from latent TB infection (LTBI) (Walzl et al., 2018). The PCR-based Xpert MTB/RIF assay (hereinafter referred to as "Xpert"), recommended by the WHO in 2011 (World-Health-Organization, 2011), shows moderate efficacy in diagnosing paucibacillary TB, such as smear-negative pulmonary TB, extra-pulmonary TB, and pediatric TB (Kay et al., 2020; Kohli et al., 2021). Xpert MTB/RIF Ultra, the next-generation Xpert, has been shown to have an improved sensitivity. However, the high costs of using and maintaining Xpert MTB/RIF Ultra hinder their widespread applications in TB diagnostics (Kay et al., 2020; Kohli et al., 2021). Therefore, there is an urgent need to develop sensitive, efficient, and cost-effective diagnostic technologies for TB to effectively control and prevent the spread of the disease.

The clustered regularly interspaced short palindromic repeats (CRISPR)-Cas (CRISPR associated) proteins system, derived from the prokaryotic adaptive immune system, consists of a Cas endonuclease (e.g., Cas9, Cas12a, Cas12b, Cas13a, Cas13b, and Cas14) and a genetically engineered guide RNA (gRNA). It has been observed that Cas and gRNA can form an effective ribonucleoprotein (RNP) complex to degrade foreign nucleic acids complementary to the gRNA sequence. CRISPR–Cas systems have been used extensively in genome editing, gene regulation, and molecular diagnostics. Several Cas endonucleases (i.e., Cas12a, Cas12b, Cas13a, and Cas14) can trans-cleave non-target single-stranded nucleic acids (including ssDNA and ssRNA) after cleaving target nucleic acids, which is termed as collateral cleavage activities. Based on such property, several CRISPR diagnostic platforms, such as CRISPR–Cas13a-based SHERLOCK (Specific High-Sensitivity Enzymatic Reporter UnLOCKing) (Gootenberg et al., 2017), CRISPR–Cas12a-based DETECTR (DNA Endonuclease Targeted CRISPR Tans Reporter) (Chen et al., 2018), HOLMES (One-Hour-Low-cost Multipurpose highly Efficient System) (Li et al., 2018), CRISPR–Cas14-based DETECTR (Harrington et al., 2018), and CRISPR–Cas12b-based HOLMESv2 (Li et al., 2019), have been developed and used for the detection of various pathogens. The CRISPR diagnostic platforms can achieve attomolar sensitivity for detecting target nucleic acids with single-base resolution.

The present study first combined an improved isothermal amplification technique (Graphene oxide-assisted multiplex recombinase polymerase amplification assay, GO-assisted multiplex RPA assay) that simultaneously targets two conserved insertion sequences (IS*6110* and IS*1081*) with a CRISPR–Cas12a-based trans-cleavage assay for a simple, rapid, sensitive, and specific diagnosis of MTBC. The application of these techniques was subsequently validated using clinical samples. This novel and cost-effective detection technique, MTBC CRISPR–Cas12a Multiplex Detection (MCMD), can detect MTBC isolates at point-of-care (POC) in resource-constrained countries or strains with low/no copy numbers of IS*6110*.

2 Materials and methods

2.1 Reagents and instruments

The QIAamp DNA Mini Kit and glass bead-based kit used for DNA extraction were purchased from Qiagen (Hilden, Germany) and CapitalBio Technology Co., Ltd. (Beijing, China). The TwistAmp Basic Kit used for isothermal amplification was purchased from TwistDx (Cambridge, United Kingdom). Graphene oxide (2 mg mL^{-1}) was purchased from Sigma Aldrich (MO, United States), and the CRISPR–Cas enzyme LbCas12a was obtained from GenScript Biotechnology Co., Ltd. (Nanjing, China). Primers, gRNAs, and ssDNA reporter molecules were synthesized by Qingke Biotechnology Co., Ltd. (Beijing, China). Lateral flow biosensors (LFB) were manufactured by HuiDeXing Biotechnology Co., Ltd. (Tianjin, China). DNA concentration was determined using the Nanodrop 2000 instrument (ThermoFisher Scientific, United Kingdom). Isothermal amplification and quantitative fluorescence PCR were performed using Eppendorf AG pro S Mastercycler (Eppendorf, Germany) and the AriaMx Real-Time PCR system (Agilent Technologies, CA, United States), respectively. The gel was imaged with the Gel Doc XR + Imaging System (Bio-Rad, CA, United States).

2.2 Primers, gRNAs and ssDNAs design

Two sets of RPA primers targeting IS*6110* and IS*1081* were designed with Primer Premier 5.0 (Table 1). A BLAST analysis of the GenBank nucleotide database was performed to confirm the specificity of the primers. The gRNAs (Table 1; Figure 1B) were designed against the 20 nt sequence following the protospacer-adjacent motif (PAM) sequences [5'-(T) TTN-3′ on the sense strand or 5′-NAA(A)-3′ on the antisense strand] that served as Cas12a recognition sites. We used two ssDNAs (a fluorescent reporter and a biotin-labeled reporter) (Table 1).

2.3 Bacterial strains and genomic DNA extraction

The MTBC reference strain H37Rv was utilized during the establishment and clinical application of the MCMD technique.

TABLE 1 Sequences of primers, gRNAs and ssDNAs used in this study.

Primers/gRNAs/ssDNAs	Sequences (5′-3′)	Length
Primers		
IS*6110*-RPA-F[a]	ATCAGTGAGGTCGCCCGTCTACTTGGTGTT	30 nt[b]
IS*6110*-RPA-R[c]	CTTCAGCTCAGCGGATTCTTCGGTCGTG	28 nt
IS*1081*-RPA-F	CGCCAGGGCAGCTATTTCCCGGACTGGCTG	30 nt
IS*1081*-RPA-R	CTTGGAAAGCTTTGTCACACCAAGTGTTTCGAC	33 nt
GRNAs		
IS*6110*-gRNA	UAAUUUCUACUAAGUGUAGAUGCUGCGCGGAGACGGUGCGU[d]	41 nt
IS*1081*-gRNA	UAAUUUCUACUAAGUGUAGAUGACCAGGCGCUCCAUCCGGC	41 nt
SsDNAs		
Fluorescent reporter	5′-FAM-TATTATTATTATTT-BHQ1-3′	14 nt
Biotin-labeled reporter	5′-Biotin-TATTATTATTATTT-FAM-3′	14 nt

[a]F, forward.
[b]nt, nucleotide.
[c]R, reverse.
[d]Underlined sequence refers to the region complementary to the IS*6110* or IS*1081* target sequence.

Mycobacterium abscessus was used as a negative control (NC). A total of 27 bacterial strains were used to determine the analytical specificity of MCMD (see Section 2.8). Genomic DNA was extracted using the QIAamp DNA Mini Kit (bacteria strains) or glass bead-based kit (sputum specimens) according to the manufacturer's instructions and stored at −80°C before use. DNA quantity and purity were determined using ultraviolet spectrophotometry at 260 and 280 nm.

2.4 GO-assisted singlex and multiplex RPA assay

The Singlex RPA assay for IS*6110* (or IS*1081*) was performed according to the manual (TwistAmp Basic Kit). A 50 μL reaction mixture was prepared as follows: dry reaction pellet, 29.5 μL rehydration buffer, 0.48 μM forward and reverse primers, 1 ng μL^{-1} target template 2 μL (5 μL for sputum specimen), and 14 mM magnesium acetate. It has been reported that RPA is an error-prone reaction and usually yields non-specific amplicons and primer dimers (Munawar, 2022). Different concentrations of GO (0, 2, 4, 8, 16, 24, 32 μg mL^{-1}) were added into the RPA mixtures at 38°C for 30 min to overcome the technical disadvantages of RPA. The reaction mixtures were incubated at 35.4°C–39.9°C (with 0.5°C–1.0°C intervals) for 20–40 min (with 10 min intervals) to determine the optimal reaction temperatures and amplification times for the RPA assay. Finally, the optimized operating conditions were used in a subsequent GO-assisted multiplex RPA assay, from which two sets of RPA primer (IS*6110* and IS*1081*) were added in one reaction system at a total concentration of 0.48 μM (1:1). *Mycobacterium abscessus* and double-distilled water (DDW) were used as NC and blank control (BC), respectively. Agarose gel electrophoresis (2.5%) was used to confirm the amplification of the RPA assay.

2.5 CRISPR–Cas12a-based trans-cleavage assay

The CRISPR–Cas12a-based trans-cleavage assay was adopted from previous studies (Chen et al., 2018; Li et al., 2018; Broughton et al., 2020) with some adjustments. Briefly, 41.7 nM of IS*6110*-gRNA and IS*1081*-gRNA (1:1) were preincubated with 33.3 nM LbCas12a in 1× NEBuffer 2.1 (NEB, MA, United States) at 37°C for 10 min to induce Cas12a-gRNA complexes that can be used immediately or stored at 4°C for up to 24 h. Subsequently, the trans-cleavage assay was conducted in a volume of 50 μL mixture, containing 25 μL 2 × NEBuffer 2.1, 13.5 μL Cas12a-gRNA complexes, 250 nM fluorescent reporter molecule, and 2 μL of the RPA products. This trans-cleavage assay was performed at 37°C, and the fluorescence signal was monitored for 20 min. The fluorescence signal increasing more than two-fold compared to BC at 10 min of the trans-cleavage assay was considered positive. A biotin-labeled reporter molecule was used instead of the fluorescent reporter for the LFB readout. After 8 min incubation at 37°C, the LFB assay was performed (see Section 2.6).

2.6 LFB assay

The LFB used for visual readout consists of several main components: sample pad, conjugate pad, nitrocellulose (NC) membrane (reaction region), and absorbent pad mounted on a backing card (Figure 2A). The streptavidin-gold nanoparticles (SA-GNPs) are adhered onto the conjugate pad and used as the indicator reagent, rabbit anti-fluorescein amide (anti-FAM) antibody and biotin-bovine serum albumin (biotin-BSA) are fixed onto the NC membrane and used as control line (CL) and test line (TL) capture reagents, respectively. Twelve microliters of trans-cleavage products and two drops of running buffer (100 mM phosphate-buffered solution, pH 7.4 with 1% Tween 20) were

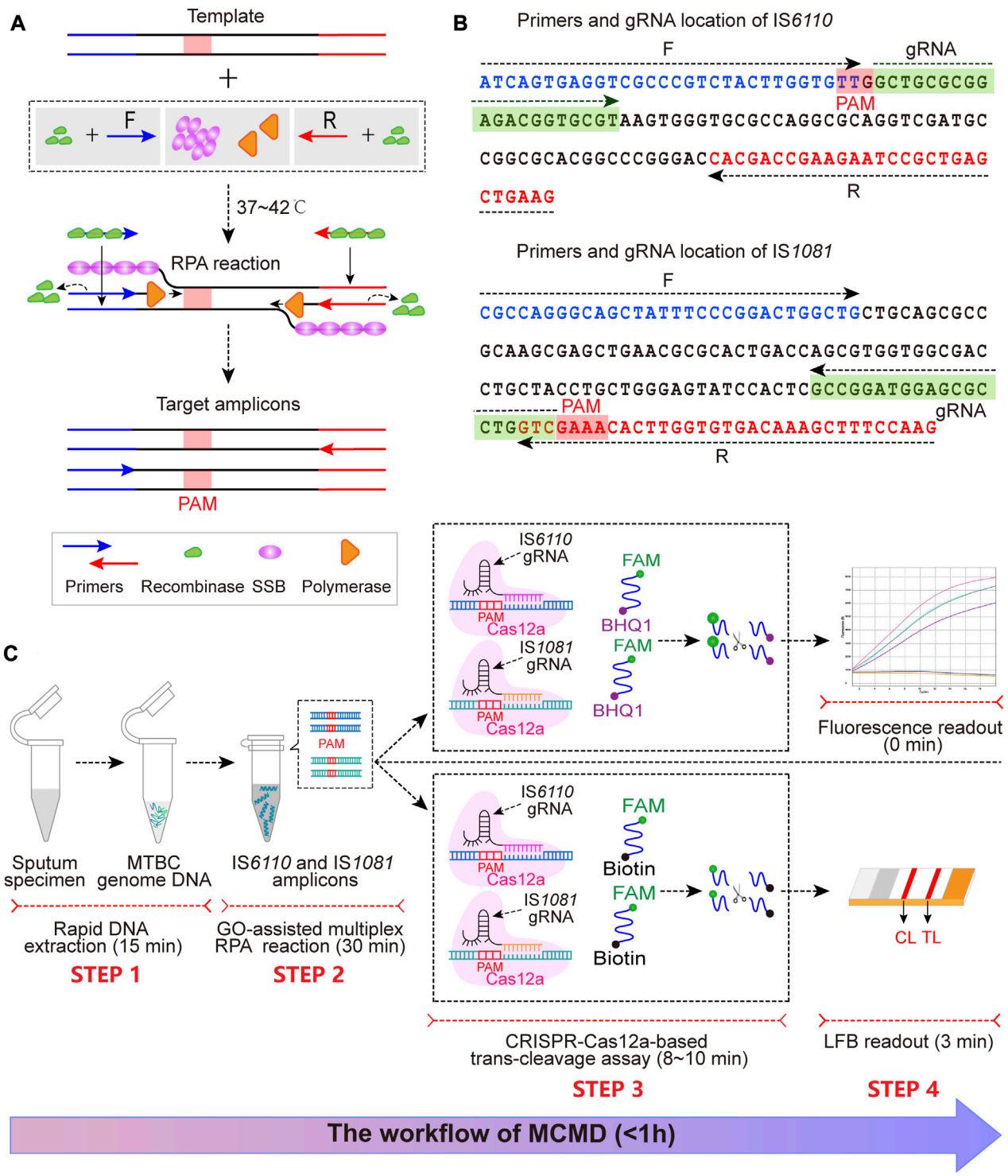

FIGURE 1
The schematic illustration of MCMD workflow. **(A)** The schematic diagram of RPA. At 37°C–42°C, recombinase (green)-primer (blue/red arrow) complexes scan the double-stranded DNA for homologous sequences (blue/red line segments), promoting the initiation of a strand exchange event at the cognate sites. The displaced template strand binds to SSB (magenta) to prevent the ejection of the primer by branch migration. The recombinase disassembles from the primer, which leaves the 3′-end of the oligonucleotide accessible to a DNA polymerase (orange), and this is followed by primer extension. Repetition of this procedure results in exponential amplification of DNA. The PAM sequence is presented in the red box. **(B)** The primer and gRNA design of MCMD. Nucleotide sequences of the amplification products from IS*6110* and IS*1081* are shown. Nucleotide sequences in blue and red are the binding positions of forward (F) and reverse (R) primers, respectively. The selected PAM sequences [(T)TTN on the sense strand or NAA (A) on the antisense strand] and the corresponding gRNA binding sequences are presented in red and green boxes. Right and left arrows signify the sense and complementary sequence, respectively, that are used. **(C)** Schematic illustration of MCMD workflow. MCMD employs four closely connected steps: rapid DNA extraction (15 min, STEP 1), GO-assisted multiplex RPA reaction (30 min, STEP 2), CRISPR–Cas12a-based trans-cleavage assay (8–10 min, STEP 3) and result readout (immediately in fluorescence and 3 min in LFB, STEP 4), which can be completed within 1 h.

10.3389/fbioe.2023.1233353

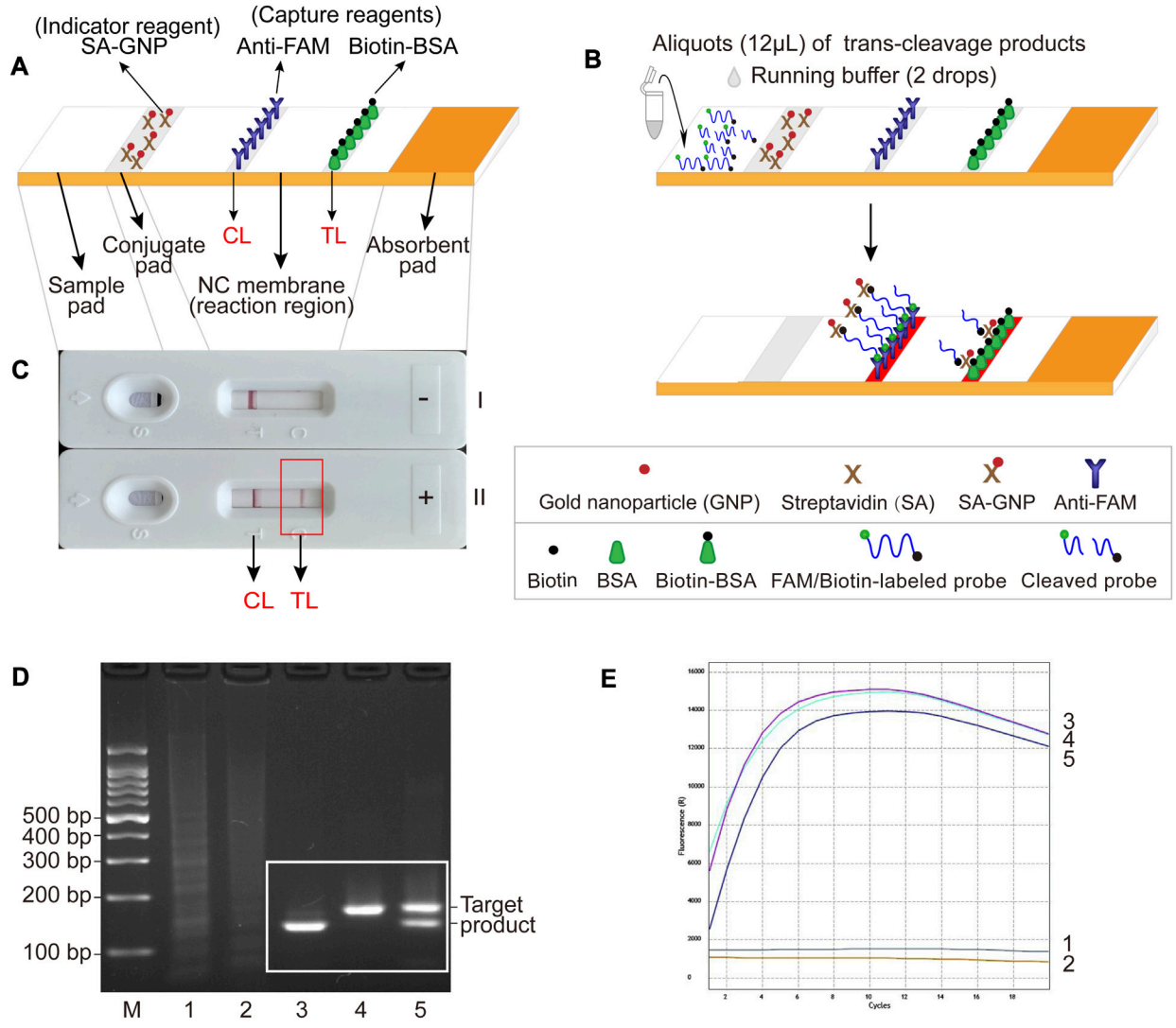

FIGURE 2
The schematic illustration of LFB assay used for visualization and feasibility validation of MCSD and MCMD. **(A)** Details of the LFB. The positions of indicator reagent (SA-GNP) and capture reagents (anti-FAM and biotin-BSA) of LFB are shown on the upper part of the diagram, and four main components (sample pad, conjugate pad, NC membrane and absorbent pad) and two lines (CL and TL) are labeled on the lower part of the diagram. **(B)** The schematic illustration of the LFB assay used for visualization. Twelve microliters of trans-cleavage products and two drops of running buffer were deposited onto the sample pad, and the results were visualized (develop red color) on CL and TL. **(C)** Interpretation of the LFB results. I, negative results (only CL appears); II, positive results (both CL and TL appear). **(D)** Agarose gel electrophoresis results of GO-assisted singlex and multiplex RPA assay. M, DNA marker; 1, blank control; 2, negative control; 3, GO-assisted IS*6110* RPA assay; 4; GO-assisted IS*1081* RPA assay; 5, GO-assisted multiplex RPA assay. **(E)** Real-time fluorescence images of MCSD and MCMD. 1, blank control; 2, negative control; 3, MCSD-IS*6110*; 4, MCSD-IS*1081*; 5, MCMD.

added to the sample pad. The detection results were visualized within 3 min as red bands on the NC membrane.

2.7 Analytical sensitivity of MTBC CRISPR–Cas12a-based Singlex detection (MCSD) and MCMD

The limit of detection (LoD) was determined using 10-fold serial dilutions of genomic DNA from reference strain H37Rv, ranging from 40,000 to 0.4 copies μL^{-1} to assess the analytical sensitivity of CRISPR–Cas12a-based singlex and multiplex detection for MTBC identification. DNA copy numbers per microliter were calculated using the following formula: $(6.02 \times 10^{23}) \times (\text{ng } \mu L^{-1} \times 10^{-9})/(\text{DNA length} \times 660)$. A volume of 2 μL from each DNA dilution was added to the RPA reaction mixture. Each dilution series was performed in triplicate. The lowest positive dilution (twice the fluorescence value of BC) in all replicates was considered the LoD.

2.8 Analytical specificity of MCMD

Reactions were conducted with genomic templates extracted from different bacterial strains, including 1 MTBC reference strain H37Rv, 1 *Mycobacterium bovis* Bacilli Calmette-Guerin (BCG), 8 clinical MTBC strains isolated from TB patients, 10 non-

tuberculous mycobacteria (NTM) strains, and 7 non-mycobacteria strains to determine the analytical specificity of MCMD (Supplementary Table S1). Each strain was tested at least twice.

2.9 Application of MCMD in clinical specimens

This study was approved by the Ethical Committee of Beijing Children's Hospital, Capital Medical University (2020-k-163). A total of 107 patients with suspected active pulmonary TB from Beijing Chest Hospital were enrolled in this study from May to June 2022. The need for informed consent was waived because the sputum specimens used in this study were leftover samples from clinical microbiology tests. According to the Chinese National Standard on Diagnosis for Pulmonary Tuberculosis (WS288-2017, National Health and Family Planning Commission of the People's Republic of China, 2017), the patients were categorized according to the composite reference standard (CRS), which combines the clinical and laboratory diagnostic criteria: (a) definite TB/laboratory-confirmed TB, patients with bacteriological confirmation of MTB (culture, smear, nucleic acid detection, or histopathological evidence positive); (b) probable TB/clinical diagnosed TB, patients with radiologic findings suggestive of TB plus at least one of the following: TB clinical symptoms or signs, positive tuberculin skin test (TST) or IGRA, bronchoscopy or histopathology consistent with TB; and (c) non-TB, patients diagnosed as other diseases and improved in the absence of anti-TB treatment.

Sputum samples (2–3 mL) collected from patients were utilized for TB culture, Xpert, and MCMD assays. A tuberculosis culture was performed using Bactec MGIT 960 system (Becton Dickinson, MD, United States). Xpert (Cepheid, CA, United States) was performed following the manufacturer's protocol. For MCMD, sputum samples were decontaminated and liquefied by adding an equal volume of 4% NaOH, and sputum DNA was extracted using the glass bead-based kit. Subsequently, 5 μL DNA solution was added to the RPA reaction mixture. All samples were detected in duplicate in multiple independent batches, and each batch included a positive control (PC) (H37Rv DNA as the template) and BC. The results from MCMD were compared to TB culture and Xpert to evaluate the diagnostic performance of this new technique.

3 Results

3.1 Schematic mechanism of MCMD

The MCMD integrated GO-assisted multiplex RPA assay that simultaneously targets IS*6110* and IS*1081* with a CRISPR–Cas12a-based trans-cleavage assay at fixed temperatures for MTBC nucleic acid detection. First, the extracted MTBC DNA templates are pre-amplified with three proteases [recombinase, single strand DNA binding protein (SSB), and DNA polymerase] at 37–42°C within 30 min (Figure 1A). Next, in the trans-cleavage stage, the PAM site in the RPA amplicon can guide the CRISPR–Cas12a-IS*6110*(or IS*1081*)-gRNA complex to its location (Figures 1B, C), activating the CRISPR–Cas12a effector. The activated Cas12a has trans-cleavage activity against ssDNA reporter. Finally, the digestion of reporter molecules can be detected via fluorescence or LFB, which confirms the presence of the target genome MTBC. The entire MCMD assay, including rapid DNA extraction (15 min, STEP 1), GO-assisted multiplex RPA reaction (30 min, STEP 2), CRISPR–Cas12a-based trans-cleavage assay (8–10 min, STEP 3), and result readout (immediately in fluorescence and 3 min in LFB, STEP 4), can be completed within 60 min.

For fluorescence readout, the fluorescent reporter, labeled at the 5′-end with a FAM fluorophore (6-carboxyfluorescein) and at the 3′-end with a black hole quencher (BHQ1), is cleaved by the activated Cas12a and released from its quencher, increasing fluorescent signaling (Figure 1C STEP 3, STEP 4). Thus, CRISPR–Cas12a-based trans-cleavage and fluorescence readout can be performed simultaneously.

3.2 Schematic illustration of LFB assay for visualization

For the LFB readout, when the cleaved products are added to the sample pad followed by the running buffer, the running buffer travels along the biosensor through capillary action, rehydrating the indicator reagent (SA-GNPs) in the conjugate pad (Figure 2B). In the negative sample, the uncleaved biotin-labeled reporter molecule (5′-Biotin-TATTATTATTATTT-FAM-3′) binds SA-GNP (via biotin at the 5′ end of the reporter), and it is captured by anti-FAM immobilized on the CL (via FAM at the 3′ end of the reporter), then CL is displayed in red for visualization. In the positive sample, the biotin-labeled reporter cleaved by activated Cas12a binds SA-GNP. It is then captured by biotin-BSA immobilized on the TL, and then TL is visualized. Therefore, the principle of visualization in the LFB assay is that the biotin–SA-GNPs complexes seized by capture reagents (anti-FAM on CL or biotin-BSA on TL) develop red bands (Figure 2C).

3.3 Establishment and optimization of RPA assay

According to our previous study, different concentrations of GO ranging from 4 μg mL^{-1}–32 μg mL^{-1} were added to the GO-assisted singlex RPA assays to improve the specificity of RPA (Wang Y et al., 2020). As shown in Supplementary Figure S1A and S1B, GO concentrations ranging from 8 μg mL^{-1}–16 μg mL^{-1} exhibited good specificity performance with no obvious decrease in RPA product yield. Concentrations less than 4 μg mL^{-1} showed no improvement in amplification specificity, while concentrations above 24 μg mL^{-1} partially inhibited the amplification reactions. Therefore, we recommend 8 μg mL^{-1} as the optimal concentration for GO-assisted RPA assays.

According to Supplementary Figures S1C, S1D, the optimal reaction temperatures for IS*6110*-RPA and IS*1081*-RPA primers were 37.4°C–39.4°C and 37.9°C–38.9°C, respectively. Thus, an ideal temperature range of 37.9°C–38.9°C was recommended for the subsequent GO-assisted multiplex RPA assays, using both IS*6110* and IS*1081* RPA primers in one reaction. As can be seen form Supplementary Figure S1E, RPA products increased with the

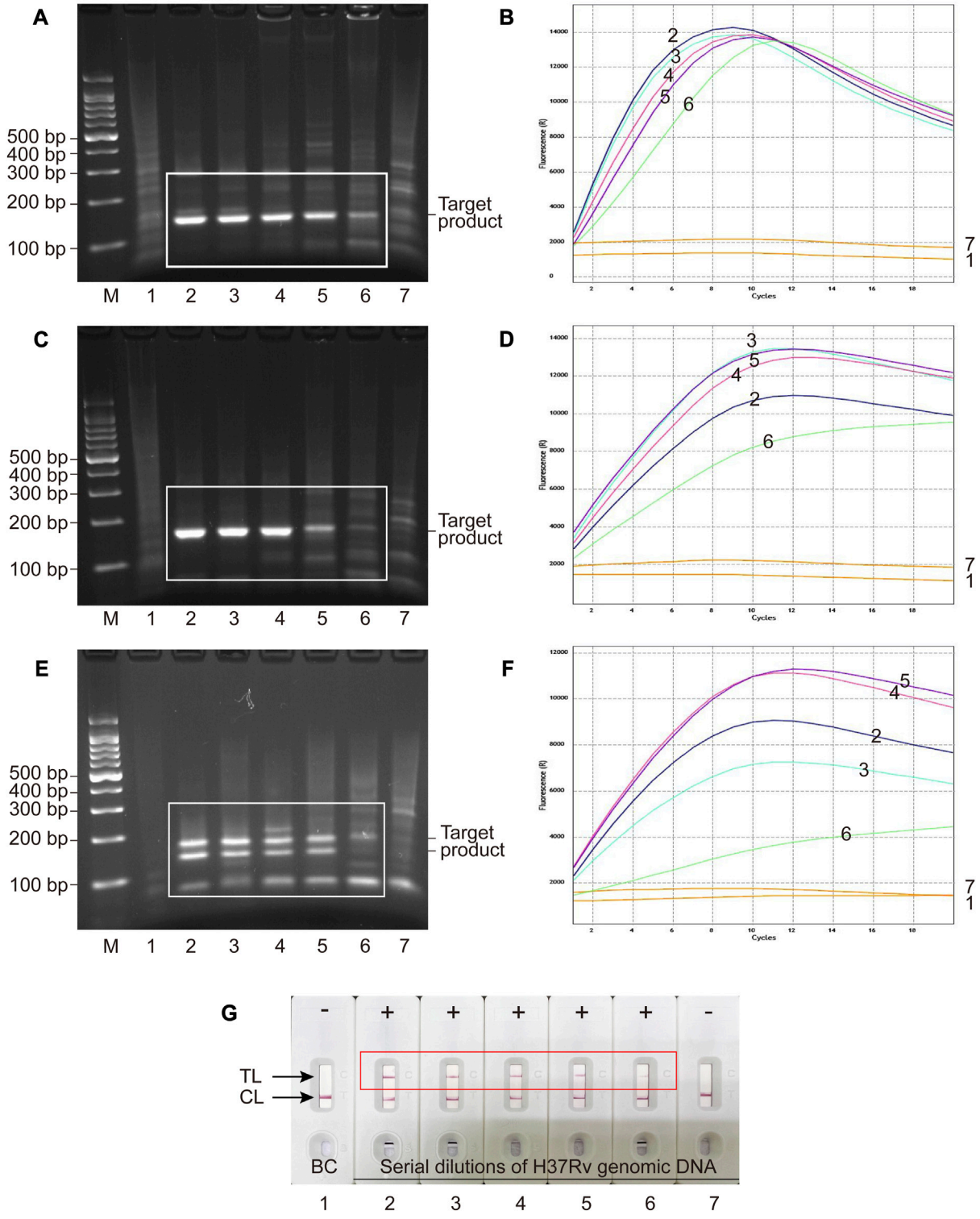

FIGURE 3
Analytical sensitivity of MCSD and MCMD as determined by serially diluted genomic DNA of H37Rv. **(A,C,E)** Agarose gel electrophoresis of GO-assisted IS*6110* RPA assay, IS*1081* RPA assay and multiplex RPA assay. **(B,D,F)** Real-time fluorescence images of MCSD-IS*6110*, MCSD-IS*1081* and MCMD. **(G)** LFB applied for reporting the results of MCMD. M, DNA marker; 1, blank control; 2 to 7, serial dilutions (40,000 copies μL^{-1}, 4,000 copies μL^{-1}, 400 copies μL^{-1}, 40 copies μL^{-1}, 4 copies μL^{-1}, 0.4 copy μL^{-1}) of H37Rv genomic DNA.

duration of amplification. Considering both a shorter test time and a higher amplification yield, the optimal amplification time was recommended to be 30 min. Figure 2D shows that specific amplification products were slightly reduced in the GO-assisted multiplex RPA assay compared to the two GO-assisted singlex RPA assays. This occurrence is presumed to be due to interference among the primers, particularly when multiple pairs of RPA primers are present. Whether this could lead to an analytical loss of sensitivity requires further experiments (see Section 3.5).

3.4 Trans-cleavage assay of MCSD and MCMD

MCMD was performed in parallel with two singlex detections (MCSD-IS*6110* and MCSD-IS*1081*). The high fluorescent signals in Figure 2E indicated that these assays could identify MTBC by targeting IS*6110* (or IS*1081*) or both. Fluorescence signals from MTBC CRISPR–Cas12a detections on various RPA products were detectable in 1 min, increased rapidly within 8 min, and decreased slowly after 12 min (Figure 2E). Finally, an optimized reaction time of 8–12 min was recommended for the trans-cleavage stage.

3.5 Analytical sensitivity of MCSD and MCMD

Serial dilutions of H37Rv genomic DNA (40,000 to 0.4 copies μL^{-1}) were used for analytical sensitivity determination of MCSD and MCMD. Electrophoresis and fluorescence results showed that two singlex detections (MCSD) and the multiplex detection (MCMD) were all sensitive with the LoDs of 4 copies μL^{-1} (Figures 3A–F). Figure 3G showed that the MCMD LFB assay also had a similar LoD value. Furthermore, the electrophoretic band brightness shown in Figures 3A, C, E indicates a dependency on the target amount in the RPA assay. However, such typical trend was not observed in the fluorescence intensity shown in Figures 3D, F. Two reasons may explain this result. First, this may be attributed to the differences in the targets of RPA assay and fluorescence detection. The RPA assay targeted serial dilutions of H37Rv DNA, whereas the fluorescence detection targeted the RPA products, which were not serial dilutions of DNA. Second, the cycle threshold (Ct) value (rather than the fluorescence intensity) is an inverse measure of the template load. The trans-cleavage reactions initiate almost instantly after the mixing of the reaction components at room temperature, resulting in the inability to read Ct values of RPA products in the resulting figures. While the curve height in Figures 3B, D, F represents the fluorescence intensity, it does not directly correspond to the concentrations of the templates. Altogether, MCMD that can juggle multiplex and unimpaired sensitivity was recommended for the subsequent experiments, including analytical specificity testing and clinical application.

3.6 Analytical specificity of MCMD

Genomic DNA extracted from 27 bacterial strains shown in Supplementary Table S1 was used to validate the analytical specificity of MCMD. As shown in Supplementary Figure S2, MTBC strains, including H37Rv strain (as a PC), BCG strain, and clinical strains from TB patients, gave positive results. In contrast, NTM strains, non-mycobacteria strains, and DDW (as a BC) showed negative results, demonstrating the absence of cross-reactions. Only MTBC genomic DNA could be detected using MCMD, indicating the extremely high specificity (100%) of this method.

3.7 Application of MCMD in clinical samples

A total of 107 pulmonary TB patients and 40 non-TB patients were included in this study. The proportion of males in the TB group was 64.5% (69/107), and the mean age was 50.84 years. The TB group comprised 79 laboratory-confirmed and 28 clinically diagnosed TB patients. In the non-TB group, 57.5% (23/40) were males, and the average age was 68.30. The diagnostic specificity of MCMD was evaluated in these non-TB patients, which consisted of 30 patients with bacterial pneumonia, seven with non-infectious inflammatory diseases, and three with malignancies. All samples were sputum specimens.

As shown in Table 2, 107 TB patients were classified into two groups, the culture-positive group (67/107) and the culture-negative group (40/107). For the culture-positive samples, the diagnostic sensitivity of Xpert and MCMD was 85.1% (57/67) and 95.5% (64/67), respectively. For the culture-negative samples, the diagnostic sensitivity of Xpert and MCMD was 27.5% (11/40) and 40.0% (16/40), respectively. Among all TB patients in this study, the pooled diagnostic sensitivity of culture, Xpert, and MCMD was 62.6% (67/107), 63.6% (68/107), and 74.8% (80/107), respectively. These results indicate that MCMD exhibits higher sensitivity compared to culture and Xpert, making it a more promising diagnostic tool for TB. In addition, the diagnostic specificity was 100% (40/40) for Xpert and MCMD when testing samples from non-TB patients.

4 Discussion

The CRISPR–Cas12a-based multiplex detection targeting two conserved sequences (IS*6110* and IS*1081*) was performed at constant temperatures (~37°C) and could be completed within 1 h. The LoD of this technique reached single-digit copies μL^{-1} (4 copies μL^{-1}), and no cross-reaction with non-MTBC bacteria strains was observed. The MCMD showed a diagnostic sensitivity of 74.8% and specificity of 100% in clinical samples compared to Xpert (63.6%, 100%).

The present study had several strengths. First, we employed an improved RPA assay with GO in the preamplification phase and exhibited good specificity performance with reduced non-specific products. RPA usually generates multiple amplified bands for one target sequence, making it difficult to establish an efficient multiplex RPA assay with multiple primer pairs. Our study and other research groups reported that GO, a single-atom-thick sheet of 2D carbon nanomaterial, could reduce primer-dimers and non-specific fragment formation in multiple-round or multiplex amplification (Wang et al., 2017; Wang Y et al., 2020). Given the strong non-covalent binding of water-soluble GO and nucleobases, enzymes, and aromatic compounds, the GO mechanism involved in the RPA assay can be as follows (Pena-Bahamonde et al., 2018; Wang Y et al.,

TABLE 2 Comparison of diagnostic performance of different methods for MTBC detection in TB patients.

	Diagnostic sensitivity, n[a] (%), (pulmonary TB patients)			Diagnostic specificity, n (%), (non-TB patients) (N = 40)
	Culture positive (N = 67)	Culture negative (N = 40)	Total (N = 107)	
Xpert	57 (85.1)	11 (27.5)	68 (63.6)	40 (100)
MCMD	64 (95.5)	16 (40.0)	80 (74.8)	40 (100)

[a]n, number of samples with positive results using a specific method.

2020): first, the negatively charged GO can rapidly attract the RPA reaction components bearing positive charges (e.g., recombinase, SSB, DNA polymerase, and Mg^{2+}) on the GO monolayer surface; second, the negatively charged RPA reaction components (e.g., nucleic acid templates, primers, and dNTPs) are attracted to the positively charged molecules on GO surface; then GO facilitates annealing of RPA primers to the target templates and extension. Consequently, the suppression of mismatched primer-template complex formation and the reduction of primer-dimers ultimately enhance the amplification specificity of RPA.

Notably, the unique strength of MCMD is its property of multiplex detection. The selection of a suitable target gene is of great significance for the high sensitivity and specificity of a diagnostic assay. So far, many conserved sequences, such as IS*6110*, IS*1081*, *MPB64*, *sdaA*, and *gyrB*, have been utilized as diagnostic targets for TB, of which IS*6110* is the most widely used (Yu et al., 2018; Acharya et al., 2020; Huang et al., 2021; Wang X et al., 2021). IS*6110* is a multi-copy insertion sequence among MTBC stains (e.g., 16 copies in H37Rv) that can increase sensitivity. However, low/no copies of IS*6110* are found in strains isolated from Southeast Asia, Europe, and America (Arora et al., 2020; Comin et al., 2021). Therefore, the techniques using a single target IS*6110* may be unsuitable in these areas. Our MCMD that combined another target IS*1081* (lower copy numbers, e.g., 5–6 copies in H37Rv) with IS*6110* can both avoid false negatives in strains with low/no copies of IS*6110* and as well as retain high sensitivity from IS*6110*. This is also why Xpert Ultra incorporated the two different multi-copy amplification targets (IS*6110* and IS*1081*) for improved detection of MTBC (Kay et al., 2022; Tang et al., 2023).

In comparison to PCR-based techniques, isothermal amplification methods eliminate the need for sophisticated equipment such as thermal cyclers and can significantly reduce amplification time (~30 min). Moreover, Cas endonucleases with collateral trans-cleavage activity can amplify cleavage signals and exhibit ultra-high sensitivity when combined with a pre-amplification step. Additionally, multiplex techniques have the distinct advantage of enabling the detection of multiple targets within a single assay. This capability is crucial for achieving precise and reliable diagnosis, reducing costs, and minimizing sample volume requirements. However, to date, some studies have employed isothermal amplification and Cas12a-based trans-cleavage in nucleic acid detection of MTBC (Ai et al., 2019; Xu et al., 2020; Sam et al., 2021; Wang Y et al., 2021), but no study enabled multiplex detection in one assay except for this present study (Supplementary Table S2). In details, studies from Ai et al. (2019), Sam et al. (2021) and Wang Y et al. (2021) used IS*6110* as the only target, and the study from Xu et al. (2020) used IS*1081* as the only target. Compared to our study, Ai et al. (2019), Sam et al. (2021) and Xu et al. (2020) did not avoid the use of large detection equipment (e.g., real-time PCR instrument), and LAMP used by Sam et al. (2021) and Wang Y et al. (2021) requires higher temperature (60°C–68°C), longer reaction time (40–80 min), and more complex primers (six primers for one target gene). The only IS*1081*-targeted study by Xu et al. (2020) exhibited a lower sensitivity with at least 20-fold higher LoD than other IS*6110*-targeted studies (Ai et al., 2019; Sam et al., 2021; Wang Y et al., 2021; this study). Our MCMD, which juggled multiplex and high sensitivity (4 copies μL^{-1} LoD), had advantages of simplicity (only heating block and two pairs of primers), rapidity (1 h) and specificity (reduced non-specific amplicons by simply adding GO). It can even use body temperature for amplification and trans-cleavage and use naked eyes for readout. In comparison to the widely-used Xpert, our MCMD technique demonstrated higher diagnostic sensitivity with an increase of >10 percentage points, while maintaining similar diagnostic specificity. Moreover, the MCMD technique offers significant cost advantages, with costs of $10 compared to $80 for Xpert in China. Additionally, the MCMD technique requires smaller sample volumes of 200 μL, in contrast to the 1–6 mL volume required by Xpert. These findings underscore the great potential of this novel technique for POT testing of TB in resource-limited countries.

In recent years, biosensors based on the CRISPR–Cas system [e.g., SHERLOCK (Gootenberg et al., 2017), DETECTR (Chen et al., 2018), HOLMES (Li et al., 2018), Cas14-DETECTR (Harrington et al., 2018), HOLMESv2 (Li et al., 2019)] have shown excellent performance in POC testing. A comparison of different CRISPR-based biosensors is shown in Supplementary Table S3. Considering the complex guide RNA design and signaling mechanism, CRISPR–Cas9 is no longer the preferred option for CRISPR diagnostics (Pardee et al., 2016; Guk et al., 2017; Zhang et al., 2017; Huang et al., 2018; Qiu et al., 2018; Zhou et al., 2018; Hajian et al., 2019; Wang et al., 2019; Wang X et al., 2020; Zhang et al., 2022). Compared to Cas9, Cas12 and Cas13 have been widely used for CRISPR diagnostics due to their unique collateral cleavage activity, which greatly simplifies signal generation (Gootenberg et al., 2017; Chen et al., 2018; Gootenberg et al., 2018; Harrington et al., 2018; Li et al., 2018; Dai et al., 2019; Li et al., 2019; Joung et al., 2020; Liu et al., 2021). Cas12a and Cas12b directly target double-stranded DNA (dsDNA) and are useful for DNA sequence detection and genotyping. Cas12f (originally denoted Cas14) shows stronger specificity and enables SNP detection with high fidelity. The multiplexing potential of Cas13 allows for the detection of multiple analytes. Some Cas effectors not restricted by PAM [e.g., uncultured archaeon (Un1) Cas12f1 (initially named Cas14a1) (Harrington et al., 2018), Cas13a, Cas13b] result in more application space in target sequences without PAM. Researchers can

reasonably select biosensor types according to their experimental requirements.

Although this study had several strengths, it also had some limitations. First, the sputum samples were all collected from a tertiary hospital specializing in tuberculosis. A multi-center prospective study should be conducted to provide high-level evidence on the diagnostic performance of MCMD. Second, only sputum samples, the most commonly used and most accessible specimen for adult TB patients, were evaluated in this study. Other paucibacillary samples (such as pleural effusion and cerebrospinal fluid) and specific populations (such as children and HIV-positive patients) should also be considered for future implementation. Third, it is recommended to design RPA primers with the incorporated PAM sequence in future studies. For CRISPR-Cas12 assays, it is essential that the target sequence contains a PAM site at the appropriate location to enable the activation of the Cas12-gRNA complex. Meanwhile, the MTBC genome is a high-GC genome, and the target gene may not have enough suitable PAM sites. Thus, improving primer design removes the limitation imposed by the PAM sequence and facilitates the screening of efficient gRNAs. Finally, in the current investigation, single-signal output biosensors (including LFB and fluorescent biosensor) were employed to indicate the presence of MTBC in the sample. However, in future studies, the utilization of distinct fluorescence or double-labeled LFB may enable differentiation between IS*6110* and IS*1081*, thereby providing additional strain-specific information. Despite major advances in the applications of CRISPR-based biosensors, many challenges remain in this promising area. Newer Cas enzymes, more robust readout systems, and more flexible strategies of signal conversion and amplification will represent the possible directions of improvement in future.

In this study, we have achieved the simultaneous detection of multiple targets from MTBC using a CRISPR-Cas-based detection method. This MCMD first combined an improved GO-assisted multiplex RPA targeting IS*6110* and IS*1081* with the CRISPR–Cas12a-based trans-cleavage assay identified by a fluorescent biosensor or LFB. Due to its multiplex property and freedom from large equipment, this MCMD is ideal for detecting strains with low/no copies of IS*6110* and MTBC POC testing in resource-limited countries.

Data availability statement

The raw data supporting the conclusion of this article will be made available by the authors, without undue reservation.

Ethics statement

The studies involving human participants were reviewed and approved by the Ethical Committee of Beijing Children's Hospital, Capital Medical University. Written informed consent for participation was not required for this study in accordance with the national legislation and the institutional requirements.

Author contributions

JX and YW conceived and supervised this study. JX and GJ performed the experiments. JX, SQ, and YCW analyzed the data. JL, YW, HH, WJ, and AS provided reagents and materials. HH provided clinical guidance. JX drafted the manuscript. WJ and AS revised the manuscript. All authors contributed to the article and approved the submitted version.

Funding

This study was supported by Beijing Municipal Natural Science Foundation (Grant number J200005), Capital Health Research and Development of Special Fund (Grant number 2020-2-1142), and Training Plan for High level Public Health Technical Talents (Grant number 2022-3-041).

Acknowledgments

We thank Home for Researchers editorial team (www.home-for-researchers.com) for language editing service.

Conflict of interest

The authors declare that the research was conducted in the absence of any commercial or financial relationships that could be construed as a potential conflict of interest.

Publisher's note

Supplementary material

The Supplementary Material for this article can be found online at: https://www.frontiersin.org/articles/10.3389/fbioe.2023.1233353/full#supplementary-material

References

Acharya, B., Acharya, A., Gautam, S., Ghimire, S. P., Mishra, G., Parajuli, N., et al. (2020). Advances in diagnosis of tuberculosis: an update into molecular diagnosis of *Mycobacterium tuberculosis*. *Mol. Biol. Rep.* 47 (5), 4065–4075. doi:10.1007/s11033-020-05413-7

Ai, J. W., Zhou, X., Xu, T., Yang, M., Chen, Y., He, G. Q., et al. (2019). CRISPR-based rapid and ultra-sensitive diagnostic test for *Mycobacterium tuberculosis*. *Emerg. Microbes Infect.* 8 (1), 1361–1369. doi:10.1080/22221751.2019.1664939

Arora, J., Suresh, N., Porwal, C., Pandey, P., Pande, J. N., and Singh, U. B. (2020). Genotyping *Mycobacterium tuberculosis* isolates with few copies of IS6110: value of additional genetic markers. *Infect. Genet. Evol.* 81, 104230. doi:10.1016/j.meegid.2020.104230

Broughton, J. P., Deng, X., Yu, G., Fasching, C. L., Servellita, V., Singh, J., et al. (2020). CRISPR-Cas12-based detection of SARS-CoV-2. *Nat. Biotechnol.* 38 (7), 870–874. doi:10.1038/s41587-020-0513-4

Chen, J. S., Ma, E., Harrington, L. B., Da Costa, M., Tian, X., Palefsky, J. M., et al. (2018). CRISPR-Cas12a target binding unleashes indiscriminate single-stranded DNase activity. *Science* 360 (6387), 436–439. doi:10.1126/science.aar6245

Comin, J., Cebollada, A., Ibarz, D., Vinuelas, J., Vitoria, M. A., Iglesias, M. J., et al. (2021). A whole-genome sequencing study of an X-family tuberculosis outbreak focus on transmission chain along 25 years. *Tuberc. (Edinb)* 126, 102022. doi:10.1016/j.tube.2020.102022

Dai, Y., Somoza, R. A., Wang, L., Welter, J. F., Li, Y., Caplan, A. I., et al. (2019). Exploring the trans-cleavage activity of CRISPR-cas12a (cpf1) for the development of a universal electrochemical biosensor. *Angew. Chem. Int. Ed. Engl.* 58 (48), 17399–17405. doi:10.1002/anie.201910772

Gootenberg, J. S., Abudayyeh, O. O., Kellner, M. J., Joung, J., Collins, J. J., and Zhang, F. (2018). Multiplexed and portable nucleic acid detection platform with Cas13, Cas12a, and Csm6. *Science* 360 (6387), 439–444. doi:10.1126/science.aaq0179

Gootenberg, J. S., Abudayyeh, O. O., Lee, J. W., Essletzbichler, P., Dy, A. J., Joung, J., et al. (2017). Nucleic acid detection with CRISPR-Cas13a/C2c2. *Science* 356 (6336), 438–442. doi:10.1126/science.aam9321

Guk, K., Keem, J. O., Hwang, S. G., Kim, H., Kang, T., Lim, E. K., et al. (2017). A facile, rapid and sensitive detection of MRSA using a CRISPR-mediated DNA FISH method, antibody-like dCas9/sgRNA complex. *Biosens. Bioelectron.* 95, 67–71. doi:10.1016/j.bios.2017.04.016

Hajian, R., Balderston, S., Tran, T., deBoer, T., Etienne, J., Sandhu, M., et al. (2019). Detection of unamplified target genes via CRISPR-Cas9 immobilized on a graphene field-effect transistor. *Nat. Biomed. Eng.* 3 (6), 427–437. doi:10.1038/s41551-019-0371-x

Harrington, L. B., Burstein, D., Chen, J. S., Paez-Espino, D., Ma, E., Witte, I. P., et al. (2018). Programmed DNA destruction by miniature CRISPR-Cas14 enzymes. *Science* 362 (6416), 839–842. doi:10.1126/science.aav4294

Huang, J., Xiao, Z., Yang, X., Chen, X., Wang, X., Chen, Y., et al. (2021). Two target genes based multiple cross displacement amplification combined with a lateral flow biosensor for the detection of *Mycobacterium tuberculosis* complex. *BMC Microbiol.* 21 (1), 267. doi:10.1186/s12866-021-02328-6

Huang, M., Zhou, X., Wang, H., and Xing, D. (2018). Clustered regularly interspaced short palindromic repeats/cas9 triggered isothermal amplification for site-specific nucleic acid detection. *Anal. Chem.* 90 (3), 2193–2200. doi:10.1021/acs.analchem.7b04542

Joung, J., Ladha, A., Saito, M., Segel, M., Bruneau, R., Huang, M. W., et al. (2020). *Point-of-care testing for COVID-19 using SHERLOCK diagnostics*. medRxiv, 2020.05.04.20091231.

Kay, A. W., Gonzalez Fernandez, L., Takwoingi, Y., Eisenhut, M., Detjen, A. K., Steingart, K. R., et al. (2020). Xpert MTB/RIF and Xpert MTB/RIF Ultra assays for active tuberculosis and rifampicin resistance in children. *Cochrane Database Syst. Rev.* 8 (8), CD013359. doi:10.1002/14651858.CD013359.pub2

Kay, A. W., Ness, T., Verkuijl, S. E., Viney, K., Brands, A., Masini, T., et al. (2022). Xpert MTB/RIF Ultra assay for tuberculosis disease and rifampicin resistance in children. *Cochrane Database Syst. Rev.* 9 (9), CD013359. doi:10.1002/14651858.CD013359.pub3

Kohli, M., Schiller, I., Dendukuri, N., Yao, M., Dheda, K., Denkinger, C. M., et al. (2021). Xpert MTB/RIF Ultra and Xpert MTB/RIF assays for extrapulmonary tuberculosis and rifampicin resistance in adults. *Cochrane Database Syst. Rev.* 1 (1), CD012768. doi:10.1002/14651858.CD012768.pub3

Li, L., Li, S., Wu, N., Wu, J., Wang, G., Zhao, G., et al. (2019). HOLMESv2: a CRISPR-cas12b-assisted platform for nucleic acid detection and DNA methylation quantitation. *ACS Synth. Biol.* 8 (10), 2228–2237. doi:10.1021/acssynbio.9b00209

Li, S. Y., Cheng, Q. X., Wang, J. M., Li, X. Y., Zhang, Z. L., Gao, S., et al. (2018). CRISPR-Cas12a-assisted nucleic acid detection. *Cell Discov.* 4, 20. doi:10.1038/s41421-018-0028-z

Liu, T. Y., Knott, G. J., Smock, D. C. J., Desmarais, J. J., Son, S., Bhuiya, A., et al. (2021). Accelerated RNA detection using tandem CRISPR nucleases. *Nat. Chem. Biol.* 17 (9), 982–988. doi:10.1038/s41589-021-00842-2

MacLean, E., Kohli, M., Weber, S. F., Suresh, A., Schumacher, S. G., Denkinger, C. M., et al. (2020). Advances in molecular diagnosis of tuberculosis. *J. Clin. Microbiol.* 58 (10), e01582-19. doi:10.1128/JCM.01582-19

Munawar, M. A. (2022). Critical insight into recombinase polymerase amplification technology. *Expert Rev. Mol. Diagnostics* 22 (7), 725–737. doi:10.1080/14737159.2022.2109964

Pardee, K., Green, A. A., Takahashi, M. K., Braff, D., Lambert, G., Lee, J. W., et al. (2016). Rapid, low-cost detection of zika virus using programmable biomolecular components. *Cell* 165 (5), 1255–1266. doi:10.1016/j.cell.2016.04.059

Pena-Bahamonde, J., Nguyen, H. N., Fanourakis, S. K., and Rodrigues, D. F. (2018). Recent advances in graphene-based biosensor technology with applications in life sciences. *J. Nanobiotechnology* 16 (1), 75. doi:10.1186/s12951-018-0400-z

Qiu, X. Y., Zhu, L. Y., Zhu, C. S., Ma, J. X., Hou, T., Wu, X. M., et al. (2018). Highly effective and low-cost MicroRNA detection with CRISPR-cas9. *ACS Synth. Biol.* 7 (3), 807–813. doi:10.1021/acssynbio.7b00446

Sam, I. K., Chen, Y. Y., Ma, J., Li, S. Y., Ying, R. Y., Li, L. X., et al. (2021). TB-QUICK: CRISPR-Cas12b-assisted rapid and sensitive detection of *Mycobacterium tuberculosis*. *J. Infect.* 83 (1), 54–60. doi:10.1016/j.jinf.2021.04.032

Tang, P., Liu, R., Qin, L., Xu, P., Xiong, Y., Deng, Y., et al. (2023). Accuracy of Xpert® MTB/RIF ultra test for posterior oropharyngeal saliva for the diagnosis of paucibacillary pulmonary tuberculosis: a prospective multicenter study. *Emerg. Microbes Infect.* 12 (1), 2148564. doi:10.1080/22221751.2022.2148564

Walzl, G., McNerney, R., du Plessis, N., Bates, M., McHugh, T. D., Chegou, N. N., et al. (2018). Tuberculosis: advances and challenges in development of new diagnostics and biomarkers. *Lancet Infect. Dis.* 18 (7), e199–e210. doi:10.1016/S1473-3099(18)30111-7

Wang, T., Liu, Y., Sun, H. H., Yin, B. C., and Ye, B. C. (2019). An RNA-guided Cas9 nickase-based method for universal isothermal DNA amplification. *Angew. Chem. Int. Ed. Engl.* 58 (16), 5382–5386. doi:10.1002/anie.201901292

Wang, X., Wang, G., Wang, Y., Quan, S., Qi, H., Sun, L., et al. (2021). Development and preliminary application of multiplex loop-mediated isothermal amplification coupled with lateral flow biosensor for detection of *Mycobacterium tuberculosis* complex. *Front. Cell Infect. Microbiol.* 11, 666492. doi:10.3389/fcimb.2021.666492

Wang, X., Xiong, E., Tian, T., Cheng, M., Lin, W., Wang, H., et al. (2020). Clustered regularly interspaced short palindromic repeats/cas9-mediated lateral flow nucleic acid assay. *ACS Nano* 14 (2), 2497–2508. doi:10.1021/acsnano.0c00022

Wang, Y., Jiao, W. W., Wang, Y., Wang, Y. C., Shen, C., Qi, H., et al. (2020). Graphene oxide and self-avoiding molecular recognition systems-assisted recombinase polymerase amplification coupled with lateral flow bioassay for nucleic acid detection. *Mikrochim. Acta* 187 (12), 667. doi:10.1007/s00604-020-04637-5

Wang, Y., Li, J., Li, S., Zhu, X., Wang, X., Huang, J., et al. (2021). LAMP-CRISPR-Cas12-based diagnostic platform for detection of *Mycobacterium tuberculosis* complex using real-time fluorescence or lateral flow test. *Mikrochim. Acta* 188 (10), 347. doi:10.1007/s00604-021-04985-w

Wang, Y., Wang, F., Wang, H., and Song, M. (2017). Graphene oxide enhances the specificity of the polymerase chain reaction by modifying primer-template matching. *Sci. Rep.* 7 (1), 16510. doi:10.1038/s41598-017-16836-x

World-Health-Organization (2021). Global tuberculosis report 2021. Available at: https://www.who.int/publications/i/item/9789240037021 (Accessed October 14, 2021).

World-Health-Organization (2020). Global tuberculosis report 2020. Available at: https://www.who.int/publications/i/item/9789240013131 (Accessed October 15, 2020).

World-Health-Organization (2022). Global tuberculosis report 2022. Available at: https://www.who.int/teams/global-tuberculosis-programme/tb-reports/global-tuberculosis-report-2022 (Accessed October 27, 2021).

World-Health-Organization (2011). Policy statement: automated real-time nucleic acid amplification technology for rapid and simultaneous detection of tuberculosis and rifampicin resistance: xpert MTB/RIF system. Available at: https://www.who.int/news/item/18-05-2011-xpert-mtb-rif—rapid-tb-test—who-publishes-policy-and-guidance-for-implementers (Accessed November 10, 2021).

Xu, H., Zhang, X., Cai, Z., Dong, X., Chen, G., Li, Z., et al. (2020). An isothermal method for sensitive detection of *Mycobacterium tuberculosis* complex using clustered regularly interspaced short palindromic repeats/cas12a cis and trans cleavage. *J. Mol. Diagn* 22 (8), 1020–1029. doi:10.1016/j.jmoldx.2020.04.212

Yu, G., Shen, Y., Zhong, F., Ye, B., Yang, J., and Chen, G. (2018). Diagnostic accuracy of the loop-mediated isothermal amplification assay for extrapulmonary tuberculosis: a meta-analysis. *PLoS One* 13 (6), e0199290. doi:10.1371/journal.pone.0199290

Zhang, Y., Qian, L., Wei, W., Wang, Y., Wang, B., Lin, P., et al. (2017). Paired design of dCas9 as a systematic platform for the detection of featured nucleic acid sequences in pathogenic strains. *ACS Synth. Biol.* 6 (2), 211–216. doi:10.1021/acssynbio.6b00215

Zhang, Y., Wang, Y., Xu, L., Lou, C., Ouyang, Q., and Qian, L. (2022). Paired dCas9 design as a nucleic acid detection platform for pathogenic strains. *Methods* 203, 70–77. doi:10.1016/j.ymeth.2021.06.003

Zhou, W., Hu, L., Ying, L., Zhao, Z., Chu, P. K., and Yu, X. F. (2018). A CRISPR-Cas9-triggered strand displacement amplification method for ultrasensitive DNA detection. *Nat. Commun.* 9 (1), 5012. doi:10.1038/s41467-018-07324-5

frontiers | Frontiers in Bioengineering and Biotechnology

TYPE Original Research
PUBLISHED 28 August 2023
DOI 10.3389/fbioe.2023.1258036

OPEN ACCESS

EDITED BY
Kang Cui,
University of Jinan, China

REVIEWED BY
Shi Gang Liu,
Hunan Agricultural University, China
Cui Liu,
Xi'an Jiaotong University, China

*CORRESPONDENCE
Baojuan Wang,
wangbaojuan@ahnu.edu.cn
Yuezhen He,
hyz2006@ahnu.edu.cn

RECEIVED 13 July 2023
ACCEPTED 10 August 2023
PUBLISHED 28 August 2023

CITATION
Wang B, Fang J, Tang H, Lu S, Chen Y, Yang X and He Y (2023), Dual-functional cellulase-mediated gold nanoclusters for ascorbic acid detection and fluorescence bacterial imaging.
Front. Bioeng. Biotechnol. 11:1258036.
doi: 10.3389/fbioe.2023.1258036

Dual-functional cellulase-mediated gold nanoclusters for ascorbic acid detection and fluorescence bacterial imaging

Baojuan Wang[1,2]*, Jinxin Fang[1,2], Huiliang Tang[1,2], Shan Lu[1,2], Yan Chen[3,4,5], Xiaoqi Yang[1,2] and Yuezhen He[3,4,5]*

[1]Anhui Provincial Key Laboratory of Molecular Enzymology and Mechanism of Major Diseases, College of Life Sciences, Anhui Normal University, Wuhu, Anhui, China, [2]Key Laboratory of Biomedicine in Gene Diseases, Health of Anhui Higher Education Institutes, College of Life Sciences, Anhui Normal University, Wuhu, Anhui, China, [3]Anhui Key Laboratory of Chemo-Biosensing, Ministry of Education, Anhui Normal University, Wuhu, China, [4]Key Laboratory of Functional Molecular Solids, Ministry of Education, Anhui Normal University, Wuhu, China, [5]Laboratory of Biosensing and Bioimaging (LOBAB), College of Chemistry and Materials Science, Anhui Normal University, Wuhu, China

Protein-protected metal nanomaterials are becoming the most promising fluorescent nanomaterials for biosensing, bioimaging, and therapeutic applications due to their obvious fluorescent molecular properties, favorable biocompatibility and excellent physicochemical properties. Herein, we pioneeringly prepared a cellulase protected fluorescent gold nanoclusters (Cel-Au NCs) exhibiting red fluorescence under the excitation wavelength of 560 nm via a facile and green one-step method. Based on the fluorescence turn-off mechanism, the Cel-Au NCs were used as a biosensor for specificity determination of ascorbic acid (AA) at the emission of 680 nm, which exhibited satisfactory linearity over the range of 10–400 μM and the detection limit of 2.5 μM. Further, the actual sample application of the Au NCs was successfully established by evaluating AA in serum with good recoveries of 98.76%–104.83%. Additionally, the bacteria, including gram-positive bacteria (*Bacillus subtilis and Staphylococcus aureus*) and gram-negative bacteria (*Escherichia coli*), were obviously stained by Cel-Au NCs with strong red emission. Thereby, as dual-functional nanoclusters, the prepared Cel-Au NCs have been proven to be an excellent fluorescent bioprobe for the detection of AA and bacterial labeling in medical diagnosis and human health maintenance.

KEYWORDS

Au nanoclusters, biomineralization, fluorescence, biosensor, bacterial labeling

Introduction

Ascorbic acid (AA, vitamin C), as one of the most vital micronutrients and antioxidants in the human body, plays an imperative role in numerous biochemical reactions involving oxidative stress reduction, disease prevention, immune response and other physiological activities (Abulizi et al., 2014; Liu et al., 2017). Furthermore, AA is also a medicine for the treatment of many diseases, including scurvy, immunodeficiency, allergic reactions and liver disease, which contributes to the absorption of iron and calcium, healthy cell development,

and normal tissue growth (Zhuang and Chen, 2020). Thus, AA detection is very important in medical diagnosis and human health maintenance. At present, various analytical methods have been developed and utilized in the quantitative determination of AA, such as electrochemistry (Ma et al., 2021), high liquid chromatography (Burini, 2007), liquid chromatography-mass spectrometry/mass spectrometry (Diep et al., 2020). Although these technologies have been successfully implemented in AA detection, most of them still have disadvantages such as complicated instrument requirements, long detection time, and low sensitivity. Nowadays, the fluorescence method has gradually become an ideal alternative method for detecting AA because of its simplicity, high sensitivity and excellent reproducibility (Gan et al., 2020). Therefore, it is urgent to develop an innovative material with exceptional fluorescent properties in biosensing.

Metal nanoclusters (NCs) consisting of several to dozens of atoms are typically ~3 nm which is equivalent to the Fermi wavelength of the electrons (Jin et al., 2016), resulting in a series of tunable metal core composition with discrete electronic states, obvious fluorescence molecular-like characteristics and excellent physicochemical properties (Zhang and Wang, 2014). Due to their inherent properties, metal NCs including Au, Ag, Cu, Pd and Pt NCs are being widely explored in biological imaging, biological sensing and advanced therapeutics fields (Guo et al., 2021; Tan et al., 2021). Notably, Au NCs become the most promising fluorescent nanomaterial owing to their excellent characteristics, such as strong photoluminescence, extraordinary photostability, explicit composition and combination properties (Guo et al., 2021). In light of this, various methods including microwave-assisted synthesis (Yue et al., 2012), sonochemistry (Xu and Suslick, 2010), photoreduction (Zhou et al., 2017), ligand-induced etching (Duan and Nie, 2007), and template-assisted synthesis (Qiao et al., 2021; Chen et al., 2022) have been developed to form the Au NCs.

Up to now, many templates, including DNA, proteins, viruses, microorganisms and plants, have been used for the preparation of Au NCs (Huang et al., 2015; Chen et al., 2018; Wang et al., 2019). Among them, due to their specific amino acid sequence composition, unique spatial conformation and chemical functional groups, proteins as an effective biological template show tremendous potential for the synthesis of Au NCs with tunable size, fluorescent properties and favourable biocompatibility (Yu et al., 2014; Guo et al., 2021). For example, Bhamore et al. prepared amylase Au NCs with red fluorescent emission and an average size of 1.75 nm for the detection of deltamethrin and glutathione (Bhamore et al., 2019). In another case, human serum albumin (HSA) directed red-emitting gold nanoclusters (HSA-AuNCs) were used as a bioprobe for *Staphylococcus aureus* (Chan and Chen, 2012). Moreover, in our recent study, using flavourzyme as a template, first prepared Fla-Au NCs with blue fluorescence were successfully utilized for the determination of carbaryl (Chen et al., 2022). Papain-encapsulated platinum nanoclusters with green fluorescence can be used not only for sensing lysozyme in biofluids but also for gram-positive bacterial identification (Chang et al., 2021). Therefore, it is urgent to develop innovative protein-coated metal nanoclusters and explore their applications in bioprobes, bioimaging and therapy.

Cellulase (Cel), as a pivotal industrial enzyme, catalyzes the decomposition of renewable lignocellulosic biomass into oligosaccharides or monosaccharides, which have been explored in numerous industries, such as textile, pulp and paper, detergent, food, and biofuel production (Ejaz et al., 2021; Areeshi, 2022). However, there are very limited reports on the synthesis and application of cellulase mediated nanostructure. Up to now, only Cel-protected copper nanoclusters (Cu NCs) with exceptional photostability, luminescence quantum yield, and colloidal stability has been investigated (Singh et al., 2016). Additionally, attributed to the oxidation resistance, conductivity, non-toxicity and stability of Au, the performance of Au NCs in biosensing and biomedicine is highly anticipated.

Hereby, we innovatively fabricated one type of red-emitting Au NCs using cellulase as the template via a one-step biomineralization method. A series of characterization techniques were used to explore the optical properties, morphology, composition, and valence state of Cel-Au NCs, including UV-vis absorption spectrometry, fluorescence spectroscopy, transmission electron microscopy (TEM), Fourier transform infrared spectroscopy (FT-IR) and X-ray crystallography (XPS). As shown in Scheme 1, this turn-off and label-free biosensor provided an alternative choice for AA detection in the biofluid. Meanwhile, owing to ultra-small size, brightly red fluorescence and good biocompatibility, dual-functional Cel-Au NCs could also be served as a bio-imaging probe for bacterial imaging.

Materials and methods

Materials

$HAuCl_4{\cdot}4H_2O$ was purchased from Sinopharm Chemical Reagent Co., Ltd. (Shanghai, China). Cellulase, pepsin, trypsin and AA were obtained from Yuanye Biotechnology Co., Ltd. (Shanghai, China). Histidine, threonine, lysine, glycine, glutathione (GSH), maltose, sucrose, glucose and metal ions were acquired from Sangon Biotechnology Co., Ltd. (Shanghai, China). All reagents were of analytical purity and used directly. Milli-Q purified water prepared by the PR03200 ultra-pure water meter (Zhongshan Keningte Cleaning Supplies Co., Ltd.) was utilized in all experiments.

Instruments

All glass containers in the laboratory were thoroughly washed with aqua regia, rinsed with ultrapure water and dried before use. UV-1800 spectrophotometer (Shimadzu, Japan), PF-5301PC fluorescence spectrophotometer (Shimadzu, Japan) and Spark-Multimode microplate reader (Tecan, Switzerland) were applied to measure the UV-vis absorption spectra, the fluorescence spectra, and the bacterial density, respectively. Transmission electron microscopy (TEM) images were collected on a JEOL 2010 LaB6 TEM (TECNAI G2, the Netherlands) at an acceleration voltage of 200 kV. Fourier transform infrared (FT-IR) spectra and X-ray photoelectron spectra (XPS) were separately detected by BW17-FTIR-650 spectrometer (Beijing, China) and X-ray photoelectron spectroscopy (Shimadzu, Japan). The fluorescence lifetime and quantum yield (QY) of the samples

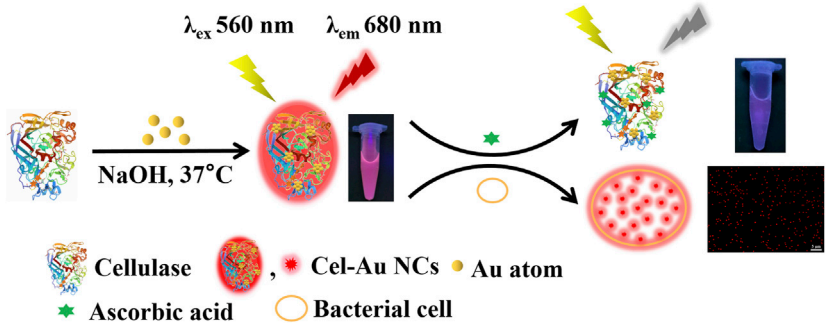

SCHEME 1
Schematic illustration of Cel-Au NCs for sensing ascorbic acid and bacterial labeling.

were recorded on an FLS920 fluorescence spectrometer (Edinburgh, UK). Zeta potential values were performed using the Malvern Zetasizer sizer NanoZS ZEM-3600 instrument (Malvern, UK). Furthermore, bacteria imaging was collected using the fluorescence microscope (Zeiss, Germany).

Synthesis of Cel-Au NCs

Typically, 0.16 mL of the $HAuCl_4$ solution (25 mM) and 9.84 mL of the cellulase solution (1 mM) were mixed thoroughly with a vortexer for 5 min. After adjusting pH to 12 with the addition of 1 M NaOH solution, the above mixture was reacted at 37°C for 12 h in the dark. Then the supernatant of the above mixture was collected by centrifugation at 8,000 rpm for 10 min, dialyzed to remove unreacted metal ions by a dialysis membrane (1, 000 MWCO) for 24 h, and placed at 4°C for future use.

The detection of AA

For AA detection, the Cel-Au NCs (40 mg/mL, 50 μL), different concentrations of AA solutions (100 μL) and deionized water (850 μL) were mixed and incubated at 25°C for 5 min in a water bath. The fluorescence signal of the above mixture was then measured using an F-4500 fluorescence spectrophotometer by exciting at 560 nm. To evaluate the selectivity and specificity of Cel-Au NCs for AA, the fluorescence variations of Cel-Au NCs were investigated toward 16 kinds of compounds (histidine, threonine, lysine, glycine, GSH, maltose, sucrose, glucose, AA, KCl, NaCl, LiCl, $ZnCl_2$, $CaCl_2$, $MgCl_2$, $MnCl_2$). The as-prepared Cel-Au NCs were mixed with different compound solutions and measured under the same experimental condition as above. All experiments were performed three times in a parallel format.

Analysis of AA in real samples

To evaluate the applicability of the method, human serum samples provided from the Hospital of Traditional Chinese Medicine (Wuhu, China) were directly diluted 40 times with Milli-Q purified water before the experiment. Then, 50 μL of 40 mg/mL as-prepared Cel-Au NCs, 850 μL of diluted serum sample and 100 μL of different concentrations of AA solution were mixed and analyzed in accordance with the procedure mentioned above.

Bacterial culture and viability assay

Bacillus subtilis (*B. subtilis*, gram-positive bacteria), *Staphylococcus aureus* (*S. aureus*, gram-positive bacteria) and *Escherichia coli* (*E. coli*, gram-negative bacteria) were separately cultured on Luria-Bertani (LB) agar plates at 37°C overnight. Subsequently, a single colony of the bacteria was separately picked and incubated in LB liquid culture medium with continuous shaking at 180 rpm at 37°C for another 16–24 h.

To estimate the biocompatibility of Cel-Au NCs, bacterial viabilities were measured by determining bacterial cell density at OD_{600} on Spark-Multimode microplate reader. When OD_{600} reached 0.6, the bacteria (*B. subtilis*, *S. aureus*, and *E. coli*) were seeded into a 96-well microplate at 1% inoculum. Then various concentrations of Cel-Au NCs (0, 10, 25, 50, 100 and 200 μg/mL) were separately added to the bacteria and cultured at 37°C and 180 rpm. The growth of organisms was observed by measuring OD_{600} until 24 h and all of the experiments were executed three times in parallel. The percentage of bacterial density without adding Au NCs was taken as 100%.

Fluorescent imaging of bacteria

After centrifuging at 8,000 rpm for 5 min, the above cultured bacterial cells were collected, washed with PBS, and incubated in the mixture of the prepared Cel-Au NCs (0.1 mL) and PBS (0.4 mL) in a shaker at 37°C for 15 min. The bacterial cultures were examined on a Zeiss upright fluorescence microscope under 605 nm.

Results and discussion

Synthesis and characterization of Cel-Au NCs

The red-emitting Cel-Au NCs were firstly prepared via a facile and green one-step biomineralization method based on the

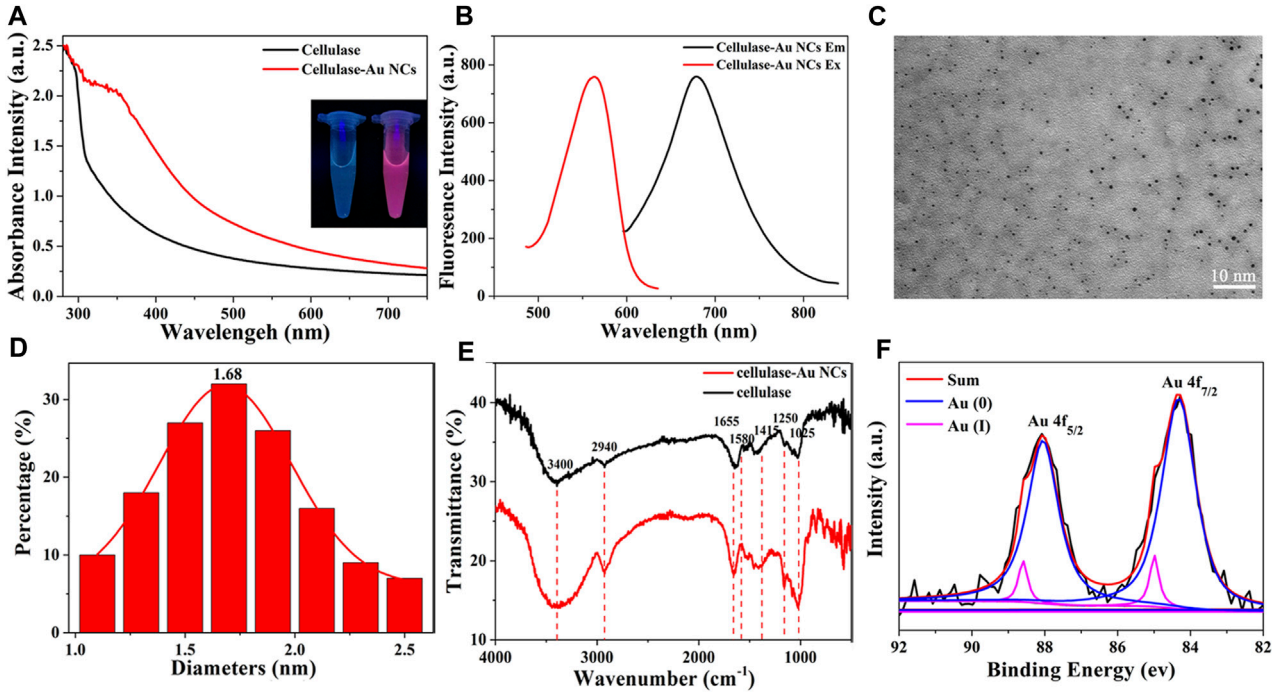

FIGURE 1
(A) UV-vis absorption spectra of Cel-Au NCs (red line) and cellulase (black line), Inset: photographs of cellulase (left) and Cel-Au NCs (right) with UV light (365 nm). **(B)** Fluorescence excitation spectra of Cel-Au NCs at emission wavelength 680 nm (red line) and emission spectra of Cel-Au NCs upon excitation at 560 nm (black line). **(C)** Transmission electron microscopy images showed the average size of Cel-Au NCs with 10 nm bar. **(D)** Size distribution histogram of Cel-Au NCs calculated from the TEM images by counting 146 samples. **(E)** FT-IR spectra of cellulase-Au NCs (red) and cellulase (black). **(F)** XPS spectra for the Au 4f of Cel-Au NCs. The original spectrum is black, the fitted spectrum is red, the Au(0) $4f_{7/2}$ spectrum is blue, and the Au(I) $4f_{7/2}$ spectrum is pink.

reduction of cellulase provided by sulfur-containing cysteines and methionines, which made the Au-S band formed between cellulase and Au atom (Balu et al., 2019; Wang et al., 2019). To obtain the optimal conditions of the synthesized Cel-Au NCs, the molar ratio (cellulase/$HAuCl_4$) and reaction pH were conducted in Supplementary Figure S1. The molar ratio of 2.5:1 and the reaction pH of 12 served as optimal conditions were selected for further study.

Initially, UV-vis absorption spectra and fluorescence spectroscopy were employed to identify related optical properties of Cel-Au NCs. The UV-vis spectrum showed that Cel-Au NCs had a shoulder peak in the region range of 300–400 nm with a continuous rise and a distinct peak at 350 nm attributed to oxidation between cellulase and Au atoms, whereas the spectrum of cellulose showed no peak in these ranges, signifying the Cel-Au NCs were fabricated (Figure 1A). As shown in Figure 1B; Supplementary Figure S2, the red-emitting cellulase protected Au NCs displayed an emission peak maximum at 680 nm upon 560 nm excitation with a marked Stokes shift of 120 nm. Additionally, the QY of Cel-Au NCs in aqueous solution was determined to be 10.19% using Rhodamine 6 G as a reference (Supplementary Figure S3).

The morphology of the prepared Cel-Au NCs was characterized by TEM, revealing that the Cel-Au NCs had a good dispersion and the average size was 1.68 nm by counting 146 samples (Figures 1C, D), which was consistent with the diameter of metal NCs prepared in previous studies (Wei et al., 2010; Bhamore et al., 2019). Subsequently, FT-IR was used to characterize the chemical composition of Cel-Au NCs. As shown in Figure 1E, the peaks of pure cellulase and Cel-Au NCs for O-H stretching, C-H stretching, C=O stretching, C-H bending, N-H stretching and C=C bending were separately observed at 3,400 cm^{-1}, 2,940 cm^{-1}, 1,655 cm^{-1}, 1,415 cm^{-1}, 1,250 cm^{-1} and 1,025 cm^{-1}, whereas a distinct peak in the spectrum of Cel-Au NCs was observed at 1,580 cm^{-1} ascribing to the formation of a bond between Au and cellulose.

XPS was used to measure the oxidation states of gold in Au NCs and it showed the peaks of Au, S, C, N and O in the XPS spectra (Supplementary Figure S4). Two peaks centered at 88.0 and 84.3 eV were separately ascribed to $4f_{5/2}$ and $4f_{7/2}$ for Au (Figure 1F). The peak of $4f_{5/2}$ of the prepared Cel-Au NCs was further deconvoluted into two different components, one at 88.05 eV corresponding to Au (0), and the second one at 88.60 eV attributed to Au (I). Also, the two peaks of $4f_{7/2}$ assigning to 84.32 and 84.99 eV showed the simultaneous presence of Au (0) and Au (I) in Cel-Au NCs. The spectra of Au $4f_{7/2}$ showed a binding energy of > 84.0 eV, indicating both Au (0) and Au (I) existed in Cel-Au NCs and the presence of Au-S complexes formed by the formation of charge transfer bands (Bothra et al., 2017).

Fluorescence quantification assay of AA

When the addition of AA was increased from 10 μM to 800 μM, a corresponding reduction in the fluorescent signal of

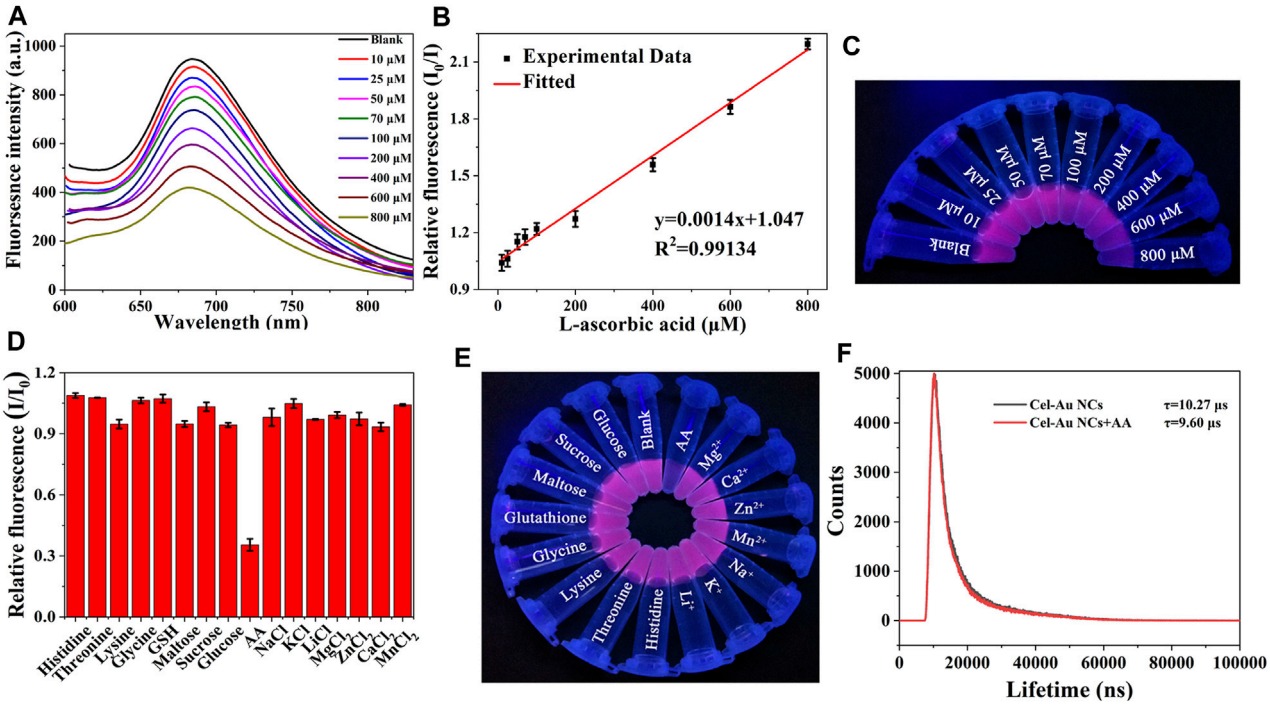

FIGURE 2
(A) Fluorescence spectra of Cel-Au NCs with varied concentrations of AA (top to bottom: 10–800 μM). **(B)** The linear relationship between I0/I and different concentrations from 10 to 800 μM of AA (I_0/I, where I_0 and I are the fluorescence intensity of Cel-Au NCs in the absence and presence of AA, respectively). **(C)** Image of Cel-Au NCs with different concentrations (10–800 μM) of AA under UV light. **(D)** Relative fluorescence intensity (I/I_0) of Cel-Au NCs when excited at 560 nm with various analytes (I/I_0, where I and I_0 are the fluorescence intensity of Cel-Au NCs in the presence and absence of various analytes, respectively). **(E)** Photographic image of Cel-Au NCs solution upon the addition of various analytes under UV light illumination at 365 nm. **(F)** Time-resolved fluorescence spectra of Cel-Au NCs in the presence or absence of 600 μM AA (λ_{ex} = 560 nm, λ_{em} = 680 nm).

TABLE 1 Comparison of the determination of AA using Cel-Au NCs and other reported fluorometric methods.

Materials	Linear range (μM)	Detection limit (μM)	References
Carbon dots	100-800	50	Gan et al. (2020)
Carbon dots	50–300	1.73	Shi et al. (2021)
Nanoparticles	0-750	4.9	Sun et al. (2019)
Carbon dots	20-500	5.13	Fan et al. (2022)
Carbon Quantum Dots	600-1600	18	Li et al. (2021)
Cel-Au NCs	10-800	2.5	This work

Cel-Au NCs was examined (Figure 2A). Figure 2B depicted the relationship between the fluorescent intensity of the Cel-Au NCs and the different concentrations of AA, and showed a good linear correlation over a range of 10–800 μM with a LOD of 2.5 μM (R^2 = 0.99134), indicating that the detection system possessed superior sensitivity. Simultaneously, the fluorescent intensity of Cel-Au NCs was correspondingly reduced with the increasing concentration of AA by UV light (Figure 2C). Furthermore, the specificity of the Cel-Au NCs for AA was conducted by testing the response of the biosensor prepared against other compounds. Interestingly, the fluorescent intensity of Cel-Au NCs was extremely decreased just after adding AA, whereas there were barely any changes in the presence of the other compounds (Figures 2D, E; Supplementary Figure S5). Compared with the published methods in AA detection (Table 1 and Supplementary Table S1), the proposed method displayed a wider detection range and an appreciable detection limit, which is simplicity, rapidity, efficiency and economics. Thus, as an alternative biosensor, it is potential for AA detection in the biological environment using Cel-Au NCs.

To elucidate the quenching mechanism of AA on the Cel-Au NCs, fluorescence resonance energy transfer (FRET), inner filter effect (IFE), dynamic and static quenching as well as photoinduced electron transfer had been investigated. As depicted in Supplementary Figure S6, AA displayed a strong absorption peak at 245 nm, which did not overlap with the Cel-

TABLE 2 The concentration of AA in 40-fold diluted serum detected using the Cel-Au NCs.

Samples	Spiked (μM)	Measured (μM)	Recovery (%)	RSD (%)
Serum 1	10	9.95 ± 0.42	99.53	4.15
	25	25.07 ± 0.76	100.29	3.05
	50	49.91 ± 1.28	99.82	2.57
Serum 2	10	10.44 ± 0.37	104.39	3.70
	25	25.26 ± 0.39	101.02	1.57
	50	49.38 ± 1.55	98.76	3.10
Serum 3	10	10.48 ± 0.23	104.83	2.25
	25	24.74 ± 1.26	98.97	5.04
	50	50.23 ± 0.53	100.47	1.05

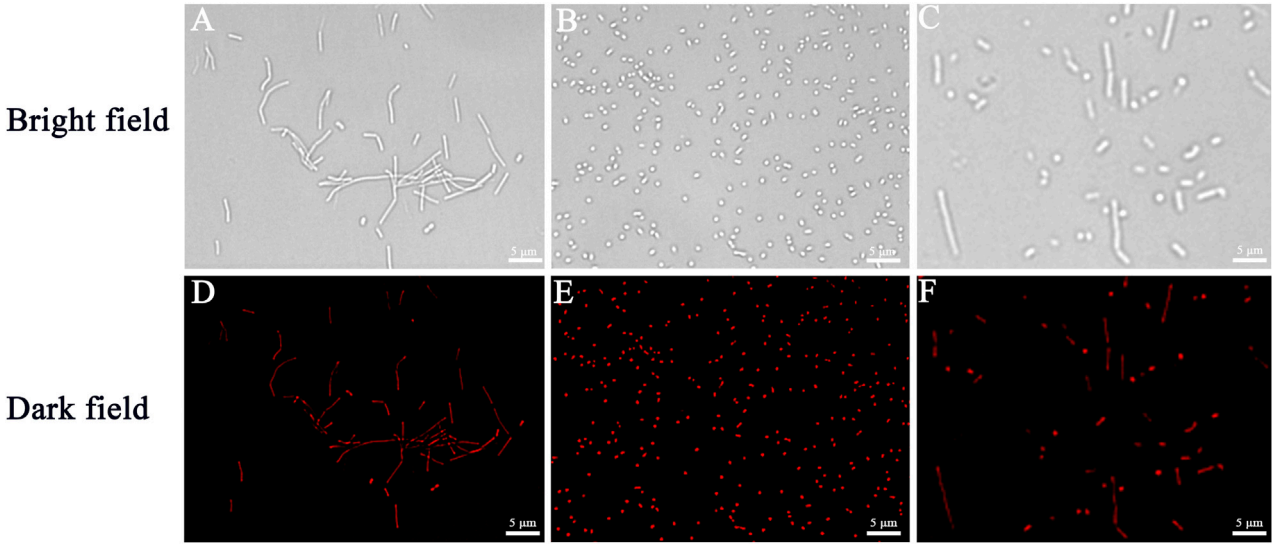

FIGURE 3
The fluorescence microscopic images of bacteria respectively correspond to bright fields and dark fields of *Bacillus subtilis* **(A,D)**, *Staphylococcus aureus* **(B,E)**, and *Escherichia coli* **(C,F)** using Cel-Au NCs as a probe.

Au NCs emission spectrum (600–800 nm), demonstrating that the mechanism of quenching mechanism caused by AA was not FRET and IFE (Fan et al., 2022). Notably, the fluorescent lifetimes were 10.27 μs and 9.60 μs for Cel-Au NCs before and after the addition of AA, separately (Figure 2F). The noticeable change in the fluorescence lifetime of Cel-Au NCs upon the addition of AA indicated that the quenching mechanism might be dynamic quenching rather than static quenching. Similarly, the fluorescence quenching of LDH-GQD caused by Fe^{3+} was determined to be dynamic quenching due to the reduction of fluorescence lifetime from 6.45 ns to 1.21 ns (Shi et al., 2021). Furthermore, the zeta potential of Cel-Au NCs increased from −15.2 mV to −13.3 mV after adding AA (Supplementary Figure S7). The negative zeta potential of the Cel-Au NCs is attributed to the presence of carboxylic groups with negative charges on the surface of cellulase, while the apparent increase in the zeta potential of Cel-Au NCs after the addition of AA confirms that the positively charged AA was attached to the surface of the negatively charged Cel-Au NCs. Additionally, the reducing power of AA caused the alteration in the oxidation state of Au (I), localized on the surface of the Au (0) core, further leading to the fluorescence quenching of Cel-Au NCs. (Li et al., 2015; Li et al., 2017). Hence, the quenching mechanism of Cel-Au NCs might be attributed to photoinduced electron transfer and dynamic quenching mechanism.

Application of AA detection in real samples

For assessing the practicality of the method in actual samples, the detection of AA in serum samples was carried

out. As depicted in Table 2, the recovery rates of AA in actual samples were in the range of 98.76%–104.83%, and the relative standard deviations (RSD) ranged from 1.05% to 5.04%. Furthermore, to demonstrate the practicability and accuracy of this biosensor, diverse concentrations of AA in serum samples were analyzed by the commercial HPLC method (Supplementary Table S2). The recoveries of AA were between 94.24% and 102.24% with RSD of 0.13%–3.07%. These results illustrated that this developed biosensor was applicable for the detection of AA in biological samples in comparison with the HPLC method.

Biocompatibility assessment of Cel-Au NCs

The biocompatibility of Cel-Au NCs was evaluated by measuring the bacterial density at OD600. The assay was conducted on three kinds of bacteria including *B. subtilis* (gram-positive bacteria), *S. aureus* (gram-positive bacteria) and *E. coli* (gram-negative bacteria). As evidenced by Supplementary Figure S8, Cel-Au NCs exhibited a negligibly inhibitory effect on bacterial cell proliferation within the range of 0–100 μg/ml and had a slight inhibitory on bacterial cell proliferation at 200 μg/ml, indicating low cytotoxicity of the Cel-Au NCs to bacteria.

Bioimaging for types of bacteria

To verify the bacterial labeling ability of Cel-Au NCs, bacterial cells incubated with Cel-Au NCs were observed under a fluorescence microscope. *B. subtilis* (gram-positive bacteria, Figures 3A, D), *S. aureus* (gram-positive bacteria, Figures 3B, E), and *E. coli* (gram-negative bacteria, Figures 3C, F) stained by Cel-Au NCs were respectively shown in the bright field and the dark field with strong red emission when excitation at 605 nm. In light of this, we hypothesized that Cel-Au NCs with ultra-small size might be absorbed by bacteria and interact with multiple proteins in the bacteria. In our previous study, *S. aureus*, *B. subtilis* as well as *Microbacterium* incubated with papain-Pt NCs could emit distinct green fluorescence (Chang et al., 2021). Besides, in the latest research, Li's group used red-fluorescent cBSA-AuAgNCs with an average diameter of 1.80 nm to label *E. coli* (Li et al., 2022). Therefore, Cel-Au NCs with satisfactory fluorescence characteristics could be explored as a bioprobe that effectively labels the microorganism cells.

Conclusion

In summary, with cellulase serving as the template, a one-step biomineralization strategy was successfully proposed to synthesize fluorescent Au NCs for the first time. The average size of as-synthesized Au NCs was found to be 1.68 nm and it displayed an emission peak maximum at 680 nm when excited at 560 nm. Notably, the fluorescent Cel-Au NCs as a "turn-off" biosensor could be used to assay AA with an extraordinary linear correlation over a range of 10–800 μM and a LOD of 2.5 μM. Furthermore, the practical application of the biosensor was successfully developed by evaluating AA in serum samples with appreciable recoveries of 98.76%–104.83%. In addition, Cel-Au NCs displayed a negligibly inhibitory effect on bacterial cell proliferation over 0–100 μg/ml, indicating low cytotoxicity of the pre-made Au NCs to bacteria. Furthermore, due to ultra-small size, obvious red fluorescence, and water solubility, Cel-Au NCs were also used as a bioprobe for various bacterial labeling, including *B. subtilis*, *S. aureus* and *E. coli*. This analytical and bioimaging procedure is notable as it can perform directly in a complicated environment and does not require any organic reagents as pretreatment. Therefore, this study provides new protein-directed and dual-functional Au NCs open alternative avenues for AA detection and bacterial imaging in biomedical fields.

Data availability statement

The original contributions presented in the study are included in the article/Supplementary Material, further inquiries can be directed to the corresponding authors.

Author contributions

BW: Conceptualization, Data curation, Funding acquisition, Methodology, Writing–original draft, Writing–review and editing. JF: Data curation, Methodology, Writing–original draft, Writing–review and editing. HT: Investigation, Methodology, Writing–original draft. SL: Conceptualization, Formal Analysis, Investigation, Methodology, Writing–review and editing. YC: Formal Analysis, Investigation, Writing–review and editing. XY: Formal Analysis, Investigation, Methodology, Writing–review and editing. YH: Investigation, Methodology, Writing–review and editing.

Funding

The author(s) declare financial support was received for the research, authorship, and/or publication of this article. This work was supported by the Provincial Project of Natural Science Research for Colleges and Universities of Anhui Province of China (KJ2016A274 and KJ2020ZD07); The Nature Science Foundation of Anhui Province (2108085MC78 and 1608085MC67); Anhui Provincial Engineering Research Centre for Molecular Detection and Diagnostics (2022AH010012); The Anhui Province Science Fund for Distinguished Young Scholars (2008085J10); Anhui Laboratory of Molecule-Based Materials, College of Chemistry and Materials Science, Anhui Normal University (fzj20003 and fzj20008); The Student's Platform for Innovation and Entrepreneurship Training Program (S202210370291); and Anhui Provincial Key Laboratory of the Conservation and Exploitation of Biological Resources.

Conflict of interest

The authors declare that the research was conducted in the absence of any commercial or financial relationships that could be construed as a potential conflict of interest.

Publisher's note

All claims expressed in this article are solely those of the authors and do not necessarily represent those of their affiliated organizations, or those of the publisher, the editors and the reviewers. Any product that may be evaluated in this article, or claim that may be made by its manufacturer, is not guaranteed or endorsed by the publisher.

Supplementary material

The Supplementary Material for this article can be found online at: https://www.frontiersin.org/articles/10.3389/fbioe.2023.1258036/full#supplementary-material

References

Abulizi, A., Okitsu, K., and Zhu, J. J. (2014). Ultrasound assisted reduction of graphene oxide to graphene in L-ascorbic acid aqueous solutions: kinetics and effects of various factors on the rate of graphene formation. *Ultrason. Sonochem.* 21, 1174–1181. doi:10.1016/j.ultsonch.2013.10.019

Areeshi, M. Y. (2022). Microbial cellulase production using fruit wastes and its applications in biofuels production. *Int. J. Food Microbiol.* 378, 109814. doi:10.1016/j.ijfoodmicro.2022.109814

Balu, R., Knott, R., Elvin, C. M., Hill, A. J., N, R. C., and Dutta, N. K. (2019). A sustainable biomineralization approach for the synthesis of highly fluorescent ultra-small Pt nanoclusters. *Biosens. (Basel)* 9, 128. doi:10.3390/bios9040128

Bhamore, J. R., Jha, S., Singhal, R. K., Murthy, Z. V. P., and Kailasa, S. K. (2019). Amylase protected gold nanoclusters as chemo- and bio- sensor for nanomolar detection of deltamethrin and glutathione. *Sens. Actuators, B* 281, 812–820. doi:10.1016/j.snb.2018.11.001

Bothra, S., Upadhyay, Y., Kumar, R., Ashok, K. S. K., and Sahoo, S. K. (2017). Chemically modified cellulose strips with pyridoxal conjugated red fluorescent gold nanoclusters for nanomolar detection of mercuric ions. *Biosens. Bioelectron.* 90, 329–335. doi:10.1016/j.bios.2016.11.066

Burini, G. (2007). Development of a quantitative method for the analysis of total L-ascorbic acid in foods by high-performance liquid chromatography. *J. Chromatogr. A* 1154, 97–102. doi:10.1016/j.chroma.2007.03.013

Chan, P. H., and Chen, Y. C. (2012). Human serum albumin stabilized gold nanoclusters as selective luminescent probes for Staphylococcus aureus and methicillin-resistant Staphylococcus aureus. *Anal. Chem.* 84, 8952–8956. doi:10.1021/ac302417k

Chang, X., Gao, P., Li, Q. F., Liu, H. M., Hou, H. H., Wu, S., et al. (2021). Fluorescent papain-encapsulated platinum nanoclusters for sensing lysozyme in biofluid and gram-positive bacterial identification. *Sens. Actuators, B* 345, 130363. doi:10.1016/j.snb.2021.130363

Chen, J., Liu, Z. Q., Fang, J. X., Wang, Y. X., Cao, Y., Xu, W. J., et al. (2022). A turn-on fluorescence biosensor for sensitive detection of carbaryl using flavourzyme-stabilized gold nanoclusters. *LWT-Food Sci. Technol.* 157, 113099. doi:10.1016/j.lwt.2022.113099

Chen, Y. X., Phipps, M. L., Werner, J. H., Chakraborty, S., and Martinez, J. S. (2018). DNA templated metal nanoclusters: from emergent properties to unique applications. *Acc. Chem. Res.* 51, 2756–2763. doi:10.1021/acs.accounts.8b00366

Diep, T. T., Pook, C., Rush, E. C., and Yoo, M. J. Y. (2020). Quantification of carotenoids, α-tocopherol, and ascorbic acid in amber, mulligan, and laird's large cultivars of New Zealand tamarillos (*Solanum betaceum* cav). *Foods* 9, 769. doi:10.3390/foods9060769

Duan, H. W., and Nie, S. M. (2007). Etching colloidal gold nanocrystals with hyperbranched and multivalent polymers: A new route to fluorescent and water-soluble atomic clusters. *J. Am. Chem. Soc.* 129, 2412–2413. doi:10.1021/ja067727t

Ejaz, U., Sohail, M., and Ghanemi, A. (2021). Cellulases: from bioactivity to a variety of industrial applications. *Biomimetics* 6, 44. doi:10.3390/biomimetics6030044

Fan, P. F., Liu, C., Hu, C. C., Li, F. F., Lin, X., Yang, S. Y., et al. (2022). Green and facile synthesis of iron-doped biomass carbon dots as a dual-signal colorimetric and fluorometric probe for the detection of ascorbic acid. *New J. Chem.* 46, 2526–2533. doi:10.1039/D1NJ05047H

Gan, L. L., Su, Q., Chen, Z. B., and Yang, X. M. (2020). Exploration of PH-responsive carbon dots for detecting nitrite and ascorbic acid. *Appl. Surf. Sci.* 530, 147269. doi:10.1016/j.apsusc.2020.147269

Guo, Y. H., Amunyela, H. T. N. N., Cheng, Y. L., Xie, Y. F., Yu, H., Yao, W. R., et al. (2021). Natural protein-templated fluorescent gold nanoclusters: syntheses and applications. *Food Chem.* 335, 127657. doi:10.1016/j.foodchem.2020.127657

Huang, J. L., Lin, L. Q., Sun, D. H., Chen, H. M., Yang, D. P., and Li, Q. B. (2015). Bio-inspired synthesis of metal nanomaterials and applications. *Chem. Soc. Rev.* 44, 6330–6374. doi:10.1039/C5CS00133A

Jin, R. C., Zeng, C. J., Zhou, M., and Chen, Y. X. (2016). Atomically precise colloidal metal nanoclusters and nanoparticles: fundamentals and opportunities. *Chem. Rev.* 116, 10346–10413. doi:10.1021/acs.chemrev.5b00703

Li, C., Zeng, J. J., Guo, D., Liu, L., Xiong, L. W., Luo, X. G., et al. (2021). Cobalt-doped carbon quantum dots with peroxidase-mimetic activity for ascorbic acid detection through both fluorometric and colorimetric methods. *ACS Appl. Mat. Interfaces* 13, 49453–49461. doi:10.1021/acsami.1c13198

Li, H. L., Zhu, W. L., Wan, A. J., and Liu, L. B. (2017). The mechanism and application of the protein-stabilized gold nanocluster sensing system. *Analyst* 142, 567–581. doi:10.1039/c6an02112c

Li, Y., Chen, T., Huang, L., Ma, L., Lin, Q., and Chen, G. (2015). A fluorescent sensor based on ovalbumin-modified Au nanoclusters for sensitive detection of ascorbic acid. *Anal. Methods.* 7, 4123–4129. doi:10.1039/C5AY00798D

Li, Y. X., Qu, S. H., Xue, Y. M., Zhang, L. B., and Li, S. (2022). Cationic antibacterial metal nanoclusters with traceable capability for fluorescent imaging the nano—bio interactions. *Nano Res.* 16, 999–1008. doi:10.1007/s12274-022-4837-x

Liu, H., Na, W., Liu, Z., Chen, X., and Su, X. (2017). A novel turn-on fluorescent strategy for sensing ascorbic acid using graphene quantum dots as fluorescent probe. *Biosens. Bioelectron.* 92, 229–233. doi:10.1016/j.bios.2017.02.005

Ma, Y., Zhang, Y., and Wang, L. (2021). An electrochemical sensor based on the modification of platinum nanoparticles and ZIF-8 membrane for the detection of ascorbic acid. *Talanta* 226, 122105. doi:10.1016/j.talanta.2021.122105

Qiao, Z. J., Zhang, J., Hai, X., Yan, Y. C., Song, W. L., and Bi, S. (2021). Recent advances in templated synthesis of metal nanoclusters and their applications in biosensing, bioimaging and theranostics. *Biosens. Bioelectron.* 176, 112898. doi:10.1016/j.bios.2020.112898

Shi, H., Chen, L., and Niu, N. (2021). An off-on fluorescent probe based on graphene quantum dots intercalated hydrotalcite for determination of ascorbic acid and phytase. *Sens. Actuators, B* 345, 130353. doi:10.1016/j.snb.2021.130353

Singh, A., Rai, T., and Panda, D. (2016). Photoluminescence dynamics of copper nanoclusters synthesized by cellulase: role of the random-coil structure. *RSC Adv.* 6, 55539–55545. doi:10.1039/C6RA09763D

Sun, L. L., Zhou, H. F., Huang, D. P., Wang, T., Gao, P., Sun, Y. Z., et al. (2019). Fluorometric determination of antioxidant capacity in human plasma by using upconversion nanoparticles and an inner filter effect mechanism. *Microchim. Acta.* 186, 502. doi:10.1007/s00604-019-3627-y

Tan, H. X., Liu, S. S., He, Y. L., Cheng, G. F., Zhang, Y., Wei, X. J., et al. (2021). Spider toxin peptide-induced NIR gold nanocluster fabrication for GSH-responsive cancer cell imaging and nuclei translocation. *Front. Bioeng. Biotechnol.* 9, 780223. doi:10.3389/fbioe.2021.780223

Wang, B. J., Zhao, M., Mehdi, M., Wang, G. F., Gao, P., and Zhang, K. Q. (2019). Biomolecule-assisted synthesis and functionality of metal nanoclusters for biological sensing: A review. *Mat. Chem. Front.* 3, 1722–1735. doi:10.1039/C9QM00165D

Wei, H., Wang, Z., Yang, L., Tian, S., Hou, C., and Lu, Y. (2010). Lysozyme-Stabilized gold fluorescent cluster: synthesis and application as Hg^{2+} sensor. *Analyst* 135, 1406–1410. doi:10.1039/C0AN00046A

Xu, H. X., and Suslick, K. S. (2010). Sonochemical synthesis of highly fluorescent Ag nanoclusters. *ACS Nano* 4, 3209–3214. doi:10.1021/nn100987k

Yu, Y., New, S. Y., Xie, J. P., Su, X. D., and Tan, Y. N. (2014). Protein-based fluorescent metal nanoclusters for small molecular drug screening. *Chem. Commun.* 50, 13805–13808. doi:10.1039/C4CC06914E

Yue, Y., Liu, T. Y., Li, H. W., Liu, Z. Y., and Wu, Y. Q. (2012). Microwave-assisted synthesis of BSA-protected small gold nanoclusters and their fluorescence-enhanced sensing of silver(I) ions. *Nanoscale* 4, 2251–2254. doi:10.1039/C2NR12056A

Zhang, L. B., and Wang, E. K. (2014). Metal nanoclusters: new fluorescent probes for sensors and bioimaging. *Nano Today* 9, 132–157. doi:10.1016/j.nantod.2014.02.010

Zhou, S., Duan, Y., Wang, F., and Wang, C. (2017). Fluorescent Au nanoclusters stabilized by silane: facile synthesis, color-tunability and photocatalytic properties. *Nanoscale* 9, 4981–4988. doi:10.1039/C7NR01052D

Zhuang, Z. H., and Chen, W. (2020). One-step rapid synthesis of $Ni_6(C_{12}H_{25}S)_{12}$ nanoclusters for electrochemical sensing of ascorbic acid. *Analyst* 145, 2621–2630. doi:10.1039/C9AN01947B

frontiers | Frontiers in Bioengineering and Biotechnology

TYPE Original Research
PUBLISHED 09 November 2023
DOI 10.3389/fbioe.2023.1303142

OPEN ACCESS

EDITED BY
Kang Cui,
University of Jinan, China

REVIEWED BY
Tian Qiang,
Jiangnan University, China
Shipeng Zhang,
Kwangwoon University, Republic of Korea
Yanan Ding,
Shandong University of Science and Technology, China

*CORRESPONDENCE
Qihui Zhou,
qihuizhou@uor.edu.cn
Yuanyue Li,
yyli@qdu.edu.cn
Zhao Yao,
yzh17@qdu.edu.cn

†These authors have contributed equally to this work

RECEIVED 27 September 2023
ACCEPTED 30 October 2023
PUBLISHED 09 November 2023

CITATION
Lv L, Liu T, Jiang T, Li J, Zhang J, Zhou Q, Dhakal R, Li X, Li Y and Yao Z (2023), A highly sensitive flexible capacitive pressure sensor with hierarchical pyramid micro-structured PDMS-based dielectric layer for health monitoring.
Front. Bioeng. Biotechnol. 11:1303142.
doi: 10.3389/fbioe.2023.1303142

A highly sensitive flexible capacitive pressure sensor with hierarchical pyramid micro-structured PDMS-based dielectric layer for health monitoring

Luyu Lv[1,2†], Tianxiang Liu[1,2†], Ting Jiang[1], Jiamin Li[1,2], Jie Zhang[1,2], Qihui Zhou[1,3*], Rajendra Dhakal[4], Xiao Li[5], Yuanyue Li[2*] and Zhao Yao[1,2*]

[1]Heart Center, Qingdao Hiser Hospital Affiliated of Qingdao University (Qingdao Traditional Chinese Medicine Hospital), Qingdao University, Qingdao, China, [2]College of Electronics and Information, Qingdao University, Qingdao, China, [3]School of Rehabilitation Sciences and Engineering, University of Health and Rehabilitation Sciences, Qingdao, China, [4]Department of Computer Science and Engineering, Sejong University, Seoul, Republic of Korea, [5]Hisense Visual Technology Co., Ltd., Qingdao, China

Herein, a flexible pressure sensor with high sensitivity was created using a dielectric layer featuring a hierarchical pyramid microstructure, both in simulation and fabrication. The capacitive pressure sensor comprises a hierarchically arranged dielectric layer made of polydimethylsiloxane (PDMS) with pyramid microstructures, positioned between copper electrodes at the top and bottom. The achievement of superior sensing performance is highly contingent upon the thickness of the dielectric layer, as indicated by both empirical findings and finite-element analysis. Specifically, the capacitive pressure sensor, featuring a dielectric layer thickness of 0.5 mm, exhibits a remarkable sensitivity of 0.77 kPa^{-1} within the pressure range below 1 kPa. It also demonstrates an impressive response time of 55 ms and recovery time of 42 ms, along with a low detection limit of 8 Pa. Furthermore, this sensor showcases exceptional stability and reproducibility with up to 1,000 cycles. Considering its exceptional achievements, the pressure sensor has been effectively utilized for monitoring physiological signals, sign language gestures, and vertical mechanical force exerted on objects. Additionally, a 5 × 5 sensor array was fabricated to accurately and precisely map the shape and position of objects. The pressure sensor with advanced performance shows broad potential in electronic skin applications.

KEYWORDS

PDMS, capacitive pressure sensor, hierarchical pyramid microstructure, high sensing performance, physiological signals monitoring

Introduction

The flexible pressure sensor serves as a core component for electronic skin (Guo et al., 2022; Zheng et al., 2022; Zhu et al., 2022), enabling the emulation of human skin's sensing mechanism and exhibiting promising potential in wearable device applications (Lin et al., 2020; Lee et al., 2021; Lyu et al., 2021), smart prosthetics (Tian et al., 2019; Khoshmanesh et al., 2021), health monitoring (Rocha et al., 2021; Wang et al., 2022; Han et al., 2022), and body motion detection (Xiong et al., 2020; Zhu et al., 2021), etc. The classification of pressure sensors can be based on five distinct sensing mechanisms: piezoresistivity (Ding et al., 2020; Wang et al., 2022b; Ji et al., 2022), capacitance (Li et al., 2020; Qin et al., 2021; Wang et al., 2022c; Duan et al., 2022), piezoelectricity (Wang et al., 2021; Luo et al., 2021; Yi et al., 2022), field-effect transistors (Shi et al., 2020; Cheng et al., 2023), and triboelectricity (Wang et al., 2021; Liu et al., 2021; Xu et al., 2022). Among them, the capacitive pressure sensor has garnered substantial research for the superiority of outstanding structural stability, rapid response time, minimal power consumption, and a compact circuit design. Similar to the conventional parallel-plate capacitor, capacitive pressure sensors typically employ a "sandwich" structure, comprising a dielectric layer sandwiched between two electrodes positioned at the top and bottom. Its capacitance (C) is determined by the dielectric layer's permittivity (ε), the effective area between two electrodes (A), and the separation distance of plate electrodes (d). Generally, the vertical force on the capacitive pressure sensor can induce variations in the dielectric layer thickness, leading to corresponding changes in the capacitance measurement. Therefore, it's vital to select a suitable material and optimize the structure configuration for the dielectric layer. Furthermore, the preparation of capacitive pressure sensors with controllable morphology on a large scale poses a significant challenge in achieving high performance.

The commonly utilized materials for fabricating the flexible dielectric layer include elastomers like polydimethylsiloxane (PDMS) (Wan et al., 2018; Hwang et al., 2021), polystyrene (Tian et al., 2020; Su et al., 2021), polyurethane (PU) (Seyedin et al., 2020; Zhu et al., 2020), etc. Among them, PDMS has emerged as the dominant choice for the dielectric layer owing to its reduced Young's modulus, enhanced thermal stability and improved chemical stability. Moreover, the implementation of the micro-structured designs on the dielectric layer, such as micro-pyramid (Yang et al., 2019; Li et al., 2020; Zhang et al., 2021; Tao et al., 2022), micro-porous (Li et al., 2020; He et al., 2020), micro-sphere (Jung et al., 2020; Xiong et al., 2020), micro-pillar (Luo et al., 2019; Cao et al., 2020), micro-wrinkles (Zeng et al., 2019; Tang et al., 2021), etc., has demonstrated its efficacy in enhancing sensor performance. Generally, the realization of the microstructure is based on the template replication approach, which consists of soft-lithography and hard-lithography. Soft-lithography technique exploits bionic micro-patterns to make microstructures via directly copying the morphology of natural substances. Wan et al. developed an exceptional sensitivity (1.2 kPa^{-1}) flexible tactile sensor by utilizing lotus leaf as template to obtain bionic microtowers array structure m-PDMS substrate (Wan et al., 2018). Jian and colleagues developed pressure sensors that exhibit exceptional performance, featuring an impressive sensitivity of 19.8 kPa^{-1} and an incredibly low detection threshold of 0.6 Pa. These sensors were constructed using a highly conductive active film combined with a bionic hierarchical microstructured PDMS substrate, which was replicated from the leaves of E. aureum plant species (Jian et al., 2017). However, it is difficult for large-scale fabrication. In addition, it suffers from an inherent flaw where the microstructure's shape, dimension, and spacing remain unalterable. Therefore, it is not feasible to fabricate structured micro-patterns with a predetermined form and dimension. The hard-lithography is an effective approach that can tackle the above problems. The hard-lithography depends on photolithography technique and wet etching to fabricate a patterned template that can be transferred to a flexible polymer material. Luo et al. have successfully designed a capacitive sensor utilizing a tilted pillar array dielectric layer, showcasing exceptional sensitivity of 0.42 kPa^{-1} below 1 kPa. The dielectric layer was molded from the tilted micro-structured template made by photolithography (Luo et al., 2019). In the same way, Tao and colleagues produced a novel dielectric layer using ionic gels with pyramidal-shaped microstructured to obtain an unprecedented sensitivity of 41 kPa^{-1} (Tao et al., 2022). Thanks to the implementation of a porous pyramid dielectric layer, Yang's group prepared an ultrahigh sensitive (44.5 kPa^{-1}) capacitive pressure sensor, which was designed to be unaffected by strain and temperature (Yang et al., 2019). The manufacturing process has merits of high precision, controllable aspect ratio, and mass production. Therefore, the hard-lithography technique enables the production of a microstructure that not only facilitates the efficient manufacturing of pressure sensors with superior performance on a large scale but also fulfills the requirement for convenient alteration of the microstructure's morphology.

In this research, an efficient hard-lithography technique was employed to fabricate an exceptional sensitivity capacitive pressure sensor. The sensor utilized copper foils for both the bottom and top electrodes, along with a PDMS dielectric layer that incorporates a hierarchical pyramid microstructure. The prepared flexible capacitive pressure sensor exhibits a remarkable sensitivity of 0.77 kPa^{-1} below 1 kPa. It also demonstrates an impressive response time of 55 ms and recovery time of 42 ms, along with a low detection limit of 8 Pa. Furthermore, this sensor showcases exceptional stability and reproducibility with up to 1,000 cycles. Moreover, the comparison was conducted to evaluate the impact of dielectric layer's microstructure and thickness on capacitive pressure sensors' sensitivity. Meanwhile, the sensing performance was further evaluated through finite element analysis (FEA) to investigate the impact of dielectric layer's microstructure and thickness. The increased deformation of the sensor with microstructure and thinner dielectric layer under identical pressure is responsible for this phenomenon. The development of a 5 × 5 sensor array was undertaken to facilitate the identification of spatial pressure allocation exerted by various objects. Ultimately, the artificially created pressure sensor exhibits a vast array of potential applications, encompassing monitoring human biological signals, detecting body motion and vertical mechanical pressure.

Experimental section

Preparation process of a patterned silicon template

The patterned template was fabricated through the utilization of photolithography on <100> silicon wafers that were covered with a

300 nm thermally grown oxide layer. The processes involved in photolithography can be described follows (Ruth et al., 2020). Firstly, the silicon wafer underwent a cleaning process using acetone/IPA/DI water, followed by drying with N_2 blowing. Secondly, the silicon wafer's surface was spin-coated with the photoresist (KXN5735-L0 negative photoresist) at 500 rpm for 6 s and a subsequent coating at 3,000 rpm for 20 s. The photoresist film was subjected to a preliminary baking process at 100°C for 90 s and exposed by the UV aligner. The wafer backed again at 120°C for 90 s. Thirdly, the photoresist film was developed by TMAH (2.38%) for 30 s and post-baked at 120°C for 3 min before wet etching. Next, the silicon oxide layer was etched by buffer oxide etchant (BOE) for 5 min. Eventually, the special hierarchical pyramid microstructure of the silicon template was fabricated by anisotropic etching using 5 M KOH solution for 5 h.

Fabrication process of a pressure sensor with hierarchical pyramid microstructure

Firstly, the PDMS and the curing agent were meticulously mixed in a 10:1 weight ratio. Secondly, after a 30-min treatment in the vacuum chamber, the mixture's bubbles were entirely eliminated. The mixture was introduced into the silicon template and subjected to spin-coating at a speed of 1,000 rpm, then cured at a temperature of 85°C for a duration of 1.5 h. It is important to mention that the spin-coating rate during the same period has an impact on the thickness of the dielectric layer. The dielectric layer was subsequently removed from the silicon template featuring a hierarchical pyramid microstructure. Ultimately, a flexible pressure sensor was developed by integrating a dielectric layer featuring hierarchical pyramid microstructures with copper foils as the upper and lower electrodes.

Fabrication of a 5 × 5 sensor array

Five strips of copper foil with dimensions of 5 mm × 80 mm were applied to the polyimide (PI) tape in parallel at 5 mm intervals as the bottom electrode array. The identical procedure was employed to fabricate the top electrode array. The dielectric layer was fabricated using template replication technique, featuring a hierarchical pyramid microstructure. Once prepared, it was equally divided into 25 portions, each measuring 5 mm × 5 mm. The dielectric layer was securely adhered to the bottom electrode strips, while the top electrode strips were arranged orthogonally to form a 5 × 5 capacitive pressure sensor arrays (Ren et al., 2022).

Measurement of sensing performance

The artificially created sensor was setup on the pressure gage (ZQ-990, Zhiqu) test platform, while its upper and lower electrodes were linked to the precision LCR meter (E4980, Keysight). The capacitive response was measured by applying varying force, utilizing a precision LCR meter with 100 kHz, 1 V bias. A USB connection was established between the LCR meter, ZQ-990, and a laptop for the purpose of post-processing and analyzing data. The surface morphologies of the patterned silicon template and the prepared PDMS film were scanned using field-emission scanning electron microscopy (FESEM, Hitachi S-4800, Japan) to obtain high-resolution images.

Results and discussion

Fabrication and characterization

The flowchart of the photolithography process for the patterned silicon template are shown in Figure 1A. The fabrication process of the capacitive pressure sensor with the hierarchical pyramid microstructure dielectric layer is depicted in Figure 1B. The experiment setup for the sensing performance measurement is illustrated in Figure 1C. The Experimental Section provides a detailed account of the fabrication techniques employed and the methodology used for measuring the sensing performance. The SEM images of the patterned silicon template and the micro-structured PDMS film are depicted in Figure 2. The top view of the patterned silicon template reveals variations in microstructure size (Figure 2A), resulting in a visually striking hierarchical pyramid appearance. The distribution of these pyramids on the template exhibits a higher central peak and lower side peaks. The base of the pyramid is either a square or a rectangle in shape. The base of the pyramid exhibits a size variation ranging from approximately 40 μm–500 μm, while its height spans between 28 μm and 350 μm. After the templating process, the PDMS films display hierarchical pyramid microstructures as shown in Figure 2B.

Pressure sensing performance of the flexible capacitive pressure sensor

The capacitive pressure sensor operates on the principle that its capacitive sensitive element converts the pressure signal into an electrical signal output that is directly proportional to the applied pressure. Similar to the conventional parallel-plate capacitor, the capacitive pressure sensor employs a "sandwich" structure, comprising a dielectric layer sandwiched between two electrodes positioned at the top and bottom (Li et al., 2018). Its capacitance C is determined by the equation:

$$C = \frac{\varepsilon_0 \varepsilon_r A}{d} \tag{1}$$

where ε_0 and ε_r denote the dielectric constants of the vacuum and the dielectric layer. When a perpendicular pressure is exerted on the sensor, there will be a change in d, resulting in a modification of C. Conversely, A undergoes alteration when subjected to shear force (Zhao et al., 2015).

By optimizing the microstructures of the dielectric layer (Cao et al., 2020; Tao et al., 2022), incorporating silver nanowires into the dielectric layer (Fu et al., 2022), or distributing nanoparticles on the surface of the dielectric layer, significant enhancements can be achieved in terms of sensitivity for capacitive pressure sensors (Kim et al., 2018). The sensitivity in the first case is attributed to a reduction in d, while in the latter case it is due to an increase in ε_r. Incorporating microstructures into the dielectric layer significantly

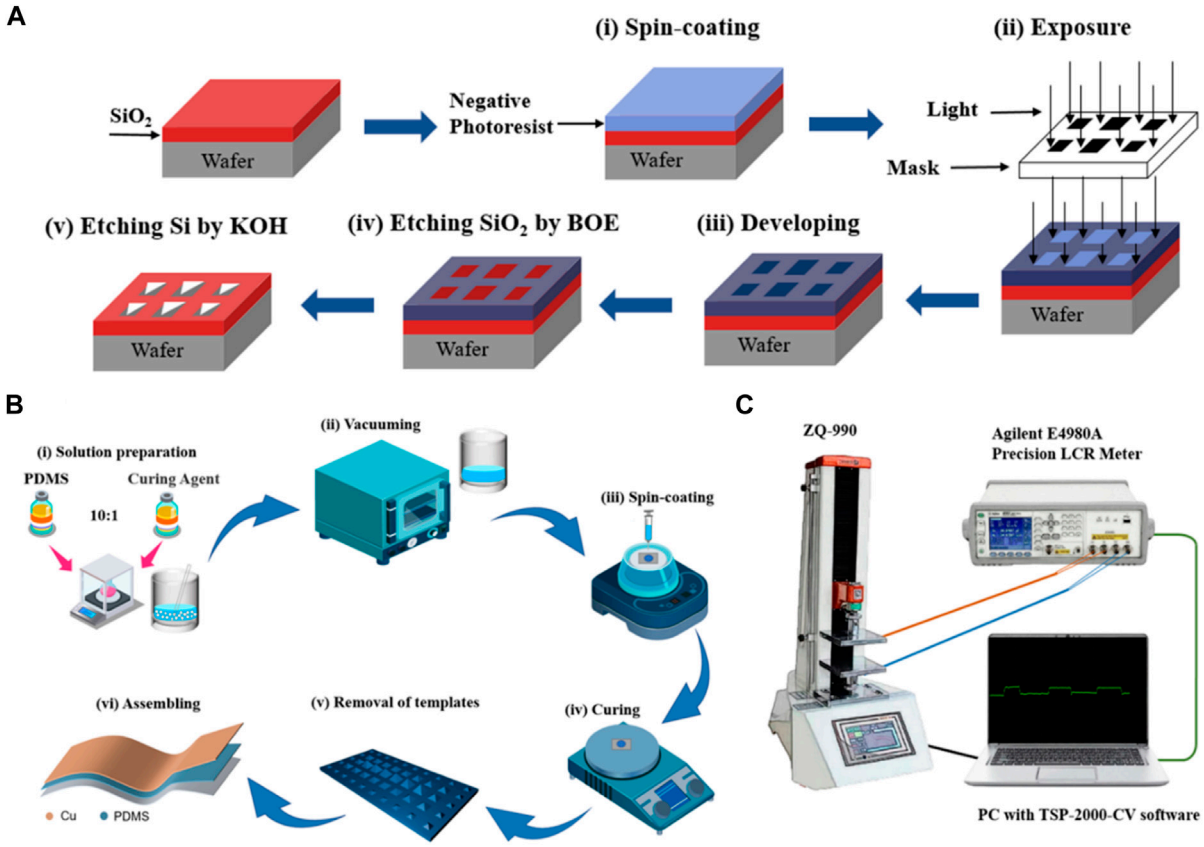

FIGURE 1
(A) Flowchart of the photolithography process for the patterned silicon template. **(B)** Schematic representation of the fabrication process for the flexible capacitive pressure sensor. **(C)** Experiment setup for the sensing performance measurement.

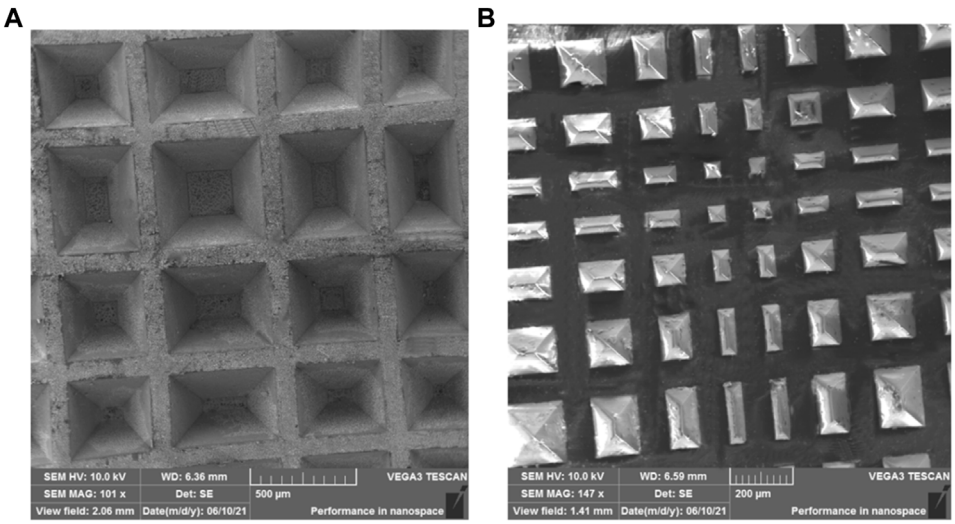

FIGURE 2
(A) SEM image of the patterned silicon template. **(B)** SEM image of the pyramid-structured PDMS film.

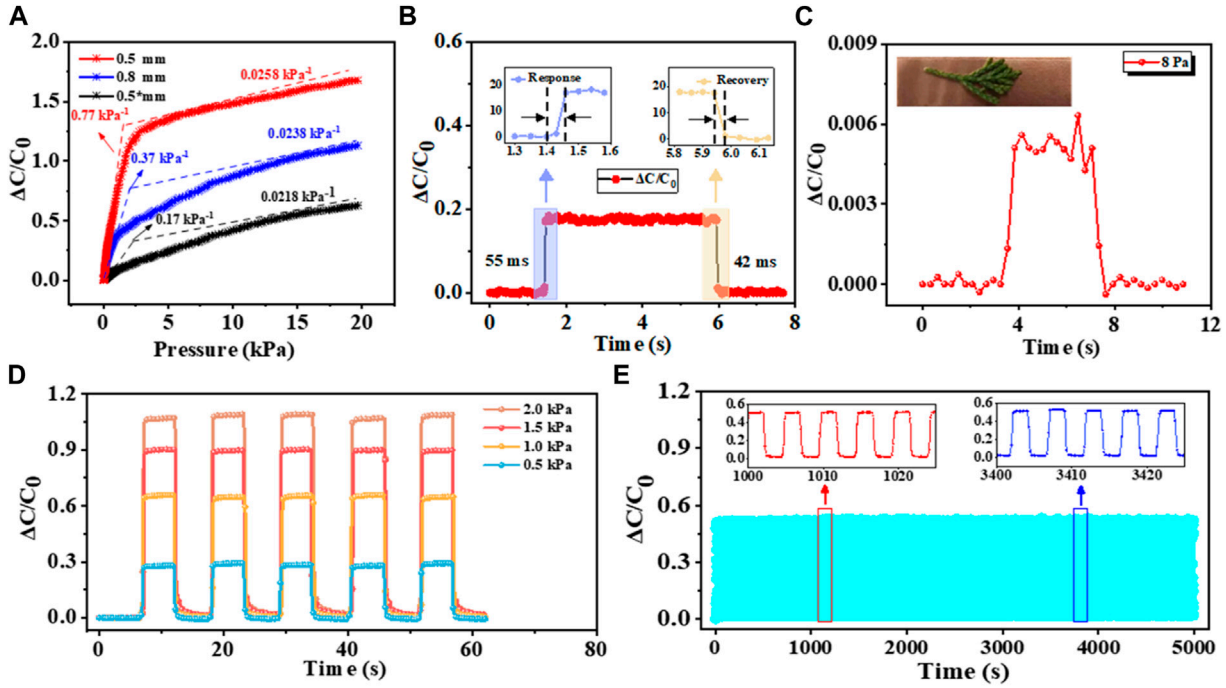

FIGURE 3
Sensing performance of the capacitive pressure sensor. **(A)** Sensitivity curves of capacitive pressure sensors based on the hierarchical pyramid microstructure dielectric layer with thicknesses of 0.5 mm (red) and 0.8 mm (blue), as well as the non-patterned dielectric layer with a thickness of 0.5 mm (black), respectively. **(B)** Real-time response under vertical pressure of ~400 Pa (the insets show response and recovery time). **(C)** Capacitance response under a small pressure of ~8 Pa. **(D)** Repeated real-time capacitance responses under 0.5, 1.0, 1.5, and 2.0 kPa. **(E)** 1,000 cycles for testing the stability of sensor under 0.8 kPa (the insets show the magnified view under different periods).

reduces its viscoelastic properties and greatly shortens both response and relaxation time. Based on the above discussion, a hierarchical pyramid microstructure dielectric layer has been designed. In comparison to other structures, this particular configuration enables greater deformation or higher change rate, resulting in rapid variations in capacitance and enhanced sensitivity.

The initial estimation of capacitive pressure sensor's fundamental sensing performance is conducted by applying vertical pressure. The evaluation of sensing performance heavily relies sensitivity (S), which is commonly characterized as (Niu et al., 2020):

$$S = \frac{\delta(\Delta C/C_0)}{\delta P} \quad (2)$$

where C_0 denotes the capacitance at the beginning and ΔC represents difference in capacitance (C-C_0), while P signifies the amount of vertical pressure exerted on the sensor. Based on the principle, the slope of the tangent of the pressure-capacitance curve reflects the level of sensitivity. As illustrated in Figure 3A, the variations in relative capacitance of the hierarchical pyramid microstructure sensor with the dielectric layer thickness of 0.5 mm was studied across a wide pressure range. To explore the impact of the dielectric layer's microstructure and thickness of on sensitivity, additional sensors with two different types of dielectric layers were produced for comparison: a planar dielectric layer measuring 0.5 mm in thickness and a hierarchical pyramid microstructure dielectric layer measuring 0.8 mm in thickness. As shown in Figure 3A, the hierarchical pyramid microstructure pressure sensor with a dielectric layer thickness of 0.5 mm outperforms the other two instances. When the pressure is below 1 kPa, the hierarchical pyramid microstructure sensor with a dielectric layer thickness of 0.5 mm exhibits a sensitivity of 0.77 kPa^{-1}, which significantly surpasses the sensitivity (0.37 kPa^{-1}) of the sensor having a dielectric layer thickness of 0.8 mm. Conversely, the sensor featuring the planar dielectric layer demonstrates a comparatively lower sensitivity of 0.17 kPa^{-1}. When the pressure exceeds 1 kPa, there is a reduction in sensitivity for the aforementioned three sensors to 0.0258 kPa^{-1}, 0.0238 kPa^{-1}, and 0.0218 kPa^{-1}, respectively. The exceptional sensitivity can be primarily attributed to the distinctive micro-pyramid architecture, as evidenced by the information provided earlier. Moreover, the correlation between the sensitivity and dielectric layer thickness becomes more evident as the dielectric layer thickness decreases from 0.8 mm to 0.5 mm, highlighting the impact of varying dielectric layer thickness on pressure sensor's sensitivity.

In addition to assessing sensitivity, an analysis on the response and recovery time measured by TSP-2000-CV was also performed. The sensor's capacitance quickly stabilizes within a mere 55 ms (top-left inset) when subjecting an object to a load of approximately 0.4 kPa, showcasing its exceptional response time, as illustrated in Figure 3B. After the elimination of the applied force, there is a rapid decline in the sensor's capacitance from its stable state to its initial value within a brief response period of 42 ms (top-right inset). It can be comparable to the human skin, typically ranging from 30 to

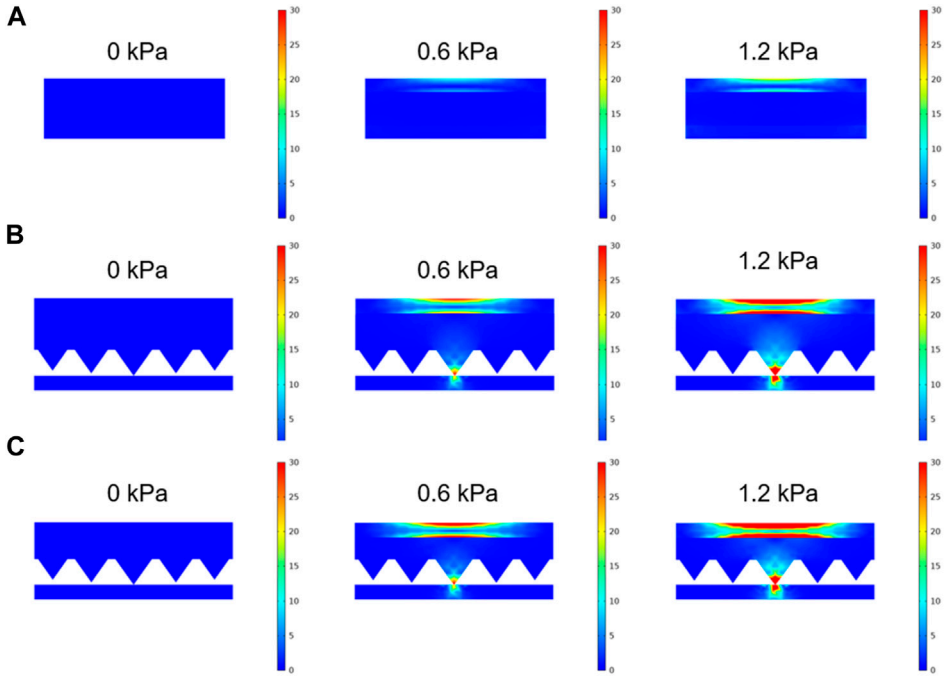

FIGURE 4
FEA simulation results of the pressure sensors. **(A)** Non-patterned sensor's contact stress distribution with a dielectric layer thickness measuring 0.5 mm under 0, 0.6, and 1.2 kPa, respectively. **(B)** Hierarchical pyramid microstructure sensor's contact stress distribution with a dielectric layer thickness of 0.8 mm under 0, 0.6, and 1.2 kPa, respectively. **(C)** Hierarchical pyramid microstructure sensor's contact stress distribution with the dielectric layer thickness of 0.5 mm under 0, 0.6, and 1.2 kPa, respectively.

50 ms. Such remarkable accomplishments can be ascribed to the PDMS's low viscoelasticity and the hierarchical pyramid microstructure. The capacitive pressure sensor is highly sensitive to detecting minute variations. With the assistance of the lightweight object (~8 Pa), the apparent alteration in capacitance during the loading/unloading process can be visible in Figure 3C. Its repeatability and discrimination capability under five repetitive exerting/releasing cycles with different vertical pressure is further assessed. The results in Figure 3D demonstrate real-time monitoring. By applied 0.5, 1.0, 1.5, and 2.0 kPa, respectively, the relative capacitance variation exhibits notable fluctuations while maintaining consistent levels under identical pressure condition. This suggests super repeatability and the ability to discern varying degrees of pressure. Moreover, given the paramount importance of long-term stability in practical applications, 1,000 loading/unloading cycles at 0.8 kPa were conducted to ensure its robustness. As shown in Figure 3E, the uniform waveforms devoid of discernible fatigue indicate that the sensor possesses prominent stability and reproducibility.

The sensing mechanism's validation was extended through FEA to examine the impact of dielectric layer's microstructure and thickness. The pressure sensors incorporated the dielectric layer configurations mentioned above were employed for comparative analysis. Figures 4A–C show the different stress distributions of the three sensors under 0, 0.6, and 1.2 kPa, respectively. As demonstrated in Figure 4A, under external vertical force, the whole contact surface of the planar sensor is deformed and the stress is distributed rather uniform. According to the parallel-plate capacitor definition, in this case, capacitance change is primarily influenced by the separation distance due to infrequent variations in the contact area. Therefore, the sensitivity is extremely low as a result of the minimal variation in the distance between adjacent planes. However, for the hierarchical pyramid microstructure pressure sensor (Figure 4B, C), the concentration of force on the microstructure is enhanced under identical pressure, resulting in increased deformation of the dielectric layer. That will increase the contact area and decrease the gap simultaneously, ultimately resulting in the improvement of the sensitivity. Moreover, when subjected to identical pressure, the thin sensor demonstrates a more extensive distribution of contact stress compared to the thick sensor. Consequently, this leads to an increase deformation. In general, the hierarchical pyramid microstructure pressure sensor with a thin dielectric layer causes the highest sensitivity, aligning well with the experimental findings.

Wearable applications of flexible capacitive pressure sensor

A pressure-sensitive device was attached to various points on the human body, including the wrist, elbow, and finger. Its purpose was to monitor physiological signals and track bodily movements including pulse rate, bending of the elbow, flexing of fingers, and twisting of the wrist, respectively. The pulse signals are crucial physiological indicators of an individual's health status. To identify wrist pulse, the pressure sensor has adhered to the participant's wrist and the resulting signals were showcased in Figure 5A. The

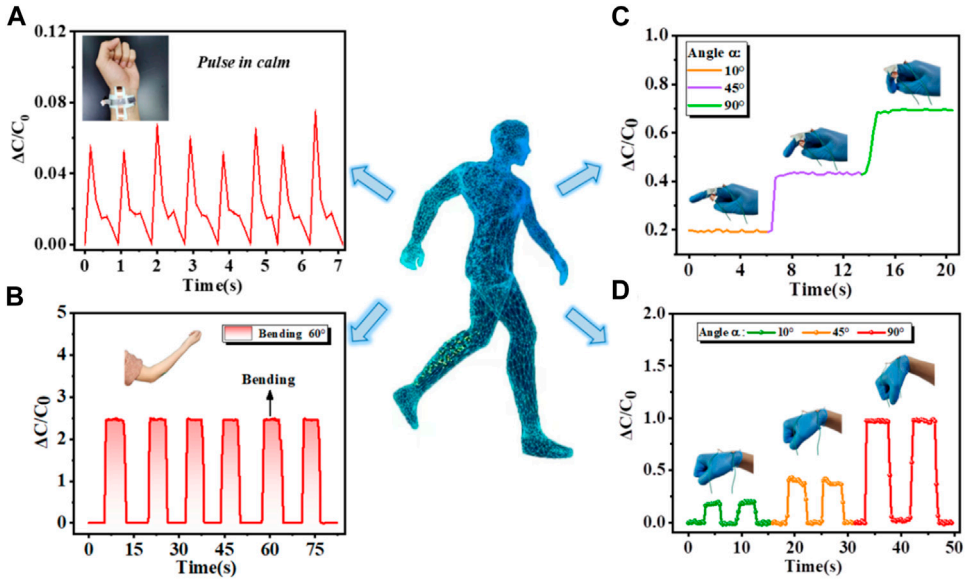

FIGURE 5
Various applications in recognition of physiological signals and human body motions. Real-time capacitance responses of different body positions including monitoring **(A)** wrist pulse under steady breath, **(B)** elbow with a bending angle of 60°, **(C)** finger, and **(D)** wrist with bending angles of 10°, 45°, and 90°, respectively.

displayed data and replicable pulse patterns, with a frequency of approximately 1 Hz that closely resembles that of a human wrist pulse. Hence, the sensor encouraging prospects in the surveillance of feeble biomedical signals. Besides, capacitance responses of the elbow bending are shown in Figure 5B. When the elbow undergoes flexion from a state of relaxation to an angle of 60°, there is a rapid and significant increase in the relative change in capacitance by up to 250%, which then stabilizes. Conversely, when the elbow is extended, there is a prompt decrease in the relative capacitance change from 250% to 0%. Then volunteer repeats the above steps and the uniform waveforms are obtained. It is indicated that the sensor demonstrates a swift response/recovery time and excellent stability in the presence of external force. Finally, the sensor's sensing performance is further assessed by placing it on the index finger and wrist while examining its response to various bending conditions. The initial position of the finger is set at a flexion angle of 10°, followed by subsequent adjustments to angles of 45° and 90°. It is evident from Figure 5C that the corresponding relative capacitance changes are ~20%, ~45%, and ~70%, respectively. The test results manifest a close correlation between the flexion angle and the proportional alteration in capacitance. Similarly, the capacitance is gradually enhanced through a controlled flexion degree of the wrist, enabling precise recognition of distinct bending movements, as can be witnessed in Figure 5D. Hence, the proposed sensor has broad application prospects in sign language gesture recognition. All of this information can be gathered in order to create a database for sign language, which will greatly facilitate the online teaching of sign language, autonomous learning, and other applications. In conclusion, the proposed sensor exhibits precise responsiveness to various repetitive dynamic flexion and extension motions and show repeatable reactions and relaxation behaviors in each cycle. The flexible pressure sensor holds potential for functioning as a wearable sensor affixed to the skin, enabling the monitoring of human movements.

Applications in vertical mechanical pressure

The pressure sensor also shows superior sensing performance in detecting vertical physical signals. The sensor was firstly mounted on the button of the remote control and constant continuous pressure is applied. The sensor's response to pressure is illustrated in Figure 6A, showing its rapid and stable characteristics. Subsequently, upon force removal, Figure 6B demonstrates a prompt reduction in relative capacitance change. Furthermore, the sensor was attached to phone screen and Figure 6C displays the synchronous and stable capacitance curves as a result of applying three sets of distinct forces repeatedly on the sensor. Due to its excellent mechanical stability and remarkable sensitivity, this technology offers a promising solution for addressing touch screen malfunctions. Finally, the sensor was attached to the sidewall of the paper cup, which was filled with different volumes of water. The relative capacitance change is relatively small when grabbing the paper cup containing a small amount of water, as illustrated in Figure 6D. As the quantity of water increases, relative capacitance change will enlarge significantly. Besides, the relative capacitance alteration remains consistent during two iterations of grasping or releasing the paper cup. It is the special micro-pyramid structure of the pressure sensor that makes it has high sensitivity and good stability. These findings demonstrate that the suggested sensor can alleviate the human condition of tactile sensory disorder and also be applied to robot tactile perception (Chen et al., 2023; Liu et al., 2023; Zhen et al., 2023).

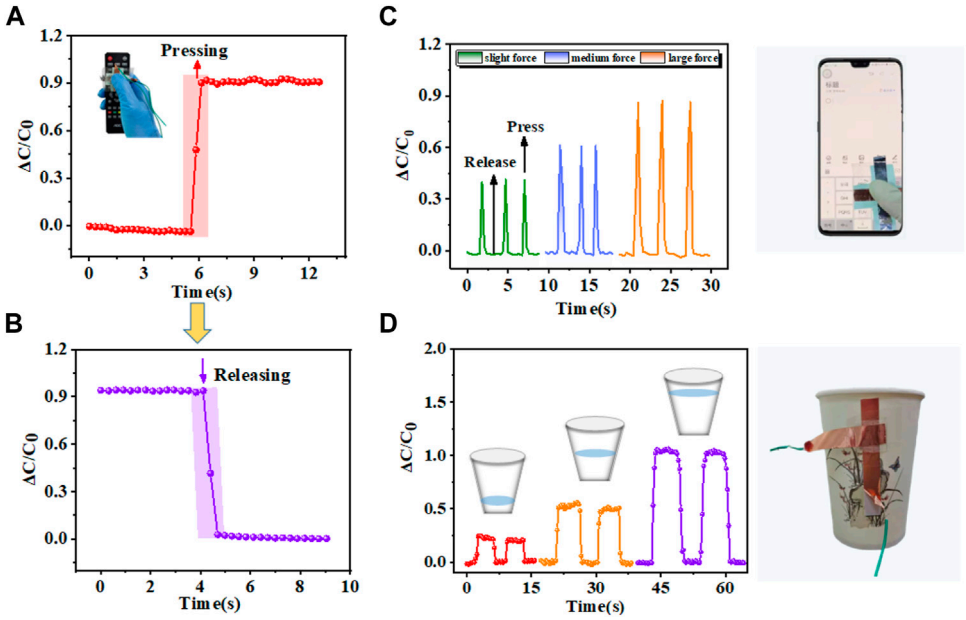

FIGURE 6
Applications in vertical mechanical pressure. **(A)** Capacitance response upon pressing the button on the remote control. **(B)** Capacitance response upon releasing the button on the remote control. **(C)** Variations in relative capacitance of sensor on phone screen pressed with different forces. **(D)** Variations in relative capacitance positioned on the lateral surface of the paper cup while handling paper cups of varying weights.

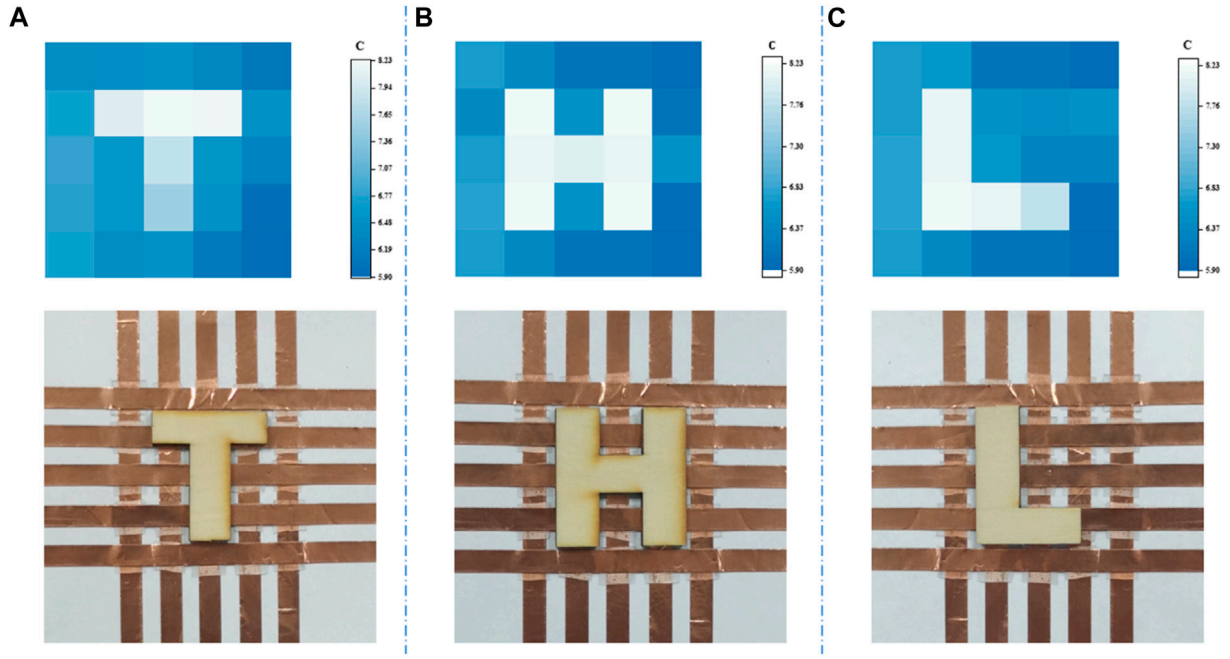

FIGURE 7
Spatial pressure allocation images of the 5 × 5 sensor array when loading wooden planks that are formed like the characters **(A)** "T", **(B)** "H", and **(C)** "L".

Pressure mapping of sensor array

A significant drawback of a solitary pressure sensor is its inherent limitation in furnishing comprehensive data. To enhance the applicability in practical scenarios, a 5 × 5 multipixel of the pressure sensor array was integrated to form a sensor array measuring 5 × 5 cm^2, in which each pressure sensor measures 5 × 5 mm^2. When the sensor array's surface was covered by

wooden boards bearing the shapes of "T", "H", and "L", their spatial distributions of the sensing response are shown in Figure 7. A noticeable contrast can be observed in the sensing response of the area that has been pressed and the one that has not. Meanwhile, the bright spot in the spatial pressure distribution image resembles the shape of a wooden board quite well, offering an efficient alternative in the wearable electronic device and flexible robot.

Conclusion

In brief, an exceptionally sensitive and highly morphology-controllable flexible capacitive pressure sensor based on the hierarchical pyramid microstructure dielectric layer was successfully developed using an efficient strategy for pattern transfer of the silicon template. The hierarchically micro-pyramid structure's distinctive design facilitates outstanding sensing performances through efficient stress concentration. The prepared flexible capacitive pressure sensor exhibits a remarkable sensitivity of 0.77 kPa^{-1} below 1 kPa. It also demonstrates an impressive response time of 55 ms and recovery time of 42 ms, along with a low detection limit of 8 Pa. Furthermore, this sensor showcases exceptional stability and reproducibility with up to 1,000 cycles. According to the findings from both experimental results and FEA simulations, it can be concluded that the sensing performance is significantly influenced by the thickness of the dielectric layer. The fabricated pressure sensor possesses the ability to continuously monitor pulse signals on the wrist and tracking human body movements in real-time. What is even more significant, an advanced 5 × 5 sensor array has been undertaken to demonstrate its capability in discerning different objects' spatial pressure distribution. It is surely believed that the hierarchical pyramid microstructure by the silicon template-assisted manufacturing strategy can spark fresh ideas for advancing flexible pressure sensor technology and will pave the way for various applications including intelligent robotics, biomedical monitoring, smart prosthetics as well as disease prevention and diagnostics.

Data availability statement

The raw data supporting the conclusion of this article will be made available by the authors, without undue reservation.

Author contributions

LL: Data curation, Formal Analysis, Investigation, Methodology, Writing–original draft. TL: Data curation, Formal Analysis, Investigation, Methodology, Writing–original draft. TJ: Data curation, Writing–review and editing. JL: Writing–review and editing, Formal Analysis, Investigation. JZ: Investigation, Writing–review and editing, Data curation. QZ: Investigation, Writing–review and editing. RD: Writing–review and editing, Resources. XL: Writing–review and editing, Methodology. YL: Conceptualization, Funding acquisition, Project administration, Resources, Supervision, Writing–review and editing. ZY: Supervision, Writing–review and editing, Funding acquisition, Project administration, Resources.

Funding

This work was supported in part by the National Natural Science Foundation of China under Grant 61904092, 62301291, and 6211101132, in part by the Youth Innovation Team Project of Shandong Provincial Education Department No. 2022KJ141, in part by the Shandong Provincial Natural Science Foundation of China under Grant ZR2021ME052, and in part by College Students Innovation and Entrepreneurship Training Program under Grant S202011065132.

Conflict of interest

Author XL was employed by Hisense Visual Technology Co., Ltd.

The remaining authors declare that the research was conducted in the absence of any commercial or financial relationships that could be construed as a potential conflict of interest.

Publisher's note

References

Cao, Z., He, K., Xiong, W., Chen, Y., Qiu, X., Yu, D., et al. (2020). Flexible micropillar array for pressure sensing in high density using image sensor. *Adv. Mater. Inter* 7, 1902205. doi:10.1002/admi.201902205

Chen, Y., Chernogor, L. F., Zheng, Y., Jin, Z., Sun, Z., Yao, Z., et al. (2023). Effect of remimazolam *vs.* propofol on hemodynamics during general anesthesia induction in elderly patients: single-center, randomized controlled trial. *IEEE Trans. Circuits Syst. II* 1, 10. doi:10.7555/JBR.37.20230110

Cheng, G., Xu, H., Gao, N., Zhang, M., Gao, H., Sun, B., et al. (2023). Carbon nanotubes field-effect transistor pressure sensor based on three-dimensional conformal force-sensitive gate modulation. *Carbon* 204, 456–464. doi:10.1016/j.carbon.2022.12.090

Ding, X., Zhong, W., Jiang, H., Li, M., Chen, Y., Lu, Y., et al. (2020). Highly accurate wearable piezoresistive sensors without tension disturbance based on weaved conductive yarn. *ACS Appl. Mat. Interfaces* 12, 35638–35646. doi:10.1021/acsami.0c07928

Duan, Y., Wu, J., He, S., Su, B., Li, Z., and Wang, Y. (2022). Bioinspired spinosum capacitive pressure sensor based on CNT/PDMS nanocomposites for broad range and high sensitivity. *Nanomaterials* 12, 3265. doi:10.3390/nano12193265

Fu, D., Wang, R., Wang, Y., Sun, Q., Cheng, C., Guo, X., et al. (2022). An easily processable silver nanowires-dual-cellulose conductive paper for versatile flexible pressure sensors. *Carbohydr. Polym.* 283, 119135. doi:10.1016/j.carbpol.2022.119135

Guo, Q., Qiu, X., and Zhang, X. (2022). Recent advances in electronic skins with multiple-stimuli-responsive and self-healing abilities. *Materials* 15, 1661. doi:10.3390/ma15051661

Han, F., Wang, T., Liu, G., Liu, H., Xie, X., Wei, Z., et al. (2022). Materials with tunable optical properties for wearable epidermal sensing in health monitoring. *Adv. Mater.* 34, 2109055. doi:10.1002/adma.202109055

He, Y., Zhao, L., Zhang, J., Liu, L., Liu, H., and Liu, L. (2020). A breathable, sensitive and wearable piezoresistive sensor based on hierarchical micro-porous PU@CNT films

for long-term health monitoring. *Compos. Sci. Technol.* 200, 108419. doi:10.1016/j.compscitech.2020.108419

Hwang, J., Kim, Y., Yang, H., and Oh, J. H. (2021). Fabrication of hierarchically porous structured PDMS composites and their application as a flexible capacitive pressure sensor. *Compos. Part B Eng.* 211, 108607. doi:10.1016/j.compositesb.2021.108607

Ji, F., Sun, Z., Hang, T., Zheng, J., Li, X., Duan, G., et al. (2022). Flexible piezoresistive pressure sensors based on nanocellulose aerogels for human motion monitoring: a review. *Compos. Commun.* 35, 101351. doi:10.1016/j.coco.2022.101351

Jian, M., Xia, K., Wang, Q., Yin, Z., Wang, H., Wang, C., et al. (2017). Flexible and highly sensitive pressure sensors based on bionic hierarchical structures. *Adv. Funct. Mater.* 27, 1606066. doi:10.1002/adfm.201606066

Jung, Y., Lee, W., Jung, K., Park, B., Park, J., Ko, J., et al. (2020). A highly sensitive and flexible capacitive pressure sensor based on a porous three-dimensional PDMS/microsphere composite. *Polymers* 12, 1412. doi:10.3390/polym12061412

Khoshmanesh, F., Thurgood, P., Pirogova, E., Nahavandi, S., and Baratchi, S. (2021). Wearable sensors: at the frontier of personalised health monitoring, smart prosthetics and assistive technologies. *Biosens. Bioelectron.* 176, 112946. doi:10.1016/j.bios.2020.112946

Kim, H., Kim, G., Kim, T., Lee, S., Kang, D., Hwang, M., et al. (2018). Transparent, flexible, conformal capacitive pressure sensors with nanoparticles. *Small* 14, 1703432. doi:10.1002/smll.201703432

Lee, S., Kim, H., Park, M. J., and Jeon, H. J. (2021). Current advances in wearable devices and their sensors in patients with depression. *Front. Psychiatry* 12, 672347. doi:10.3389/fpsyt.2021.672347

Li, J., Bao, R., Tao, J., Peng, Y., and Pan, C. (2018). Recent progress in flexible pressure sensor arrays: from design to applications. *J. Mat. Chem. C* 6, 11878–11892. doi:10.1039/C8TC02946F

Li, M., Liang, J., Wang, X., and Zhang, M. (2020a). Ultra-sensitive flexible pressure sensor based on microstructured electrode. *Sensors* 20, 371. doi:10.3390/s20020371

Li, W., Jin, X., Zheng, Y., Chang, X., Wang, W., Lin, T., et al. (2020b). A porous and air gap elastomeric dielectric layer for wearable capacitive pressure sensor with high sensitivity and a wide detection range. *J. Mat. Chem. C* 8, 11468–11476. doi:10.1039/D0TC00443J

Lin, J., Zhu, Z., Cheung, C. F., Yan, F., and Li, G. (2020). Digital manufacturing of functional materials for wearable electronics. *J. Mat. Chem. C* 8, 10587–10603. doi:10.1039/D0TC01112F

Liu, L., Chen, H., Sun, H., Jin, Z., Chernogor, L. F., Batrakov, D. O., et al. (2023). A broadband circularly polarized antenna based on transparent conformal metasurface. *Antennas Wirel. Propag. Lett.*, 1–5. doi:10.1109/LAWP.2023.3316427

Liu, S., Yuan, G., Zhang, Y., Xie, L., Shen, Q., Lei, H., et al. (2021). A self-powered gas sensor based on coupling triboelectric screening and impedance matching effects. *Adv. Mater. Technol.* 6, 2100310. doi:10.1002/admt.202100310

Luo, J., Zhang, L., Wu, T., Song, H., and Tang, C. (2021). Flexible piezoelectric pressure sensor with high sensitivity for electronic skin using near-field electrohydrodynamic direct-writing method. *Extreme Mech. Lett.* 48, 101279. doi:10.1016/j.eml.2021.101279

Luo, Y., Shao, J., Chen, S., Chen, X., Tian, H., Li, X., et al. (2019). Flexible capacitive pressure sensor enhanced by tilted micropillar arrays. *ACS Appl. Mat. Interfaces* 11, 17796–17803. doi:10.1021/acsami.9b03718

Lyu, Q., Gong, S., Yin, J., Dyson, J. M., and Cheng, W. (2021). Soft wearable healthcare materials and devices. *Adv. Healthc. Mater.* 10, 2100577. doi:10.1002/adhm.202100577

Niu, H., Gao, S., Yue, W., Li, Y., Zhou, W., and Liu, H. (2020). Highly morphology-controllable and highly sensitive capacitive tactile sensor based on epidermis-dermis-inspired interlocked asymmetric-nanocone arrays for detection of tiny pressure. *Small* 16, 1904774. doi:10.1002/smll.201904774

Qin, R., Hu, M., Li, X., Liang, T., Tan, H., Liu, J., et al. (2021). A new strategy for the fabrication of a flexible and highly sensitive capacitive pressure sensor. *Microsyst. Nanoeng.* 7, 100. doi:10.1038/s41378-021-00327-1

Ren, M., Sun, Z., Zhang, M., Yang, X., Guo, D., Dong, S., et al. (2022). A high-performance wearable pressure sensor based on an MXene/PVP composite nanofiber membrane for health monitoring. *Nanoscale Adv.* 4, 3987–3995. doi:10.1039/D2NA00339B

Rocha, H., Semprimoschnig, C., and Nunes, J. P. (2021). Sensors for process and structural health monitoring of aerospace composites: a review. *Eng. Struct.* 237, 112231. doi:10.1016/j.engstruct.2021.112231

Ruth, S. R. A., Beker, L., Tran, H., Feig, V. R., Matsuhisa, N., and Bao, Z. (2020). Rational design of capacitive pressure sensors based on pyramidal microstructures for specialized monitoring of biosignals. *Adv. Funct. Mater.* 30, 1903100. doi:10.1002/adfm.201903100

Seyedin, S., Uzun, S., Levitt, A., Anasori, B., Dion, G., Gogotsi, Y., et al. (2020). MXene composite and coaxial fibers with high stretchability and conductivity for wearable strain sensing textiles. *Adv. Funct. Mater.* 30, 1910504. doi:10.1002/adfm.201910504

Shi, W., Guo, Y., and Liu, Y. (2020). When flexible organic field-effect transistors meet biomimetics: a prospective view of the internet of things. *Adv. Mater.* 32, 1901493. doi:10.1002/adma.201901493

Su, X., Luo, C., Yan, W., Jiao, J., and Zhong, D. (2021). Microdome-tunable graphene/carbon nanotubes pressure sensors based on polystyrene array for wearable electronics. *Materials* 14, 7385. doi:10.3390/ma14237385

Tang, X., Yang, W., Yin, S., Tai, G., Su, M., Yang, J., et al. (2021). Controllable graphene wrinkle for a high-performance flexible pressure sensor. *ACS Appl. Mat. Interfaces* 13, 20448–20458. doi:10.1021/acsami.0c22784

Tao, K., Chen, Z., Yu, J., Zeng, H., Wu, J., Wu, Z., et al. (2022). Ultra-sensitive, deformable, and transparent triboelectric tactile sensor based on micro-pyramid patterned ionic hydrogel for interactive human–machine interfaces. *Adv. Sci.* 9, 2104168. doi:10.1002/advs.202104168

Tian, L., Zimmerman, B., Akhtar, A., Yu, K. J., Moore, M., Wu, J., et al. (2019). Large-area MRI-compatible epidermal electronic interfaces for prosthetic control and cognitive monitoring. *Nat. Biomed. Eng.* 3, 194–205. doi:10.1038/s41551-019-0347-x

Tian, Q., Yan, W., Li, Y., and Ho, D. (2020). Bean pod-inspired ultrasensitive and self-healing pressure sensor based on laser-induced graphene and polystyrene microsphere sandwiched structure. *ACS Appl. Mat. Interfaces* 12, 9710–9717. doi:10.1021/acsami.9b18873

Wan, Y., Qiu, Z., Hong, Y., Wang, Y., Zhang, J., Liu, Q., et al. (2018). A highly sensitive flexible capacitive tactile sensor with sparse and high-aspect-ratio microstructures. *Adv. Elect. Mater.* 4, 1700586. doi:10.1002/aelm.201700586

Wang, H., Li, Z., Liu, Z., Fu, J., Shan, T., Yang, X., et al. (2022a). Flexible capacitive pressure sensors for wearable electronics. *J. Mat. Chem. C* 10, 1594–1605. doi:10.1039/D1TC05304C

Wang, J., Cui, P., Zhang, J., Ge, Y., Liu, X., Xuan, N., et al. (2021a). A stretchable self-powered triboelectric tactile sensor with EGaIn alloy electrode for ultra-low-pressure detection. *Nano Energy* 89, 106320. doi:10.1016/j.nanoen.2021.106320

Wang, S., Shao, H.-Q., Liu, Y., Tang, C.-Y., Zhao, X., Ke, K., et al. (2021b). Boosting piezoelectric response of PVDF-TrFE via MXene for self-powered linear pressure sensor. *Compos. Sci. Technol.* 202, 108600. doi:10.1016/j.compscitech.2020.108600

Wang, Y., Haick, H., Guo, S., Wang, C., Lee, S., Yokota, T., et al. (2022b). Skin bioelectronics towards long-term, continuous health monitoring. *Chem. Soc. Rev.* 51, 3759–3793. doi:10.1039/D2CS00207H

Wang, Y., Yue, Y., Cheng, F., Cheng, Y., Ge, B., Liu, N., et al. (2022c). $Ti_3C_2T_x$ MXene-based flexible piezoresistive physical sensors. *ACS Nano* 16, 1734–1758. doi:10.1021/acsnano.1c09925

Xiong, Y., Shen, Y., Tian, L., Hu, Y., Zhu, P., Sun, R., et al. (2020). A flexible, ultra-highly sensitive and stable capacitive pressure sensor with convex microarrays for motion and health monitoring. *Nano Energy* 70, 104436. doi:10.1016/j.nanoen.2019.104436

Xu, R., Luo, F., Zhu, Z., Li, M., and Chen, B. (2022). Flexible wide-range triboelectric sensor for physiological signal monitoring and human motion recognition. *ACS Appl. Electron. Mat.* 4, 4051–4060. doi:10.1021/acsaelm.2c00681

Yang, J. C., Kim, J.-O., Oh, J., Kwon, S. Y., Sim, J. Y., Kim, D. W., et al. (2019). Microstructured porous pyramid-based ultrahigh sensitive pressure sensor insensitive to strain and temperature. *ACS Appl. Mat. Interfaces* 11, 19472–19480. doi:10.1021/acsami.9b03261

Yi, Z., Liu, Z., Li, W., Ruan, T., Chen, X., Liu, J., et al. (2022). Piezoelectric dynamics of arterial pulse for wearable continuous blood pressure monitoring. *Adv. Mater.* 34, 2110291. doi:10.1002/adma.202110291

Zeng, X., Wang, Z., Zhang, H., Yang, W., Xiang, L., Zhao, Z., et al. (2019). Tunable, ultrasensitive, and flexible pressure sensors based on wrinkled microstructures for electronic skins. *ACS Appl. Mat. Interfaces* 11, 21218–21226. doi:10.1021/acsami.9b02518

Zhang, Z., Gui, X., Hu, Q., Yang, L., Yang, R., Huang, B., et al. (2021). Highly sensitive capacitive pressure sensor based on a micropyramid array for health and motion monitoring. *Adv. Elect. Mater.* 7, 2100174. doi:10.1002/aelm.202100174

Zhao, X., Hua, Q., Yu, R., Zhang, Y., and Pan, C. (2015). Flexible, stretchable and wearable multifunctional sensor array as artificial electronic skin for static and dynamic strain mapping. *Adv. Elect. Mater.* 1, 1500142. doi:10.1002/aelm.201500142

Zhen, Q., Mao, Z., Cui, J., Guo, M., Chernogor, L. F., Jin, Z., et al. (2023). RCS reduction effect based on transparent and flexible polarization conversion metasurface arrays. *Results Phys.* 52, 106886. doi:10.1016/j.rinp.2023.106886

Zheng, S., Li, W., Ren, Y., Liu, Z., Zou, X., Hu, Y., et al. (2022). Moisture-wicking, breathable, and intrinsically antibacterial electronic skin based on dual-gradient poly(ionic liquid) nanofiber membranes. *Adv. Mater.* 34, 2106570. doi:10.1002/adma.202106570

Zhu, G.-J., Ren, P.-G., Wang, J., Duan, Q., Ren, F., Xia, W.-M., et al. (2020). A highly sensitive and broad-range pressure sensor based on polyurethane mesodome arrays embedded with silver nanowires. *ACS Appl. Mat. Interfaces* 12, 19988–19999. doi:10.1021/acsami.0c03697

Zhu, M., Li, J., Yu, J., Li, Z., and Ding, B. (2022). Superstable and intrinsically self-healing fibrous membrane with bionic confined protective structure for breathable electronic skin. *Angew. Chem. Int. Ed.* 61, e202200226. doi:10.1002/anie.202200226

Zhu, Y., Sun, F., Jia, C., Zhao, T., and Mao, Y. (2021). A stretchable and self-healing hybrid nano-generator for human motion monitoring. *Nanomaterials* 12, 104. doi:10.3390/nano12010104

frontiers | Frontiers in Bioengineering and Biotechnology

TYPE Review
PUBLISHED 28 November 2023
DOI 10.3389/fbioe.2023.1288049

OPEN ACCESS

EDITED BY
Li Wang,
Jiangxi Normal University, China

REVIEWED BY
Chang Won Jeong,
Wonkwang University, Republic of Korea
Yue Cao,
Nanjing University of Posts and Telecommunications, China

*CORRESPONDENCE
Sana Sabahat,
s.sabahat@comsats.edu.pk
Aisha Naeem,
a.naeem@qu.edu.qa

RECEIVED 03 September 2023
ACCEPTED 14 November 2023
PUBLISHED 28 November 2023

CITATION
Shahid A, Nazir F, Khan MJ, Sabahat S and Naeem A (2023), A concise overview of advancements in ultrasensitive biosensor development.
Front. Bioeng. Biotechnol. 11:1288049.
doi: 10.3389/fbioe.2023.1288049

A concise overview of advancements in ultrasensitive biosensor development

Ammara Shahid[1], Fazila Nazir[1], Muhammad Jawad Khan[2], Sana Sabahat[1]* and Aisha Naeem[3]*

[1]Department of Chemistry, COMSATS University Islamabad, Islamabad, Pakistan, [2]Department of Biosciences, COMSATS University Islamabad, Islamabad, Pakistan, [3]QU Health, Qatar University, Doha, Qatar

Electrochemical biosensing has evolved as a diverse and potent method for detecting and analyzing biological entities ranging from tiny molecules to large macromolecules. Electrochemical biosensors are a desirable option in a variety of industries, including healthcare, environmental monitoring, and food safety, due to significant advancements in sensitivity, selectivity, and portability brought about by the integration of electrochemical techniques with nanomaterials, bio-recognition components, and microfluidics. In this review, we discussed the realm of electrochemical sensors, investigating and contrasting the diverse strategies that have been harnessed to push the boundaries of the limit of detection and achieve miniaturization. Furthermore, we assessed distinct electrochemical sensing methods employed in detection such as potentiometers, amperometers, conductometers, colorimeters, transistors, and electrical impedance spectroscopy to gauge their performance in various contexts. This article offers a panoramic view of strategies aimed at augmenting the limit of detection (LOD) of electrochemical sensors. The role of nanomaterials in shaping the capabilities of these sensors is examined in detail, accompanied by insights into the chemical modifications that enhance their functionality. Furthermore, our work not only offers a comprehensive strategic framework but also delineates the advanced methodologies employed in the development of electrochemical biosensors. This equips researchers with the knowledge required to develop more accurate and efficient detection technologies.

KEYWORDS

electrochemical sensor, nanoparticles, miRNA, limit of detection, biosensor

Introduction

Biosensing, or the detection and analysis of biological entities, is important in many domains of science and technology such as medicine, environmental monitoring, and food safety. The capacity to identify and measure biological molecules and organisms precisely and quickly is critical for disease diagnosis, environmental evaluation, and maintaining the safety and quality of food items (Singh et al., 2021). In recent years, electrochemical biosensing has emerged as a powerful tool in this field, offering a number of advantages over conventional detection (Singh et al., 2021). These biosensors convert a target analyte recognition event into an electrical signal using electrochemical principles, allowing for sensitive and targeted detection. To deliver accurate and trustworthy findings, they incorporate transducers, bio-recognition components, and electrochemical processes.

Electrochemical biosensors now offer significantly better sensitivity, selectivity, mobility, and cost-effectiveness owing to advancements in nanotechnology, biochemistry, and microfabrication (Luong et al., 2020).

One of the main benefits of electrochemical biosensors is their ability to do real-time measurements with high sensitivity, specificity, and resolution (Sumitha and Xavier, 2023). Amperometric biosensors, for example, measure the electrical current produced as a result of an analyte's redox interaction with an electrode surface and provide precise and quantitative information about the concentration of the target molecule (Sumitha and Xavier, 2023). Potentiometric biosensors detect the potential difference between two electrodes in a solution, whereas impedance-based biosensors analyze changes in the system's electrical impedance (Banakar et al., 2022). In addition, the incorporation of nanoparticles has significantly improved the performance of electrochemical biosensors. Many nanomaterials such as carbon-based, metallic, quantum dots, and nanowires have special properties such as a larger surface area, higher catalytic activity, and superior electron transfer kinetics that contribute significantly to amplified signals and increased sensor performance (Pérez-Fernández and de la Escosura-Muniz, 2022).

Electrochemical biosensors can be used to detect various biological molecules such as enzymes, antibodies, nucleic acids, aptamers, and molecularly imprinted polymers. An electrode is employed as a solid support for immobilization of these biomolecules depending on the specificity of chemical groups attached to the surface of electrodes which is necessary for the effective detection of the complementary target molecule (Naresh and Lee, 2021). Their coupling with electrochemical transducers facilitates the translation of biological interactions into detectable electrical impulses. Biological interactions can be transformed into measurable electrical impulses by integration with the electrochemical transducers (Lu et al., 2014; Banakar et al., 2022).

Electrochemical biosensors are appropriate for point-of-care testing and field applications because these technologies allow for reduced sample and reagent amounts, shorter analysis times, and increased automation (Goda et al., 2023). Microfluidics and lab-on-a-chip technologies have transformed the area of electrochemical biosensing by enabling sample preparation and analysis to be miniaturized, portable, and integrated. These biosensors have been demonstrated to be crucial in clinical diagnostics and on-the-spot testing for identifying infectious microorganisms, detecting disease biomarkers, and monitoring therapeutic prescription levels (Valera et al., 2023). Environmental monitoring uses electrochemical biosensors to find contaminants, heavy metals, and pathogens in water, soil, and air (He et al., 2023). Despite all these developments, further research is inevitable in miniaturization, the creation of reliable and precise sample preparation procedures, and the incorporation of data processing algorithms (Mehrvar and Abdi, 2004; Kucherenko et al., 2020; Mariani et al., 2022).

In this comprehensive review article, we explored diverse fabrication strategies involving various nanocomposites to provide a deeper insight into the electrochemical detection phenomena of ultrasensitive biosensors. Throughout the review, we meticulously emphasize and draw comparisons among different strategies that were aimed at two key objectives: augmenting the limit of detection (LOD) and advancing the miniaturization process of electrochemical sensors. We shed light on the intricacies of each approach, offering insights into their effectiveness and potential applications. Our focus extends to a detailed examination of the various nanomaterials currently harnessed within electrochemical sensors, where we illuminate their respective merits and demerits. We specifically pinpointed most recently reported the top ten strategies to develop ultrasensitive biosensors. This evaluation is further refined by comparing the performance of distinct sensors or sensing methods including potentiometers, amperometers, conductometers, colorimeters, transistors, and electrical impedance spectroscopy, which are employed for the purpose of detection. The introduction of nanomaterials can improve electrochemical sensors in several aspects, such as sensitivity, selectivity, response times, detection limits, and detection range. Along with working in a variety of electrochemical ways, these sensors are also portable and energy efficient. *In-situ* monitoring is made possible by nanomaterials, which are also used extensively in the environmental and medical monitoring fields. In a nutshell, this article offers a succinct overview of high-performance biosensor development, focusing on nanomaterial utilization, electrochemical sensing, and fabrication strategies.

Diversity of nanomaterials in electrochemical sensors

The utilization of nanomaterials capitalizes on their large surface area-to-volume ratio, providing additional binding sites for bio-recognition and element immobilization, consequently augmenting the potential for target analyte binding, and simultaneously contributing significantly to the miniaturization process. Nanomaterials play a pivotal role in boosting signal transduction and enhancing detection limits, acting as effective amplifiers within the electrochemical sensors (Bezinge et al., 2020). Microscale environment within sensor technology addresses many challenges such as non-uniform pH distribution, electrical distortion, and uneven application of electrical perturbation (Algamili et al., 2021). These problems are managed primarily through the control of spatiotemporal fluctuations and the choice of nanomaterials (Ferrag and Kerman, 2020). Micro/nanopatterning for biosensor design, microfluidic biosensors, and microelectromechanical Systems (MEMs)-based biosensors exemplify microfabricated sensing devices (Algamili et al., 2021).

The development and fabrication of electrochemical sensors largely revolve around incorporating various types of nanoparticles onto electrode surfaces (Figure 1; Table 1). These nanoparticles encompass metallic elements such as gold (Au), silver (Ag), cadmium (Cd), ruthenium (Ru), terbium (Tb), molybdenum (Mo), platinum (Pt), copper (Cu), palladium (Pd), cobalt (Co), indium (In), osmium (Os), and lead (Pb), as well as non-metallic elements like carbon (C), silicon (Si), and phosphorus (P). Additionally, substrates derived from organic sources, such as metal-organic frameworks (MOFs) (Tian et al., 2019; Liu et al., 2022), and polyaniline (PAn) (Fan et al., 2007) have also been employed in research (Figure 1; Table 1). The choice of nanomaterial depends on the specific requirements of the biosensing application. The article explores the integration of various nanomaterials into electrochemical sensors, outlining the

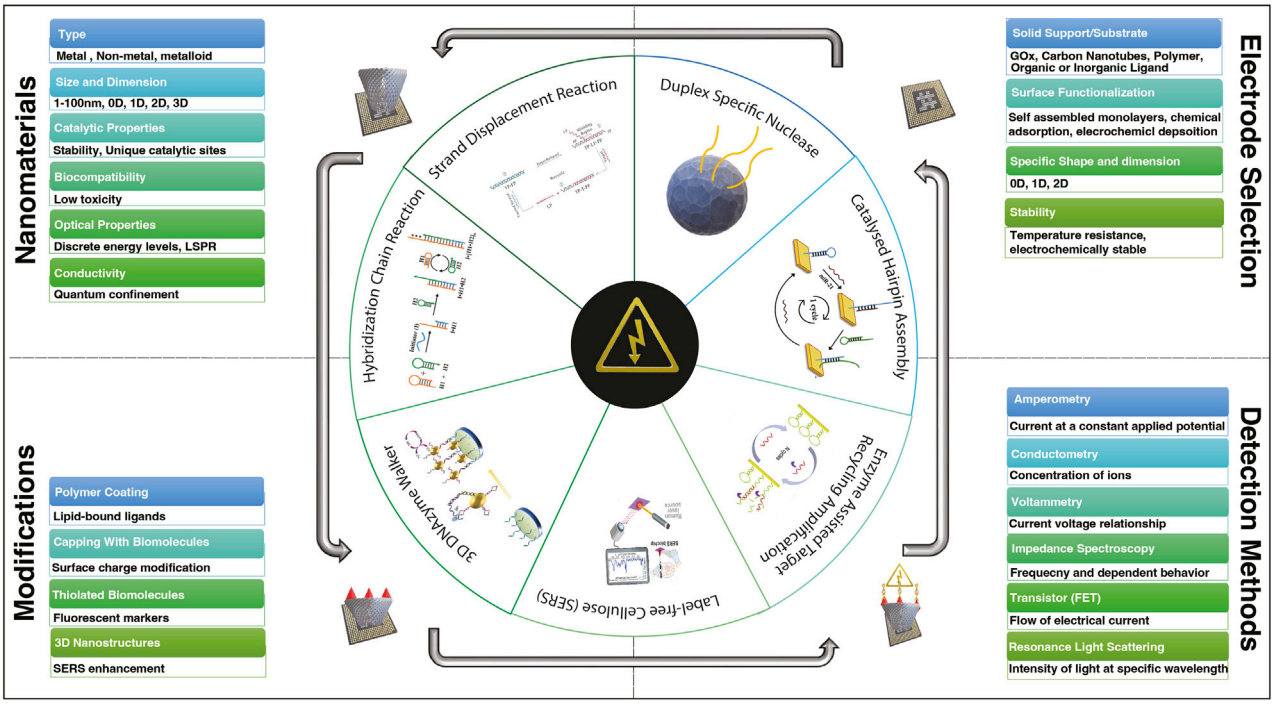

FIGURE 1
Diversity of nanomaterials, electrode selection, ligand variability, and electrochemical sensing techniques in the framework of biosensor development for detecting various miRNAs.

merits and drawbacks associated with their usage in sensor enhancement along with the integral role they play in the miniaturization of biosensors.

Non-metallic and metalloid nanomaterials

With the distinctive properties they possess, carbon-based nanomaterials like carbon nanotubes (CNTs) and graphene have attracted a lot of interest in the field of electrochemical biosensing. CNTs along with graphene can be utilized as transducers or to modify electrodes (Deng et al., 2018). Their combination improves the kinetics of electron transfer and improves the immobilization of bio-recognition components due to their high surface area and good conductivity, which offers a reliable analyte detection platform (Naresh and Lee, 2021). Also, by functionalizing carbon-based nanomaterials with specific groups such as Fe_2O_3, $Mg(OH)_2$, graphene oxides, and polymers for selective binding, improving the sensitivity and selectivity of biosensors significantly (Tran et al., 2013; Chen et al., 2018; Deng et al., 2018; Wang et al., 2021a).

Using an electroactive polymer and interconnected network of CNTs, an—unlabelled and reagent-free sensor design was introduced in 2013 (Table 1) (Liu et al., 2021). The polyfluorene contained in the polymer backbone exhibits high fluorescence quantum yield, photo-stability, as well as non-toxic and easy structural modification, which gives the nanostructured polymer film a highly distinct electroactivity in the cathodic potential domain in a neutral aqueous medium which response strongly to miRNA responses due to higher polymer electroactivity (Liu et al., 2021). Similarly, in research thionin loading capacity was studied on shorter multi-walled carbon nanotubes (S-MWCNTs) and modified multi-walled carbon nanotubes (A-MWCNTs) (Deng et al., 2018). Because of the enormous effective surface area of MWCNTs, quick electron shuttle of MWCNTs, and high-loaded thionin on S-MWCNTs (Huang et al., 2020) developed a uniform, large-area, layered graphene composite of graphene oxide/graphene (GO/G).

Furthermore, a fluorescent-based sensing framework was established using the integration of carbon-based nanomaterials, and the process was initiated through target recycling activated by duplex-specific nuclease (DSN). Because of the weak contact between the short DNA segments and GO, GO induces a high fluorescence emission (Guo et al., 2014). Another study (Chen et al., 2018), introduced a novel sensing substrate involving the assembly of carbon spheres coated with molybdenum disulfide nanosheets (CS-MoS_2 NSs). The combination of CS-MoS_2 into a sensor configuration contributed to a high specific surface area, improved stability, and enhanced dispersibility of the sensor. The researchers focused on a target recycling amplification technique known as Catalytic hairpin assembly (CHA) to deal with the DNA structure transition which hinders the access of quenching probes due to steric hindrance (Jiang et al., 2020; Zhang et al., 2020).

Further advancements are also carried out based on non-metallic nanomaterials have gained popularity due to their low cost, ease of manufacture, biocompatibility, and considerable electrochemical and optical capabilities. Graphene and its derivatives, CNTs, and carbon dots have been explored in the literature for the development of various electrochemical and

TABLE 1 The electrochemical detection methods with their linear range and limit of detection for various miRNAs.

Nanomaterials used	Electro-chemical method	Detection limit (fM)	Linear range (fM)	Target analyte	Reference
Silicon Nanowire	AMP	1	NA	miR-21	Liu et al. (2012)
AuNP	AMP	0.044, 0.0136	NA	RSV DNA, let-7a	Li et al. (2023)
Ruthenium oxide NP-catalyzed polyaniline	AMP	2	NA	Let-7c	Kim and Kang (2023)
AuNP	CV	0.12	$2.5–2.5 \times 10^{7}$	miR-21	Liu et al. (2022)
Pyrrolidinyl peptide nucleic acid/Ag NF- GCE	CV	0.20	NA	miR-21	Ranjan Srivastava et al. (2022)
Cobalt Ferrite Magnetic NP	CV	0.3	$1–2 \times 10^{6}$	miR-21	Wang et al. (2015b)
Platinum@Cerium oxide NS	CV/EIS	1.41	$10–1 \times 10^{6}$	miR-21	Mohammadnejad et al. (2023)
AuNP	DPV	0.12	$10–2 \times 10^{3}$	miR-182	Yoon et al. (2022)
AuNP	DPV	0.058	$1–2 \times 10^{3}$	miR-182	Kim et al. (2018)
Magnetic NP (DNA1/Fe3O4 NPs/Thi and DNA2/Fe3O4 NPs/Fc)	DPV	0.28, 0.36	NA	miR-141, -21	Szunerits et al. (2022)
Catalytic hairpin assembly + B12	DPV	4.5	$10–1 \times 10^{7}$	miR-141	Khazaei et al. (2023)
Catalytic hairpin assembly	DPV	3.608	$10–1 \times 10^{6}$	miR-21	Das et al. (2022)
AuNP@Mxenes	DPV	0.204, 0.138	$0.5–5 \times 10^{7}$	miR-21, -141	Li et al. (2021)
AuNP/polypyrrole-reduced graphene oxide	DPV	1.57	$10–5 \times 10^{6}$	miR-16	Gao et al. (2020)
Iron oxide/Cerium oxide/Au	DPV	0.33	$1–1 \times 10^{6}$	miR-21	Tian et al. (2023)
PdNP	DPV	0.0086	$0.05–1 \times 10^{2}$	miR-21	Tran et al. (2013)
Iron-embedded nitrogen-rich carbon NT	DPV	0.853	$1–1 \times 10^{6}$	miR-486	Bao et al. (2019)
Carbon Spheres-Molybdenum disulphide	DPV	0.016	$0.1–1 \times 10^{5}$	miR-21	Wang et al. (2021b)
T7 exonuclease/Copper NP	DPV	0.045	$1–1 \times 10^{3}$	miR-141	Deng et al. (2018)
AgNPs@N,O-C BLHS	DPV	0.01	NA	ctDNA	Cui et al. (2019)
DNA hairpin probes (cDNA, H1, and H2)	EIS	4.63	$10–5 \times 10^{4}$	miR-21	Chen et al. (2022)
Graphene oxide@AuPd NP	ECL	0.0319	$0.1–1 \times 10^{6}$	miR-141	Safari et al. (2023)
AuPd alloy seeds NP/Graphitic carbon nitride NS	ECL	0.331	$1–1 \times 10^{7}$	miR-141	Naikoo et al. (2021)
Au@luminol NPs	ECL	0.004	$0.01–1 \times 10^{3}$	miR-21	Xu et al. (2020)
SnO2 QDs	ECL	0.002	$0.01–1 \times 10^{5}$	miR-21	Meng et al. (2020)
ABEI@AuPd NPs	ECL	0.0319	$0.1–1 \times 10^{8}$	miR-141	Safari et al. (2023)
Poly (9,9-di-n-octylfluorenyl-2,7-diyl) polymer NPs	ECL	0.017	$0.05–1 \times 10^{5}$	miR-155	Castro et al. (2023)
DPA@Pe MCs	ECL	0.00414	$0.01–1 \times 10^{3}$	miR-21	Kim et al. (2020)
BP-CdTe QDs	ECL	0.029	NA	miR-126	Várallyay et al. (2008)
PtNPs-modified GCE	ECL	0.027	$0.1–1 \times 10^{5}$	HIV DNA	Fan et al. (2007)
Silicon nanowires	FET	1	N/A	Let-7b	Molla and Youk (2023)
Graphene oxide	FL	0.17	1×10^{5}	miR-16,-21;-26a	Lao et al. (2006)
AgNC	FL	0.002	NA	miR-141	Gao and Yu (2007b)
Zirconium porphyrin MOF	FL	0.011	NA	miR-21	Chen et al. (2018)
Methylammonium lead halide QDs	PEC	0.005	$0.01–2 \times 10^{7}$	miR-155	Qin et al. (2023)

(Continued on following page)

TABLE 1 (*Continued*) The electrochemical detection methods with their linear range and limit of detection for various miRNAs.

Nanomaterials used	Electro-chemical method	Detection limit (fM)	Linear range (fM)	Target analyte	Reference
AuNP	SWV	0.03113	0.1–1 × 10^6	miR-182–5p	Tian et al. (2019)
DNA circle capture probe @ tetrahedron DNA nanostructure	SWV	0.0189 0.0396	0.1–1 × 10^7	miR-21,-155	Liu et al. (2018)
Pt@Copper MOFs	SWV	0.1	1–1 × 10^6	miR-21,-141	Wang et al. (2021a)
Iron Oxide@AuNS	SWV	1.5, 1.8	5–2 × 10^6	miR-21,-155	Sabahat et al. (2023)
DNA tetrahedron nanostructures	SWV	0.01217	0.05–1 × 10^4	miR-133a	Munusami et al. (2022)
Copper-based MOF @PtNP	SWV	0.3	0.5–1 × 10^5	miR-155	Walcarius et al. (2013)
AuNPs-P-DM probe	SWV	0.0331	0.1–1 × 10^6	miR-21	Wang et al. (2020b)

Au, gold; NP, nanoparticles; Pd, palladium; NS, nanospheres; NT, nanotubes; DM, DNAzyme; P, protected strand; MOF, metal organic framework; NC, nanoclusters; Ag, silver; QDs, quantum dots; Pt, platinum; SnO_2, tin oxide; GCE, glassy carbon electrode; BP, black phosphorus; DPA, 9,10-diphenylanthracene; Pe, perylene; MCs, microcrystals; ABEI, N-(4-Aminobutyl)-N-(elthylisoluminol); BLHS, broom-like hierarchical nanomaterials; NT, nanotubes; NF, nanoflower; Fc, ferrocene; AMP, amperometry; DPV, differential pulse voltammetry; SWV, square wave voltammetry; CV, cyclic voltammetry; EIS, electrochemical impedance spectroscopy; ECL, electrochemiluminescence; FL, fluorescence; FET, field-effect transistor; PEC, photoelectrochemical.

optical cancer-detecting biosensors (Wang et al., 2021b; Castro et al., 2023; Safari et al., 2023).

Non-metallic nanoparticle-based biosensors are proven to be instrumental in establishing a microscale environment. The endeavor to downsize non-metallic nanoparticle-based biosensors achieved a significant advancement (Sobhanie et al., 2022; Castro et al., 2023; Khazaei et al., 2023). The methodology entailed combining paper-based microfluidics with an electrochemical sensor, resulting in a feasible and efficient framework for creating small, cost-effective analytical devices (Das et al., 2022). Leveraging the unique properties of paper as a substrate, microchannels were formed to facilitate fluid transportation and manipulation within the context of paper-based microfluidics. The combination of these microfluidic capabilities with electrochemical sensing technologies leads to innovative approaches for the development of diminutive, efficient, and disposable sensing devices. These innovations have immense potential to revolutionize the landscape of diagnostic tools, offering an affordable and portable analytical solution across various biosensing applications.

In contrast to metallic sensors, sensors based on non-metallic and metalloid elements exhibit reduced sensitivity, selectivity, and range due to their lower abundance of free electrons essential for detection. Furthermore, their increased vulnerability to environmental oxidation and degradation renders them less robust and enduring than their metallic biosensor counterparts (Kim et al., 2020; Naikoo et al., 2021).

Metal nanoparticles

Metal nanoparticles like gold and silver nanoparticles are the most frequently used in the construction and design of electrochemical biosensors (Ndolomingo et al., 2020). These nanoparticles have special optical, electrical, and catalytic abilities that are used to improve the performance of biosensors (Mehmood et al., 2015; Ndolomingo et al., 2020). Due to their localized surface plasmon resonance (LSPR) properties, they can serve as signal amplifiers (Wang et al., 2015a). The analyte interacts with the bio-recognition component on the nanoparticle surface, changing the LSPR and resulting in detectable signals (Kangkamano et al., 2018). Metal nanoparticles not only function as redox catalysts but also provide increased surface area for immobilizing bio-recognition components, enhancing the sensitivity of biosensors (Gao and Yu, 2007a; Wang et al., 2015a; Hao et al., 2017).

The use of AuNP in conjunction with magnetic microbeads (MMBs) in the fabrication of DNA nanomachines amplified strand displacement reaction (SDR) signal, resulting in increased sensitivity and selectivity in electrochemical miRNA detection. The combination of AuNP-SA MMBs with 3D DNA nanomachines (DNM) utilizing a toehold-mediated SDR (TSDR) maintained a stable signal for AuNP-streptavidin MMBs, thus mitigating the influence of environmental factors (Lu et al., 2020). In contrast, a similar approach was used by replacing streptavidin with Fe_2O_3 (Gao et al., 2022), resulting in significantly improved detection sensitivity by using electrochemical detection as compared to the conventional method such as northern blotting (Várallyay et al., 2008) and reverse-transcription polymerase chain reaction (Lao et al., 2006). In another approach, 3D DNAzyme walker and the gold nanoparticles/graphene aerogels carbon fiber paper-based (AuNPs/GAs/CFP) combined with streptavidin-modified magnetic beads (MBs) were used to detect miR-155 (Zhao et al., 2023).

The field of biosensor miniaturization with metallic nanoparticles has witnessed several intriguing advancements. For early diagnosis of SAH-induced cerebral vasospasm and hydrocephalus, a team of researchers designed a label-free cellulose (SERS) biosensor chip with pH-functionalized, AuNP-enhanced LSPR effects (Kim et al., 2018; Ranjan Srivastava et al., 2022; Chandra et al., 2023; Ray et al., 2023). The label free cellulose SERS biosensor chip was integrated by transferring positively charged AuNPs onto a negatively charged cellulose substrate via a synthesis procedure. The zeta potential, nanostructural characteristics, nanocrystallinity, and computational calculation-based electric field distributions of cellulose-derived AuNPs were optimized and characterized to maximize LSPR phenomena. The miniaturization process facilitated high resolution, high sensitivity, and multiplexing of bioanalytics characterized to maximize the detection (Kim et al., 2018; Yoon et al., 2022). Another study (Ulucan-Karnak et al., 2023), designed a sensor based on metal-

oxide nanomaterials (MONs) which played a substantial role in the development of flexible/wearable sensors due to their tunable band gap, low-cost, wide specific area, ease of fabrication, and multiplexing properties.

While metallic nanoparticles possess numerous adjustable characteristics, their potential cytotoxicity to living tissues and cells poses limitations on their biosensor applications. Drastic variations in pH or temperature can render metallic nanoparticles unstable, compromising sensitivity and selectivity and potentially leading to false positive or negative results. Maintaining consistent production of metallic nanoparticles is challenging, leading to performance discrepancies among biosensors. Furthermore, metallic biosensors exhibit a narrower detection range in comparison to optical biosensors (Cho et al., 2020; Naresh and Lee, 2021).

Nanowires and quantum dots

Nanowires (NW), quantum dots (QDs), metal nanoparticles, and carbon-based nanomaterials all have special features that may be customized to certain biosensing uses. Given their distinctive optical and electrical properties, NW and QDs are appealing materials for electrochemical biosensors (Ozkan-Ariksoysal and Uslu, 2021) (Table 1). QDs are semiconductor nanocrystals with remarkable detection-grade photoluminescence signals and size-dependent fluorescence characteristics. They are functionalized with bio-recognition elements and can be utilized as labels for target analyte detection to enable multiplexed analysis (Algar et al., 2010; Yuan et al., 2017). They facilitate improvements in healthcare, environmental monitoring, and other sectors by improving the performance of electrochemical biosensors.

The uses and advantages of QDs in electrochemical sensing have been extensively documented recently (He et al., 2023; Pourmadadi et al., 2023). The incorporation of CH3NH3PbI3 QDs was documented to lead to a notable improvement in the sensitivity and light-absorption capabilities of ZnO-NSs (Pang et al., 2016). These CH3NH3PbI3 QDs, characterized by their optimal band gap energy and efficient sunlight absorption, offer a novel approach for enhancing the sensitivity of ZnO-NSs and have been seamlessly integrated into a photoelectrochemical (PEC) aptasensor for miRNA detection (Pang et al., 2016). However, the utilization of QDs comes with some drawbacks as well, particularly their toxicity. Future research is warranted toward employing less toxic QDs, such as graphene-based QDs with unique optical properties, which hold promise for diverse applications including bioimaging and biosensing (Mohamed et al., 2021).

Nanowires, on the other hand, have a high aspect ratio that enables direct electron transmission from the analyte to the electrode surface (Zhou et al., 2023). Their one-dimensional structure makes it easier to immobilize bio-recognition components and increases the efficiency of charge transfer, increasing the sensitivity of the biosensors (Gao et al., 2013). A study (He et al., 2017) explored the potential of silicon nanowire (SiNW) biosensors which are a promising tool for miRNA detection due to their rapid reaction times and heightened sensitivity. They present a well-established method involving poly-silicon nanowire biosensors for detecting miRNA (let-7b), achieving LOD of 1 fM (femtomolar) (He et al., 2017) (Table 1). In another study, PAn-modified SiNW was used to detect miRNAs by means of a nano-gapped microelectrode-based biosensor. The conductivity of the deposited PAn NW is directly proportional to the amount of hybridized miRNA. Under optimal conditions, this approach enables good detection of target miRNA with a LOD of 5.0 fM (Fan et al., 2007). Recent developments have been made on NW sensors by incorporating several nanoparticles with specific binding ability (Tran et al., 2023; Zhou et al., 2023).

Although these investigations yield remarkable detection limits, showcasing the potential of QDs and NW-based sensors, there remains a significant need for further investigation to tackle their constraints. These limitations encompass potential toxicity concerns and challenges associated with precise control over size, shape, and composition during the synthesis process (Zhou et al., 2023).

Strategies for enhancing LOD of electrochemical sensors

The ongoing progress in ultrasensitive biosensor development encompasses a wide array of approaches, introducing innovative techniques like DNA, tetrahedron, DNA walkers, ratiometric electrochemiluminescence (ECL) methods, and the integration of various nanoparticles and their modifications. With advancements in sensitivity and specificity in recent years, the boundaries of biosensing capabilities have been pushed by making it possible to detect biomolecules at extremely low concentrations with unprecedented precision. In this article, we have curated a selection of research findings that have demonstrated a linear range spanning from 0.01 to 1×10^8 fM, accompanied by corresponding LOD ranging from 0.002 to 5 fM (Table 1). Additionally, we have specifically highlighted recent attempts aimed at developing ultrasensitive biosensors, achieving LOD below 0.009 fM (Figure 2).

Notable advancements include the work of Yang et al. (2021a), who introduced a groundbreaking ultrasensitive biosensor based on Ag NPs/SnO_2 QDs/MnO_2 nanoflowers (NFs). Their innovation involved integrating three co-reaction accelerators to expedite charge transfer, ultimately revealing catalytic active sites. The resultant "on-off-super on" ECL biosensor was coupled with a 3D DNA walker, enabling the remarkably sensitive detection of miR-21 (0.002 fM) (Yang et al., 2021a) (Figure 2D). Another groundbreaking approach was proposed by Wang et al. (2020a) involving the creation of a tripedal DNA walker through DNA self-assembly. This walker, which employed a catalytic hairpin assembly (CHA) method, moved along a track strand-functionalized electrode and facilitated ultrasensitive ECL biosensing of miRNA (Wang et al., 2020a). The DNA walker's unique design demonstrated high efficiency in driving the detection process (Figure 2G).

Liao et al. (2020) introduced an ingenious approach utilizing 9,10-diphenyl anthracene doped perylene microcrystals (DPA@Pe MCs) to mitigate aggregation-caused quenching (ACQ). This method harnessed spatial configuration alterations to enhance ECL response, resulting in an effective avoidance of ACQ-induced limitations (Liao et al., 2020) (Figure 2J). Qin et al. (2023) engineered an enzyme-free electrochemical sensor employing Ag@

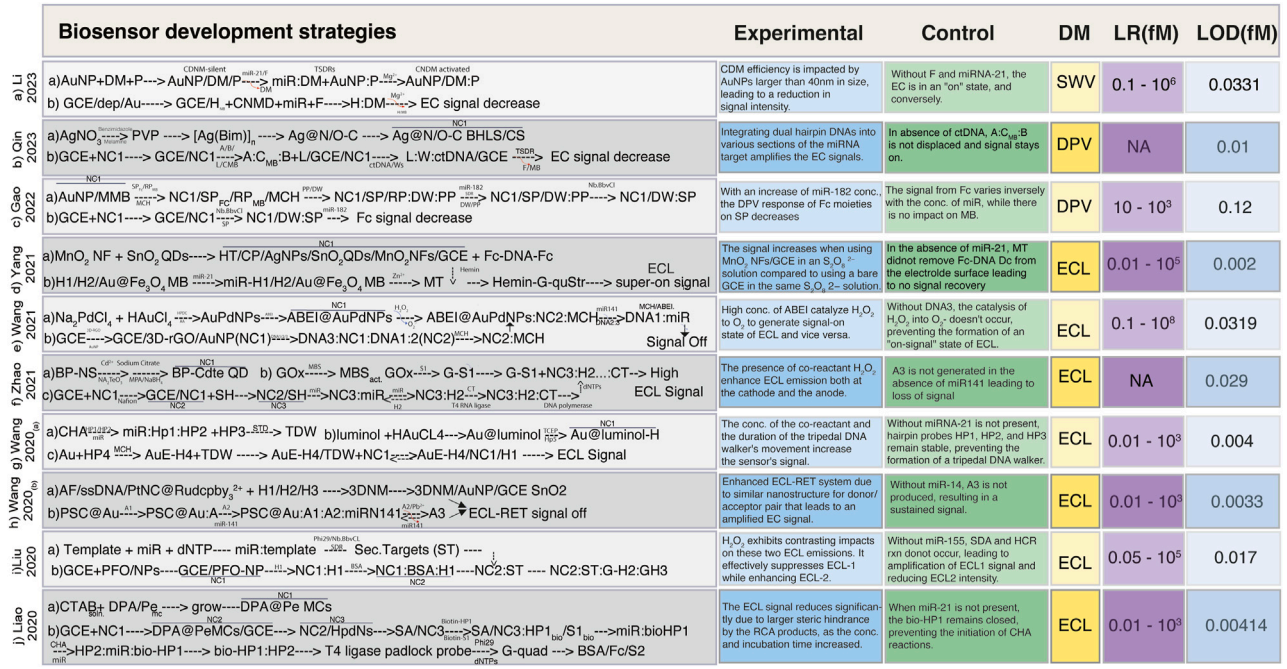

FIGURE 2
Simplified schemes of the fabrication of ultrasensitive biosensors. **(A)** Schematic illustration of the preparation of the CDNM via target-triggered TSDRs and the walking process of the CDNM in the presence of target miRNA (Li et al., 2023). **(B)** Schematic of Ag@N,O-C BLHS synthesis, and electrochemical sensing mechanism for ctDNA detection sensitized with Ag@N, O-C BLHS driven by DNA walker (Qin et al., 2023). **(C)** Construction of a ratiometric electrochemical sensor based on the 3D-DNA nanomachine with multiple hybridization and cleavage cycles for miRNA detection (Gao et al., 2022). **(D)** Fabrication scheme for the Ag NPs/SnO2 QDs/MnO2 NFs based-ECL biosensor for miR-21 detection (Yang et al., 2021a). **(E)** Creation of ABEI@AuPd NPs sensor with DNA nanomachines walking freely on ECL electrodes for the detection of miR-141 (Wang et al., 2021a). **(F)** BP-CdTe QDs biosensor construction and GOx conjugation to S1 for miR-126 detection (Zhao et al., 2021). **(G)** Schematic based on the CHA-tripedal DNA walker strategy along with the walking process of the tripedal DNA walker on the electrode of ECL for the detection of miRNA-21 (Wang et al., 2020a). **(H)** AF-PtNPs@Ru (dcbpy)$^{2/3+}$ assembly with 3D DNM using target recycling amplification technology and the multiple ECL-RET biosensor for the detection of miR-141 (Wang et al., 2020b). **(I)** Schematic illustration of the preparation of ST, its assembly steps, and signal conversion mechanism of the ratiometric biosensor for detecting miR-155 (Liu et al., 2021). **(J)** DPA@Pe biosensor fabrication strategy based on affinity switch using CHA and RCA amplification strategy for miR-21 detection (Liao et al., 2020). *Abbreviations*: AA, ascorbic acid; A_1 and A_2, helper SSDNA; A_3, secondary target DNA; ABEI, N-(4-Aminobutyl)-N-(elthylisoluminol); (A:C-MB:B), three stranded substrate complex; AF, Alexa fluor; $[Ag(Bin)]_n$, silver based benzimidazole polymer; AuNP, gold nanoparticles; bioHP1, biotinylated hairpin probe 1; bioHP2, biotinylated hairpin probe 2; BP, black phosphorus; BSA/Fc/S2, bovine serum albumin labeled with ferrocene and DNA strand S2; CDNM, controlled 3D DNA nanomachine; CHA, Catalytic hairpin assembly; CP, capture probe; CS, chitosan; CTAB, hexyltrimethyl ammonium bromide; CtDNA, circulating tumor DNA; CTQDs, CdTe quantum dots; dep/Au, electrodeposited with gold particles; 3DNM, 3D DNA nanomachine; DM, DNAzyme; dNTPs, deoxyribose nucleotide triphosphate; DPA, 9,10-diphenylanthracene; DPV, differential pulse voltammetry; 3D-rGO, three dimensional reduced graphene oxide; DW, DNA walker; ECL, electrochemiluminescence; Fc, Ferrocene; (Fc-DNA-Fc), double labeled ferrocene quencher probes; F, fuel; GCE, glassy carbon electrode; GH2, graphene oxide with hairpin 2; GH3, graphene oxide with hairpin 3; G-quad, G-quadruplex structure; H, hairpin chain; Hemin-G-quStr, Hemin/G-quadruplex structures; HDPC, chlorohexadecyl pyridine; HPdNs, hollow palladium nanospheres; HT, hexanethiol; LR, linear range; MBS, maleimidobenzoic acid N-hydroxy-succinimide ester; MCs, microcrystals; MCH, modified carbon hairpin chain; miR, microRNA; Mg^{+2}, magnesium ion cofactor; MMB, magnetic micro beads; MT, mimic targets; NC1, Nanocomposite 1; NC2, Nanocomposite 2; NC3, nanocomposite3; NFs, nanoflowers; NPs. Nanoparticles; NS, nanosheet; P, protected strand; Pe, perylene; PFO, poly (9,9-di-n-octylflurenyl-2,7-diyl); Phi29, DNA polymerase; PP, protect probe; PSC, polystyrene microspheres; PtNCs, polyethyleneamine platinum nanoclusters; PVP, polyvinyl pyrrolidone; QDS, quantum dots; RP, reference probe; Ru (dcbpy)$^{2/3+}$, tris (4, 4′-dicarboxyylic acid - 2,2′-bipyridyl) ruthenium II; S1, single strand; SA, streptavidin; SH, thiol modified hairpin; SP, signal probe; ss DNA, single strand DNA; ST, selected target; SWV, square wave voltammetry.

N,O-C hierarchical nanomaterials and an entropy-driven DNA walker. This construct enhanced active sites for DNA walking substrates, facilitating electron transmission, and enabling the ultrasensitive quantification of PIK3CA E545K ctDNA (Qin et al., 2023) (Figure 2B). Gao et al. (2022) designed an electrochemical sensor by merging 3D DNA NM with a TSDR, exhibiting robustness against environmental fluctuations leveraging their properties for sensitive miR-182 detection (Gao et al., 2022) (Figure 2C). In another approach (Zhu et al., 2019), DNA tetrahedron nanostructure was used based on dual amplified ratiometric biosensor with hybridization chain reaction (HCR) for the ultrasensitive detection of microRNA-133a (Zhu et al., 2019).

Liu et al. (2021) devised an innovative method involving the opposing effects of H_2O_2 on two distinct ECL emissions. This potential-regulated ECL ratiometric method leveraged glucose oxidase (GOx) in conjunction with HCR and strand displacement amplification (SDA) for ultrasensitive miR-155 detection (Liu et al., 2021) (Figure 2I). Zhao et al. (2021) innovatively employed black phosphorus (BP) NSs to modulate the emission of quantum CdTe QDs, leading to simultaneous cathodic and anodic ECL signals. Their approach, utilizing BP-CdTe QDs, H_2O_2 and tripropylamine as the cathodic and anodic co-reactants, respectively enabled an ultrasensitive miR-126 detection (Zhao et al., 2021) (Figure 2F). Wang et al. (2021a) developed ABEI@AuPd NPs loaded with

ABEI and synthesized 3D-rGO@Au NPs to establish strong electron transmission channels. This setup significantly amplified the ECL signal, allowing the detection of miR-141 at a low concentration of 0.0319 fM (Wang et al., 2021a) (Figure 2E). Another investigation (Wang et al., 2020b) demonstrated that the integration of 3D DNM with PtNCs@Ru (dcbpy)$^{2/3+}$ improved the efficiency and sensitivity of the ECL biosensor (Figure 2H). This enhancement can be attributed to the presence of multiple energy donor/acceptor pairs, the utilization of Pb^{+2} dependent DNAzyme-assisted target recycling amplification technology, and the incorporation of multiple ECL resonance energy transfer (RET) mechanisms. These features collectively resulted in a more efficient electron-transfer process, reduced energy loss, and ultimately, heightened RET efficiency (Wang et al., 2020b; Tian et al., 2023) (Figure 2H).

Li et al. (2023) explored the effect of core diameter and DNAzyme cantilever length on 3D DNA nanomachine (CDNM) efficiency. By optimizing these parameters, they enhanced the walking rate and activity space of the CDNM, leading to the ultrasensitive detection of miR-21 at 0.0331 fM compared to traditional DNMs (Figure 2A). Another study (Liu et al., 2012) reported an exceptional sensitivity of 0.002 fM by integration of target-assisted isothermal exponential amplification, combined with the utilization of fluorescent DNA-scaffolded AgNCs. The successful implementation of this method was exemplified by its application in detecting miRNA within real samples that include human pancreatic cancer (AsPc-1), prostate carcinoma (22Rv1), hepatocellular carcinoma (BEL-7404), cervical cancer cell lines (HeLa), and breast cancer (MDA-MB231) cell line for early diagnosis, thereby showcasing its feasibility, simplicity, and cost-effectiveness. By achieving such remarkable sensitivity levels, this method opened up new avenues for the quantitative, accurate, and reliable assessment of miRNA expression. Recent research (Molla and Youk, 2023) employed the use of carbon-based nanomaterials for the detection of both small molecules and biomolecules (Table 1). The authors compared the performance of different analytes by increasing sensitivity or selectivity via modifications to the electrode and catalytic system. Using different electrodes, sensing applications for CdS (cadmium sulfide) are addressed and categorized depending on their composition. For electroanalytic applications, many electrochemical techniques have been taken into consideration, including electrochemical impedance spectroscopy (EIS), cyclic voltammetry (CV), differential pulse voltammetry (DPV), and ECL.

In other attempts to enhance the performance of biosensors for miRNA detection, two distinct research teams achieved an astonishing level of sensitivity, successfully detecting miRNA at concentrations lower than 0.009 fM (Pang et al., 2016; Zhang et al., 2019a). Both studies adopted distinct strategies, underscoring the diversity in their approaches to reach the exceptional LOD (Pang et al., 2016; Zhang et al., 2019a). Pang et al. (2016) developed an electrochemical sensor by employing a PEC aptasensor configuration. The approach hinged on the utilization of ZnO-NSs combined with $CH_3NH_3PbI_3$ QDs. The establishment of a heterojunction between $CH_3NH_3PbI_3$ QDs and ZnO-NSs facilitated a notable increase in the PEC signal. This aptasensor architecture facilitated the precise and accurate identification of miR-155 at a level of 0.005 fM (Pang et al., 2016). While Zhang and co-researchers (Zhang et al., 2019b) introduced an ultrasensitive, label-free electrochemical biosensor leveraging palladium nanoparticles (PdNPs) alongside rolling circle amplification (RCA). The biosensor was constructed by affixing electrode-immobilized dual-functionalized hairpin probes, which successfully detected miRNA at a detection threshold of 0.0086 fM. This newly developed biosensor also showcased remarkable selectivity, repeatability, and stability (Zhang et al., 2019b). The hairpin probe sensors hold tremendous potential for advancing the realm of ultralow-level miRNA diagnostics, boasting extraordinary levels of selectivity, repeatability, and stability (Meng et al., 2020).

Comparatively, Xu et al. (2020) reported the construction of a biosensor that relied on a novel DNA circular capture probe equipped with multiple target recognition domains achieving an LOD of <0.05 fM. They employed a mimetic proximity ligation assay which facilitated the capture of beacons labeled with ferrocene (Fc)-A1 and methylene blue (MB)-A2 to detect miRNAs (Xu et al., 2020). By comparing this approach with the conventional strategies of electrochemical biosensing using label-free (Cui et al., 2019) or label-based configurations with different electrochemical techniques such as amperometry, DPV, SWV, EIS, and potentiometry, they not only increased the reaction concentration but also avoided interference from capture probes (Munusami et al., 2022).

In another unique approach, Lu et al. (2020) developed an electrochemical sensor by combining 3D DNM with a TSDR. The signal of Fc-labeled dsDNA was reversely proportional to target miR-182 while the signal of AuNP-SA MMBs remained stable. The method offered a strong ability to eliminate interference from environmental changes, thus the enlarged AuNP-SA MMB depicted a detection limit of 0.058 fM (Lu et al., 2020). In contrast, when a similar approach was used by replacing SA with Fe_2O_3 the LOD decreased to 0.12 fM (Gao et al., 2022) (Figure 2C). Therefore, this significant advancement resulted in greatly improved detection sensitivity by declining hindrance from intricate biosystems (Lao et al., 2006; Várallyay et al., 2008).

Reported enhancements to sensor performance have been achieved through modifications involving various ligands, encompassing thionine (Deng et al., 2018), Pd (Gao and Yu, 2007b; Wang et al., 2021a), SA (Hao et al., 2017), silver sulfide (Ag_2S) (Miao et al., 2016), iron oxides (Fe_2O_3/Fe_3O_4) (Yu et al., 2017; Zhou et al., 2017), cerium oxide (CeO2) (Deng et al., 2018; Liu et al., 2018; Chen et al., 2022), titanium dioxide (TiO2), GO (Erdem et al., 2017; Bao et al., 2019), MOFs (Liang et al., 2019; Sun et al., 2020), PAn (Peng et al., 2010; Wang et al., 2015b) and MXenes (Mohammadniaei et al., 2020). The enhancement of both LOD and miniaturization can be amplified by synergistically amalgamating diverse nanoparticle compositions and modification strategies that encompass ligands. The employment of appropriate ligands not only underscores the adaptability of nanoparticles in sensor design but also showcases the potential for attaining elevated sensor performance across a multitude of applications (Szunerits et al., 2022).

Electrochemical sensing methods

Electrochemical techniques have garnered significant attention in the field of biosensing due to their numerous advantages including high sensitivity, cost-effectiveness, rapid analysis, low

detection limits, user-friendly operation, and portability. Figure 1 illustrates a range of widely employed electrochemical sensing methods in biosensors. This comprehensive suite of electrochemical techniques empowers biosensing with a diverse array of tools to cater to various analytical requirements. It's important to highlight that the wide range of LOD values seen in the studies listed in Table 1 underscores the critical role of careful selection of sensing methods and nanocomposites, as both can significantly impact the final sensor performance.

Voltammetry stands out as one of the most frequently employed detection methods, driven by its fundamental exploration of redox reactions, electron transfer at electrode surfaces, reaction kinetics, and reaction mechanisms. Diverse subtypes of voltammetry, including CV, DPV, and square wave voltammetry (SWV), offer distinct approaches to analysis. CV involves a potential variation over a constant time, while DPV employs potential pulses at specific time intervals (Elgrishi et al., 2018; Sabahat et al., 2023). Table 1 shows a range of detection limits associated with voltammetry sensing techniques, spanning from 67 to 0.0089 fM. The diversity in detection limits underscores the significance of considering the compatibility of techniques with the choice of nanomaterial and fabrication strategy.

Noteworthy achievements in detection sensitivity have been reported by Zhang et al. (2019b) and Xu et al. (2020) (Zhang et al., 2019b) who utilized DPV in conjunction with metallic nanoparticle-based biosensors. In a different study, Kangkamano et al. (2018) demonstrated miRNA-based biosensors employing CV and EIS, utilizing a modified electrode incorporating pyrrolidinyl peptide nucleic acid (acpcPNA), polypyrrole (PPy), and silver nanofoam (AgNF). The fabrication of AgNF was characterized through EIS while CV measured the resulting current (Kangkamano et al., 2018). This electrode modification aimed to heighten sensitivity and selectivity for the mRNA probe, achieving increased surface area and safeguarding against unwanted materials. CV, beyond its sensing applications, serves to characterize electrochemical processes transpiring on electrode surfaces. Notably, this electrochemical approach achieved an ultrasensitive biosensor with LOD of 0.20 fM (Kangkamano et al., 2018).

Within the realm of biosensing, PEC has captured the attention of researchers due to its unique capabilities. PEC sensing involves exciting photoactive material using light to generate charge species, such as electrons and holes. The transfer of these charge carriers plays a pivotal role in redox reactions and charge recombination dynamics. The photoactive material not only offers active sites to enhance reaction kinetics but also minimizes charge recombination events (Gao et al., 2020). Zhou et al. (2023), utilizing a Cu_2O(PTB7-Th/PDA+) designed a PEC biosensor for miRNA detection. In this setup, (Poly ([2,6′-4,8-di (5-ethylhexylthienyl)benzo [1,2- b; 3,3- b] dithiophene] {3-fluoro-2 [(2-ethylhexyl)carbonyl]thieno [3,4-b] thiophenediyl}) (PTB7-Th) boosts Cu_2O signals, facilitating charge separation in the bulk material, while *N*,*N*-bis(2-(trimethyl ammonium iodide)propylene)perylene-3,4,9,10 tetra -carboxydiimide (PDA^+) acts as a mediator for charge transfer. To amplify signals, a 3D DNA walker connected to a dumbbell HCR was employed. The photoanode electrode, when exposed to light, exhibited substantially increased peak current compared to the pristine material, attributable to enhanced electron and hole movement and separation (Zhou et al., 2023). Another research group (Cui et al., 2023) employed a similar PEC sensing method for methylated RNA protein detection, utilizing a molybdenum diselenide/bismuth oxide ($MoSe_2$/BiO) heterojunction as the photocathode. This heterojunction was synthesized via an *in-situ* method to augment $MoSe_2$ activity. Signal amplification was achieved using poly aspartic acid-loaded alkaline phosphatase, resulting in an improved LOD (Cui et al., 2023). In a different study by Liu et al. (2020), a TI_3C_2/CdS nanocomposite was deposited on a Fluorine-doped Tin Oxide (FTO electrode), with chitosan as a binder for miRNA. Signal enhancement for PEC detection was accomplished using TMPyP, acting as an amplification agent, thereby enhancing sensitivity (Liu et al., 2020). These innovative approaches in PEC biosensing showcase the potential for highly sensitive and selective detection through synergistic interactions between photoactive materials, charge transfer mediators, and signal amplification strategies.

The electrochemical impedance spectroscopy (EIS) serves as a widely utilized technique for investigating the rate of electron transfer and diffusion in electrochemical reactions (Table 1). Through impedance analysis, the interaction between the electrode and the surface can be effectively probed by modulating the current (Walcarius et al., 2013; Naresh and Lee, 2021). A recent advancement involves an electrochemical biosensor employing reduced graphene oxide (RGO) and AuNPs to detect miR-128, showcasing sensitivity with a LOD of 0.08761 fM and 0.00956 fM using label-free and labeling approaches, respectively (Mohammadnejad et al., 2023). Kim and Kang (2023) developed an electrochemical biosensor using a graphitic nano-onion/molybdenum disulfide (MoS_2) NSs composite for the detection of human papillomavirus (HPV)-16 and HPV-18 which will help in early diagnosis of cervical cancer (Kim and Kang, 2023). The acyl bonds on the surfaces of functionalized nano-onions and the amine groups on functionalized MoS_2-NSs were chemically combined to create the electrode surface for testing DNA chemisorption, inducing an alteration in the electrochemical signal. When used as a sensing technique, this novel biosensor achieves LOD of 0.00696 fM using DPV and produces a current signal along with background noise. EIS, on the other hand, helps assess the developed electrode (Kim and Kang, 2023). These developments underscore the vital role of EIS in refining biosensing capabilities, allowing for sensitive and specific detection with diverse applications, from AuNP-based sensors to targeted DNA-triggered diagnostic tools.

A field-effect transistor (FET) is a specific type of transistor that harnesses electric fields to facilitate the conduction of electrons between its three essential electrodes: the source, drain, and gate electrode. Its functionality pivots around the control of material conductivity, achieved by manipulating the electric field of the gate electrode relative to the other electrodes. Depending on the semiconductor's dopant and structure, the potential applied to the gate electrode can lead to either electron absorption or elimination within the channel (Grieshaber et al., 2008; Thriveni and Ghosh, 2022). Consequently, this process enables the adjustment of the depletion region, thereby shaping and reshaping the channels. This orchestration governs the conductance between the source and drain electrodes. This FET framework proves apt for amplifying weak signals and accommodating high impedance in biosensors (Grieshaber et al., 2008).

By substituting the gate electrode with a bio-sensitive surface in contact with a supporting solution, the FET can seamlessly

transform into a biosensor. This configuration enables the FET biosensor to detect subtle changes caused by interactions between the bio-sensitive surface and target analytes, allowing for sensitive and selective measurements (Wang et al., 2020a; Liu et al., 2020). Li et al. (2021) research focused on a FET built on a foundation of CNTs, aimed at detecting exosomal miRNA associated with breast cancer. This biosensor is composed of CNTs functioning as a floating gate, a thin yttrium oxide (Y_2O_3) layer acting as an insulator, and AuNPs serving as linkers for probe capture. The detection of the target probe is accomplished by monitoring changes in current, resulting in heightened sensitivity and an impressively low LOD (0.00087 fM) (Li et al., 2021).

ECL stands as a chemiluminescent process, distinguished by the emergence of a luminophore at the surface of an electrode through the application of an electric voltage. This electrical manipulation triggers the transfer of high-energy electrons, ultimately generating an excited state that gives rise to luminescent signals. In ECL systems, nanomaterials act as catalysts to amplify the activation of molecules. This catalytic activity leads to the formation of oxidizing and reducing agents, which subsequently engage with the luminophores, culminating in the creation of electronically excited molecules. Co-catalysts plays an important role in this process and profoundly influence the activation of molecules and the resulting ECL phenomena (Jiao et al., 2023). Wang et al. (2021a) developed an innovative biosensor using DNA walkers and AuPd nanomaterials to achieve highly sensitive (low 0.0319 fM) detection of miR-141, employing the ECL technique. The design of the biosensor employs graphene as a conducting layer, while the inclusion of AuPd nanoparticles serves as an accelerator, enhancing the ECL signals.

As shown in Table 1, an array of studies has used amperometry as their preferred detection method for a variety of miRNAs. The exceptional sensitivity of this technique is based on the precise measurement of current during the electroactive material's redox reaction. As seen in the study by Cai et al. (2013) an exceptionally low LOD (<0.05 fM) was achieved through the utilization of a gold electrode. This specific technique is particularly geared towards detecting metal ions, with its efficacy stemming from the selective reduction of only metal ions (Cai et al., 2013). However, the diverse range of LOD values recorded through amperometry can be ascribed to various factors, including the distinct nanocomposites chosen, the methodologies implemented, and the selection of appropriate sensing techniques (Table 1).

In another study, Yang et al. (2021b), engineered an ultrasensitive biosensor tailored for the detection of HPV miRNA. Within this biosensor, authors deployed a triple signal amplification strategy that ingeniously combined AuNPs with reverse transcription loop-mediated isothermal amplification (RT-LAMP) and a high-affinity biotin-avidin system. This multi-pronged approach yielded an extraordinary LOD, reaching an impressive 0.08 fM. Notably, this sensing paradigm incorporated the use of EIS for electrode fabrication assessment, while the performance stability, specificity, and miRNA detection were evaluated through amperometry. This adoption of the amperometric method bears notable advantages, primarily in the capability to discern HPV miRNA copies across a range spanning from 10^1–10^8 fM. The synergy of EIS and amperometry contributes to the overall efficacy of the biosensor, ensuring robust performance and the ability to detect analytes. The intricate combination of these techniques underscores the biosensor's exceptional sensitivity and its potential to revolutionize the field of biosensors (Yang et al., 2021b).

Zhang et al. (2019a) engineered a biosensor centered on a multi-step process. This novel biosensing approach utilized duplex-specific nuclease (DSN)-assisted target recycling, followed by the integration of AuNPs and enzymatic signal amplification, all aimed at the precise detection of miR-21. Notably, the amperometric method emerges as a key player in signal amplification, operating on the principle of monitoring current changes over time. To ascertain the feasibility of this biosensor, CV was judiciously employed. CV enables the identification of miRNA presence through the observation of peak elevation (Zhang et al., 2019a).

Li et al. (2023) utilized a CDNM-based electrochemical biosensor to detect miR-21 achieving an LOD of 0.0331 fM. In contrast to previous methods using various electrochemical detection techniques, a significant improvement in LOD was observed. For instance, fluorescence yielded an LOD of 0.01 fM, ECL ranged from 2.44 to 4.92 fM, PEC exhibited 0.29 fM, and electrochemical methods ranged from 0.27 to 2.20 fM. The CDNM-based biosensor showcased a broader response range and lower sensing limit for miRNA detection due to the synergistic amplification from the combination of CDNM and TSDRs (Li et al., 2023).

Furthermore, the biosensor's fabrication underwent rigorous investigation through EIS ensuring the optimal construction of the sensor, with LOD of 0.0433 fM. This achievement highlights the biosensor's unparalleled sensitivity, rooted in the orchestrated amalgamation of DSN-assisted target recycling, AuNPs, and enzymatic signal amplification. The strategic integration of amperometric signal amplification, combined with the use of CV and EIS, demonstrates the advanced nature of this biosensing platform, ultimately leading to exceptionally accurate and reliable detection of miR-21 (Zhang et al., 2019b).

In summary, the choice of sensing technique depends on the unique characteristics of the material under investigation and construction strategies. Several factors drive the suitability of modified electrodes in this context. One prominent rationale stem from the fact that certain materials fail to manifest a discernible response within the potential range of conventional solid electrodes. To overcome this limitation, a higher potential is often necessitated, leading to the generation of a more pronounced background current. This scenario can consequently lead to a reduced LOD, impacting the sensor's sensitivity. Furthermore, the employment of modified electrodes is warranted due to the potential for surface deactivation. The adsorption of biological molecules onto the electrode surface can significantly impact its stability, potentially compromising the accuracy and reliability of measurements. This is a crucial consideration, as the stability of the electrode is paramount for maintaining consistent and reproducible results.

Most biosensors employed in biomedical applications require a sizeable sample to detect an object, which may lead to false-positive or false-negative results. Only a few biosensors have been successful in the marketplace globally. More research is required in this area, and we anticipate that businesses will soon transform the scholarly work now being done into commercially viable prototypes.

The development of ultra-sensitive biosensors is still faced with several formidable challenges, each influencing the ultimate detection capabilities. One of the primary concerns is the need to achieve high specificity in biosensors. Complex samples often contain interfering compounds, which can lead to erroneous results, including false positives or false negatives. Gown (2016) conducted a study that highlighted false-negative results caused by various factors such as inadequate sensitivity, poor sample preparation, insufficient calibration, or interference from other substances. Additionally, the cost associated with the production and development of biosensors has limited their widespread use in various applications. The expenses can be significant, encompassing manufacturing, calibration, and integration costs related to immobilizing, purifying, and storing components. On the other hand, legal and ethical challenges also exist, including issues related to safety, quality, validation, standardization, and approval, which can vary from country to country and market to market (Sharma et al., 2015; Fogel and Limson, 2016).

Reproducibility is a critical aspect of biosensor development, influenced by multiple variables, including the quality of materials used, intricacies in the production process, and prevailing environmental conditions. The condition of electrode surfaces and unintended substance adsorption can significantly impact the challenges faced in biosensor development, making replication and electrode regeneration difficult tasks (Carpenter et al., 2018; Naresh and Lee, 2021). Naresh and Lee (2021) proposed several approaches for the replication of biosensors, including inkjet printing, screen printing, and microcontact printing. Further research is warranted to enhance the efficiency and effectiveness of these techniques.

Analyte detection in biosensors presents additional challenges, such as potential loss, diffusion, non-specific binding, and analyte degradation during their delivery to the electrode surface, as observed in various studies (Varshney and Mallikarjunan, 2009; Elgrishi et al., 2018; Vu and Chen, 2019; Naresh and Lee, 2021; Manimekala et al., 2022; Thriveni and Ghosh, 2022). Recent efforts have focused on addressing these obstacles and devising innovative strategies to enhance biosensor performance and reliability. In the context of FET biosensors, maintaining robust electrical performance and stability in liquid environments remains a significant concern (Vu and Chen, 2019; Cho et al., 2020; Manimekala et al., 2022). Vu and Chen (2019) enhanced the anti-interference capabilities of FET biosensors by addressing the issue of non-specific binding between unmodified linkers and targets through the mitigation of blocking surface sensors.

Recent advances in the realm of ultra-sensitive biosensors have been witnessed across various categories, including optical biosensors, colorimetric biosensors, nano-electronic biosensors, MOFs-based biosensors, and aptamer-based sensors. Despite these commendable developments, a notable observation is the disproportionate attention given to the calculation of LOD and linear range, while essential validation parameters, crucial for the establishment of an ultrasensitive electrochemical sensor, namely, precision, accuracy, repeatability, selectivity/specificity, linearity, and limit of quantification, have received relatively less emphasis and scrutiny.

Conclusion

In conclusion, the landscape of biosensor development has seen a transformative shift towards achieving ultrasensitive detection capabilities. Innovative methodologies such as novel DNA walker strategies, controllable 3D DNM, advanced and ultrasensitive biosensing methods such as ratiometric ECL techniques, and nanoparticle modification with ligands integration have revolutionized the field, enabling the detection of biomolecules at unprecedentedly low concentrations with remarkable precision. These innovations have ushered in a new era in biosensing, empowering the precise detection of biomolecules at previously unimaginable low concentrations while ensuring exceptional precision and accuracy. The review has highlighted a selection of groundbreaking research findings, illustrating linear detection ranges spanning from 0.01 to 1×10^8 fM and corresponding LOD ranging from 0.002 to 5 fM. Some studies have even surpassed these benchmarks, achieving LOD levels below 0.009 fM. The adaptability of nanoparticles in sensor design and the potential for elevated performance across various applications have been prominently demonstrated. Continued research in this domain is expected to yield further enhancements, opening up new horizons for applications in diagnostics, disease monitoring, and biomedical research. Collectively, these innovations mark significant progress in biosensing technologies, carrying profound implications for the field of diagnostic research.

Author contributions

AS: Data curation, Formal Analysis, Methodology, Validation, Writing–original draft, Writing–review and editing. FN: Data curation, Methodology, Writing–review and editing. MK: Writing–review and editing. SS: Conceptualization, Methodology, Supervision, Writing–review and editing. AN: Conceptualization, Investigation, Project administration, Supervision, Writing–original draft, Writing–review and editing.

Funding

The author(s) declare financial support was received for the research, authorship, and/or publication of this article. Open Access funding provided by the Qatar National Library.

Conflict of interest

The authors declare that the research was conducted in the absence of any commercial or financial relationships that could be construed as a potential conflict of interest.

Publisher's note

References

Algamili, A. S., Khir, M. H. M., Dennis, J. O., Ahmed, A. Y., Alabsi, S. S., Ba Hashwan, S. S., et al. (2021). A review of actuation and sensing mechanisms in MEMS-based sensor devices. *Nanoscale Res. Lett.* 16 (1), 16. doi:10.1186/s11671-021-03481-7

Algar, W. R., Tavares, A. J., and Krull, U. J. (2010). Beyond labels: a review of the application of quantum dots as integrated components of assays, bioprobes, and biosensors utilizing optical transduction. *Anal. Chim. Acta* 673 (1), 1–25. doi:10.1016/j.aca.2010.05.026

Banakar, M., Hamidi, M., Khurshid, Z., Zafar, M. S., Sapkota, J., Azizian, R., et al. (2022). Electrochemical biosensors for pathogen detection: an updated review. *Biosensors* 12 (11), 927. doi:10.3390/bios12110927

Bao, J., Hou, C., Zhao, Y., Geng, X., Samalo, M., Yang, H., et al. (2019). An enzyme-free sensitive electrochemical microRNA-16 biosensor by applying a multiple signal amplification strategy based on Au/PPy–rGO nanocomposite as a substrate. *Talanta* 196, 329–336. doi:10.1016/j.talanta.2018.12.082

Bezinge, L., Suea-Ngam, A., deMello, A. J., and Shih, C.-J. (2020). Nanomaterials for molecular signal amplification in electrochemical nucleic acid biosensing: recent advances and future prospects for point-of-care diagnostics. *Mol. Syst. Des. Eng.* 5 (1), 49–66. doi:10.1039/c9me00135b

Cai, Z., Song, Y., Wu, Y., Zhu, Z., James Yang, C., and Chen, X. (2013). An electrochemical sensor based on label-free functional allosteric molecular beacons for detection target DNA/miRNA. *Biosens. Bioelectron.* 41, 783–788. doi:10.1016/j.bios.2012.10.002

Carpenter, A. C., Paulsen, I. T., and Williams, T. C. (2018). Blueprints for biosensors: design, limitations, and applications. *Genes* 9 (8), 375. doi:10.3390/genes9080375

Castro, K. P., Colombo, R. N., Iost, R. M., da Silva, B. G., and Crespilho, F. N. (2023). Low-dimensionality carbon-based biosensors: the new era of emerging technologies in bioanalytical chemistry. *Anal. Bioanal. Chem.* 415, 3879–3895. doi:10.1007/s00216-023-04578-x

Chandra, P., Mahato, K., Baranwal, A., Kumari, R., Srivastava, A., and Azad, U. (2023). Differential electrochemical behaviour of phytofabricated and chemically synthesized silver nanoparticles towards hydrogen peroxide sensing. *Electroanalysis* 35, e202300094. doi:10.1002/elan.202300094

Chen, P., Jiang, L., Xie, X., Sun, D., Liu, J., Zhao, Y., et al. (2022). Rapid electrochemical detection of MiRNA-21 facilitated by the excellent catalytic ability of Pt@ CeO 2 nanospheres. *RSC Adv.* 12 (19), 11867–11876. doi:10.1039/d2ra01047j

Chen, Y.-X., Wu, X., and Huang, K.-J. (2018). A sandwich-type electrochemical biosensing platform for microRNA-21 detection using carbon sphere-MoS2 and catalyzed hairpin assembly for signal amplification. *Sensors Actuators B Chem.* 270, 179–186. doi:10.1016/j.snb.2018.05.031

Cho, I.-H., Kim, D. H., and Park, S. (2020). Electrochemical biosensors: perspective on functional nanomaterials for on-site analysis. *Biomaterials Res.* 24 (1), 6. doi:10.1186/s40824-019-0181-y

Cui, L., Wang, M., Sun, B., Ai, S., Wang, S., and Zhang, C.-y. (2019). Substrate-free and label-free electrocatalysis-assisted biosensor for sensitive detection of microRNA in lung cancer cells. *Chem. Commun.* 55 (8), 1172–1175. doi:10.1039/c8cc09688k

Cui, X., Zheng, Y., Zhou, Y., Jiang, T., Wang, S., Cao, L., et al. (2023). Antibody-free photoelectrochemical strategy for simultaneous detection of methylated RNA, METTL3/METTL14 protein and MazF protein based on enhanced photoactivity of MoSe2–BiOI nanocomposite. *Biosens. Bioelectron.* 222, 115015. doi:10.1016/j.bios.2022.115015

Das, S., Gagandeep, and Bhatia, R. (2022). Paper-based microfluidic devices: fabrication, detection, and significant applications in various fields. *Rev. Anal. Chem.* 41 (1), 112–136. doi:10.1515/revac-2022-0037

Deng, K., Liu, X., Li, C., and Huang, H. (2018). Sensitive electrochemical sensing platform for microRNAs detection based on shortened multi-walled carbon nanotubes with high-loaded thionin. *Biosens. Bioelectron.* 117, 168–174. doi:10.1016/j.bios.2018.05.055

Elgrishi, N., Rountree, K. J., McCarthy, B. D., Rountree, E. S., Eisenhart, T. T., and Dempsey, J. L. (2018). A practical beginner's guide to cyclic voltammetry. *J. Chem. Educ.* 95 (2), 197–206. doi:10.1021/acs.jchemed.7b00361

Erdem, A., Eksin, E., Isin, D., and Polat, D. (2017). Graphene oxide modified chemically activated graphite electrodes for detection of microRNA. *Electroanalysis* 29 (5), 1350–1358. doi:10.1002/elan.201600761

Fan, Y., Chen, X., Trigg, A. D., Tung, C.-h., Kong, J., and Gao, Z. (2007). Detection of MicroRNAs using target-guided formation of conducting polymer nanowires in nanogaps. *J. Am. Chem. Soc.* 129 (17), 5437–5443. doi:10.1021/ja067477g

Ferrag, C., and Kerman, K. (2020). Grand challenges in nanomaterial-based electrochemical sensors. *Front. Sensors* 1. doi:10.3389/fsens.2020.583822

Fogel, R., and Limson, J. (2016). Developing biosensors in developing countries: South Africa as a case study. *Biosensors* 6 (1), 5. doi:10.3390/bios6010005

Gao, A., Lu, N., Dai, P., Li, T., and Wang, Y. (2013). "Label-free and ultrasensitive detection of microrna biomarkers in lung cancer cells based on silicon nanowire FET biosensors," in *2013 transducers and eurosensors XXVII: the 17th international conference on solid-state sensors* (Actuators and Microsystems TRANSDUCERS and EUROSENSORS XXVII), 2439–2442.

Gao, C., Low, J., Long, R., Kong, T., Zhu, J., and Xiong, Y. (2020). Heterogeneous single-atom photocatalysts: fundamentals and applications. *Chem. Rev.* 120 (21), 12175–12216. doi:10.1021/acs.chemrev.9b00840

Gao, J., Liu, L., Liu, A., He, Y., Yi, X., and Wang, J. (2022). Ratiometric electrochemical detection of miRNA based on DNA nanomachines and strand displacement reaction. *Microchim. Acta* 189 (3), 133. doi:10.1007/s00604-022-05240-6

Gao, Z., and Yu, Y. H. (2007a). A microRNA biosensor based on direct chemical ligation and electrochemically amplified detection. *Sensors Actuators B Chem.* 121 (2), 552–559. doi:10.1016/j.snb.2006.04.090

Gao, Z., and Yu, Y. H. (2007b). Direct labeling microRNA with an electrocatalytic moiety and its application in ultrasensitive microRNA assays. *Biosens. Bioelectron.* 22 (6), 933–940. doi:10.1016/j.bios.2006.04.020

Goda, K., Lu, H., Fei, P., and Guck, J. (2023). *Revolutionizing microfluidics with artificial intelligence: a new dawn for lab-on-a-chip technologies*. Lab on a Chip.

Gown, A. M. (2016). Diagnostic immunohistochemistry: what can go wrong and how to prevent it. *Archives Pathology Laboratory Med.* 140 (9), 893–898. doi:10.5858/arpa.2016-0119-ra

Grieshaber, D., MacKenzie, R., Vörös, J., and Reimhult, E. (2008). Electrochemical biosensors-sensor principles and architectures. *Sensors* 8 (3), 1400–1458. doi:10.3390/s80314000

Guo, S., Yang, F., Zhang, Y., Ning, Y., Yao, Q., and Zhang, G.-J. (2014). Amplified fluorescence sensing of miRNA by combination of graphene oxide with duplex-specific nuclease. *Anal. Methods* 6 (11), 3598–3603. doi:10.1039/c4ay00345d

Hao, K., He, Y., Lu, H., Pu, S., Zhang, Y., Dong, H., et al. (2017). High-sensitive surface plasmon resonance microRNA biosensor based on streptavidin functionalized gold nanorods-assisted signal amplification. *Anal. Chim. Acta* 954, 114–120. doi:10.1016/j.aca.2016.12.006

He, J., Zhu, J., Jiang, B., and Zhao, Y. (2017). "Label-free direct detection of MiRNAs with poly-silicon nanowire biosensors," in *MicroRNA detection and target identification: methods and protocols*. Editor T. Dalmay (New York, NY: Springer New York), 297–302.

He, Q., Wang, B., Liang, J., Liu, J., Liang, B., Li, G., et al. (2023). Research on the construction of portable electrochemical sensors for environmental compounds quality monitoring. *Mater. Today Adv.* 17, 100340. doi:10.1016/j.mtadv.2022.100340

Huang, C.-H., Huang, T.-T., Chiang, C.-H., Huang, W.-T., and Lin, Y.-T. (2020). A chemiresistive biosensor based on a layered graphene oxide/graphene composite for the sensitive and selective detection of circulating miRNA-21. *Biosens. Bioelectron.* 164, 112320. doi:10.1016/j.bios.2020.112320

Jiang, L., Yang, Y., Lin, Y., Chen, Z., Xing, C., Lu, C., et al. (2020). An electrochemical sensor based on enzyme-free recycling amplification for sensitive and specific detection of miRNAs from cancer cells. *Analyst* 145 (9), 3353–3358. doi:10.1039/d0an00275e

Jiao, L., Xu, W., Wu, Y., Wang, H., Hu, L., Gu, W., et al. (2023). On the road from single-atom materials to highly sensitive electrochemical sensing and biosensing. *Anal. Chem.* 95 (1), 433–443. doi:10.1021/acs.analchem.2c01722

Kangkamano, T., Numnuam, A., Limbut, W., Kanatharana, P., Vilaivan, T., and Thavarungkul, P. (2018). Pyrrolidinyl PNA polypyrrole/silver nanofoam electrode as a novel label-free electrochemical miRNA-21 biosensor. *Biosens. Bioelectron.* 102, 217–225. doi:10.1016/j.bios.2017.11.024

Khazaei, M., Hosseini, M. S., Haghighi, A. M., and Misaghi, M. (2023). Nanosensors and their applications in early diagnosis of cancer. *Sens. Bio-Sensing Res.* 41, 100569. doi:10.1016/j.sbsr.2023.100569

Kim, H., Jang, G., and Yoon, Y. (2020). Specific heavy metal/metalloid sensors: current state and perspectives. *Appl. Microbiol. Biotechnol.* 104 (3), 907–914. doi:10.1007/s00253-019-10261-y

Kim, W., Lee, S. H., Ahn, Y. J., Lee, S. H., Ryu, J., Choi, S. K., et al. (2018). A label-free cellulose SERS biosensor chip with improvement of nanoparticle-enhanced LSPR effects for early diagnosis of subarachnoid hemorrhage-induced complications. *Biosens. Bioelectron.* 111, 59–65. doi:10.1016/j.bios.2018.04.003

Kim, Y., and Kang, E. (2023). A graphitic nano-onion/molybdenum disulfide nanosheet composite as a platform for HPV-associated cancer-detecting DNA biosensors. *J. Nanobiotechnology* 21 (1), 187. doi:10.1186/s12951-023-01948-6

Kucherenko, I., Soldatkin, O., Dzyadevych, S., and Soldatkin, A. (2020). Electrochemical biosensors based on multienzyme systems: main groups, advantages and limitations–a review. *Anal. Chim. acta* 1111, 114–131. doi:10.1016/j.aca.2020.03.034

Lao, K., Xu, N. L., Yeung, V., Chen, C., Livak, K. J., and Straus, N. A. (2006). Multiplexing RT-PCR for the detection of multiple miRNA species in small samples. *Biochem. biophysical Res. Commun.* 343 (1), 85–89. doi:10.1016/j.bbrc.2006.02.106

Li, D., Zhang, X.-L., Chai, Y.-Q., and Yuan, R. (2023). Controllable three-dimensional DNA nanomachine-mediated electrochemical biosensing platform for rapid and ultrasensitive detection of MicroRNA. *Anal. Chem.* 95 (2), 1490–1497. doi:10.1021/acs.analchem.2c04519

Li, T., Liang, Y., Li, J., Yu, Y., Xiao, M.-M., Ni, W., et al. (2021). Carbon nanotube field-effect transistor biosensor for ultrasensitive and label-free detection of breast cancer exosomal miRNA21. *Anal. Chem.* 93 (46), 15501–15507. doi:10.1021/acs.analchem.1c03573

Liang, Z., Ou, D., Sun, D., Tong, Y., Luo, H., and Chen, Z. (2019). Ultrasensitive biosensor for microRNA-155 using synergistically catalytic nanoprobe coupled with improved cascade strand displacement reaction. *Biosens. Bioelectron.* 146, 111744. doi:10.1016/j.bios.2019.111744

Liao, N., Liu, J.-L., Chai, Y.-Q., Yuan, R., and Zhuo, Y. (2020). DNA structure transition-induced affinity switch for biosensing based on the strong electrochemiluminescence platform from organic microcrystals. *Anal. Chem.* 92 (5), 3940–3948. doi:10.1021/acs.analchem.9b05433

Liu, D., Yang, G., Zhang, X., Chen, S., and Yuan, R. (2021). A novel potential-regulated ratiometric electrochemiluminescence sensing strategy based on poly(9,9-di-n-octylfluorenyl-2,7-diyl) polymer nanoparticles for microRNA detection. *Sensors Actuators B Chem.* 329, 129210. doi:10.1016/j.snb.2020.129210

Liu, S., Huo, Y., Fan, L., Ning, B., Sun, T., and Gao, Z. (2022). Rapid and ultrasensitive detection of DNA and microRNA-21 using a zirconium porphyrin metal-organic framework-based switch fluorescence biosensor. *Anal. Chim. Acta* 1192, 339340. doi:10.1016/j.aca.2021.339340

Liu, S., Yang, Z., Chang, Y., Chai, Y., and Yuan, R. (2018). An enzyme-free electrochemical biosensor combining target recycling with Fe3O4/CeO2@ Au nanocatalysts for microRNA-21 detection. *Biosens. Bioelectron.* 119, 170–175. doi:10.1016/j.bios.2018.08.006

Liu, S.-T., Liu, X.-P., Chen, J.-S., Mao, C.-j., and Jin, B.-K. (2020). Highly sensitive photoelectrochemical biosensor for microRNA159c detection based on a Ti3C2: CdS nanocomposite of breast cancer. *Biosens. Bioelectron.* 165, 112416. doi:10.1016/j.bios.2020.112416

Liu, Y.-Q., Zhang, M., Yin, B.-C., and Ye, B.-C. (2012). Attomolar ultrasensitive MicroRNA detection by DNA-scaffolded silver-nanocluster probe based on isothermal amplification. *Anal. Chem.* 84 (12), 5165–5169. doi:10.1021/ac300483f

Lu, H., Hailin, T., Yi, X., and Wang, J. (2020). Three-dimensional DNA nanomachine combined with toehold-mediated strand displacement reaction for sensitive electrochemical detection of MiRNA. *Langmuir* 36 (36), 10708–10714. doi:10.1021/acs.langmuir.0c01415

Lu, N., Gao, A., Dai, P., Song, S., Fan, C., Wang, Y., et al. (2014). CMOS-compatible silicon nanowire field-effect transistors for ultrasensitive and label-free MicroRNAs sensing. *Small* 10 (10), 2022–2028. doi:10.1002/smll.201302990

Luong, J. H., Narayan, T., Solanki, S., and Malhotra, B. D. (2020). Recent advances of conducting polymers and their composites for electrochemical biosensing applications. *J. Funct. Biomaterials* 11 (4), 71. doi:10.3390/jfb11040071

Manimekala, T., Sivasubramanian, R., and Dharmalingam, G. (2022). Nanomaterial-based biosensors using field-effect transistors: a review. *J. Electron. Mater.* 51 (5), 1950–1973. doi:10.1007/s11664-022-09492-z

Mariani, F., Gualandi, I., Schuhmann, W., and Scavetta, E. (2022). Micro- and nano-devices for electrochemical sensing. *Microchim. Acta* 189 (12), 459. doi:10.1007/s00604-022-05548-3

Mehmood, S., Naeem, A., Sabahat, S., Ciancio, R., Carlino, E., Bhopal, M. F., et al. (2015). Modified structural and optical characteristics of Au-NPs–MWCNTs nanohybrids. *Superlattices Microstruct.* 81, 248–264. doi:10.1016/j.spmi.2015.01.020

Mehrvar, M., and Abdi, M. (2004). Recent developments, characteristics, and potential applications of electrochemical biosensors. *Anal. Sci.* 20 (8), 1113–1126. doi:10.2116/analsci.20.1113

Meng, T., Zhao, D., Ye, H., Feng, Y., Wang, H., and Zhang, Y. (2020). Construction of an ultrasensitive electrochemical sensing platform for microRNA-21 based on interface impedance spectroscopy. *J. Colloid Interface Sci.* 578, 164–170. doi:10.1016/j.jcis.2020.05.118

Miao, P., Tang, Y., Wang, B., and Meng, F. (2016). Near-infrared Ag2S quantum dots-based DNA logic gate platform for miRNA diagnostics. *Anal. Chem.* 88 (15), 7567–7573. doi:10.1021/acs.analchem.6b01044

Mohamed, W. A. A., El-Gawad, H. A., Mekkey, S., Galal, H., Handal, H., Mousa, H., et al. (2021). Quantum dots synthetization and future prospect applications. *Nanotechnol. Rev.* 10 (1), 1926–1940. doi:10.1515/ntrev-2021-0118

Mohammadnejad, J., Basirhaghighi, N., Yazdian, F., Pourmadadi, M., Shayeh, J. S., Omidi, M., et al. (2023). Electrochemical nanobiosensor based on reduced graphene oxide and gold nanoparticles for ultrasensitive detection of microRNA-128. *Int. Immunopharmacol.* 117, 109960. doi:10.1016/j.intimp.2023.109960

Mohammadniaei, M., Koyappayil, A., Sun, Y., Min, J., and Lee, M.-H. (2020). Gold nanoparticle/MXene for multiple and sensitive detection of oncomiRs based on synergetic signal amplification. *Biosens. Bioelectron.* 159, 112208. doi:10.1016/j.bios.2020.112208

Molla, A., and Youk, J. H. (2023). Recent progress on electroanalytical sensing of small molecules and biomolecules using carbon dots: a review. *J. Industrial Eng. Chem.* 127, 62–81. doi:10.1016/j.jiec.2023.07.037

Munusami, R., and Ramasamy, M. (2022). "Multiplexed biosensors for efficient diagnosis of the clinical conditions toward Health management," in *Miniaturized biosensing devices: fabrication and applications*. Editors P. Chandra and K. Mahato (Singapore: Springer Nature Singapore), 205–225.

Naikoo, G. A., Salim, H., Hassan, I. U., Awan, T., Arshad, F., Pedram, M. Z., et al. (2021). Recent advances in non-enzymatic glucose sensors based on metal and metal oxide nanostructures for diabetes management- A review. *Front. Chem.* 9, 748957. doi:10.3389/fchem.2021.748957

Naresh, V., and Lee, N. (2021). A review on biosensors and recent development of nanostructured materials-enabled biosensors. *Sensors* 21 (4), 1109. doi:10.3390/s21041109

Ndolomingo, M. J., Bingwa, N., and Meijboom, R. (2020). Review of supported metal nanoparticles: synthesis methodologies, advantages and application as catalysts. *J. Mater. Sci.* 55 (15), 6195–6241. doi:10.1007/s10853-020-04415-x

Ozkan-Ariksoysal, D. (2021). "Chapter 5 - electrochemical DNA biosensors based on quantum dots," in *Electroanalytical applications of quantum dot-based biosensors*. Editor B. Uslu (Elsevier), 155–184.

Pang, X., Qi, J., Zhang, Y., Ren, Y., Su, M., Jia, B., et al. (2016). Ultrasensitive photoelectrochemical aptasensing of miR-155 using efficient and stable CH3NH3PbI3 quantum dots sensitized ZnO nanosheets as light harvester. *Biosens. Bioelectron.* 85, 142–150. doi:10.1016/j.bios.2016.04.099

Peng, Y., Yi, G., and Gao, Z. (2010). A highly sensitive microRNA biosensor based on ruthenium oxide nanoparticle-initiated polymerization of aniline. *Chem. Commun.* 46 (48), 9131–9133. doi:10.1039/c0cc01990a

Pérez-Fernández, B., and de la Escosura-Muniz, A. (2022). Electrochemical biosensors based on nanomaterials for aflatoxins detection: a review (2015–2021). *Anal. Chim. Acta* 1212, 339658. doi:10.1016/j.aca.2022.339658

Pourmadadi, M., Rahmani, E., Rajabzadeh-Khosroshahi, M., Samadi, A., Behzadmehr, R., Rahdar, A., et al. (2023). Properties and application of carbon quantum dots (CQDs) in biosensors for disease detection: a comprehensive review. *J. Drug Deliv. Sci. Technol.* 80, 104156. doi:10.1016/j.jddst.2023.104156

Qin, L., Han, X., Feng, Q., and Wang, P. (2023). Construction of broom-like Ag@N,O-C sensing interface for electrochemical detection of circulating tumor DNA using entropy-driven DNA walker. *Sensors Actuators B Chem.* 378, 133157. doi:10.1016/j.snb.2022.133157

Ranjan Srivastava, V., Kumari, R., and Chandra, P. (2022). Miniaturized surface engineered technologies for multiplex biosensing devices. *Electroanalysis* 35, e202200355. doi:10.1002/elan.202200355

Ray, A., Mohan, J. M., Amreen, K., Dubey, S. K., Javed, A., Ponnalagu, R., et al. (2023). Ink-jet-printed CuO nanoparticle-enhanced miniaturized paper-based electrochemical platform for hypochlorite sensing. *Appl. Nanosci.* 13 (3), 1855–1861. doi:10.1007/s13204-021-02235-2

Sabahat, S., Ejaz, M., F Saira, F., Saleem, R. S. Z., Nazish, Y., Khalil, L., et al. (2023). Surface plasmon resonance-based synthesis of gold nanorods for sensing applications. *Chem. Pap.* 77, 5901–5911. doi:10.1007/s11696-023-02909-x

Safari, M., Moghaddam, A., Salehi Moghaddam, A., Absalan, M., Kruppke, B., Ruckdäschel, H., et al. (2023). Carbon-based biosensors from graphene family to carbon dots: a viewpoint in cancer detection. *Talanta* 258, 124399. doi:10.1016/j.talanta.2023.124399

Sharma, S., Zapatero-Rodríguez, J., Estrela, P., and Kennedy, R. (2015). Point-of-Care diagnostics in low resource settings: present status and future role of microfluidics. *Biosensors* 5 (3), 577–601. doi:10.3390/bios5030577

Singh, A., Sharma, A., Ahmed, A., Sundramoorthy, A. K., Furukawa, H., Arya, S., et al. (2021). Recent advances in electrochemical biosensors: applications, challenges, and future scope. *Biosensors* 11 (9), 336. doi:10.3390/bios11090336

Sobhanie, E., Roshani, A., and Hosseini, M. (2022). "Chapter 16 - microfluidic systems with amperometric and voltammetric detection and paper-based sensors and biosensors," in *Carbon nanomaterials-based sensors*. Editors J. G. Manjunatha and C. M. Hussain (Elsevier), 275–287.

Sumitha, M., and Xavier, T. (2023). Recent advances in electrochemical biosensors–A brief review. *Hybrid. Adv.* 2, 100023. doi:10.1016/j.hybadv.2023.100023

Sun, Y., Jin, H., Jiang, X., and Gui, R. (2020). Black phosphorus nanosheets adhering to thionine-doped 2D MOF as a smart aptasensor enabling accurate capture and ratiometric electrochemical detection of target microRNA. *Sensors Actuators B Chem.* 309, 127777. doi:10.1016/j.snb.2020.127777

Szunerits, S., Pagneux, Q., Swaidan, A., Mishyn, V., Roussel, A., Cambillau, C., et al. (2022). The role of the surface ligand on the performance of electrochemical SARS-CoV-2 antigen biosensors. *Anal. Bioanal. Chem.* 414 (1), 103–113. doi:10.1007/s00216-020-03137-y

Thriveni, G., and Ghosh, K. (2022). Advancement and challenges of biosensing using field effect transistors. *Biosensors* 12 (8), 647. doi:10.3390/bios12080647

Tian, L., Zhang, J., Zhang, Y., Fan, H., Liu, C., Wang, Y., et al. (2023). Dual-model photoelectrochemical biosensor via DNAzyme walker integrated nanoprobe for ultrasensitive ratiometric detection of microRNA-155. *Sensors Actuators B Chem.* 390, 133993. doi:10.1016/j.snb.2023.133993

Tian, R., Li, Y., and Bai, J. (2019). Hierarchical assembled nanomaterial paper based analytical devices for simultaneously electrochemical detection of microRNAs. *Anal. Chim. Acta* 1058, 89–96. doi:10.1016/j.aca.2019.01.036

Tran, H. V., Piro, B., Reisberg, S., Tran, L. D., Duc, H. T., and Pham, M. C. (2013). Label-free and reagentless electrochemical detection of microRNAs using a conducting

polymer nanostructured by carbon nanotubes: application to prostate cancer biomarker miR-141. *Biosens. Bioelectron.* 49, 164–169. doi:10.1016/j.bios.2013.05.007

Tran, V. A., Vo, G. N., Vo, T.-T. T., Doan, V. D., Vo, V., and Le, V. T. (2023). Recent applications and prospects of nanowire-based biosensors. *Processes* 11 (6), 1739. doi:10.3390/pr11061739

Ulucan-Karnak, F., Mishra, S., and Koduru, J. R. (2023). "Recent trends on functionalized nanohybrids enhanced biosensors performances and their applications," in *Hybrid nanomaterials for sustainable applications* (Elsevier), 221–251.

Valera, E., Kindratenko, V., Jankelow, A. M., Heredia, J., Kim, A. Y., Cowell, T. W., et al. (2023). Electrochemical point-of-care devices for the diagnosis of sepsis. *Curr. Opin. Electrochem.* 39, 101300. doi:10.1016/j.coelec.2023.101300

Várallyay, E., Burgyán, J., and Havelda, Z. (2008). MicroRNA detection by northern blotting using locked nucleic acid probes. *Nat. Protoc.* 3 (2), 190–196. doi:10.1038/nprot.2007.528

Varshney, M., and Mallikarjunan, K. (2009). Challenges in Biosensor Development--Detection limit, detection time, and specificity. *Resour. Mag.* 16 (7), 18–21. doi:10.13031/2013.29328

Vu, C.-A., and Chen, W.-Y. (2019). Field-effect transistor biosensors for biomedical applications: recent advances and future prospects. *Sensors* 19 (19), 4214. doi:10.3390/s19194214

Walcarius, A., Minteer, S. D., Wang, J., Lin, Y., and Merkoci, A. (2013). Nanomaterials for bio-functionalized electrodes: recent trends. *J. Mater. Chem. B* 1 (38), 4878–4908. doi:10.1039/c3tb20881h

Wang, C., Chen, M., Han, Q., Wu, J., Zhao, X., and Fu, Y. (2020b). A three-dimensional DNA nanomachine with target recycling amplification technology and multiple electrochemiluminescence resonance energy transfer for sensitive microRNA-141 detection. *Biosens. Bioelectron.* 156, 112146. doi:10.1016/j.bios.2020.112146

Wang, C., Zhang, H., Zeng, D., Sun, W., Zhang, H., Aldalbahi, A., et al. (2015b). Elaborately designed diblock nanoprobes for simultaneous multicolor detection of microRNAs. *Nanoscale* 7 (38), 15822–15829. doi:10.1039/c5nr04618a

Wang, L., Liu, P., Liu, Z., Zhao, K., Ye, S., Liang, G., et al. (2020a). Simple tripedal DNA walker prepared by target-triggered catalytic hairpin assembly for ultrasensitive electrochemiluminescence detection of MicroRNA. *ACS Sensors* 5 (11), 3584–3590. doi:10.1021/acssensors.0c01864

Wang, Q., Liu, Y., Wang, X., Wang, F., Zhang, L., Ge, S., et al. (2021a). Ternary electrochemiluminescence biosensor based on DNA walkers and AuPd nanomaterials as a coreaction accelerator for the detection of miRNA-141. *ACS Appl. Mater. Interfaces* 13 (22), 25783–25791. doi:10.1021/acsami.1c05368

Wang, Q., Liu, Y., Yan, J., Liu, Y., Gao, C., Ge, S., et al. (2021b). 3D DNA walker-assisted CRISPR/Cas12a trans-cleavage for ultrasensitive electrochemiluminescence detection of miRNA-141. *Anal. Chem.* 93 (39), 13373–13381. doi:10.1021/acs.analchem.1c03183

Wang, W., Kong, T., Zhang, D., Zhang, J., and Cheng, G. (2015a). Label-free microRNA detection based on fluorescence quenching of gold nanoparticles with a competitive hybridization. *Anal. Chem.* 87 (21), 10822–10829. doi:10.1021/acs.analchem.5b01930

Xu, S., Chang, Y., Wu, Z., Li, Y., Yuan, R., and Chai, Y. (2020). One DNA circle capture probe with multiple target recognition domains for simultaneous electrochemical detection of miRNA-21 and miRNA-155. *Biosens. Bioelectron.* 149, 111848. doi:10.1016/j.bios.2019.111848

Yang, F., Yang, F., Tu, T.-T., Liao, N., Chai, Y.-Q., Yuan, R., et al. (2021a). A synergistic promotion strategy remarkably accelerated electrochemiluminescence of SnO2 QDs for MicroRNA detection using 3D DNA walker amplification. *Biosens. Bioelectron.* 173, 112820. doi:10.1016/j.bios.2020.112820

Yang, N., Liu, P., Cai, C., Zhang, R., Sang, K., Shen, P., et al. (2021b). Triple signal amplification strategy for the ultrasensitive electrochemical detection of human papillomavirus 16 E6/E7 mRNA. *Enzyme Microb. Technol.* 149, 109855. doi:10.1016/j.enzmictec.2021.109855

Yoon, Y., Truong, P. L., Lee, D., and Ko, S. H. (2022). Metal-oxide nanomaterials synthesis and applications in flexible and wearable sensors. *ACS Nanosci. Au* 2 (2), 64–92. doi:10.1021/acsnanoscienceau.1c00029

Yu, N., Wang, Z., Wang, C., Han, J., and Bu, H. (2017). Combining padlock exponential rolling circle amplification with CoFe2O4 magnetic nanoparticles for microRNA detection by nanoelectrocatalysis without a substrate. *Anal. Chim. Acta* 962, 24–31. doi:10.1016/j.aca.2017.01.069

Yuan, R., Yu, X., Zhang, Y., Xu, L., Cheng, W., Tu, Z., et al. (2017). Target-triggered DNA nanoassembly on quantum dots and DNAzyme-modulated double quenching for ultrasensitive microRNA biosensing. *Biosens. Bioelectron.* 92, 342–348. doi:10.1016/j.bios.2016.11.002

Zhang, C., Li, D., Li, D., Wen, K., Yang, X., and Zhu, Y. (2019b). Rolling circle amplification-mediated *in situ* synthesis of palladium nanoparticles for the ultrasensitive electrochemical detection of microRNA. *Analyst* 144 (12), 3817–3825. doi:10.1039/c9an00427k

Zhang, H., Fan, M., Jiang, J., Shen, Q., Cai, C., and Shen, J. (2019a). Sensitive electrochemical biosensor for MicroRNAs based on duplex-specific nuclease-assisted target recycling followed with gold nanoparticles and enzymatic signal amplification. *Anal. Chim. Acta* 1064, 33–39. doi:10.1016/j.aca.2019.02.060

Zhang, W., Xu, H., Zhao, X., Tang, X., Yang, S., Yu, L., et al. (2020). 3D DNA nanonet structure coupled with target-catalyzed hairpin assembly for dual-signal synergistically amplified electrochemical sensing of circulating microRNA. *Anal. Chim. Acta* 1122, 39–47. doi:10.1016/j.aca.2020.05.002

Zhao, J., He, C., Long, Y., Lei, J., Liu, H., Hou, J., et al. (2023). 3D DNAzyme walker based electrochemical biosensor for attomolar level microRNA-155 detection. *Anal. Chim. Acta* 1276, 341642. doi:10.1016/j.aca.2023.341642

Zhao, J., He, Y., Tan, K., Yang, J., Chen, S., and Yuan, R. (2021). Novel ratiometric electrochemiluminescence biosensor based on BP-CdTe QDs with dual emission for detecting MicroRNA-126. *Anal. Chem.* 93 (36), 12400–12408. doi:10.1021/acs.analchem.1c02408

Zhou, L., Wang, J., Chen, Z., Li, J., Wang, T., Zhang, Z., et al. (2017). A universal electrochemical biosensor for the highly sensitive determination of microRNAs based on isothermal target recycling amplification and a DNA signal transducer triggered reaction. *Microchim. Acta* 184 (5), 1305–1313. doi:10.1007/s00604-017-2129-z

Zhou, Y., Ai, S., Chai, Y., Yuan, R., and Liu, H. (2023). Ultrasensitive photocathodic biosensor based on the Cu2O/PTB7-Th/PDA+ composite with enhanced photoelectrochemical performance for the detection of MicroRNA-375-3p. *Anal. Chem.* 95, 12383–12390. doi:10.1021/acs.analchem.3c01935

Zhu, L., Ye, J., Wang, S., Yan, M., Zhu, Q., Huang, J., et al. (2019). Dual amplification ratiometric biosensor based on a DNA tetrahedron nanostructure and hybridization chain reaction for the ultrasensitive detection of microRNA-133a. *Chem. Commun.* 55 (77), 11551–11554. doi:10.1039/c9cc05592d

frontiers | Frontiers in Bioengineering and Biotechnology

TYPE Original Research
PUBLISHED 07 December 2023
DOI 10.3389/fbioe.2023.1310258

OPEN ACCESS

EDITED BY
Kang Cui,
University of Jinan, China

REVIEWED BY
Sandeep Surendra Panikar,
Washington University in St. Louis, United States
Nan-Fu Chiu,
National Taiwan Normal University, Taiwan

*CORRESPONDENCE
Weimin Lu,
yifan201802@126.com

†These authors have contributed equally to this work

RECEIVED 09 October 2023
ACCEPTED 23 November 2023
PUBLISHED 07 December 2023

CITATION
Cheng L, Xu J, Yuan H, Zhao Q, Yue W, Ma S and Lu W (2023), An aptamer and Au/Si CCA based SERS sensor for ultra-sensitive detection of Vimentin during EMT in gastric cancer.
Front. Bioeng. Biotechnol. 11:1310258.
doi: 10.3389/fbioe.2023.1310258

An aptamer and Au/Si CCA based SERS sensor for ultra-sensitive detection of Vimentin during EMT in gastric cancer

Lingling Cheng[1†], Jianlin Xu[1†], Hua Yuan[2], Qihao Zhao[3], Wei Yue[1], Shuang Ma[1] and Weimin Lu[4*]

[1]Department of Oncology, Yancheng TCM Hospital Affiliated to Nanjing University of Chinese Medicine, Yancheng, Jiangsu, China, [2]Pharmacy Department, Yancheng TCM Hospital Affiliated to Nanjing University of Chinese Medicine, Yancheng, Jiangsu, China, [3]Department of Laboratory Medicine, Yancheng TCM Hospital Affiliated to Nanjing University of Chinese Medicine, Yancheng, Jiangsu, China, [4]General Internal Medicine, Affiliated Hospital of Nanjing University of Chinese Medicine, Jiangsu Province Hospital of Chinese Medicine, Nanjing, Jiangsu, China

Introduction: In this study, a surface-enhanced Raman scattering (SERS) sensor based on a functionalized Au/Si cap-cone array (Au/Si CCA) was constructed using the identity-release strategy to detect Vimentin changes during epithelial-mesenchymal transition (EMT) in gastric cancer (GC).

Methods: The periodic structure of Au/Si CCA, which can form "hot spots" with high density and regular arrangement, is a substrate with excellent performance. Au/Si CCA was functionalized with aptamers as the capture substrate, and Au nanocubes (AuNCs) were modified with 5-carboxyfluorescein (5-FAM) labelled complementary strand as SERS probe. The capture substrate and SERS probe were assembled by hybridization, and the SERS signal intensity of 5-FAM was greatly enhanced. The binding of Vimentin to the aptamer resulted in a broken connection between the SERS sensor Au/Si CCA array and AuNCs, which resulted in a decrease in the signal intensity of 5-FAM. The identity-release strategy requires only a simple step of reaction to achieve rapid detection of target proteins, which has clinical practicability.

Results: Using this protocol, the concentration of Vimentin in GES-1 cells could be successfully detected, and the detection limit was as low as 4.92 pg/mL. Biological experiments of Vincristine, Oncovin (VCR)-treated GES-1 cells effectively mimicked the EMT process, and Vimentin changes during EMT could be accurately detected by this method.

Discussion: This study provides a selective, ultra-sensitive and accurate assay for Vimentin detection, which may provide a means for the future detection of EMT process in GC.

KEYWORDS

Au/Si CCA, epithelial-mesenchymal transition, gastric cancer, surface-enhanced Raman scattering, Vimentin

1 Introduction

Gastric cancer (GC) is one of the most common and high-risk malignant tumors in the digestive system (Li et al., 2020). It originates from mucosal epithelial cells on the inner surface of the gastric wall and can occur in various parts of the stomach (Liang et al., 2023; Liu et al., 2023). The onset of GC is relatively hidden and the early symptoms are not typical, leading to many patients usually being diagnosed in the late stage (Monster et al., 2022). GC has the characteristics of easy metastasis and recurrence (Wei et al., 2017). GC patients are often accompanied by lymph node metastasis, peritoneal metastasis and liver metastasis, so their prognosis is extremely poor (Mita et al., 2023). Infiltration and metastasis of tumors are one of the most common causes of death. Metastasis is a complex multi-step process and epithelial-mesenchymal transition (EMT) is a key step in GC metastasis (Mahmoudian et al., 2023). The transformation of adherent epithelial cells into mesenchymal cells during EMT enables the cells to acquire powerful pro-tumor properties, including motility, aggressiveness, dryness, the ability to form metastasis and drug resistance (Zhang Z. et al., 2023b). The abnormal activation of EMT plays an important role in the invasion, metastasis and recurrence of GC (Pretzsch et al., 2022; An and Liu, 2023; Eddin et al., 2023). At present, GC has become a major burden on society, early detection of the key factor in the EMT process and subsequent treatment will improve patient prognosis.

Vimentin is a cytoskeletal intermediate filament protein, which is mainly expressed in mesenchymal origin tissues and the cytoplasm of mesenchymal tumor cells, and plays an important role in epithelial cell development, incision healing and tumor invasion and metastasis (Paulin et al., 2022). Expression of waveform proteins in epithelial cells is critical for continuous EMT through interactions with actin and other intermediate filaments. Waveform protein expression in epithelial cells has been reported to be associated with the malignant phenotype of cancer cells. Also patients with waveform protein-positive gastric cancer have significantly worse prognosis than patients with waveform protein-negative gastric cancer, and waveform protein expression may be a useful biomarker for determining the biological aggressiveness of gastric cancer (Brzozowa et al., 2015). In addition waveform protein expression in epithelial cells is crucial for EMT, which is associated with the acquisition of invasive properties of cancer cells (Yin et al., 2018). Several studies related to GC have shown that Vimentin can induce EMT and promote the invasion and metastasis of GC cells (Keyghobadi et al., 2022; Wang et al., 2023). It can be used as an important marker in EMT process (Yin et al., 2018). In the past, Vimentin was detected by immunological, electrochemical and fluorescent methods (Fhied et al., 2014; Wei et al., 2020; Peng et al., 2023). These methods have drawbacks such as susceptibility to interference, time-consuming, high cost, and complex to operate. Therefore, it is crucial to find a rapid and simple detection method with high sensitivity and specificity.

To address the above issues, an aptamer composed of nucleic acids was introduced as a molecular recognition probe. Aptamers are artificial short single-stranded oligonucleotides of DNA or RNA selected by Systematic Evolution of Ligands by Exponential Enrichment (SELEX) (Tuerk and Gold, 1990). Aptamer has excellent chemical stability and is not easily limited by the environmental conditions of the biosensing method (Liu et al., 2022; Nourizad et al., 2023). Aptamers are linked to complementary DNA or RNA strands by hybridization, a signaling strategy guided by preprogrammed Watson-Crick base-pairing, to form

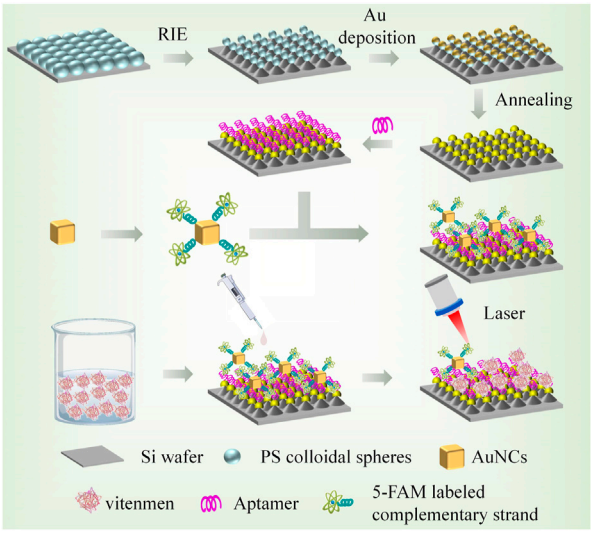

FIGURE 1
Preparation of capture substrate and SERS probe and schematic diagram of SERS sensor for Vimentin detection.

TABLE 1 The sequence of Vimentin aptamer and complementary strand.

Name	Sequence (5′–3′)
Aptamer	SH-TAGACCCAGCTGGTCCGGAAAATAAGATG
	TCACGGATCCTC
Complementary strand	SH-GAGGATCCGTGACATCTT-5-FAM

double-stranded structures called duplexed aptamer (DA), which regulate aptamer function (Nutiu and Li, 2003). In DA, the aptamer acts as a ligand-binding agent, whereas the complementary strand, which initially hybridizes to a defined portion of the aptamer, acts as a competing binding agent and generates signals during ligand-dependent dehybridization (Munzar et al., 2018; 2019). Conformational selection assumes that the complementary chain is first dehybridized from the DA to produce a free aptamer, which is able to fold into a three-dimensional structure and bind with high affinity and specificity to a particular target molecule (Song et al., 2008). The development of sensors based on the advantages of aptamers such as simplicity, speed, low cost, high sensitivity and high specificity has attracted much attention (Arishi et al., 2023; Gao et al., 2023; Park et al., 2023).

Surface-enhanced Raman scattering (SERS) can identify molecular "fingerprint" information, parameters such as characteristic peak position and intensity of the spectral signal can reflect the composition and structure of functional groups and chemical bonds in the molecule, thus achieving the specific detection of the molecule (Gu et al., 2023). Precious metal materials (Au, Ag, Cu) are the strongest metal materials in SERS effect, and their morphology, size and aggregation state have great influence on SERS effect (Yang et al., 2018; Sai et al., 2023).

Au/Si CCA, when used as a SERS substrate, ensures the uniform distribution of hot spots and adsorbed target molecules on the chip, enabling excellent signal reproducibility and accurate quantitative SERS detection. The edges and corners of AuNCs generate significantly enhanced localized electromagnetic fields on individual nanoparticles or between coupled nanoparticles, which can lead to

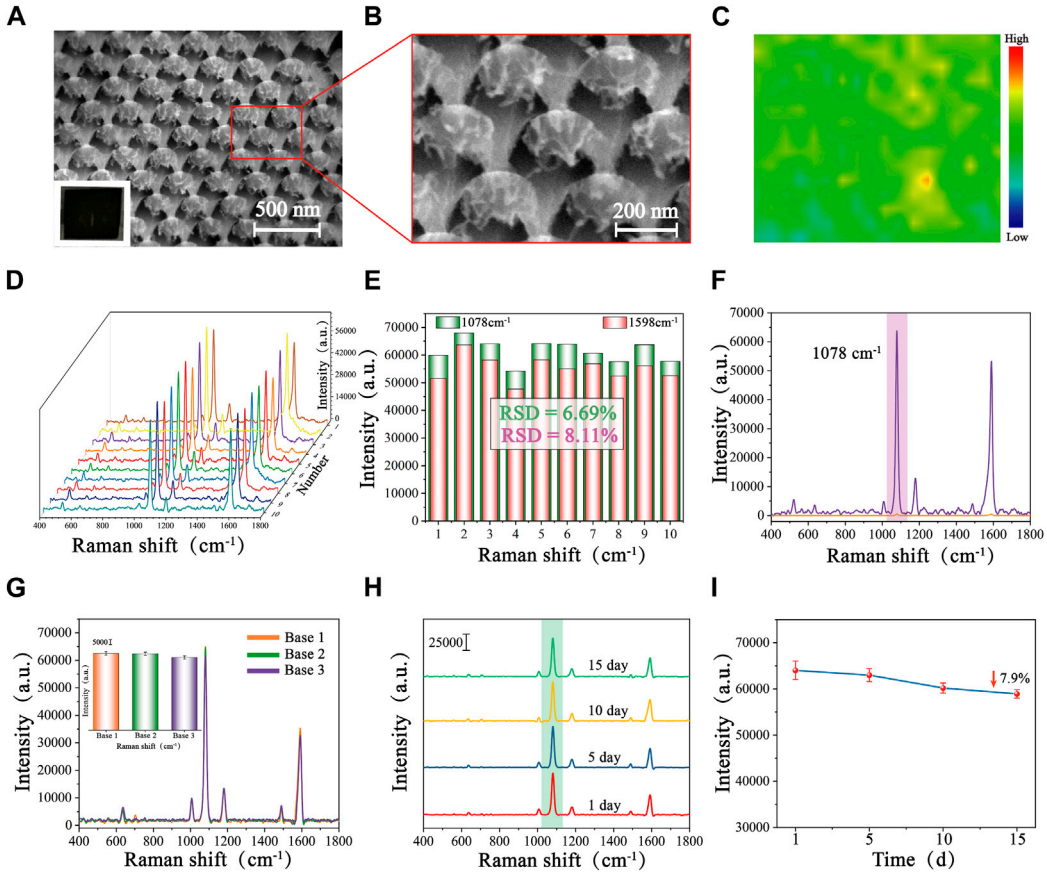

FIGURE 2
SEM images of Au/Si CCA with different magnifications: **(A)** Low magnification, and **(B)** High magnification. **(C)** SERS mapping of Au/Si CCA modified with 4-MBA (1×10^{-8} M). **(D)** SERS spectra of 10 randomly selected points on the surface of the 4-MBA-labelled Au/Si CCA and **(E)** the corresponding histogram of the intensity at 1,078 cm^{-1} and 1,598 cm^{-1}. **(F)** SERS spectra of Au/Si CCA were modified with 4-MBA (1×10^{-8} M) and pure 4-MBA (1×10^{-1} M). **(G)** SERS spectra of 4-MBA-labelled Au/Si CCA prepared in different batches and the corresponding histogram. **(H)** SERS spectra of 4-MBA-labelled Au/Si CCA were stored at room temperature for 1 day, 5 days, 10 days, 15 days, and **(I)** the corresponding line graphs of the intensity at 1,078 cm^{-1}.

significant SERS enhancement (Park et al., 2018). Therefore, SERS technology has the advantages of high sensitivity, good specificity, simple and fast operation (López-Lorente, 2021). Pan et al. (2022) developed a sensitive and direct SERS aptamer sensor to detect exosomes. The as-fabricated SERS aptasensor was capable of detecting exosomes in a wide range from 55 to 5.5×10^5 particles μL^{-1} with a detection limit of 17 particles μL^{-1}. Zhang et al. designed a ratiometric SERS biosensor for highly sensitive detection of exosomes that accurately identifies breast cancer cell-derived exosomes in clinical serum samples with ultra-low detection limits as low as 1.5×10^2 particles/mL (Zhang Q. et al., 2023a). Zhao developed a novel SERS-based aptasensor to detect prostate-specific antigen biomarkers with an The limit of detection (LOD) is 6 pg/mL (Zhao et al., 2022). Thus, by combining SERS with aptamers, the sensitivity and accuracy of the assay were significantly improved.

Herein, a novel SERS sensor based on identity-release strategy, Au/Si cap-cone array (Au/Si CCA) and Au nanocubes (AuNCs) were constructed. In this study, aptamer functionalized Au/Si CCA was used as the capture substrate, and AuNCs was combined with 5-carboxyfluorescein (5-FAM) labelled complementary strand as the SERS probe. When the target Vimentin was present on the capture substrate, the aptamer specifically recognizes the target protein and stably bound to it. At this time, the SERS probe was moved away from the substrate due to the competition of the target, resulting in the reduction of hot spots and the weakening of the Raman signal. Use this SERS sensor to detect and collect Raman signal from 5-FAM. Analyzing its data can qualitatively and quantitatively reflect the concentration of the target object. The schematic diagram is shown in Figure 1. The SERS sensor has the following advantages. First, Au/Si CCA can form a high density and uniform "hot spot" due to its periodic arrangement structure, so that it has excellent SERS performance. Second, the identity-release strategy was selected to significantly improve the specificity. Third, in addition to excellent sensitivity and specificity, the sensor also has the advantages of simple operation, short time consumption and strong anti-interference. These advantages showed the excellent performance of the SERS sensor in the detection of EMT in GC.

2 Experimental section

2.1 Materials

Hexadecyl trimethyl ammonium bromide (CTAB), chloroauric acid tetrahydrate ($HAuCl_4$), sodium borohydride ($NaBH_4$), ascorbic

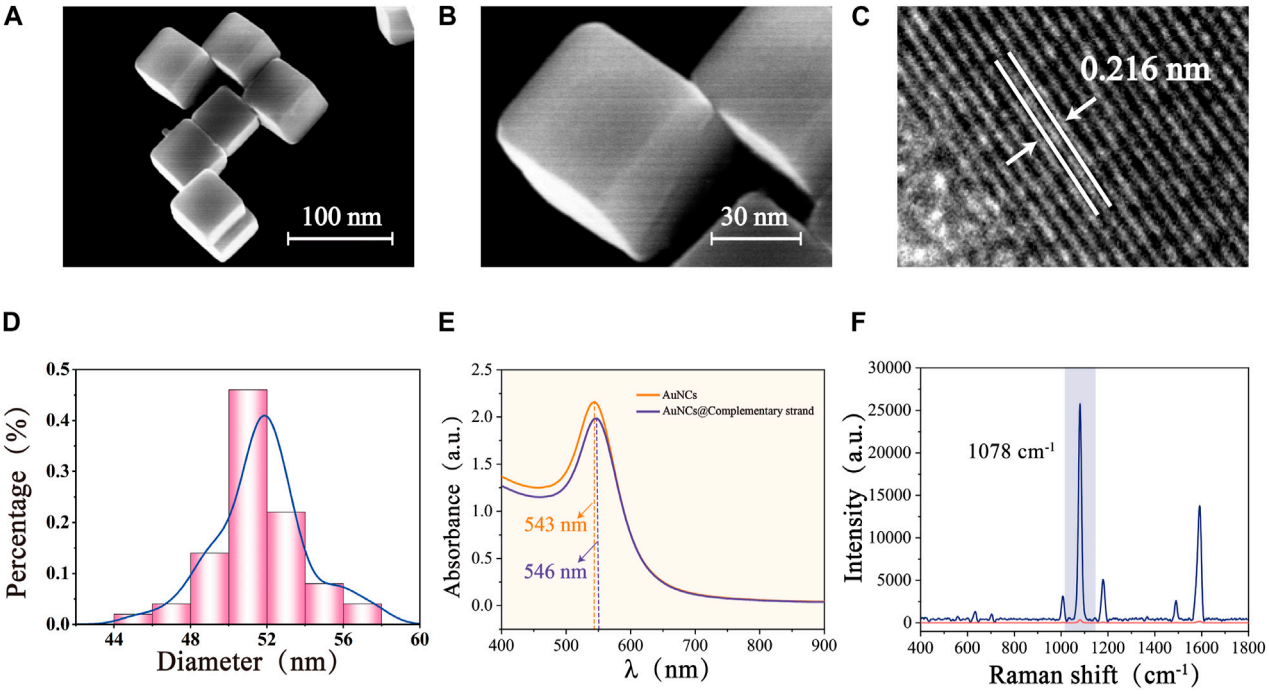

FIGURE 3
SEM images of AuNCs with different magnifications: **(A)** Low magnification, and **(B)** High magnification. **(C)** HRTEM image of AuNCs. **(D)** Size distribution of AuNCs. **(E)** UV-Vis-NIR spectra of AuNCs and AuNCs@ complementary strand. **(F)** SERS spectra of pure 4-MBA (1×10^{-2} M) and 4-MBA-labelled Au- AuNCs (1×10^{-7} M).

acid (AA), Mercaptobenzoic acid (4-MBA), Absolute ethanol, 6-Mercapto-1-hexanol (6-MCH), Vincristine, Oncovin (VCR), and polystyrene sphere (PS) suspension were all purchased from Sinopharm Chemical Reagent Suzhou Co. Sulfur hexa-fluoride (SF_6) etching gas from Wuhan NewRead Specialty Gases Co. Glycerin, Phosphate buffer, and the whole protein extraction kit were purchased from China Solaibo Co. Australian Fetal Bovine Serum was purchased from Thermo Fisher Scientific (China) Co. Antibodies to Vimentin, E-Cadherin, N-Cadherin, C-Reactive Protein, Ki67, and ACTIN were purchased from Beijing Boosun Biotechnology Co. BSA, paraformaldehyde, PBS, trypsin, FPS, and DMEM were purchased from Gibco; Antibody dilution, BCA protein concentration kit, penicillin-streptomycin solution were purchased from China Biyuntian Biotechnology Co. Ultrapure water is obtained through Milli-Q purifiers (resistivity>18 MΩ cm); GES-1 cells were obtained from the School of Clinical Medicine of Yangzhou University; Table 1 shows the DNA sequences utilised in this work, which were bought from Shanghai Sangong Biological Engineering Co.

2.2 Instrumentation

S-4800 II Field emission scanning electron microscope (SEM, Hitachi, Japan); Tecnai G2 F30 Field emission transmission electron microscope (TEM, FEI, United States); Cary UV-5000 Ultraviolet absorption spectrometer (Agilent, United States); InVia Reflex microscopic Raman spectrometer (Renishaw, United Kingdom); DXR3xi Raman imaging microscope (Thermo Fisher, United States).

2.3 Fabrication of functionalized Au/Si CCA

Au/Si CCA is fabricated by PS colloidal sphere template-assisted reactive ion etching (RIE) process and combined with magnetron sputtering deposition technique. Firstly, a layer of tightly stacked PS colloidal spheres was laid flat on a silicon wafer with an area of 5 × 5 cm by the Langmuir-Blodgett (L-B) film method, which was placed in an oven at 70°C for 20 min, so that the colloidal sphere template could be in close contact with the silicon wafer. Subsequent etching of PS colloidal sphere template-covered wafers in RIE machine using SF_6 plasma (Power 120 W, gas flow rate 50 sccm). After 150 s of etching, highly ordered arrays of silicon cones were formed, with PS colloidal spheres at the top that shrank residually after etching. Notably, a cap-like Au layer was deposited on the PS colloidal spheres at the top of the silicon cone arrays using a magnetron sputtering apparatus at a sputtering rate of 1 nm/s and finally rinsed with ethanol and annealed for 2 h to remove the residual PS colloidal spheres.

2.4 Synthesis of AuNCs

First, mixing CTAB (7.5 mL, 0.2 mol/L), $HAuCl_4$ (0.5 mL, 0.01 mol/L), and 7.5 mL of ultrapure water in a clean beaker. The solution was stirred vigorously (900 rpm) at 30°C before adding ice $NaBH_4$ (1.2 mL, 0.01 mol/L), which was changed from colorless to brown after stirring was continued for 5 min. The solution was then allowed to stand at 30°C for 2 h. Thus, the Au seed solution was made. The prepared Au seed solution was diluted 100-fold and set aside.

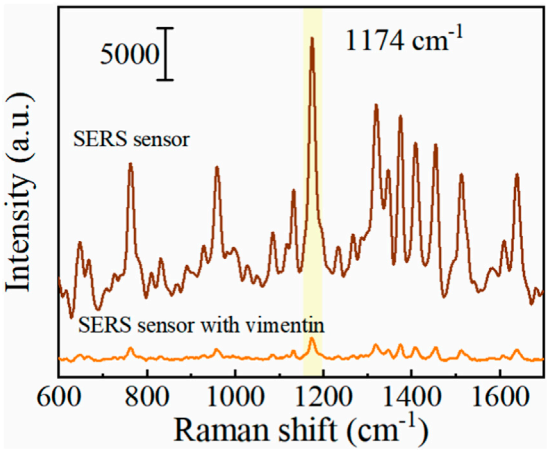

FIGURE 4
SERS spectra with and without the addition of Vimentin detection.

CTAB (7.2 mL, 0.1 mol/L), $HAuCl_4$ (0.18 mL, 0.01 mol/L), AA (2.7 mL, 0.1 mol/L), and 35 mL of ultrapure water were added sequentially in a beaker and stirred well. After 0.6 mL of the Au seed solution was added, the solution of Au octahedral seeds was obtained by vigorously stirring for 10 min and then left for 12 h. Subsequently, $HAuCl_4$ (0.75 mL, 0.025 mol/L) was added to the beaker, mixed well, and left for 2 h to obtain AuNCs. After centrifugation twice to remove the supernatant, it was dispersed in CTAB and stored.

2.5 Assembly of Vimentin SERS sensors

The Vimentin aptamer and complementary strand were assembled on Au/Si cap-cone arrays and AuNCs, respectively, referring to the freeze-thaw cycle assembly method of Lou et al. (Lou et al., 2011). In concrete terms, after the Vimentin aptamer and the complementary strand of the aptamer were added to ultrapure water to prepare the solutions (1 mmol/L), 100 mL of the aptamer solution with Au/Si cap-cone arrays were soaked in centrifuge tubes, and 150 mL of the aptamer complementary strand solution was mixed with AuNCs into centrifuge tubes. Then, they were placed in the refrigerator (−20°C) to freeze for 2 h simultaneously before being taken out to thaw. Next, 150 mL of 6-MCH was added to each centrifuge tube and reacted for 2 h. Afterward, the Vimentin aptamer product and the aptamer complementary strand product were water-bathed for 5 min at 95°C, and finally, the two were mixed and reacted for 4 h.

2.6 SERS testing

GES-1 cells were cultured in DMEM medium containing 10% FBS and dual antibodies (penicillin 100 U/mL, streptomycin 100 μg/mL) in an incubator at 37°C and 5% CO_2. Cellular proteins were extracted according to the instructions of the whole protein extraction kit and stored in a −80°C refrigerator. Vimentin protein was dissolved in aqueous glycerol solution and configured into a solution of 100 mg/mL, which was added to the protein extract, and the Vimentin protein spiked concentration was obtained by gradient dilution as 100 pg/mL–100 mg/mL. The droplet to be measured was added to the prepared SERS sensor for reaction for 10 min, then dried, and then SERS detected. The Raman spectrometer was used to select a 785 nm excitation laser with a laser power of 5 mW, and the acquisition time of each spectrum was 10 s.

3 Results and discussions

3.1 Characterization of Au/Si CCA

From the SEM images and localized magnified images of Au/Si CCA (Figures 2A, B), it could be seen that the Au/Si CCA from a perspective was arranged in an ordered periodicity with a period of 200 nm, corresponding to the diameter of the PS colloidal spheres. The single Au/Si cap-cone could visibly observe the Au cap structure, whose superior specific surface area could provide abundant binding sites for the immobilization of biomolecules, facilitating the follow-up functionalization. To assess the signal homogeneity of the Au/Si CCA, 4-mercaptobenzoic acid (4-MBA) was added dropwise as a Raman signal molecule on the surface of the arrays, which was then allowed to dry naturally before being subjected to SERS mapping, with the scanning range set to 50 × 40 mm. The color change was utilized to illustrate the SERS signal strength at 1,078 cm^{-1} (blue is the lowest, and red is the highest). Figure 2C reveals that the color distribution of the SERS-mapped image of the array is regular, indicating its excellent uniformity. Furthermore, 10 sites on the Au/Si CCA surface were randomly chosen for spectral detection to obtain the average spectra of the characteristic peak intensities at 1,078 cm^{-1} and 1,598 cm^{-1} (Figures 2D, E), and the obtained SERS spectra were similar in shape, with relative standard deviations (RSD) of the signal intensities at 1,078 cm^{-1} and 1,598 cm^{-1} being only 6.69% and 8.11%, demonstrating the benefits of the array's high uniformity. The enhancement factor (EF) of Au/Si CCA was calculated to be 9.2×10^8 based on the SERS spectra recorded in Figure 2F, employing the formula: $EF = (I_{SERS}/C_{SERS})/(I_R/C_R)$, where I_{SERS} and I_R were the intensities obtained from 4-MBA-modified Au/Si CCA and silicon wafers, respectively, at 1×10^{-8} M and 1×10^{-1} M concentrations. Next, to assess the reproducibility of the array, three batches of Au/Si CCA were prepared at different times and subjected to SERS measurements. The average spectrogram and histogram of the intensity of the characteristic peaks at 1,078 cm^{-1} are shown in Figure 2G, with only minor differences in the shapes and intensities of the spectra, indicating that the Au/Si CCA has decent reproducibility. The stability of the arrays is crucial for subsequent applications, so the same batch of Au/Si CCA was stored at room temperature for 1 day, 5 days, 10 days, and 15 days to evaluate the stability of the arrays (Figure 2H). As shown in Figure 2I, the SERS signal intensity collected with Au/Si CCA stored for different days was not significantly reduced, which only decreased by 7.9% after 15 days of storage compared to the first day, indicating that the Au/Si CCA prepared in this study is very stable.

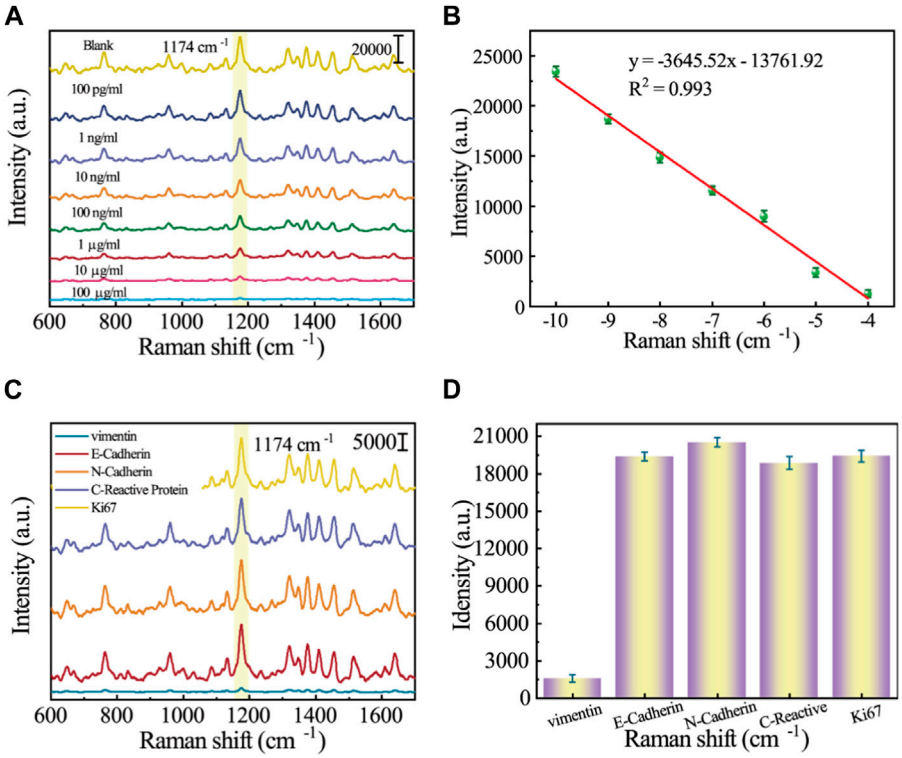

FIGURE 5
(A) SERS spectrograms of protein extracts of different Vimentin concentrations (100 pg/mL–100 mg/mL; **(B)** Corresponding calibration curve for SERS intensity at 1,174 cm^{-1}; **(C)** SERS spectrograms for specificity analysis of different proteins (E-Cadherin, N-Cadherin, C-Reactive Protein, Ki67, and Vimentin); **(D)** Corresponding histogram of SERS intensity at 1,174 cm^{-1}.

TABLE 2 Comparison for determination of different proteins using different methods.

Analyte	Method	Time (min)	LOD	Ref
Cancer antigen 125 (CA-125)	SERS-based lateral flow immunoassay	20	7.182 pg/mL	Xia et al. (2020)
Transferrin	Molecularly imprinted plasmonic nanosensor	15	10^{-8} mol/L	Lv et al. (2016)
Soluble epithermal growth factor receptor (sEGFR)	SERS	240	69.86 pg/mL	Li et al. (2018)
Vimentin	Bead-based immunoassay	30	0.1852 μg/mL	Fhied et al. (2014)
Vimentin	SERS	10	4.92 pg/mL	This work

3.2 Characterization of AuNCs

The low magnification SEM image (Figure 3A) showed that the AuNCs synthesized by the seed-mediated growth method were uniform in shape and size, well dispersed, and characterized by a typical cubic structure. The sharp vertices and edges could be clearly observed under high magnification (Figure 3B), which served as a carrier for a large number of "hot spots," ensuring excellent SERS enhancement. The HRTEM image of the sample (Figure 3C) obtained following centrifugation to remove a significant quantity of the protective CTAB and drop it onto a copper mesh, which demonstrated a lattice spacing of 0.216 nm for AuNCs, coinciding with the growth interface of gold crystals. As a precious metal nanomaterial, gold nanoparticles possessed excellent stability and superior optical properties. Figure 3D showed a histogram of the particle size of AuNCs (50 AuNCs were randomly selected by Nano Measurement software, and their particle sizes were counted individually), calculating that the average particle size of AuNCs and its deviation was 51.73 ± 3.775 nm, with good size uniformity. Meanwhile, UV-Vis-NIR spectra showed a visible absorption band at 543 nm. Due to the 5-FAM labelled complementary strand modification, the maximum wavelength peak of AuNCs has a slight redshift at 3 nm, along with a decrease in the SERS signal intensity (Figure 3E). This may be attributed to the reduction of interstitial hotspots between neighboring AuNCs due to the interaction between the 5-FAM labelled complementary strand and AuNCs. This result surfaces that the 5-FAM labelled complementary strand has been successfully modified to the surface of AuNCs. The computed EF of AuNCs modified with 4-MBA (1×10^{-7} M) was 7.3×10^{6}, demonstrating outstanding SERS performance and aiding in the Vimentin SERS detection (Figure 3F).

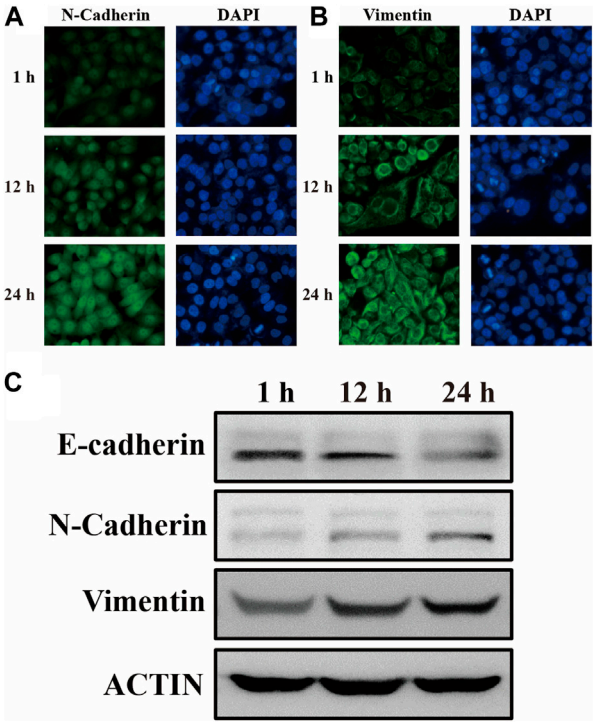

FIGURE 6
The expression of **(A)** N-calmodulin and **(B)** Vimentin in GES-1 cells after 1 h, 12 h, and 24 h of differentiation was examined by immunofluorescence labelling. **(C)** After 1 h, 12 h, and 24 h of GES-1 cell differentiation, immunoblotting revealed the expression of E-cadherin, N-cadherin, Vimentin, and ACTIN, which was used as an internal control.

3.3 Experimental feasibility analysis

In the absence of Vimentin, the Vimentin aptamers on the surface of Au/Si CCA arrays binds to the 5-FAM labelled complementary strand on the surface of AuNCs. The Au/Si CCA arrays and AuNCs together provide a SERS "hotspot" that enables the sensor to produce a large SERS enhancement effect. Moreover, the SERS reporter 5-FAM is located within and very close to the "hotspot," thus generating a 5-FAM SERS spectrum with very high signal intensity. Upon addition of Vimentin, the connection between the Au/Si CCA arrays and AuNCs is broken due to the fact that the Vimentin aptamer on the surface of the Au/Si CCA arrays reacts preferentially with Vimentin and partially de-hybridizes with their complementary strand. As a result, the "hot spot" part of the sensor disappears and the signal intensity of 5-FAM is reduced. The experimental results in Figure 4 are in perfect agreement with the principle. The SERS signal intensity after the addition of Vimentin is significantly lower than that without Vimentin, which indicates the feasibility of this method.

3.4 Sensitivity and specificity of the SERS assay

The sensitivity of the SERS sensor to low concentrations of analytes is an important factor in evaluating its performance. Protein extracts of different Vimentin concentrations (100 pg/mL–100 mg/mL) were taken for SERS detection. As can be obtained from Figure 5A, the SERS signal intensity at 1,174 cm^{-1} showed a clear dependence on Vimentin concentration, and remained slightly different from the blank group at Vimentin concentrations as low as 100 pg/mL. Figure 5B shows the scatter plot of its SERS signal intensity versus Vimentin concentration with a linear regression equation of $y = -3{,}645.52x - 13{,}761.92$ and $R^2 = 0.993$. The LOD of the SERS sensor for Vimentin is as low as 4.92 pg/mL. As shown in Table 2, this method has better detection performance compared to other methods, and was competitive in terms of detection time and LOD. Due to the presence of other proteins in protein extracts from GES-1 cells, in order to assess the specificity of the SERS sensor for Vimentin detection, we introduced different proteins in our experiments (E-Cadherin, N-Cadherin, C-Reactive Protein and Ki67). The results are shown in Figure 5C, where other interfering proteins were unable to affect the SERS spectra of 5-FAM, while Vimentin made the intensity of the spectra significantly weakened, suggesting that the SERS sensor reacts only with Vimentin. Figure 5D shows the corresponding SERS intensity

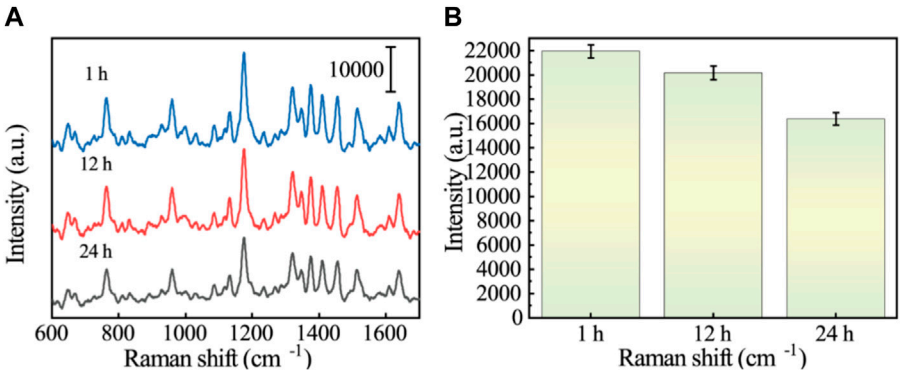

FIGURE 7
(A) SERS spectra of Vimentin in GES-1 cells after treatment with VCR for different times (1 h, 12 h, and 24 h). **(B)** Histogram corresponding to the SERS signal intensity at the 1,174 cm^{-1} characteristic peak.

at the characteristic peak of 1,174 cm^{-1}. The SERS intensity of Vimentin is much lower than that of other interfering proteins, and it is extremely resistant to interference.

3.5 EMT process confirmed by biological assay

It is widely known that epithelial cells undergo a phenotypic change during EMT by losing their cell polarity and epithelial markers like E-calmodulin and acquiring mesenchymal markers like N-calmodulin and Vimentin to create mesenchymal cells (Theys et al., 2011). Among them, the upregulation of vimentin expression was the theoretical basis for this experiment to realize the early discovery of the EMT process. In order to observe the phenotypic and functional changes of human gastric mucosal epithelial cells during EMT more intuitively, GES-1 cells were co-cultured with VCR (1 μg/mL) for 1 h, 12 h, and 24 h (Xue et al., 2012). Subsequently, cellular proteins were extracted and biological experiments were performed. As we expected, the mesenchymal markers N-calmodulin and Vimentin expression levels were progressively upregulated after the antitumor drug VCR induction, reaching the highest level after 24 h (Figures 6A, B). As a further confirmation, the expression levels of E-calmodulin, N-calmodulin, and Vimentin during EMT were validated by Western blotting, and the experimental results were consistent with the immunofluorescence results (Figure 6C). Hence, the results of biological experiments could effectively underpin the SERS spectral analysis of the actual samples in the subsequent EMT process.

3.6 Real sample analysis

GES-1 cells were co-cultured with VCR (1 μg/mL) for 1 h, 12 h, and 24 h, and protein was extracted. SERS sensors were used to detect changes in Vimentin during EMT. Figures 7A, B show the SERS spectra of GES-1 cells at different induction times. According to the images, we can see that at the characteristic peak at 1,174 cm^{-1}, the SERS intensity gradually decreases with the increase of induction time. The reason is that the Vimentin aptamer on the surface of Au/Si CCA arrays preferentially binds to the Vimentin reaction and partially dehybridizes with its complementary strand, resulting in the connection breakage between Au/Si CCA arrays and AuNCs. As a result, the "hot spot" part of the sensor disappears and the signal intensity of 5-FAM is reduced. Therefore, it can be analyzed that the content of GES-1 cells in VCR co-culture is increased by the content of cellular Vimentin. This demonstrates the reliability of the method.

4 Conclusion

In this study, a SERS sensor based on functionalized Au/Si CCA was prepared using the identity-release strategy for the ultra-sensitive detection of Vimentin during GC EMT. The periodic structure of the capture substrate (Au/Si CCA) in this study exhibited good SERS signal enhancement performance and homogeneity. The SERS sensor has a very low detection limit (4.92 pg/mL). The simultaneous identity-release strategy enables the proposed method to have excellent anti-interference ability. GES-1 cells were treated with VCR to simulate the EMT process of GC. The SERS detection results could fully reflect the change of Vimentin in the EMT process. Therefore, this SERS sensor provides a selective, reproducible, and ultra-sensitive method for Vimentin detection, which has great potential for future clinical applications for early GC screening.

Data availability statement

The original contributions presented in the study are included in the article/Supplementary material, further inquiries can be directed to the corresponding author.

Author contributions

LC: Data curation, Formal Analysis, Investigation, Methodology, Validation, Visualization, Writing–original draft, Writing–review and editing. JX: Data curation, Formal Analysis, Investigation, Methodology, Resources, Validation, Writing–original draft. HY: Methodology, Software, Validation, Writing–review and editing. QZ: Resources, Writing–review and editing. WY: Methodology, Software, Validation, Writing–review and editing. SM: Conceptualization, Methodology, Writing–review and editing. WL: Funding acquisition, Project administration, Supervision, Visualization, Writing–review and editing.

Funding

The author(s) declare financial support was received for the research, authorship, and/or publication of this article. This work was supported by the Guiding project of Jiangsu Commission of Health (Z2021049).

Conflict of interest

The authors declare that the research was conducted in the absence of any commercial or financial relationships that could be construed as a potential conflict of interest.

Publisher's note

References

An, L., and Liu, Y. (2023). ZNF460 mediates epithelial-mesenchymal transition to promote gastric cancer progression by transactivating APOC1 expression. *Exp. Cell Res.* 422 (2), 113452. doi:10.1016/j.yexcr.2022.113452

Arishi, W. A., Eissa, S., Al-Kattan, K., and Zourob, M. (2023). Aptamer-based label-free electrochemical biosensors for the diagnosis of sickle cell anemia. *Biosens. Bioelectron. X* 14, 100389. doi:10.1016/j.biosx.2023.100389

Brzozowa, M., Wyrobiec, G., Kołodziej, I., Sitarski, M., Matysiak, N., Reichman-Warmusz, E., et al. (2015). The aberrant overexpression of vimentin is linked to a more aggressive status in tumours of the gastrointestinal tract. *Gastroenterol. Review/Przegląd Gastroenterol.* 10 (1), 7–11. doi:10.5114/pg.2014.47502

Eddin, T. M. J., Nasr, S. M., Gupta, I., Zayed, H., and Al Moustafa, A.-E. (2023). *Helicobacter pylori* and epithelial mesenchymal transition in human gastric cancers: an update of the literature. *Heliyon* 9, e18945. doi:10.1016/j.heliyon.2023.e18945

Fhied, C., Kanangat, S., and Borgia, J. A. (2014). Development of a bead-based immunoassay to routinely measure vimentin autoantibodies in the clinical setting. *J. Immunol. Methods* 407, 9–14. doi:10.1016/j.jim.2014.03.011

Gao, S., Li, Q., Zhang, S., Sun, X., Zhou, H., Zhang, Y., et al. (2023). Peptide–nucleic acid aptamer pair biosensor for disease biomarker detection in clinical samples. *Chem. Eng. J.* 458, 141499. doi:10.1016/j.cej.2023.141499

Gu, Y., Li, Y., Qiu, H., Yang, Y., Wu, Q., Fan, X., et al. (2023). Recent progress on noble-free substrates for surface-enhanced Raman spectroscopy analysis. *Coord. Chem. Rev.* 497, 215425. doi:10.1016/j.ccr.2023.215425

Keyghobadi, N., Bagheri, V., Rahnamaii, M. S., and Sarab, G. A. (2022). Evaluation of hydroalcoholic extract effects of Ferula assa-foetida on expression change of EMT and CD44-related genes in gastric cancer stem cell. *Gene Rep.* 27, 101535. doi:10.1016/j.genrep.2022.101535

Li, J., Wang, J., Grewal, Y. S., Howard, C. B., Raftery, L. J., Mahler, S., et al. (2018). Multiplexed SERS detection of soluble cancer protein biomarkers with gold–silver alloy nanoboxes and nanoyeast single-chain variable fragments. *Anal. Chem.* 90 (17), 10377–10384. doi:10.1021/acs.analchem.8b02216

Li, Y., Liu, H., Chen, H., Shao, J., Su, F., Zhang, S., et al. (2020). DERL3 functions as a tumor suppressor in gastric cancer. *Comput. Biol. Chem.* 84, 107172. doi:10.1016/j.compbiolchem.2019.107172

Liang, D., Tang, S., Liu, L., Zhao, M., Ma, X., Zhao, Y., et al. (2023). Tanshinone I attenuates gastric precancerous lesions by inhibiting epithelial mesenchymal transition through the p38/STAT3 pathway. *Int. Immunopharmacol.* 124, 110902. doi:10.1016/j.intimp.2023.110902

Liu, R., Zhang, F., Sang, Y., Katouzian, I., Jafari, S. M., Wang, X., et al. (2022). Screening, identification, and application of nucleic acid aptamers applied in food safety biosensing. *Trends Food Sci. Technol.* 123, 355–375. doi:10.1016/j.tifs.2022.03.025

Liu, S., Deng, Z., Zhu, J., Ma, Z., Tuo, B., Li, T., et al. (2023). Gastric immune homeostasis imbalance: an important factor in the development of gastric mucosal diseases. *Biomed. Pharmacother.* 161, 114338. doi:10.1016/j.biopha.2023.114338

López-Lorente, Á. I. (2021). Recent developments on gold nanostructures for surface enhanced Raman spectroscopy: particle shape, substrates and analytical applications. A review. *Anal. Chim. Acta* 1168, 338474. doi:10.1016/j.aca.2021.338474

Lou, T., Wang, Y., Li, J., Peng, H., Xiong, H., and Chen, L. (2011). Rapid detection of melamine with 4-mercaptopyridine-modified gold nanoparticles by surface-enhanced Raman scattering. *Anal. Bioanal. Chem.* 401, 333–338. doi:10.1007/s00216-011-5067-3

Lv, Y., Qin, Y., Svec, F., and Tan, T. (2016). Molecularly imprinted plasmonic nanosensor for selective SERS detection of protein biomarkers. *Biosens. Bioelectron.* 80, 433–441. doi:10.1016/j.bios.2016.01.092

Mahmoudian, R. A., Akhlaghipour, I., Lotfi, M., Shahidsales, S., and Moghbeli, M. (2023). Circular RNAs as the pivotal regulators of epithelial-mesenchymal transition in gastrointestinal tumor cells. *Pathology-Research Pract.* 245, 154472. doi:10.1016/j.prp.2023.154472

Mita, H., Katoh, H., Komura, D., Kakiuchi, M., Abe, H., Rokutan, H., et al. (2023). Aberrant Cadherin11 expression predicts distant metastasis of gastric cancer. *Pathology-Research Pract.* 242, 154294. doi:10.1016/j.prp.2022.154294

Monster, J. L., Kemp, L. J., Gloerich, M., and van der Post, R. S. (2022). Diffuse gastric cancer: emerging mechanisms of tumor initiation and progression. *Biochimica Biophysica Acta (BBA)-Reviews Cancer* 1877 (3), 188719. doi:10.1016/j.bbcan.2022.188719

Munzar, J. D., Ng, A., and Juncker, D. (2018). Comprehensive profiling of the ligand binding landscapes of duplexed aptamer families reveals widespread induced fit. *Nat. Commun.* 9 (1), 343. doi:10.1038/s41467-017-02556-3

Munzar, J. D., Ng, A., and Juncker, D. (2019). Duplexed aptamers: history, design, theory, and application to biosensing. *Chem. Soc. Rev.* 48 (5), 1390–1419. doi:10.1039/C8CS00880A

Nourizad, A., Golmohammadi, S., Aghanejad, A., and Tohidkia, M. R. (2023). Recent trends in aptamer-based nanobiosensors for detection of vascular endothelial growth factors (VEGFs) biomarker: a review. *Environ. Res.* 236, 116726. doi:10.1016/j.envres.2023.116726

Nutiu, R., and Li, Y. (2003). Structure-switching signaling aptamers. *J. Am. Chem. Soc.* 125 (16), 4771–4778. doi:10.1021/ja028962o

Pan, H., Dong, Y., Gong, L., Zhai, J., Song, C., Ge, Z., et al. (2022). Sensing gastric cancer exosomes with MoS2-based SERS aptasensor. *Biosens. Bioelectron.* 215, 114553. doi:10.1016/j.bios.2022.114553

Park, H., Kwon, N., Park, G., Jang, M., Kwon, Y., Yoon, Y., et al. (2023). Fast-response electrochemical biosensor based on a truncated aptamer and MXene heterolayer for West Nile virus detection in human serum. *Bioelectrochemistry* 154, 108540. doi:10.1016/j.bioelechem.2023.108540

Park, J.-E., Lee, Y., and Nam, J.-M. (2018). Precisely shaped, uniformly formed gold nanocubes with ultrahigh reproducibility in single-particle scattering and surface-enhanced Raman scattering. *Nano Lett.* 18 (10), 6475–6482. doi:10.1021/acs.nanolett.8b02973

Paulin, D., Lilienbaum, A., Kardjian, S., Agbulut, O., and Li, Z. (2022). Vimentin: regulation and pathogenesis. *Biochimie* 197, 96–112. doi:10.1016/j.biochi.2022.02.003

Peng, Y., Ou, S., Li, M., Hu, Z., Zeng, Z., and Feng, N. (2023). An electrochemical biosensor based on network-like DNA nanoprobes for detection of mesenchymal circulating tumor cells. *Biosens. Bioelectron.* 238, 115564. doi:10.1016/j.bios.2023.115564

Pretzsch, E., Lampert, C., Bazhin, A. V., Link, H., Jacob, S., Guba, M., et al. (2022). EMT-related genes are unlikely to be involved in extracapsular growth of lymph node metastases in gastric cancer. *Pathology-Research Pract.* 229, 153688. doi:10.1016/j.prp.2021.153688

Sai, C. D., Nguyen, Q. H., Tran, T. N. A., Nguyen, T. B., Do, H. H., Vu, T. D., et al. (2023). CuO nanorods decorated gold nanostructures as an ultra-sensitive and recyclable SERS substrate. *Mater. Chem. Phys.* 293, 126962. doi:10.1016/j.matchemphys.2022.126962

Song, S., Wang, L., Li, J., Fan, C., and Zhao, J. (2008). Aptamer-based biosensors. *TrAC Trends Anal. Chem.* 27 (2), 108–117. doi:10.1016/j.trac.2007.12.004

Theys, J., Jutten, B., Habets, R., Paesmans, K., Groot, A. J., Lambin, P., et al. (2011). E-Cadherin loss associated with EMT promotes radioresistance in human tumor cells. *Radiotherapy Oncol.* 99 (3), 392–397. doi:10.1016/j.radonc.2011.05.044

Tuerk, C., and Gold, L. (1990). Systematic evolution of ligands by exponential enrichment: RNA ligands to bacteriophage T4 DNA polymerase. *Science* 249 (4968), 505–510. doi:10.1126/science.2200121

Wang, F., Yi, J., Chen, Y., Bai, X., Lu, C., Feng, S., et al. (2023). PRSS2 regulates EMT and metastasis via MMP-9 in gastric cancer. *Acta Histochem.* 125 (6), 152071. doi:10.1016/j.acthis.2023.152071

Wei, H., Yu, Y., Wang, Y., Ying, Z., Cheng, W., Tian, X., et al. (2020). Vimentin-targeting AIEgen-peptide conjugates: wash-free fluorescence detection of EMT-type cancer cells and tissues. *Sensors Actuators B Chem.* 321, 128536. doi:10.1016/j.snb.2020.128536

Wei, Y., Wang, T., Song, H., Tian, L., Lyu, G., Zhao, L., et al. (2017). CC motif chemokine 22 ligand (CCL22) concentrations in sera of gastric cancer patients are related to peritoneal metastasis and predict recurrence within one year after radical gastrectomy. *J. Surg. Res.* 211, 266–278. doi:10.1016/j.jss.2016.11.067

Xia, J., Liu, Y., Ran, M., Lu, W., Bi, L., Wang, Q., et al. (2020). The simultaneous detection of the squamous cell carcinoma antigen and cancer antigen 125 in the cervical cancer serum using nano-Ag polydopamine nanospheres in an SERS-based lateral flow immunoassay. *RSC Adv.* 10 (49), 29156–29170. doi:10.1039/d0ra05207h

Xue, Z., Yan, H., Li, J., Liang, S., Cai, X., Chen, X., et al. (2012). Identification of cancer stem cells in vincristine preconditioned SGC7901 gastric cancer cell line. *J. Cell. Biochem.* 113 (1), 302–312. doi:10.1002/jcb.23356

Yang, C., Liang, P., Tang, L., Zhou, Y., Cao, Y., Wu, Y., et al. (2018). Synergistic effects of semiconductor substrate and noble metal nano-particles on SERS effect both theoretical and experimental aspects. *Appl. Surf. Sci.* 436, 367–372. doi:10.1016/j.apsusc.2017.12.074

Yin, S., Chen, F.-f., and Yang, G.-f. (2018). Vimentin immunohistochemical expression as a prognostic factor in gastric cancer: a meta-analysis. *Pathology-Research Pract.* 214 (9), 1376–1380. doi:10.1016/j.prp.2018.07.014

Zhang, Q., Ma, R., Zhang, Y., Zhao, J., Wang, Y., and Xu, Z. (2023a). Dual-aptamer assisted ratiometric SERS biosensor for ultrasensitive and precise identification of breast cancer exosomes. *ACS Sensors* 8 (2), 875–883. doi:10.1021/acssensors.2c02587

Zhang, Z., Li, Y., Fan, L., Wang, B., Liu, W., Cui, J., et al. (2023b). LncRNA THUMPD3-AS1 promotes invasion and EMT in gastric cancer by regulating the miR-1297/BCAT1 pathway. *iScience* 26, 107673. doi:10.1016/j.isci.2023.107673

Zhao, J., Wang, J., Liu, Y., Han, X. X., Xu, B., Ozaki, Y., et al. (2022). Detection of prostate cancer biomarkers via a SERS-based aptasensor. *Biosens. Bioelectron.* 216, 114660. doi:10.1016/j.bios.2022.114660

frontiers | Frontiers in Bioengineering and Biotechnology

TYPE Original Research
PUBLISHED 08 December 2023
DOI 10.3389/fbioe.2023.1292136

OPEN ACCESS

EDITED BY
Yizhong Huang,
Nanyang Technological University,
Singapore

REVIEWED BY
Helena Maria Rodrigues Gonçalves,
Chemistry and Technology Network (REQUIMTE), Portugal
Forough Ghasemi,
Agricultural Biotechnology Research Institute of Iran, Iran

*CORRESPONDENCE
Qianchuang Sun,
sunqianchuang@jlu.edu.cn

RECEIVED 11 September 2023
ACCEPTED 27 November 2023
PUBLISHED 08 December 2023

CITATION
Kan B, Li L, Hou J, Liu S, Tian Z and Sun Q (2023), Eu-doped carbon quantum dot as a selective probe for visualizing and monitoring sulfite in biological systems. *Front. Bioeng. Biotechnol.* 11:1292136. doi: 10.3389/fbioe.2023.1292136

Eu-doped carbon quantum dot as a selective probe for visualizing and monitoring sulfite in biological systems

Bo Kan[1], Li Li[2], Jiaoyu Hou[3], Shuyan Liu[4], Zhenwei Tian[5] and Qianchuang Sun[6]*

[1]Department of Clinical Laboratory, The Second Hospital of Jilin University, Changchun, Jilin, China, [2]College of Chemistry, Jilin University, Changchun, Jilin, China, [3]Department of Geriatrics, The First Hospital of Jilin University, Changchun, Jilin, China, [4]Department of Ophthalmology, The Second Hospital of Jilin University, Changchun, Jilin, China, [5]Department of Emergency and Critical Care, The Second Hospital of Jilin University, Changchun, China, [6]Department of Anesthesiology, The Second Hospital of Jilin University, Changchun, Jilin, China

The detection of SO_3^{2-} in complex environments and its visualization at the cellular level are critical for understanding its role in biological processes. In this study, we developed an Eu-doped long-wavelength fluorescent carbon quantum dot (CD2) and investigated the detection mechanism, interference effects and cellular imaging applications of the fluorescent probe CD2. The results show that the addition of SO_3^{2-} induces an electronic rearrangement that restores CD2 to its original structure, leading to a rapid increase in fluorescence intensity. Selectivity experiments showed that CD2 has excellent selectivity to SO_3^{2-}, with minimal interference from common anions. In addition, CD2 shows good biocompatibility for cellular imaging applications, as evidenced by the high cell viability observed in HeLa cells. Using confocal microscopy, we detected a significant enhancement of red fluorescence in HeLa cells after addition of exogenous SO_3^{2-}, demonstrating the potential of CD2 as a probe for monitoring cellular SO_3^{2-} levels. These findings highlight the promise of CD2 as a selective SO_3^{2-} detection probe in complex environments and its utility in cellular imaging studies. Further studies are necessary to fully exploit the potential of CD2 in various biological and biomedical applications.

KEYWORDS

fluorescent probe, selectivity, cellular imaging, sulfite detection, biocompatibility

1 Introduction

The detection of intracellular sulfite ions (SO_3^{2-}) is of great significance in the field of biomedical engineering (Tian et al., 2013; Wang et al., 2019; Li Q. et al., 2023). These ions play a critical role in various cellular processes and provide valuable insights into cell function and health. Accurate measurement of sulfite ions is crucial for disease diagnosis, drug development, and understanding the impact of environmental factors on cellular function (Maiti, 2022; Săcărescu et al., 2023).

Within cells, sulfite ions are generated through the oxidation of sulfur-containing amino acids, including cysteine and methionine. These ions are involved in critical intracellular processes such as protein folding, enzyme regulation, and antioxidant defense mechanisms

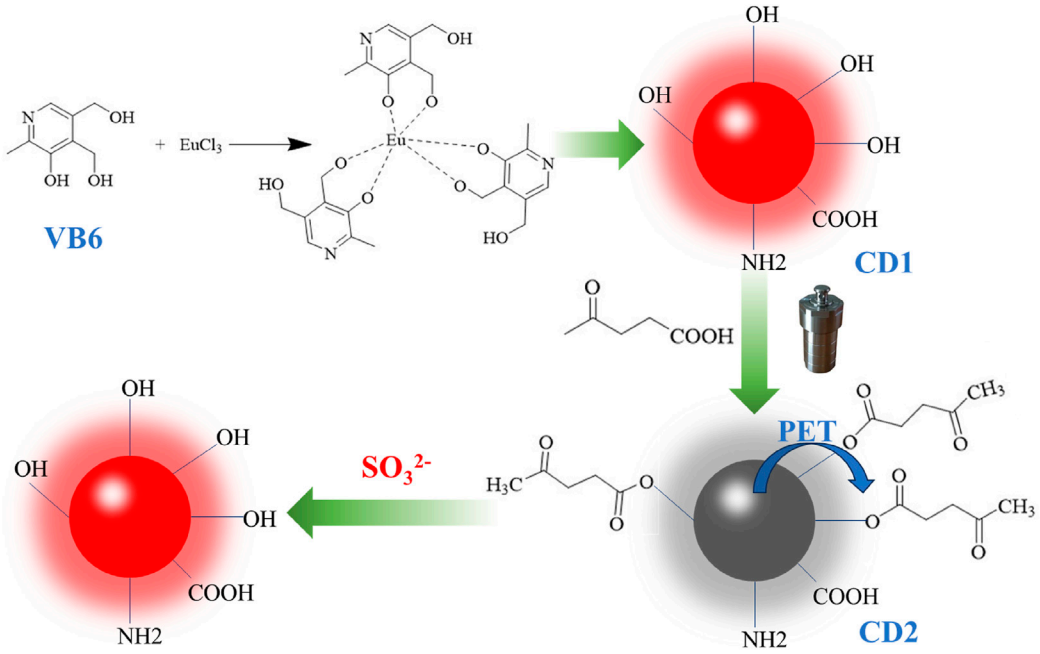

SCHEME 1
The demonstration diagram of the preparation of carbon dots and the process of SO_3^{2-} detection.

(Buerman et al., 2021). By modulating cellular signaling pathways, sulfite ions influence gene expression and cellular responses to a wide range of stimuli.

Maintaining an appropriate balance of intracellular sulfite ions is essential for optimal cell health and functionality (Kimura et al., 2019). Imbalances in sulfite ion levels have been associated with the occurrence and progression of several diseases, including cardiovascular disorders, neurodegenerative diseases, and cancer (Zhang et al., 2004). Elevated sulfite concentrations can lead to oxidative stress and cell damage, as excess sulfite can react with reactive oxygen species (ROS) to form toxic compounds (Mitsuhashi et al., 2005). Conversely, abnormally low sulfite ion levels can disrupt cellular processes dependent on sulfite signaling, resulting in impaired antioxidant defenses and compromised cell function (Vincent et al., 2004).

Accurate measurement of intracellular sulfite ion concentrations is instrumental in biomedical research and applications. Sulfite ion detection enables the assessment of sulfite-related diseases, aids in diagnosis, and guides the development of targeted treatment approaches. Additionally, it provides a means to evaluate the impact of potential therapeutic compounds on sulfite-mediated signaling pathways, thereby contributing to advancements in drug development (Danışman et al., 2022; Guo et al., 2023).

Various techniques have been developed for the quantitative detection of intracellular sulfite ion levels (Zhang et al., 2016; Wang P. et al., 2021). Prominent examples include fluorescence-based detection methods (Fu et al., 2022), mass spectrometry analysis (Robbins et al., 2015), and electrochemical biosensors (Badihi-Mossberg et al., 2007). Fluorescent probes allow for real-time visualization and monitoring of sulfite ions within live cells, while mass spectrometry offers high sensitivity and accurate measurements. Electrochemical biosensors provide a simple and rapid detection method suitable for point-of-care applications.

In this study, we propose a novel approach for sulfite ion detection by synthesizing long-wavelength emission fluorescence carbon quantum dots (CD1). These CD1 dots, derived from pyridoxine (vitamin B6) as the carbon source and doped with Eu^{3+}, possess exceptional properties such as low toxicity, high biocompatibility, and intense fluorescence (Li et al., 2021; Wareing et al., 2021; Đorđević et al., 2022). To achieve sulfite ion detection, the CD1 dots are subjected to surface modification with pyruvic acid, which quenches their fluorescence through the photoinduced electron transfer (PET) effect (Sun et al., 2019; Allen et al., 2022), rendering them non-fluorescent (hereafter referred to as CD2). Upon reaction with sulfite ions, the removal of pyruvic acid from the surface of CD2 leads to a considerable fluorescence enhancement (Deng et al., 2019; Li W.-B. et al., 2023), enabling highly sensitive detection of sulfite ions (Scheme 1).

Accurate measurement of sulfite ions is vitally important for disease diagnosis, drug development, and understanding the influence of environmental factors on cellular function. The proposed synthesis of long-wavelength emission fluorescence carbon quantum dots, coupled with surface modification, presents a promising approach for achieving sensitive and reliable detection of sulfite ions.

2 Materials and methods

2.1 Materials and instrumentation

Pyridoxine, $EuCl_3$, Na_2SO_3 and other compounds were unpurified using commercially available standard chemicals. Deionized water used in the experiments was prepared in the laboratory.

Transmission electron microscopy (TEM) and high-resolution TEM (HRTEM) images of the CDs were recorded using a JEOL-

2100F. Fourier transform infrared spectra (FTIR) were obtained using a Nicolet IS-10 FTIR spectrophotometer (Thermo Fisher Scientific). Fourier transform infrared spectra (FTIR) were obtained using a Nicolet IS-10 FTIR spectrophotometer (Thermo Fisher). X-ray photoelectron spectroscopy (XPS) was performed using an X-ray photoelectron spectrometer (AXIS ULTRA DLD). UV-vis absorption spectra were tested on an Agilent Cary 300 Scan. The zeta potential and hydrodynamic size of the samples were determined using a Zetasizer Nano ZS-90 analyzer (Malvern Instruments). Absolute QY and lifetimes were determined using a FLS1000 instrument (Edinburgh Instruments). Fluorescence spectra were obtained using an F97 Pro fluorescence spectrophotometer. Cells were imaged using a Leica TCS-SP8 confocal microscope.

2.2 Preparation of the CD1 and CD2

0.5 g of pyridoxine and 0.1 g of EuCl3 were dissolved in 40 mL of deionized water and sonicated for 10 min, then the solution was transferred to a 100 mL Teflon-lined stainless-steel autoclave. CD1 solution was obtained after cooling. To the CD1 solution 0.3 g of pyruvic acid was added, stirred well and returned to the reactor for secondary heating for 4 h (130°C). After cooling to room temperature, the reaction product was eluted with a mixture of dichloromethane and methanol (10:1) to give a bright red liquid CD2, which was dried by rotary evaporator. The dried solid was stored at 4°C in a dark place for future characterization and use.

2.3 Detection of SO_3^{2-}

The fluorescence spectra of the samples were recorded after adding different concentrations of SO_3^{2-} (1–25 μM) to the CD2 solution at 20 μg/mL.

2.4 Cytotoxicity assays and cell targeting

The cytotoxicity of CD2 was tested using WST-1. HeLa cells were cultured in 96-well plates at 10^4 cells per well. The culture medium consisted of 10% FBS, 100 U/mL penicillin-streptomycin solution and 90% RPMI 1640 medium. After 24 h of incubation, the medium was removed, fresh complete medium containing different concentrations of CD2 (dissolved in DMSO, 5 mg/mL) was added, and the cells were incubated for another 24 h. Finally, the medium was removed, and the cells were rinsed three times with PBS, and the viability of the cells was assessed by the WST-1 assay. Absorption was recorded for all plates using a microplate reader with a wavelength of 450 nm.

To assess the ability of CD2 to detect intracellular SO_3^{2-}, HeLa cells were seeded into 35-mm glass-bottomed Petri dishes and cultured at 37°C in a humidified environment with 5% CO_2. After 24 h of incubation, the initial medium was removed, and then 20 μg/mL of CD2 was added with 2 mL of fresh medium for another 6 h. An additional 25 μM of SO_3^{2-} was added to the control experiments. Then, after rinsing the cells three times with PBS, the fluorescence images of the samples were observed using a laser fluorescence confocal microscope.

3 Results and discussion

3.1 Preparation and characterization of the CDs

CD1 was synthesized through a hydrothermal reaction using VB6 as the carbon source and Eu^{3+} as the dopant. CD1 possesses hydroxyl groups on its surface, which can be easily reacted with pyruvic acid through a two-step hydrothermal process. By utilizing the photoinduced electron transfer (PET) effect, the fluorescence of CD1 can be quenched. TEM analysis (Figure 1A) revealed that CD1 exhibited a regular spherical structure with a uniform size and single dispersion in water. The individual particle diameter was determined to be approximately 8 nm, which was further confirmed by DLS measurements (Figure 1B).

The infrared spectrum of CD1 (Figure 1C) exhibited several characteristic peaks. The peak at around 750 cm^{-1} originated from the stretching vibration of Eu-O bonds, indicating the successful doping of Eu^{3+} into the CD1 structure. The peak at 1,240 cm^{-1} represented the stretching vibration of C=O and N-C=O bonds, while the peak at 1,396 cm^{-1} was attributed to the stretching vibration of C-N bonds and the bending vibration of N-O bonds. The peak at 1716 cm^{-1} indicated the presence of the C=C-CO bending vibration, suggesting the existence of conjugated olefin or aromatic ketone structures in CD1. The peak at 2,992 cm^{-1} represented the stretching vibration of C-H bonds and alkynyl groups. The peak at 3,423 cm^{-1} corresponded to the stretching vibration of O-H and N-H bonds, indicating the presence of hydroxyl and amino groups in CD1. X-ray photoelectron spectroscopy (XPS) analysis (Figure 1D) confirmed that CD1 primarily consisted of carbon (C), nitrogen (N), and oxygen (O), with a small amount of Eu (atomic percentage of 0.22%). Furthermore, energy-dispersive X-ray spectroscopy (EDS) elemental analysis (Figure 1E) provided additional confirmation that CD1 was composed of C, N, O, and Eu elements.

Overall, the results demonstrate the successful synthesis of CD1 with a well-defined structure and composition. The incorporation of Eu^{3+} as a dopant and the surface modification with pyruvic acid provide CD1 with favorable properties for sulfite ion detection.

3.2 Optical properties of carbon dots

The optical properties of the carbon dots are depicted in Figure 2. CD1 shows absorption throughout the visible light range, with a shoulder peak around 470 nm. Its emission peak is located at 650 nm, with an optimal excitation peak at 580 nm. In contrast, CD2 exhibits nearly no fluorescence, with emission intensity even less than 1/50th of CD1's. Thus, CD1 displays bright red fluorescence under excitation, while CD2 exhibits minimal fluorescence (shown in the top left corner of the image). This indicates that the reaction of pyruvic acid with CD1 through the secondary hydrothermal process leads to the quenching of its fluorescence.

The significant contrast in fluorescence between CD1 and CD2 provides the basis for the detection of sulfite ions. The presence of sulfite ions can cause the removal of pyruvic acid from the surface of CD2, restoring its fluorescence. This fluorescence enhancement can be utilized for sensitive and selective detection of sulfite ions. The changes in the optical properties of the carbon dots upon interaction with sulfite ions will allow for the quantification of sulfite ion concentrations in various biological and environmental samples.

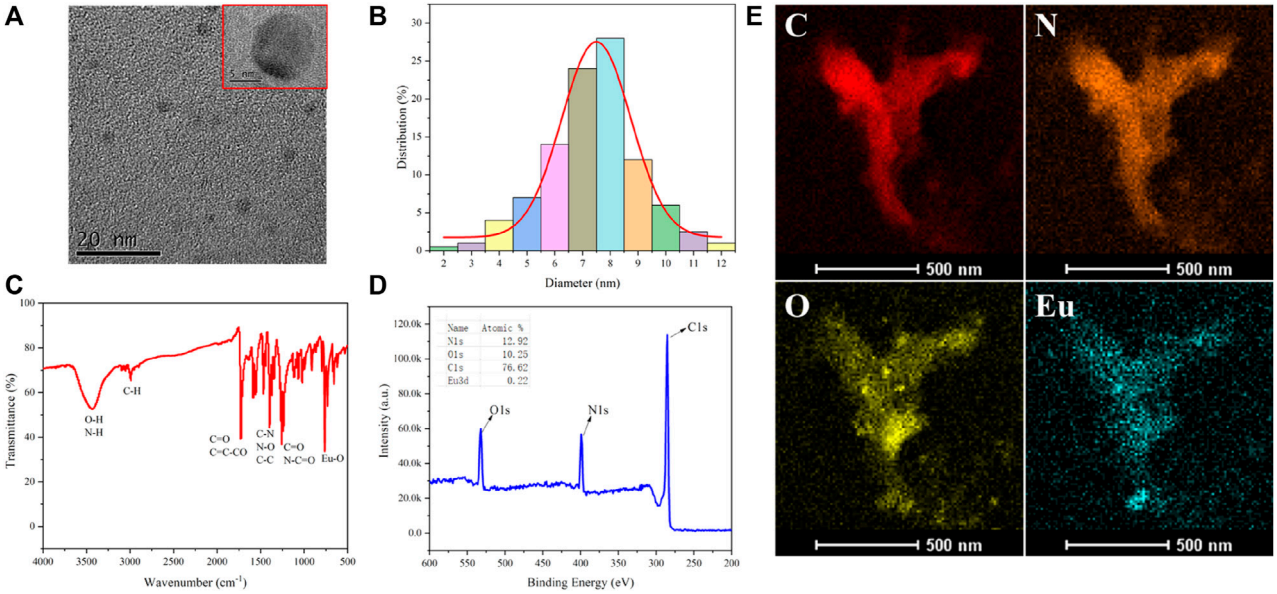

FIGURE 1
(A) TEM picture of CD1; **(B)** DLS particle size distribution; **(C)** IR spectra; **(D)** XPS analysis; **(E)** EDS elemental analysis.

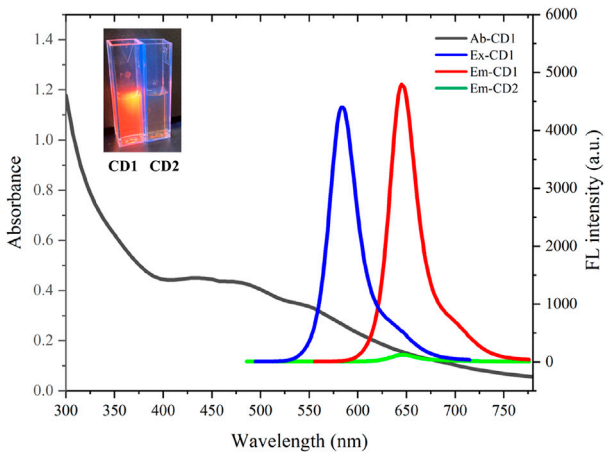

FIGURE 2
Absorption (black line), excitation (blue line) and emission (red line) spectra of CD1; emission (green line) of CD2.

3.3 Detection of SO_3^{2-} in solution

The fluorescence-quenched CD2 has been utilized for highly sensitive detection of SO_3^{2-}. A certain concentration of CD2 aqueous solution (20 μg/mL) was prepared, and different concentrations of SO_3^{2-} (ranging from 1–25 μM) were added. As the concentration of SO_3^{2-}- increased, the fluorescence intensity of the solution rapidly intensified. Even with the addition of 5 μM SO_3^{2-}, the fluorescence intensity increased by more than six times. When 25 μM SO_3^{2-} was added, the intensity increase slowed down, eventually reaching over 30 times the initial intensity (Figure 3A).

The fluorescence of the CD2 solution enhanced almost instantaneously upon the addition of SO_3^{2-}, reaching stability within 2 min (Figure 3B). This indicates the high sensitivity of CD2 to SO_3^{2-} and its potential as a rapid detection probe. Figure 3C displays the relationship between SO_3^{2-} concentration and the fluorescence intensity of the CD2 solution. It shows good linearity within the range of 1–20 μM (R^2 = 0.998), following equation F/F_0—1 = 0.429 + 1.968x, where F represents the fluorescence intensity of the CD2 solution after the addition of SO_3^{2-}, and F_0 represents the initial fluorescence intensity of the CD2 solution.

To determine the limit of detection (LOD), the equation LOD = 3σ/S was used, in which σ is the standard deviation of the fluorescence intensity of the CD2 solution without the addition of SO_3^{2-}, and S is the slope of the fitting line. Based on this calculation, the LOD was estimated to be approximately 0.15 μM, which is lower than both electrochemical and colorimetric methods, and at the same level as other fluorescent probes (Table 1). And the limit of quantification (LOQ) was calculated as 0.5 μM.

Meanwhile, the effect of pH on the detection process was considered. The probe CD2 itself is almost non-fluorescent at different pH values, and the detection of sulfites remains stable in the pH range of 7.0–10.0 (Figure 3D). The pH values of human sulfite metabolism sites are mainly between 7.0 and 8.5 (e.g., brain 7.1, heart 7.0–7.4, bile 7.8, liver 7.2, blood 7.3–7.45, pancreatic secretion 8.0–8.3, and bone 7.4) (Hashim et al., 2011; Yue et al., 2017), and therefore, CD2 is almost sufficient for the detection.

These results suggest that the quenching and recovery of fluorescence in CD2 can be effectively applied for the sensitive and selective detection of sulfite ions in solution. The high sensitivity, rapid response, and low limit of detection make CD2 a promising candidate for sulfite ion detection in various applications.

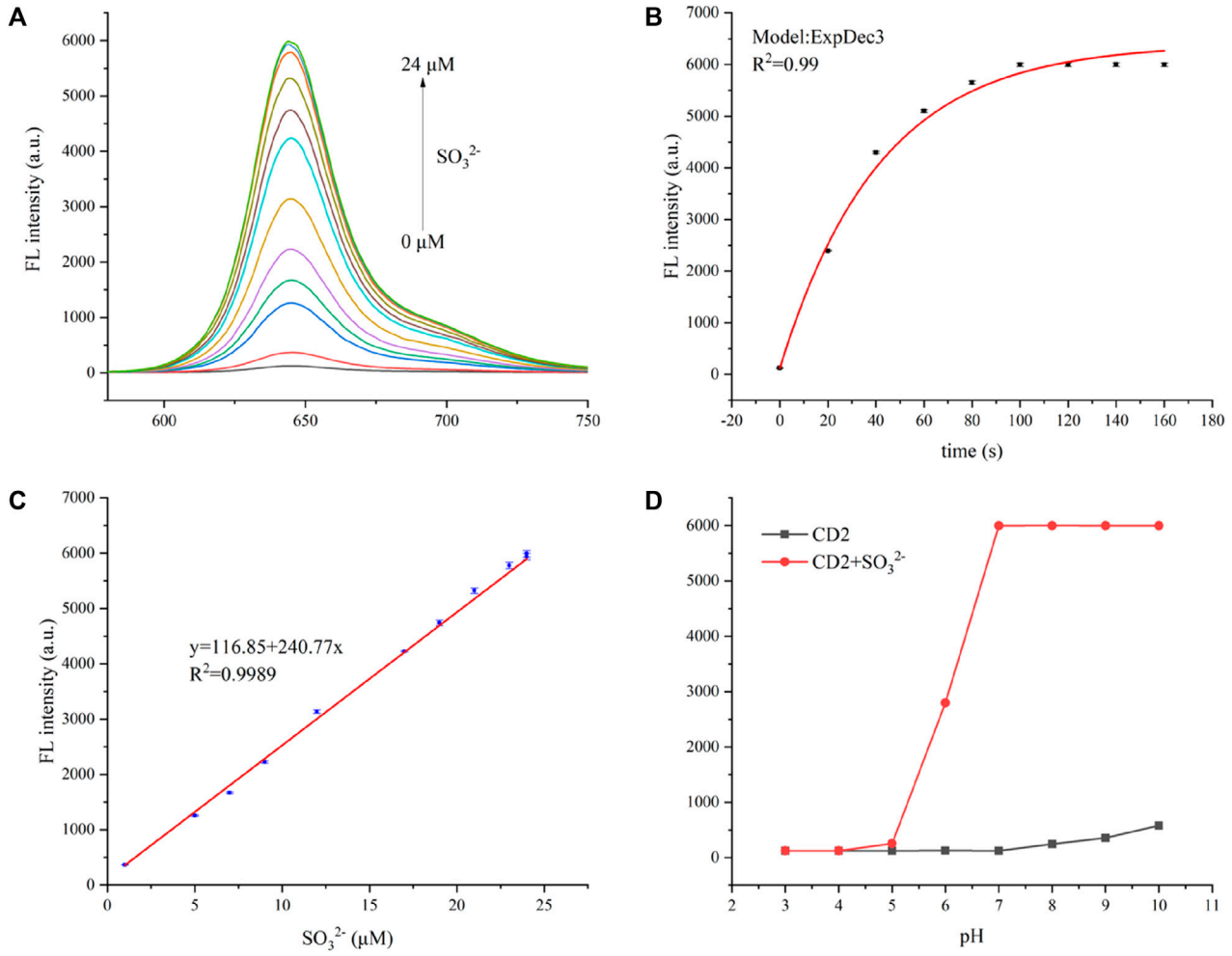

FIGURE 3
(A) Fluorescent spectra of the CD2 solution with the addition of different concentrations of SO_3^{2-} at an excitation wavelength of 580 nm. **(B)** Time-dependent fluorescence intensity spectra of CD2 (20 μg/mL) at 650 nm in the presence of SO_3^{2-} (25 μM). **(C)** The linear relationship between (F0/F−1) and the concentration of SO_3^{2-} over the range of 1–25 μM. **(D)** The fluorescence intensity of CD2 (20 μg/mL) at 650 nm in the absence and presence of SO_3^{2-} (25 μM) in various pH conditions (3.0–10.0). Incubation temperature: 37°C.

TABLE 1 Comparison with existing SO_3^{2-} detection methods.

Materials	Method	Linear range	LOD (μM)	References
Nanostructured copper-salen film	electrochemical sensor	4–69 μM	1.2	Dadamos and Teixeira (2009)
Ag_2O nanoparticles	colorimetric detection	100–500 μM	10	Lu et al. (2015)
rhodamine-derivated probe	fluorescent	0–80 μM	0.6	Wang et al. (2021a)
ratiometric fluorescent probe	fluorescent	0–100 μM	0.57	Venkatachalam et al. (2020)
Carbon dots	fluorescent	0–25 μM	0.15	This work

3.4 Mechanisms for the detection of SO_3^{2-}

To gain insight into the detection mechanism of SO_3^{2-}, we conducted tests on the particle size (Figures 4A, B) and surface potential (Figure 4C) of the solution before and after the reaction. Upon the addition of SO_3^{2-}, the particle size of CD2 decreased from approximately 18 nm to around 10 nm, which is close to the average particle size of CD1. Additionally, the surface potential increased from +0.69 mV to +3.58 mV. These observations provide valuable information for proposing a possible detection mechanism for SO_3^{2-} (Figure 4D).

In the two-step hydrothermal method, pyruvic acid is chemically modified onto the surface of CD1 through an ester linkage, resulting in the formation of CD2. The fluorescence of CD2 is quenched due to the photoinduced electron transfer (PET) effect. Upon the addition of SO_3^{2-}

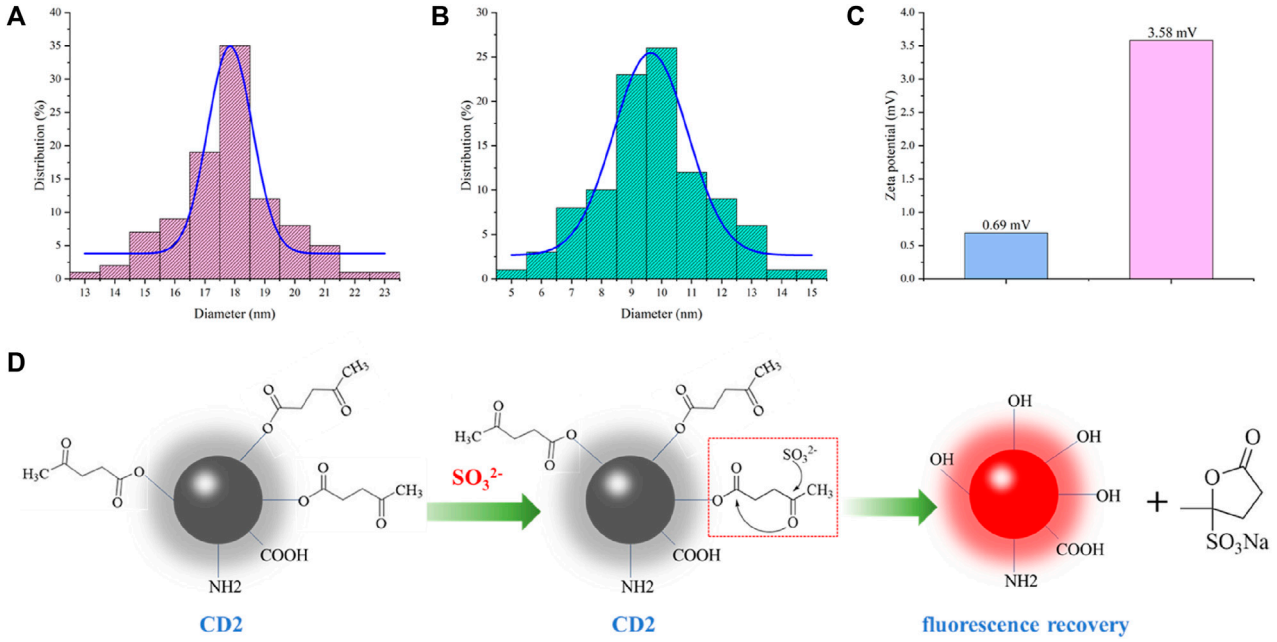

FIGURE 4
(A) Particle size of CD2 before addition of SO_3^{2-}; **(B)** Particle size of CD2 after addition of SO_3^{2-}; **(C)** Zeta potential of CD2 before and after addition of SO_3^{2-}; **(D)** Predicted detection mechanism.

to the CD2 solution, the oxygen atom in SO_3^{2-} interacts with the aldehyde group of pyruvic acid. This interaction leads to electron rearrangement and the formation of a transition state involving the oxygen atom on the carbonyl carbon of the ester moiety. Finally, the transition state decomposes, breaking the ester bond and generating a sulfonate-substituted furanone derivative. As a result, CD2 is restored to the structure of CD1, and the fluorescence intensity rapidly increases.

Further investigations are necessary to fully understand the detailed mechanism of SO_3^{2-} detection using CD2. Nevertheless, these preliminary findings provide important insights and a plausible explanation for the observed fluorescence enhancement upon the addition of SO_3^{2-} in the CD2 solution.

3.5 Interference experiments

To assess the interference of other ions in the detection process of SO_3^{2-}, we conducted experiments to test the effects of commonly encountered anions, such as Cl^-, I^-, NO^{3-}, HCO^{3-}, SO_4^{2-}, AcO^-, CN^-, and $H_2PO_4^-$, on the fluorescence of the CD2 solution. Figure 5 illustrates the results obtained.

Upon adding 25 μM of Na^+, K^+, NH_4^+, Cl^-, I^-, NO^{3-}, HCO^{3-}, SO_4^{2-}, and $H_2PO_4^-$ individually, the fluorescence intensity of the CD2 solution remained almost unchanged. Most of common cations and anions do not interfere with the detection, consistent with other research (Wang K. et al., 2021). Only CN^- and AcO^- caused a slight increase in fluorescence intensity, approximately three times higher. However, when comparing this increase to the 30-fold amplification observed with SO_3^{2-}, it is negligible.

These findings indicate that CD2 exhibits exceptional selectivity for SO_3^{2-}. The lack of interference from commonly encountered anions suggests that the detection of SO_3^{2-} in complex environments holds promising potential for various applications.

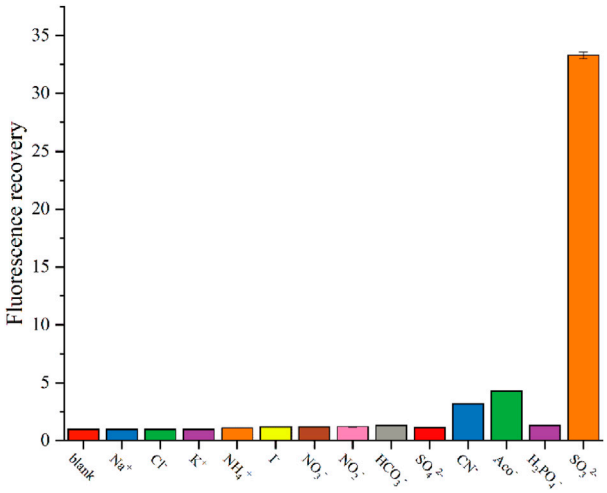

FIGURE 5
Change in fluorescence intensity of CD2 solution after addition of interfering substances.

3.6 Toxicity assays and cellular imaging applications of CD2

To assess the feasibility of using CD2 for cell imaging, a cell viability assay was conducted using the WST-1 reagent. The results

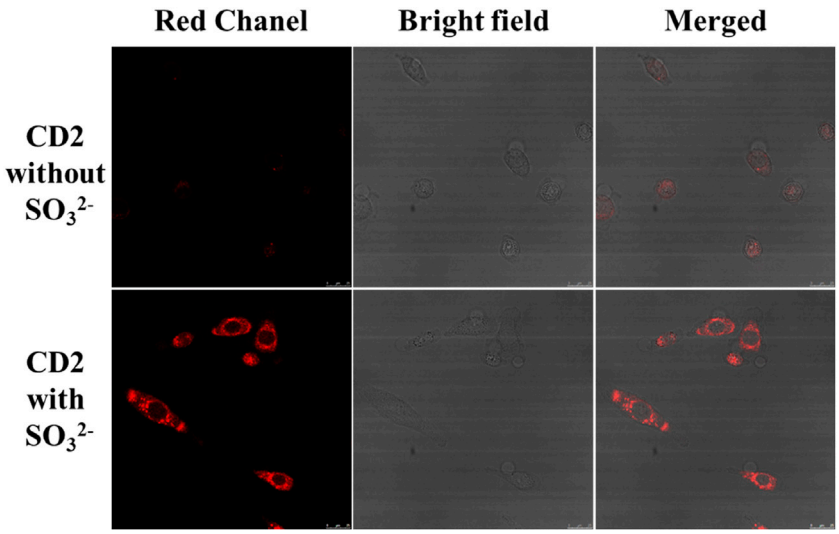

FIGURE 6
Changes in fluorescence intensity of HeLa cells before and after addition of SO_3^{2-} (scale bar: 25 μm).

demonstrated that the cell viability of HeLa cells remained above 90% when different concentrations of CD2 (ranging from 0 to 100 μg/mL) were added. This indicates that CD2 exhibits good biocompatibility for cell imaging purposes.

Subsequently, the potential application of CD2 in cell imaging was further explored using a Leica SP8 confocal microscope. The fluorescence changes of CD2 were studied at the cellular level by introducing exogenous SO_3^{2-} into HeLa cells. Figure 6 illustrates the results obtained. As shown, a significant enhancement of red fluorescence was observed in HeLa cells following the addition of 20 μM of SO_3^{2-}. This observation suggests that CD2 can effectively detect the level of SO_3^{2-} in HeLa cells and has the potential to serve as a probe for cellular imaging applications.

These findings demonstrate the potential of CD2 for cellular imaging and highlight its ability to detect and monitor the levels of SO_3^{2-} in living cells.

4 Conclusion

In conclusion, our study investigated the detection mechanism, interference effects, and potential applications of CD2 in the detection of SO_3^{2-}. The results indicated that CD2 exhibits a promising detection mechanism, where the addition of SO_3^{2-} leads to electron rearrangement and the restoration of CD2 to its original structure, resulting in a rapid increase in fluorescence intensity. Furthermore, CD2 demonstrated excellent selectivity for SO_3^{2-}, as evidenced by minimal interference from commonly encountered anions.

To assess the biocompatibility of CD2 for cellular imaging applications, a cell viability assay exhibited high cell viability when different concentrations of CD2 were added to HeLa cells. This indicates that CD2 has good biocompatibility for cell imaging. Moreover, cellular imaging experiments using CD2 revealed its ability to detect and monitor the levels of SO_3^{2-} in living cells, as manifested by a significant enhancement of red fluorescence upon the addition of exogenous SO_3^{2-} to HeLa cells.

Overall, these findings suggest that CD2 holds promise as a probe for the detection of SO_3^{2-} in complex environments and its application in cellular imaging. Further studies are warranted to explore the full potential and specific mechanisms of CD2 in various applications.

Data availability statement

The original contributions presented in the study are included in the article/supplementary material, further inquiries can be directed to the corresponding author.

Author contributions

BK: Conceptualization, Formal Analysis, Investigation, Methodology, Writing–original draft, Writing–review and editing. LL: Conceptualization, Formal Analysis, Writing–review and editing. JH: Conceptualization, Data curation, Formal Analysis, Writing–original draft. SL: Data curation, Formal Analysis, Software, Writing–original draft. ZT: Data curation, Investigation, Software, Writing–original draft. QS: Conceptualization, Funding acquisition, Writing–review and editing.

Funding

The authors declare that no financial support was received for the research, authorship, and/or publication of this article.

Conflict of interest

The authors declare that the research was conducted in the absence of any commercial or financial relationships that could be construed as a potential conflict of interest.

Publisher's note

References

Allen, A. R., Noten, E. A., and Stephenson, C. R. J. (2022). Aryl transfer strategies mediated by photoinduced electron transfer. *Chem. Rev.* 122 (2), 2695–2751. doi:10.1021/acs.chemrev.1c00388

Badihi-Mossberg, M., Buchner, V., and Rishpon, J. (2007). Electrochemical biosensors for pollutants in the environment. *Electroanal. Environ.* 19 (19-20), 2015–2028. doi:10.1002/elan.200703946

Buerman, E. C., Worobo, R. W., and Padilla-Zakour, O. I. (2021). High pressure processing of heat and pressure resistant fungi as affected by pH, water activity, sulfites, and dimethyl dicarbonate in a diluted apple juice concentrate. *Food Control.* 120, 107551. doi:10.1016/j.foodcont.2020.107551

Dadamos, T. R. L., and Teixeira, M. F. S. (2009). Electrochemical sensor for sulfite determination based on a nanostructured copper-salen film modified electrode. *Electrochimica Acta* 54 (19), 4552–4558. doi:10.1016/j.electacta.2009.03.045

Danışman, B., Akçay, G., Gökçek-Saraç, Ç., Kantar, D., Aslan, M., and Derin, N. (2022). The role of acetylcholine on the effects of different doses of sulfite in learning and memory. *Neurochem. Res.* 47 (11), 3331–3343. doi:10.1007/s11064-022-03684-z

Deng, K., Wang, L., Xia, Q., Liu, R., and Qu, J. (2019). A turn-on fluorescent chemosensor based on aggregation-induced emission for cyanide detection and its bioimaging applications. *Sensors Actuators B Chem.* 296, 126645. doi:10.1016/j.snb.2019.126645

Đorđević, L., Arcudi, F., Cacioppo, M., and Prato, M. (2022). A multifunctional chemical toolbox to engineer carbon dots for biomedical and energy applications. *Nat. Nanotechnol.* 17 (2), 112–130. doi:10.1038/s41565-021-01051-7

Fu, Y., Zhang, X., Liu, J., Qian, G., Xu, Z. P., and Zhang, R. (2022). Fluorescence detection and imaging of intracellular sulphite using a remote light activatable photochromic nanoprobe. *J. Mater. Chem. B* 10 (17), 3366–3374. doi:10.1039/D2TB00021K

Guo, J., Wang, W., Xie, S., Zhang, Y., Li, J., Xu, J., et al. (2023). Performance and mechanism of sulfite mediated oxidation of organic contaminants using iron(III) titanium oxide as catalyst. *J. Environ. Chem. Eng.* 11 (5), 110449. doi:10.1016/j.jece.2023.110449

Hashim, A. I., Zhang, X., Wojtkowiak, J. W., Martinez, G. V., and Gillies, R. J. (2011). Imaging pH and metastasis. *Imaging P. H. metastasis* 24 (6), 582–591. doi:10.1002/nbm.1644

Kimura, Y., Shibuya, N., and Kimura, H. (2019). Sulfite protects neurons from oxidative stress. *Br. J. Pharmacol.* 176 (4), 571–582. doi:10.1111/bph.14373

Li, Q., Yan, S., Song, H., Su, Y., Sun, M., and Lv, Y. (2023a). A simple and stable chemiluminescence resonance energy transfer system based on Ce(IV)-MOFs for detection of sulfite. *Sensors Actuators B Chem.* 376, 132990. doi:10.1016/j.snb.2022.132990

Li, S., Li, L., Tu, H., Zhang, H., Silvester, D. S., Banks, C. E., et al. (2021). The development of carbon dots: from the perspective of materials chemistry. *Mater. Today* 51, 188–207. doi:10.1016/j.mattod.2021.07.028

Li, W.-B., Wu, Y., Zhong, X.-F., Chen, X.-H., Liang, G., Ye, J.-W., et al. (2023b). Fluorescence enhancement of a metal-organic framework for ultra-efficient detection of trace benzene vapor. *Angew. Chem. Int. Ed. Engl.* 62 (24), e202303500. doi:10.1002/anie.202303500

Lu, W., Shu, J., Wang, Z., Huang, N., and Song, W. (2015). The intrinsic oxidase-like activity of Ag2O nanoparticles and its application for colorimetric detection of sulfite. *Mater. Lett.* 154, 33–36. doi:10.1016/j.matlet.2015.04.051

Maiti, B. K. (2022). Cross-talk between (Hydrogen)Sulfite and metalloproteins: impact on human health. *Impact Hum. Health* 28 (23), e202104342. doi:10.1002/chem.202104342

Mitsuhashi, H., Yamashita, S., Ikeuchi, H., Kuroiwa, T., Kaneko, Y., Hiromura, K., et al. (2005). Oxidative stress-dependent conversion of hydrogen sulfide to sulfite by activated neutrophils. *Shock* 24 (6), 529–534. doi:10.1097/01.shk.0000183393.83272.de

Robbins, K. S., Shah, R., MacMahon, S., and de Jager, L. S. (2015). Development of a liquid chromatography–tandem mass spectrometry method for the determination of sulfite in food. *J. Agric. Food Chem.* 63 (21), 5126–5132. doi:10.1021/jf505525z

Săcărescu, L., Chibac-Scutaru, A.-L., Roman, G., Săcărescu, G., and Simionescu, M. (2023). Selective detection of metal ions, sulfites and glutathione with fluorescent pyrazolines: a review. *Environ. Chem. Lett.* 21 (1), 561–596. doi:10.1007/s10311-022-01508-8

Sun, W., Li, M., Fan, J., and Peng, X. (2019). Activity-based sensing and theranostic probes based on photoinduced electron transfer. *Accounts Chem. Res.* 52 (10), 2818–2831. doi:10.1021/acs.accounts.9b00340

Tian, H., Qian, J., Sun, Q., Bai, H., and Zhang, W. (2013). Colorimetric and ratiometric fluorescent detection of sulfite in water via cationic surfactant-promoted addition of sulfite to α,β-unsaturated ketone. *Anal. Chim. Acta* 788, 165–170. doi:10.1016/j.aca.2013.06.020

Venkatachalam, K., Asaithambi, G., Rajasekaran, D., and Periasamy, V. (2020). A novel ratiometric fluorescent probe for "naked-eye" detection of sulfite ion: applications in detection of biological SO32− ions in food and live cells. *Spectrochimica Acta Part A Mol. Biomol. Spectrosc.* 228, 117788. doi:10.1016/j.saa.2019.117788

Vincent, A. S., Lim, B. G., Tan, J., Whiteman, M., Cheung, N. S., Halliwell, B., et al. (2004). Sulfite-mediated oxidative stress in kidney cells. *Kidney Int.* 65 (2), 393–402. doi:10.1111/j.1523-1755.2004.00391.x

Wang, K., Wang, W., Chen, S.-Y., Guo, J.-C., Li, J.-H., Yang, Y.-S., et al. (2021a). A novel Near-Infrared rhodamine-derivated turn-on fluorescence probe for sensing SO32− detection and their bio-imaging *in vitro* and *in vivo*. *Dyes Pigments* 188, 109229. doi:10.1016/j.dyepig.2021.109229

Wang, K.-N., Zhu, Y., Xing, M., Cao, D., Guan, R., Zhao, S., et al. (2019). Two-photon fluorescence probes for mitochondria imaging and detection of sulfite/bisulfite in living cells. *Sensors Actuators B Chem.* 295, 215–222. doi:10.1016/j.snb.2019.05.077

Wang, P., Zhang, Y., Liu, Y., Pang, X., Liu, P., Dong, W.-F., et al. (2021b). Starch-based carbon dots for nitrite and sulfite detection. *Front. Chem.* 9, 782238. doi:10.3389/fchem.2021.782238

Wareing, T. C., Gentile, P., and Phan, A. N. (2021). Biomass-based carbon dots: current development and future perspectives. *ACS Nano* 15 (10), 15471–15501. doi:10.1021/acsnano.1c03886

Yue, Y., Huo, F., Lee, S., Yin, C., and Yoon, J. (2017). A review: the trend of progress about pH probes in cell application in recent years. *Analyst* 142 (1), 30–41. doi:10.1039/C6AN01942K

Zhang, L.-J., Wang, Z.-Y., Cao, X.-J., Liu, J.-T., and Zhao, B.-X. (2016). An effective ICT-based and ratiometric fluorescent probe for sensing sulfite. *Sensors Actuators B Chem.* 236, 741–748. doi:10.1016/j.snb.2016.06.055

Zhang, X., Vincent, A. S., Halliwell, B., and Wong, K. P. (2004). A mechanism of sulfite neurotoxicity: direct inhibition of glutamate dehydrogenase. *J. Biol. Chem.* 279 (41), 43035–43045. doi:10.1074/jbc.M402759200

frontiers | Frontiers in Bioengineering and Biotechnology

TYPE Original Research
PUBLISHED 08 February 2024
DOI 10.3389/fbioe.2024.1338920

OPEN ACCESS

EDITED BY
Kang Cui,
University of Jinan, China

REVIEWED BY
Forough Ghasemi,
Agricultural Biotechnology Research Institute of Iran, Iran
Javeed Mahmood,
King Abdullah University of Science and Technology, Saudi Arabia

*CORRESPONDENCE
Umar Nishan,
umarnishan85@gmail.com
Ke Chen,
chen_ke@swmu.edu.cn

RECEIVED 15 November 2023
ACCEPTED 29 January 2024
PUBLISHED 08 February 2024

CITATION
Nishan U, Zahra T, Badshah A, Muhammad N, Afridi S, Shah M, Khan N, Asad M, Ullah R, Ali EA and Chen K (2024), Colorimetric sensing of hydrogen peroxide using capped *Morus nigra*-sawdust deposited zinc oxide nanoparticles via *Trigonella foenum* extract.
Front. Bioeng. Biotechnol. 12:1338920.
doi: 10.3389/fbioe.2024.1338920

Colorimetric sensing of hydrogen peroxide using capped *Morus nigra*-sawdust deposited zinc oxide nanoparticles via *Trigonella foenum* extract

Umar Nishan[1]*, Tabassum Zahra[1], Amir Badshah[1], Nawshad Muhammad[2], Saifullah Afridi[1], Mohibullah Shah[3], Naeem Khan[1], Muhammad Asad[1], Riaz Ullah[4], Essam A. Ali[5] and Ke Chen[6]*

[1]Department of Chemistry, Kohat University of Science and Technology, Kohat, Pakistan, [2]Department of Dental Materials, Institute of Basic Medical Sciences Khyber Medical University, Peshawar, Pakistan, [3]Department of Biochemistry, Bahauddin Zakariya University, Multan, Pakistan, [4]Department of Pharmacognosy, College of Pharmacy, King Saud University, Riyadh, Saudi Arabia, [5]Department of Pharmaceutical Chemistry, College of Pharmacy, King Saud University Riyadh, Riyadh, Saudi Arabia, [6]Department of Infectious Diseases, The Affiliated Hospital of Southwest Medical University, Luzhou, China

Hydrogen peroxide (H_2O_2) is one of the main byproducts of most enzymatic reactions, and its detection is very important in disease conditions. Due to its essential role in healthcare, the food industry, and environmental research, accurate H_2O_2 determination is a prerequisite. In the present work, Morus nigra *sawdust deposited* zinc oxide (ZnO) nanoparticles (NPs) were synthesized by the use of Trigonella foenum extract via a hydrothermal process. The synthesized platform was characterized by various techniques, including UV-Vis, FTIR, XRD, SEM, EDX, etc. FTIR confirmed the presence of a Zn–O characteristic peak, and XRD showed the hexagonal phase of ZnO NPs with a 35 nm particle size. The EDX analysis confirmed the presence of Zn and O. SEM images showed that the as-prepared nanoparticles are distributed uniformly on the surface of sawdust. The proposed platform (acetic acid-capped ZnO NPs deposited sawdust) functions as a mimic enzyme for the detection of H_2O_2 in the presence of 3,3′,5,5′-tetramethylbenzidine (TMB) colorimetrically. To get the best results, many key parameters, such as the amount of sawdust-deposited nanoparticles, TMB concentration, pH, and incubation time were optimized. With a linear range of 0.001–0.360 μM and an R^2 value of 0.999, the proposed biosensor's 0.81 nM limit of quantification (LOQ) and 0.24 nM limit of detection (LOD) were predicted, respectively. The best response for the proposed biosensor was observed at pH 7, room temperature, and 5 min of incubation time. The acetic acid-capped sawdust deposited ZnO NPs biosensor was also used to detect H_2O_2 in blood serum samples of diabetic patients and suggest a suitable candidate for *in vitro* diagnostics and commercial purposes.

KEYWORDS

diabetes, cancer, TMB, hydrothermal process, colorimetric biosensing

1 Introduction

Hydrogen peroxide (H_2O_2) monitoring in diverse matrices has crucial roles in cell metabolism and has diverse applications in industrial processes (Zhang et al., 2018). H_2O_2 is used in medical diagnostics, clinical research and industrial sectors including textiles, paper, pharmaceuticals, food processing, cleaning, disinfection, etc (Patel et al., 2020). Additionally, in the biosystem, it regulates metabolic activity, cell apoptosis, immune cell activation, and different physiological processes (Miller et al., 2010). It serves as an oxidative agent, a stress marker, and a cell defensive agent. Similarly, it is an important biomarker for a variety of diseases and disorders, including cardiovascular, Alzheimer's, Parkinson's, diabetes, and neurodegenerative disorders (Rao and Balachandran, 2002). Furthermore, H_2O_2 is a byproduct of lactate, alcohol, glucose, glutamate, and cholesterol oxidases. In the past, different detection methods for H_2O_2 quantifications were applied. These include chemiluminescence (Irani-nezhad et al., 2019), chromatography (Nakashima et al., 1994), electrochemistry (Lee et al., 2016), fluorescence (Senthamizhan et al., 2016), electrochemical methods, etc (Chen et al., 2014). However, most of these approaches are toxic to living cells, thus making them ineffective for *in situ* H_2O_2 detection in biological materials. Besides, some of these techniques are time-consuming, expensive, and complex, restricting their application in laboratories with limited resources (Nishan et al., 2021a). Conversely, in comparison to other complex approaches, colorimetric methods for detecting H_2O_2 have been getting key attention nowadays due to their easy handling and low cost. The progress of colorimetric reactions can be monitored with the naked eye (Khaliq et al., 2023).

Cellulose is the main constituent of sawdust. It is one of the most abundant, natural, renewable, biocompatible, and environmentally

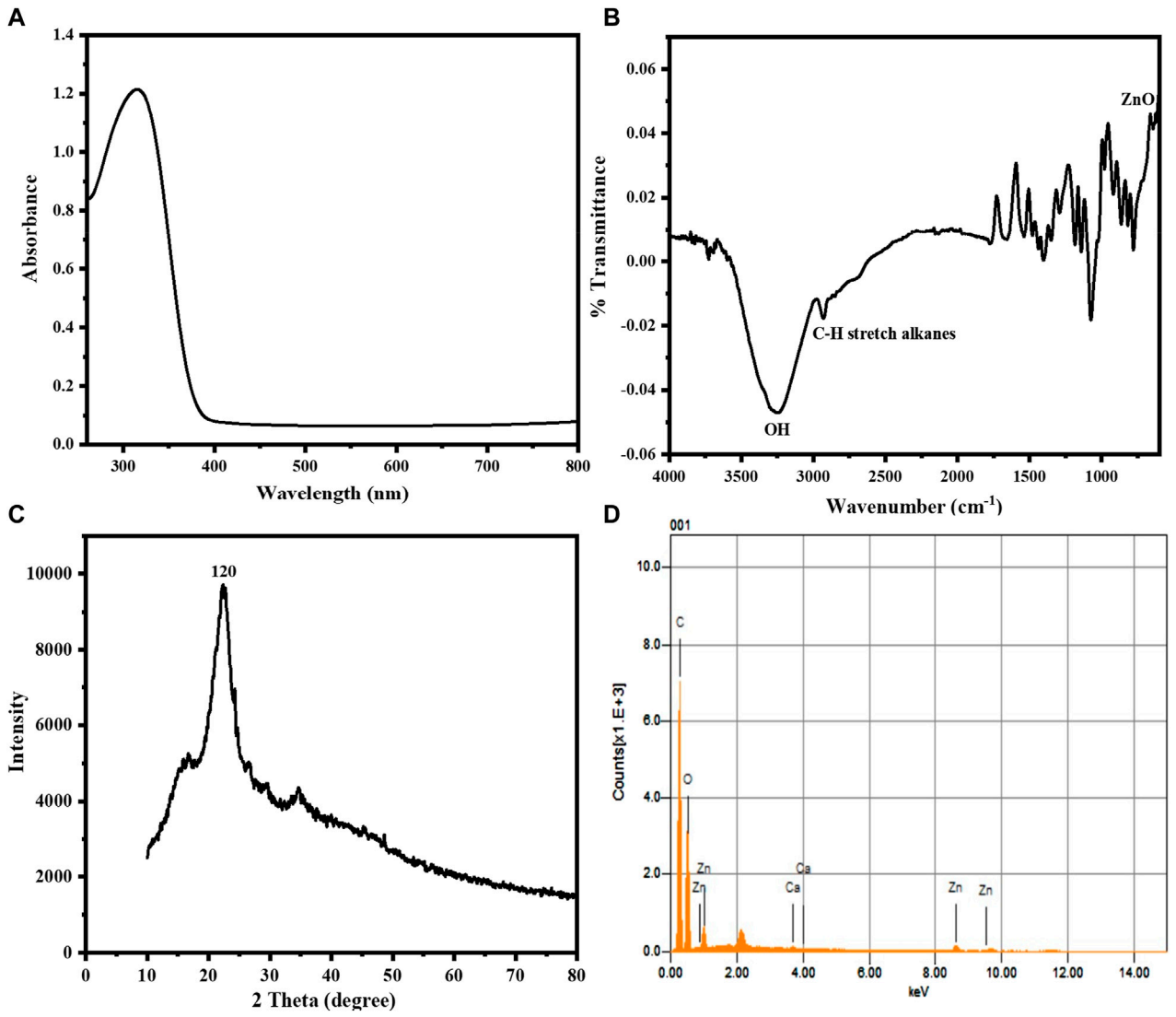

FIGURE 1
(A) UV-Vis absorption spectrum of the sawdust-deposited@ZnO NPs showing its characteristic surface Plasmon resonance peak at 320 nm. **(B)** FTIR spectrum of the synthesized sawdust-deposited@ZnO NPs showing the presence of a ZnO band. **(C)** XRD pattern of the synthesized sawdust-deposited@ZnO NPs, indicating the orthorhombic phase of ZnO. **(D)** EDX spectral analysis of the synthesized sawdust-deposited@ZnO showing the presence of C, Zn, and O.

TABLE 1 EDX elemental analysis of the synthesized sawdust-deposited@ZnO

Element	Weight %	Atomic %
C	49.90	58.45
O	46.95	40.71
Ca	0.17	0.06
Zn	3.64	0.78
Total	100.00	100.00

friendly macromolecules (Park et al., 2019). Cellulosic materials have adaptable surface characteristics, low cost, better mechanical properties, a higher aspect ratio, a lower density, a higher surface area, and a lower density. Cellulose-based sawdust has been utilized as a sacrificial porous template because it is non-edible, cheap, renewable, and readily available biomass (Khaliq et al., 2023).

Various nanomaterials, including positively charged gold nanoparticles (Jv et al., 2010), CuS nanoparticles (Dutta et al., 2013), graphene oxide (Song et al., 2010), ceria nanoparticles (Ornatska et al., 2011), cupric oxide nanoparticles (Chen et al., 2011), and $CoFe_2O_4$ NPs (Shi et al., 2011), have been found to exhibit peroxidase-like activity and are employed to detect H_2O_2 visually. Additionally, acetic acid-capped ZnO NPs are recyclable, highly stable, and efficient, have good sensing and catalytic capabilities, and have a tremendous potential to replace expensive noble metal NPs in biosensing. Because ZnO NPs have a large band gap (3.3 eV), they can be employed for UV luminescence at room temperature (Khranovskyy et al., 2012). Furthermore, ZnO NPs have a high isoelectric point (pI) of 9.5, allowing effective immobilization of enzymes with a low pI, i.e., ≤5 (Wei et al., 2010). ZnO NPs are also biocompatible, have the largest family of nanostructures, are crystalline, and have a high surface-to-volume ratio (Abou Chaaya et al., 2014).

In the present study, the hydrothermal method was used for the synthesis of *Morus nigra*-deposited ZnO NPs with the use of *Trigonella foenum* extract as a reductant. To further improve their sensing abilities, the synthesized NPs were capped with acetic acid. The oxidation of chromogenic substrate, i.e., TMB, by H_2O_2 in the presence of acetic acid-capped sawdust deposited@ZnO is being reported for the first time. The proposed platform is a new, simple, quick, highly sensitive, and selective approach for H_2O_2 detection. The amount of capped NPs, pH, TMB concentration, and incubation time were among the various reaction parameters that were adjusted to achieve the best performance out of the suggested

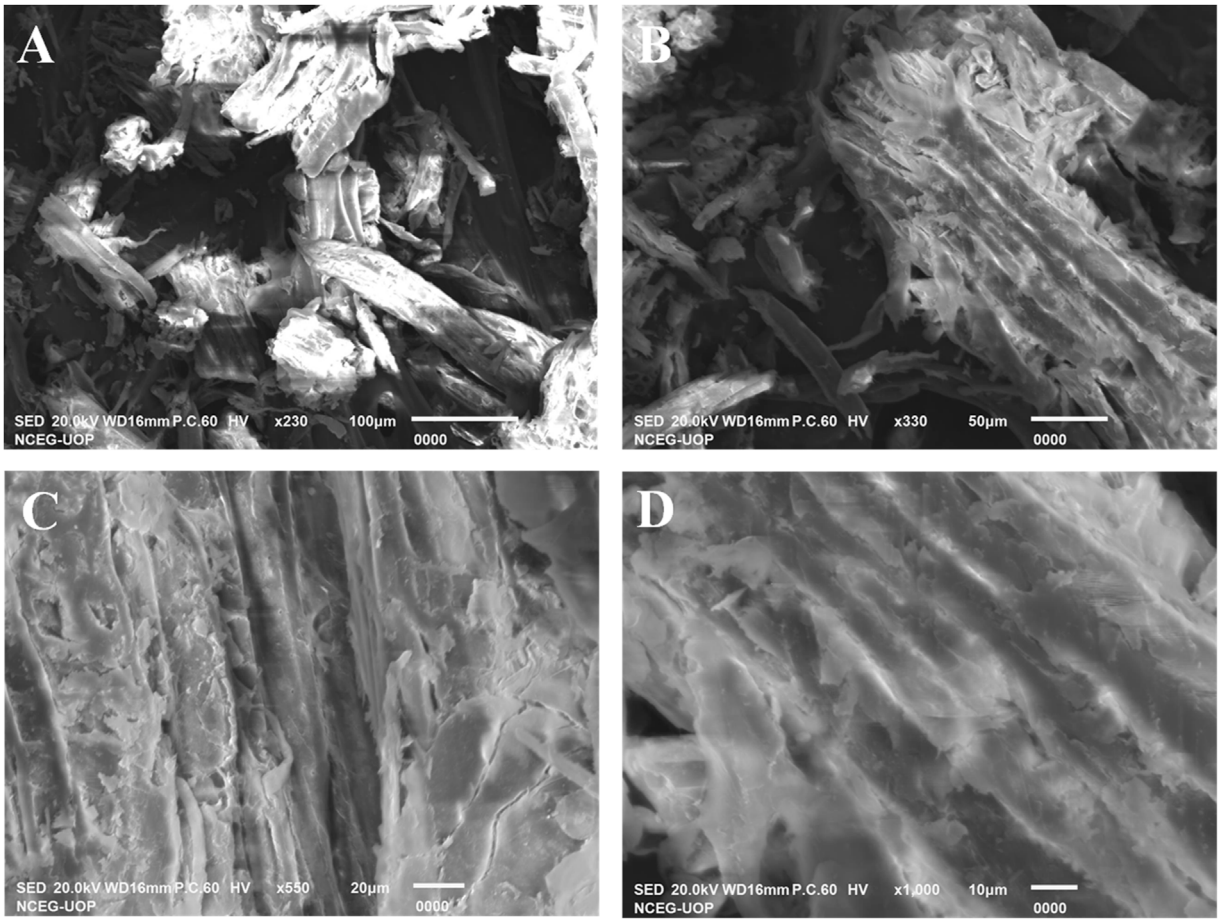

FIGURE 2
SEM images **(A–D)** were taken at different magnifications. The results depict that the nanoparticles are distributed uniformly over the surface of sawdust to enhance its catalytic activity.

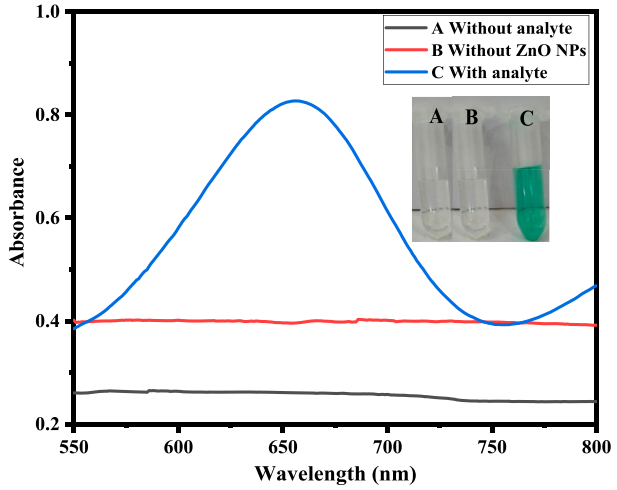

FIGURE 3
Shows sawdust-deposited@ZnO NPs-based H_2O_2 biosensing. It shows UV-Vis spectra of the solution containing capped sawdust-deposited@ZnO NPs (20 µL), PBS pH 7 (500 µL), TMB (18 mM: 150 µL), and H_2O_2 (0.360 µM: 100 µL). Spectra were obtained without H_2O_2 as well as in the presence of H_2O_2. The Figure shows the UV-Vis spectra of a peculiar solution. Curve A represents the reaction system without analyte, B represents the reaction in which sawdust was used without ZnO NPs. Curve C represents the colorimetric change and peak at 652 nm that occurred when H_2O_2 was introduced to the sawdust-deposited@ZnO NPs.

sensor. The sensitivity and selectivity were also investigated under the aforementioned optimum conditions. Finally, H_2O_2 levels were also measured in blood serum samples to testify to the fabricated platform.

2 Experimental procedure

2.1 Materials and reagents

In the entire experimental procedure, all chemicals used were of analytical grade, and no further purification was performed. Double-distilled water was used in the preparation of solutions. NaOH (97%), HCl (37%), acetic acid (97%), ascorbic acid (97%), urea (99.5%), and 3,3′,5,5′-tetramethylbenzidine (TMB) were procured from Daejung, South Korea. KGaA and H_2O_2 (35%) were purchased from Merck. The collection of blood serum was performed at a local lab close to the divisional teaching hospital in Kohat, KP, from three diabetic individuals. The serum was twice diluted with a PBS solution to decrease the complexity of the matrix, according to the earlier reports (Singh et al., 2022).

2.2 Instrumentation

Fourier transform infrared spectroscopy (FTIR, Nicolet 6,700, US) was used to find the characteristic peaks of the synthesized platform in the range of 4,000–500 cm^{-1}. The morphology of the synthesized NPs was confirmed using a scanning electron microscope (SEM) with INCAx-act Oxford Instruments (TESCAN VEGA (LMU)). X-ray diffraction was used to identify the phases of the produced ZnO NPs (JCPDS, file No. 04-0783). The absorption spectra were taken with a Shimadzu UV-Vis spectrophotometer (1,800, Japan).

2.3 Synthesis of Sawdust-deposited@ ZnO NPs

The green leaves of *T. foenum* were collected, washed with distilled water, and dried in sunlight for 4 days. The leaves were ground into a fine powder with the help of a blender. Extract was prepared in distilled water by suspending 5 g of leaf powder in 200 mL of distilled water on a hot plate with a magnetic stirrer (1,000 rpm) for 1 h at 65°C. The mixture was filtered, and the extract was poured into a beaker. One Gram of zinc acetate was dissolved in 50 mL of distilled water and placed on a hot plate. Subsequently, 50 mL of extract solution was added dropwise to the zinc acetate solution, and 1 g of sawdust from *M. nigra* was gradually added while stirring at 65°C for 4 h. The synthesized sawdust-deposited@ ZnO NPs solution was centrifuged for 15 min at 4,500 rpm to obtain solid material.

2.4 Capping of sawdust-deposited@ZnO NPs with acetic acid

The Sawdust-deposited@ZnO NPs were capped with an acetic acid solution such that 0.12 g of the mimic enzyme was mixed with 2 mL of acetic acid for 30 min through a mortar and pestle thoroughly. It resulted in the formation of a brown mixture that was placed in an Eppendorf tube for further use (Asad et al., 2022; Nishan et al., 2022).

2.5 Colorimetric sensing of H_2O_2

Capped sawdust-deposited@ZnO NPs (25 µL) were suspended in 500 µL phosphate buffer (pH 7), followed by the addition of 150 µL TMB solution (18 mM). Add 90 µL of H_2O_2 (0.360 µM) to the reaction mixture and incubate at room temperature for the colorimetric reaction. The absorption spectrum of the resultant solution was recorded using a UV-Vis spectrophotometer. Some experimental parameters, such as response time, pH, the amount of capped NPs, and the concentration of TMB solution, have been tuned up to achieve the best results of the proposed platform.

3 Results and discussion

3.1 Characterization of the sawdust-deposited@ZnO NPs

3.1.1 UV-vis spectroscopy

To investigate the optical characteristics of the sawdust-deposited@ZnO NPs, a UV-Visible spectrophotometer was used. The UV-Vis absorption spectrum of the synthesized sawdust-deposited@ZnO NPs with a peculiar absorption band at 320 nm

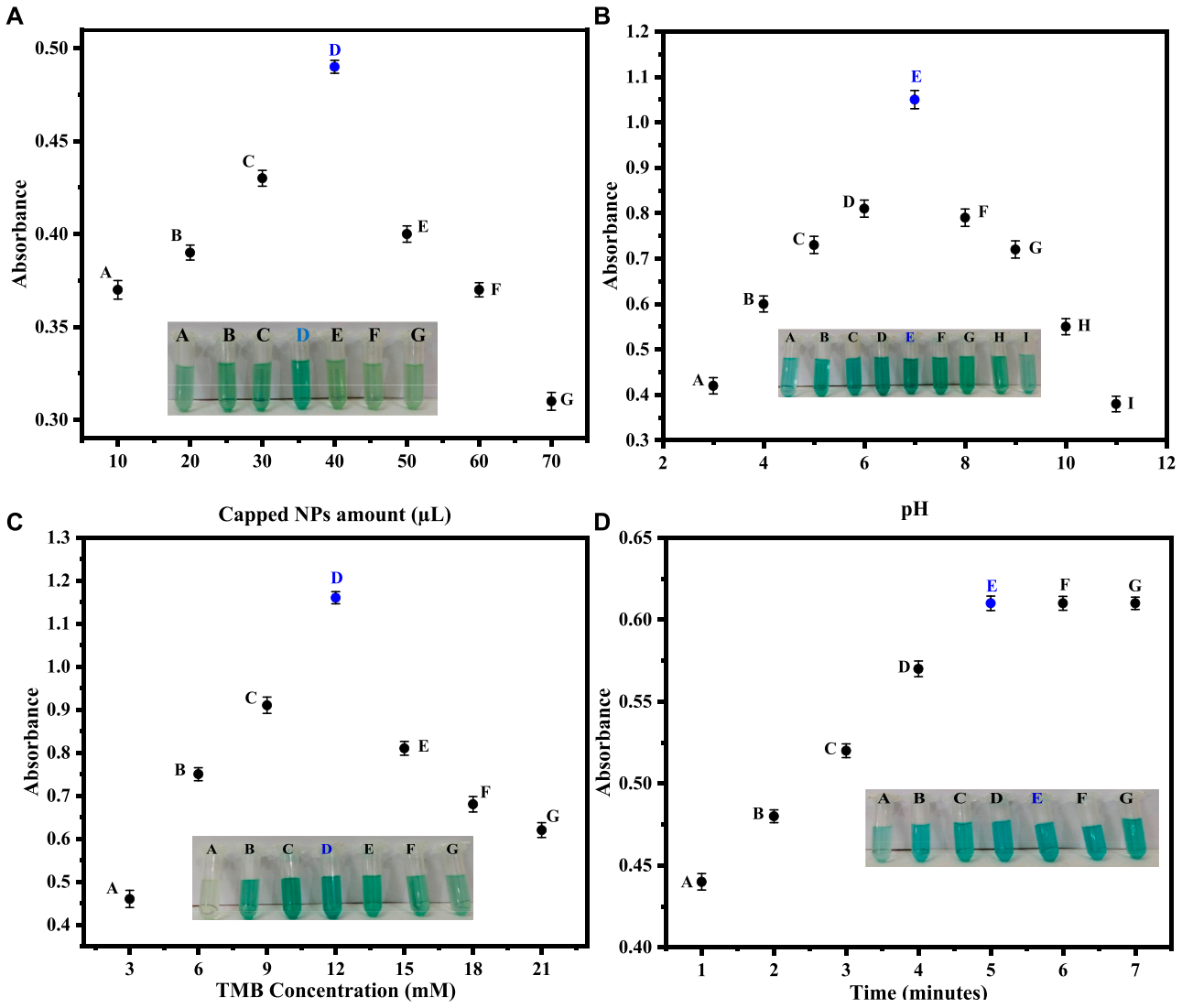

FIGURE 4
(A) Optimization of the capped sawdust-deposited@ZnO NPs [Reaction cond. PBS 500 µL (pH 7), TMB 150 µL (18 mM), H_2O_2 100 µL (0.360 µM). **(B)** Different pH optimizations for the proposed capped sawdust-deposited@ZnO NPs show the best colorimetric response at pH 7. [Reaction cond. Capping 20 µL, TMB 150 µL (18 mM), H_2O_2 100 µL (0.360 µM)]. **(C)** The optimization of TMB concentration of the capped sawdust-deposited@ZnO NPs [Reaction cond. Capping 40 µL, PBS 500 µL (pH 7), H_2O_2 100 µL (0.360 µM)]. **(D)** Reaction time optimization for the suggested capped sawdust-deposited@ZnO NPs [reaction cond. Capping 40 µL, PBS 500 µL (pH 7), TMB 150 µL (12 mM), H_2O_2 100 µL (0.360 µM)].

is shown in Figure 1A. The fact that ZnO has a considerable, sharp absorption implies that the nanoparticles distribution is monodispersed (Talam et al., 2012).

3.1.2 FTIR analysis of the sawdust-deposited@ZnO NPs

FTIR analysis in the range of 4,000–500 cm^{-1}, was used to determine the different functional groups found on the surface of the sawdust-deposited@ZnO NPs. The broad absorption band at 3,310 cm^{-1} indicates the presence of an OH group from the plant source on the surface of the synthesized platform. The peak around 2,950 cm^{-1} shows the C-H stretching vibration of the alkyl group present in the mimic enzyme. The most important characteristic peak around 580 cm^{-1} represents the presence of Zn–O bond present in our synthesized platform, indicating that the ZnO nanoparticles present in the sawdust-deposited@ZnO NPs are as shown in Figure 1B. A similar pattern of peaks has already been reported for ZnO in the literature (Xiong et al., 2006).

3.1.3 XRD analysis

The X-ray diffraction pattern of the synthesized sawdust-deposited@ZnO NPs is shown in Figure 1C. The XRD results of the prepared platform centered at $2\theta = 21$ reveal a diffraction peak with miller indices of 120. When compared to standard data, it was found that the peak matched the hexagonal phase of ZnO NPs standard data (JCPDS card no. 36–1451) (Srivastava et al., 2013). The average crystal size of orthorhombic-phase ZnO NPs was calculated to be about 35 nm using Scherer equation.

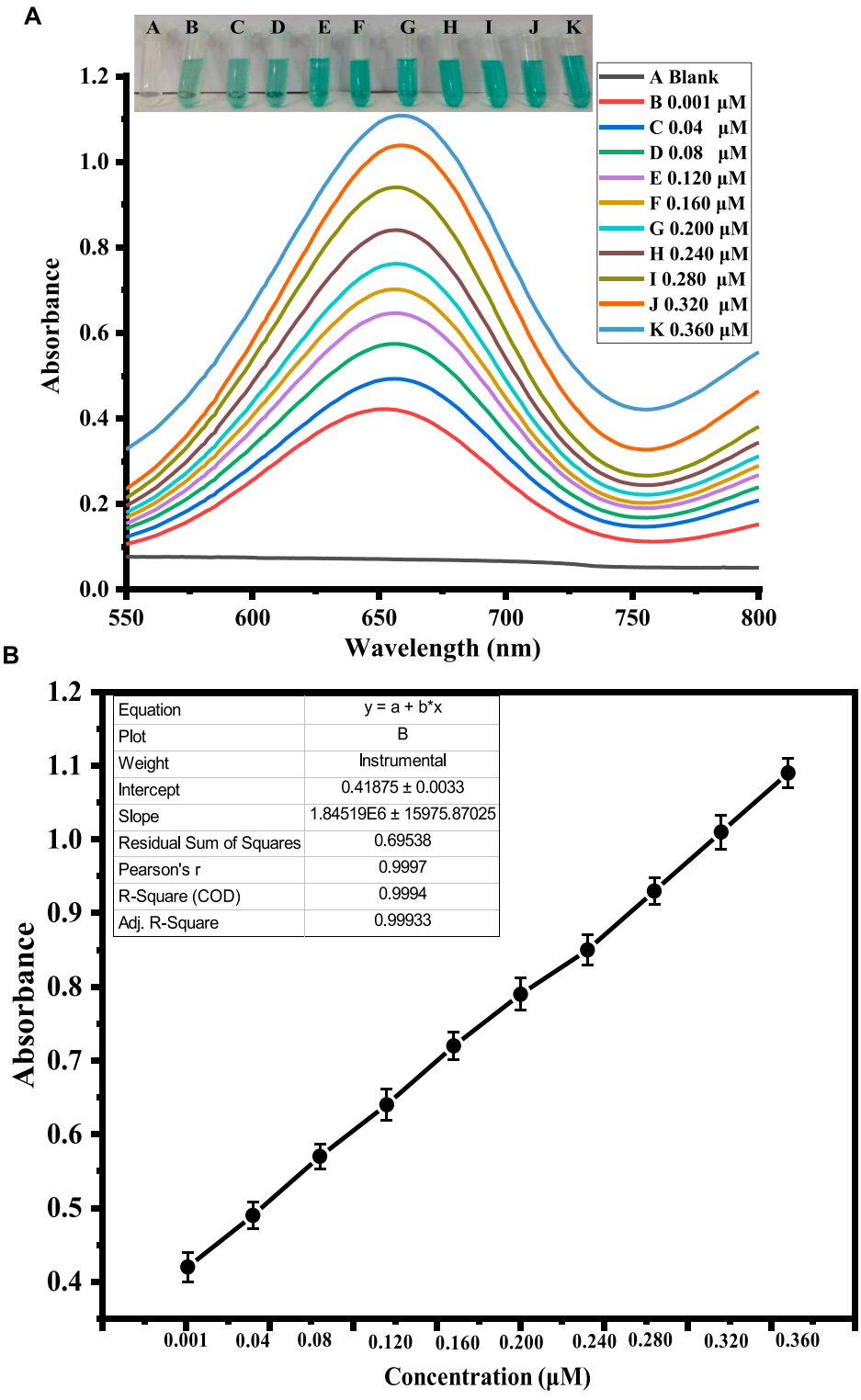

FIGURE 5
Shows the optimization of H_2O_2 concentration. Figure **(A)** shows the UV-Vis response recorded at different concentrations of H_2O_2. The inset figure shows varying color changes with the addition of different concentrations of H_2O_2. Figure **(B)** shows the corresponding calibration curve of the absorbance at different H_2O_2 concentrations.

3.1.4 EDX analysis

The chemical composition of the sawdust-deposited@ZnO NPs was examined using EDX analysis, as shown in Figure 1D and Table 1. The results showed the presence of Zn and O in the sawdust-deposited@ZnO sample. In addition to Zn and O, some other elements like Ca and C are also present. The percent contents

TABLE 2 Comparison of different colorimetric biosensors for H_2O_2.

S. No.	Materials used	Method applied	Linear range (μM)	Limit of detection (μM)	References
1	CuS	Colorimetric	1–1,000	0.11	Guan et al. (2015)
2	PB NPs	Colorimetric	0.1–50	0.031	Zhang et al. (2014)
3	Ag NPs	Colorimetric	0.01–30	0.014	Teodoro et al. (2019)
4	RhNPs	Colorimetric	1–100	0.75	Choleva et al. (2018)
5	Cu(II)-coated Fe_3O_4 NPs	Colorimetric	2.5–100	0.2	Liu et al. (2019)
6	GQDs/CuO	Colorimetric	0.5–10	0.17	Zhang et al. (2017)
7	ZV-Mn NPs	Colorimetric	10–280	0.2	Rauf et al. (2020)
8	FeCDs	Colorimetric	6–42	0.93	Bandi et al. (2021)
9	Ni NPs	Colorimetric	400–4,000	120	Zarif et al. (2020)
10	TiO2 NPs	Colorimetric	0.001–0.360	0.08	Nishan et al. (2021a)
11	lignin-based Ag NPs	Colorimetric	0.001–0.360	0.0137	Nishan et al. (2021b)
12	Ag-Fe2O3 NPs	Colorimetric	0.001–0.320	0.0107	Nishan et al. (2023)
13	Capped sawdust-deposited@ZnO NPs	Colorimetric	0.001–0.360	0.00024	This work

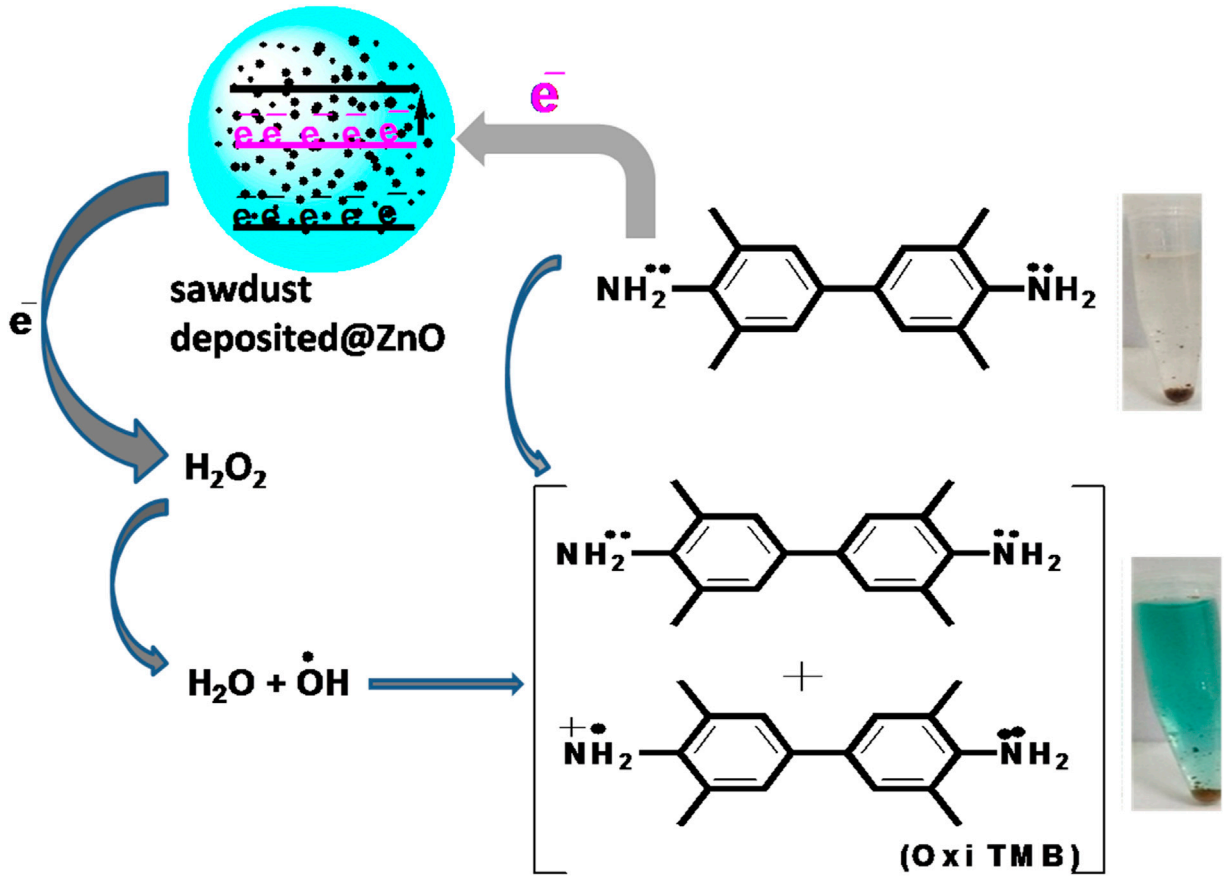

SCHEME 1
Showing the proposed reaction for the colorimetric sensing of hydrogen peroxide based on the fabricated mimic enzyme.

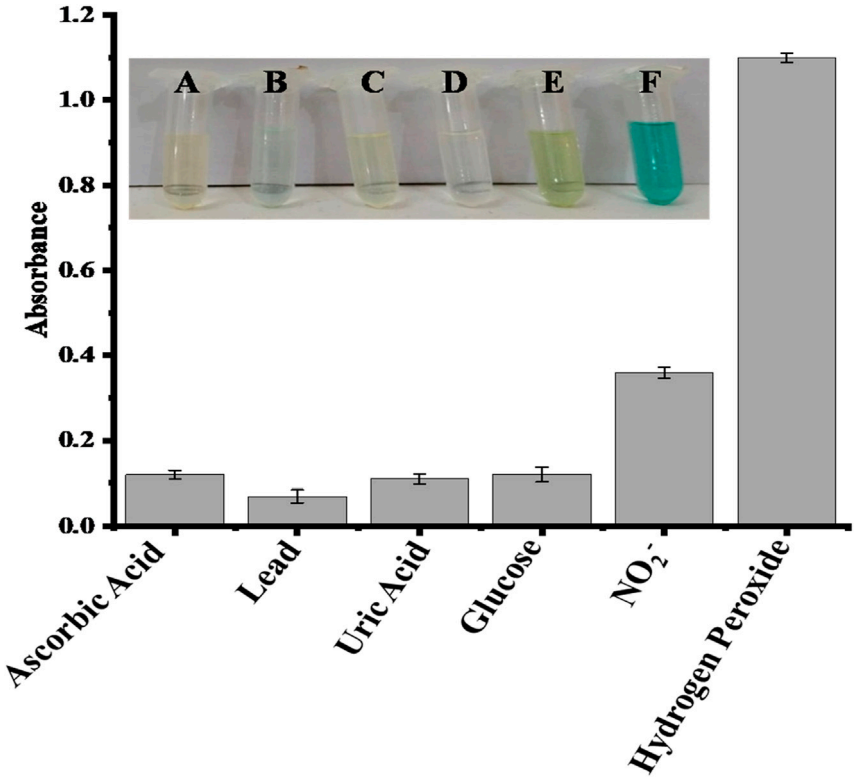

FIGURE 6
Comparative interference study of the proposed capped sawdust-deposited@ZnO NPs sensor for the detection of hydrogen peroxide with other analytes, indicating high selectivity of the proposed platform for the sensing of H_2O_2. In the inset Figure, the letters A, B, C, D, E, and F represent ascorbic acid, lead, uric acid, glucose, nitrite, and hydrogen peroxide, respectively.

of Zn, O, C, and Ca are 3.64, 46.95, 49.90, and 0.17, respectively, by weight as shown in the table.

3.1.5 SEM analysis

To investigate the surface morphology of the synthesized sawdust-deposited@ZnO NPs, SEM images of different resolutions were taken, as shown in Figure 2A–D. SEM images confirmed that the prepared ZnO NPs are distributed uniformly over the surface of sawdust. This uniform distribution of the nanoparticles is highly desirable and helpful in terms of the surface area of the nanoparticles for their catalytic activity.

3.2 Colorimetric detection of H_2O_2

H_2O_2 sensing by the proposed sawdust-deposited@ZnO NPs was done using a very simple and highly selective colorimetric approach. The optical sensing and UV-Vis absorption spectra are shown in Figure 3. When H_2O_2 is introduced to the sensor system, it produces a blue-green color from the colorless TMB. Mechanistically, adsorption of H_2O_2 on the surface of NPs produces OH radicals, which oxidize the colorless TMB substrate into a blue-green product, as can be seen with the naked eye, as shown in Figure. The colorimetric change was confirmed by a UV-Vis spectrophotometer. To confirm that the colorimetric change was due to the synthesized sawdust-deposited@ZnO NPs, we used *M. nigra* sawdust without ZnO NPs as a negative control. When H_2O_2 was added, no color change was detected; indicating that the color change was caused only by the capped sawdust-deposited@ZnO NPs. UV-Vis spectroscopic investigation validated the negative control experiment, as indicated in Figure.

3.3 Proposed mechanism of the reaction

In the current work, mimic enzyme (acetic acid-capped ZnO NPs deposited sawdust) receive electrons from TMB. It results in an increase in the conductivity of electrons in the mimic enzyme, which provides an active site for the proposed chemical reaction. The mobility of electrons results in the transfer of electrons to H_2O_2. It results in the generation of hydroxyl free radicals. The generated hydroxyl free radicals oxidize the TMB, resulting in the formation of a blue-green complex. This colorimetric change is visible to the naked eye and was also confirmed with a UV-Vis spectrophotometer. The maximum absorption was found to be at 652 nm. The detailed proposed reaction can be in seen in Scheme 1.

3.4 Optimization of parameters

3.4.1 Amount of capped ZnO NPs

In order to get the best colorimetric response, we first optimized the amount of capped sawdust-deposited@ZnO NPs. Briefly, different amounts (10–70 μL) of the capped sawdust-deposited@

TABLE 3 Detection of hydrogen peroxide in blood serum sample of diabetes patient (n = 3).

Samples	Detected (μM)	H_2O_2 added (μM)	H_2O_2 found (μM)	Recovery (%)	RSD (%)
1	0.004	0.017	0.021	123.53	0.271
2	0.007	0.120	0.127	105.83	0.451
3	0.013	0.206	0.219	106.31	0.214

ZnO NPs were tested, and the best colorimetric response was obtained at a 40 μL concentration, as shown in Figure 4A. No significant colorimetric response was obtained below 40 μL, so the 40 μL amount was taken as the optimum amount for further experiments. Previously, we reported about 25 μL of capped TiO_2 NPs as an optimum concentration for the colorimetric sensing of H_2O_2 (Nishan et al., 2021a). Under the given conditions, an increase in the concentration of the mimic enzyme from 40 μL up to 70 μL results in a lower response. This can possibly be explained by the fact that unreacted mimic enzyme interferes with the already oxidized TMB, resulting in much lower absorption.

3.4.2 pH optimization

Different pH optimizations were done to get the maximum colorimetric response. Briefly, different pH solutions of PBS were made, and their respective pH values were adjusted using sodium hydroxide and hydrochloric acid solutions. The best colorimetric response shown by the capped sawdust-deposited@ZnO NPs was recorded on pH 7, as shown in Figure 4B. No significant colorimetric response was noticed above or below this optimum pH of 7, therefore pH 7 was selected as the optimum pH for further experiments. At a lower pH, the concentration of hydrogen ions increases, which results in the protonation of the amino group of the chromogenic substrate TMB. This protonation of TMB makes it less susceptible to oxidation, resulting in a lower colorimetric change. The increase in pH above 7 results in an increase in hydroxyl ion concentration. As a result, the oxidation of TMB reduces, and hence less colorimetric change can be observed. Similarly an earlier study reported pH 7.5 to be optimum for the colorimetric sensing of hydrogen peroxide (Nishan et al., 2021b).

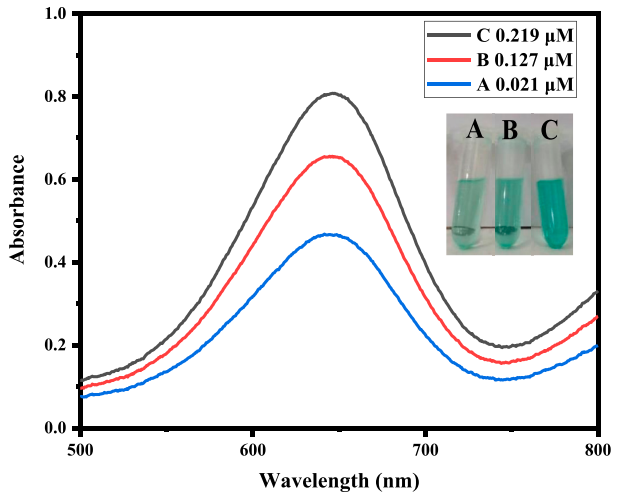

FIGURE 7
Real sample analysis of a blood serum sample of a diabetes patient at optimized conditions by the addition of different concentrations of hydrogen peroxide, such as 0.017, 0.120, and 0.206 μM.

3.4.3 Optimization of TMB concentration

TMB solutions of different concentrations ranging from 3 to 21 mM were prepared. Initially, the colorimetric response increased up to 12 mM and then decreased as the concentration of TMB increased from 13 mM to 21 mM. The best colorimetric response was noticed at 12 mM, as shown in Figure 4C. Recently, for the detection of hydrogen peroxide, the 8 mM optimum TMB concentration was reported by our groups for another nanostructure (Nishan et al., 2023). This could possibly be explained by the fact that in the reported work, a pristine form of nanomaterial functionalized with ionic liquid was used as a mimic enzyme. In the current work, sawdust was used as a matrix material, hence the higher concentration of TMB.

3.4.4 Optimization of time

In colorimetric detection of hydrogen peroxide, the reaction incubation time was also optimized. A colorimetric response was noticed at various time intervals (1–7 min) after adding hydrogen peroxide. The reaction time at various intervals was recorded by UV-Vis spectroscopy. After 5 min, no further change in color or absorbance was noticed, indicating that 5 min is the optimal time for a complete reaction, as shown in Figure 4D. According to the literature, the optimum time for the detection of hydrogen peroxide was 10 min, as reported by (Zarif et al., 2020), which is much higher than our present work.

3.5 Optimization of hydrogen peroxide concentration

H_2O_2 was detected using a quick and easy colorimetric method based on capped sawdust-deposited@ZnO NPs under ideal experimental circumstances. As seen in Figure 5, the developed biosensor's sensitivity for H_2O_2 detection was tested using a range of H_2O_2 concentrations. At lower H_2O_2 concentrations, the sensor response and peak intensity were negligible, but as the concentration rose, they grew linearly. H_2O_2 detection with an R^2 value of 0.999 and a linear range of 0.001–0.360 μM was made possible by this method. It was determined that the limits of quantification (LOQ) and detection (LOD) were, respectively, 0.24 nM and 0.81 nM. The suggested colorimetric approach had the advantages of a low detection limit, low cost, and naked eye observation over other previously published detection methods. Based on the linear range and limit of detection, we compared

this work for H_2O_2 detection with previously reported colorimetric approaches, as shown in Table 2. It is clear from the results that the fabricated sensor showed an exceptional limit of detection and a comparable wide linear range with previous works from our group.

3.6 Selectivity analysis the proposed sensor

The potential interfering chemicals, including ascorbic acid, lead, uric acid, glucose, and nitrite, were used to test the selectivity of the proposed sensor. All these interfering chemicals had substantially lower absorbance than H_2O_2, as shown in Figure 6. The recorded absorbance was highest when H_2O_2 was added, and no significant absorbance change was seen when a co-existing material was added. In the presence of higher amounts of ascorbic acid, lead, uric acid, glucose, and nitrite ions, the suggested sensor has a substantially stronger selectivity for H_2O_2. All the experiments were performed in the presence of 0.360 μM H_2O_2 and a double concentration of other interfering substances.

3.7 Real sample analysis

To assess the practical application of the proposed sensor to detect H_2O_2 content, the measurement of H_2O_2 in the blood serum sample of a diabetes patient was carried out as shown in Table 3. The present amount of H_2O_2 was calculated from the already calibrated graph by using the spiking method. Different concentrations of H_2O_2 solution, such as 0.017, 0.120, and 0.206 μM, were spiked into the blood serum sample of a diabetes patient and analyzed, as shown in Figure 7. The results demonstrated that the H_2O_2 concentrations in the real samples determined by the current assay are in good agreement with the spiked H_2O_2 concentrations.

4 Conclusion

Morus nigra-deposited ZnO@NPs were successfully synthesized from *T. foenum* extract. The synthesized platform was characterized with various standard analytical techniques, including FTIR, SEM, XRD, and EDX. The synthesized sawdust-deposited@ZnO NPs were capped with acetic acid and successfully used for the colorimetric sensing of H_2O_2. Our current finding demonstrates that acetic acid-capped sawdust-deposited@ZnO NPs show enhanced intrinsic peroxidase-like activity. The proposed platform showed good sensitivity and selectivity in the presence of a double amount of potential interfering species. The fabricated platform shows a number of advantages over natural enzymes, including easy preparation, low cost, quick reaction times, and high stability. These advantages make it a suitable candidate peroxidase-mimic for future applications in biotechnology, medical diagnostics, and hydrogen peroxide monitoring.

Data availability statement

The raw data supporting the conclusion of this article will be made available by the authors, without undue reservation.

Author contributions

UN: Conceptualization, Formal Analysis, Investigation, Project administration, Supervision, Writing–original draft, Writing–review and editing. TZ: Data curation, Investigation, Methodology, Writing–original draft. AB: Investigation, Methodology, Project administration, Supervision, Visualization, Writing–review and editing. NM: Conceptualization, Formal Analysis, Methodology, Visualization, Writing–review and editing. SA: Data curation, Formal Analysis, Investigation, Validation, Writing–review and editing. MS: Data curation, Investigation, Software, Writing–original draft. NK: Formal Analysis, Methodology, Validation, Visualization, Writing–review and editing. MA: Data curation, Formal Analysis, Investigation, Methodology, Software, Writing–original draft. RU: Funding acquisition, Investigation, Project administration, Resources, Software, Visualization, Writing–review and editing. EA: Formal Analysis, Funding acquisition, Methodology, Project administration, Resources, Visualization, Writing–original draft. KC: Conceptualization, Funding acquisition, Investigation, Methodology, Project administration, Resources, Supervision, Writing–original draft, Writing–review and editing.

Funding

The author(s) declare financial support was received for the research, authorship, and/or publication of this article. This research work is supported by the Doctoral research fund of the Affiliated Hospital of Southwest Medical University, Luzhou 646000, China, awarded to KC. The authors thank researchers supporting Project number (RSP2024R110) King Saud University, Riyadh, Saudi Arabia.

Acknowledgments

KC acknowledges the doctoral research fund of the Affiliated Hospital of Southwest Medical University, Luzhou 646000, China. Authors wish to thanks Researchers Supporting Project Number (RSP2024R110) at King Saud University Riyadh Saudi Arabia for financial support.

Conflict of interest

The authors declare that the research was conducted in the absence of any commercial or financial relationships that could be construed as a potential conflict of interest.

Publisher's note

References

Abou Chaaya, A., Bechelany, M., Balme, S., and Miele, P. (2014). ZnO 1D nanostructures designed by combining atomic layer deposition and electrospinning for UV sensor applications. *J. Mater. Chem. A* 2, 20650–20658. doi:10.1039/c4ta05239k

Asad, M., Muhammad, N., Khan, N., Shah, M., Khan, M., Khan, M., et al. (2022). Colorimetric acetone sensor based on ionic liquid functionalized drug-mediated silver nanostructures. *J. Pharm. Biomed. Analysis* 221, 115043. doi:10.1016/j.jpba.2022.115043

Bandi, R., Alle, M., Park, C.-W., Han, S.-Y., Kwon, G.-J., Kim, N.-H., et al. (2021). Cellulose nanofibrils/carbon dots composite nanopapers for the smartphone-based colorimetric detection of hydrogen peroxide and glucose. *Sensors Actuators B Chem.* 330, 129330. doi:10.1016/j.snb.2020.129330

Chen, W., Chen, J., Liu, A. L., Wang, L. M., Li, G. W., and Lin, X. H. (2011). Peroxidase-like activity of cupric oxide nanoparticle. *ChemCatChem* 3, 1151–1154. doi:10.1002/cctc.201100064

Chen, X., Wu, G., Cai, Z., Oyama, M., and Chen, X. (2014). Advances in enzyme-free electrochemical sensors for hydrogen peroxide, glucose, and uric acid. *Microchim. Acta* 181, 689–705. doi:10.1007/s00604-013-1098-0

Choleva, T. G., Gatselou, V. A., Tsogas, G. Z., and Giokas, D. L. (2018). Intrinsic peroxidase-like activity of rhodium nanoparticles, and their application to the colorimetric determination of hydrogen peroxide and glucose. *Microchim. Acta* 185, 22–29. doi:10.1007/s00604-017-2582-8

Dutta, A. K., Das, S., Samanta, S., Samanta, P. K., Adhikary, B., and Biswas, P. (2013). CuS nanoparticles as a mimic peroxidase for colorimetric estimation of human blood glucose level. *Talanta* 107, 361–367. doi:10.1016/j.talanta.2013.01.032

Guan, J., Peng, J., and Jin, X. (2015). Synthesis of copper sulfide nanorods as peroxidase mimics for the colorimetric detection of hydrogen peroxide. *Anal. Methods* 7, 5454–5461. doi:10.1039/c5ay00895f

Irani-nezhad, M. H., Khataee, A., Hassanzadeh, J., and Orooji, Y. (2019). A chemiluminescent method for the detection of H2O2 and glucose based on intrinsic peroxidase-like activity of WS2 quantum dots. *Molecules* 24, 689. doi:10.3390/molecules24040689

Jv, Y., Li, B., and Cao, R. (2010). Positively-charged gold nanoparticles as peroxidiase mimic and their application in hydrogen peroxide and glucose detection. *Chem. Commun.* 46, 8017–8019. doi:10.1039/c0cc02698k

Khaliq, A., Nazir, R., Khan, M., Rahim, A., Asad, M., Shah, M., et al. (2023). Co-doped CeO_2/activated C nanocomposite functionalized with ionic liquid for colorimetric biosensing of H_2O_2 via peroxidase mimicking. *Molecules* 28, 3325. doi:10.3390/molecules28083325

Khranovskyy, V., Lazorenko, V., Lashkarev, G., and Yakimova, R. (2012). Luminescence anisotropy of ZnO microrods. *J. Luminescence* 132, 2643–2647. doi:10.1016/j.jlumin.2012.04.048

Lee, J. H., Huynh-Nguyen, B.-C., Ko, E., Kim, J. H., and Seong, G. H. (2016). Fabrication of flexible, transparent silver nanowire electrodes for amperometric detection of hydrogen peroxide. *Sensors Actuators B Chem.* 224, 789–797. doi:10.1016/j.snb.2015.11.006

Liu, H., Zhu, L., Ma, H., Wen, J., Xu, H., Qiu, Y., et al. (2019). Copper (II)-coated Fe3O4 nanoparticles as an efficient enzyme mimic for colorimetric detection of hydrogen peroxide. *Microchim. Acta* 186, 518–519. doi:10.1007/s00604-019-3599-y

Miller, E. W., Dickinson, B. C., and Chang, C. J. (2010). Aquaporin-3 mediates hydrogen peroxide uptake to regulate downstream intracellular signaling. *Proc. Natl. Acad. Sci.* 107, 15681–15686. doi:10.1073/pnas.1005776107

Nakashima, K., Wada, M., Kuroda, N., Akiyama, S., and Imai, K. (1994). High-performance liquid chromatographic determination of hydrogen peroxide with peroxyoxalate chemiluminescence detection. *J. Liq. Chromatogr. Relat. Technol.* 17, 2111–2126. doi:10.1080/10826079408013535

Nishan, U., Haq, S. U., Rahim, A., Asad, M., Badshah, A., Ali Shah, A.-u.-H., et al. (2021a). Ionic-liquid-stabilized TiO2 nanostructures: a platform for detection of hydrogen peroxide. *ACS omega* 6, 32754–32762. doi:10.1021/acsomega.1c04548

Nishan, U., Khan, H. U., Rahim, A., Asad, M., Qayum, M., Khan, N., et al. (2022). Non-enzymatic colorimetric sensing of nitrite in fortified meat using functionalized drug mediated manganese dioxide. *Mater. Chem. Phys.* 278, 125729. doi:10.1016/j.matchemphys.2022.125729

Nishan, U., Niaz, A., Muhammad, N., Asad, M., Khan, N., Khan, M., et al. (2021b). Non-enzymatic colorimetric biosensor for hydrogen peroxide using lignin-based silver nanoparticles tuned with ionic liquid as a peroxidase mimic. *Arabian J. Chem.* 14, 103164. doi:10.1016/j.arabjc.2021.103164

Nishan, U., Ullah, I., Muhammad, N., Afridi, S., Asad, M., Haq, S. U., et al. (2023). Investigation of silver-doped iron oxide nanostructures functionalized with ionic liquid for colorimetric sensing of hydrogen peroxide. *Arabian J. Sci. Eng.* 48, 7703–7712. doi:10.1007/s13369-023-07791-z

Ornatska, M., Sharpe, E., Andreescu, D., and Andreescu, S. (2011). Paper bioassay based on ceria nanoparticles as colorimetric probes. *Anal. Chem.* 83, 4273–4280. doi:10.1021/ac200697y

Park, N.-M., Choi, S., Oh, J. E., and Hwang, D. Y. (2019). Facile extraction of cellulose nanocrystals. *Carbohydr. Polym.* 223, 115114. doi:10.1016/j.carbpol.2019.115114

Patel, V., Kruse, P., and Selvaganapathy, P. R. (2020). Solid state sensors for hydrogen peroxide detection. *Biosensors* 11 (9), 9. doi:10.3390/bios11010009

Rao, A., and Balachandran, B. (2002). Role of oxidative stress and antioxidants in neurodegenerative diseases. *Nutr. Neurosci.* 5, 291–309. doi:10.1080/1028415021000033767

Rauf, S., Ali, N., Tayyab, Z., Shah, M. Y., Yang, C. P., Hu, J., et al. (2020). Ionic liquid coated zerovalent manganese nanoparticles with stabilized and enhanced peroxidase-like catalytic activity for colorimetric detection of hydrogen peroxide. *Mater. Res. Express* 7, 035018. doi:10.1088/2053-1591/ab7f10

Senthamizhan, A., Balusamy, B., Aytac, Z., and Uyar, T. (2016). Ultrasensitive electrospun fluorescent nanofibrous membrane for rapid visual colorimetric detection of H 2 O 2. *Anal. Bioanal. Chem.* 408, 1347–1355. doi:10.1007/s00216-015-9149-5

Shi, W., Zhang, X., He, S., and Huang, Y. (2011). CoFe 2 O 4 magnetic nanoparticles as a peroxidase mimic mediated chemiluminescence for hydrogen peroxide and glucose. *Chem. Commun.* 47, 10785–10787. doi:10.1039/c1cc14300j

Singh, J., Singh, R., Singh, S., Mitra, K., Mondal, S., Vishwakarma, S., et al. (2022). Colorimetric detection of hydrogen peroxide and cholesterol using Fe3O4-brominated graphene nanocomposite. *Anal. Bioanal. Chem.* 414, 2131–2145. doi:10.1007/s00216-021-03848-w

Song, Y., Qu, K., Zhao, C., Ren, J., and Qu, X. (2010). Graphene oxide: intrinsic peroxidase catalytic activity and its application to glucose detection. *Adv. Mater.* 22, 2206–2210. doi:10.1002/adma.200903783

Srivastava, V., Gusain, D., and Sharma, Y. C. (2013). Synthesis, characterization and application of zinc oxide nanoparticles (n-ZnO). *Ceram. Int.* 39, 9803–9808. doi:10.1016/j.ceramint.2013.04.110

Talam, S., Karumuri, S. R., and Gunnam, N. (2012). Synthesis, characterization, and spectroscopic properties of ZnO nanoparticles. *Int. Sch. Res. Notices* 2012, 1–6. doi:10.5402/2012/372505

Teodoro, K. B., Migliorini, F. L., Christinelli, W. A., and Correa, D. S. (2019). Detection of hydrogen peroxide (H2O2) using a colorimetric sensor based on cellulose nanowhiskers and silver nanoparticles. *Carbohydr. Polym.* 212, 235–241. doi:10.1016/j.carbpol.2019.02.053

Wei, Y., Li, Y., Liu, X., Xian, Y., Shi, G., and Jin, L. (2010). ZnO nanorods/Au hybrid nanocomposites for glucose biosensor. *Biosens. Bioelectron.* 26, 275–278. doi:10.1016/j.bios.2010.06.006

Xiong, G., Pal, U., Serrano, J., Ucer, K., and Williams, R. (2006). Photoluminesence and FTIR study of ZnO nanoparticles: the impurity and defect perspective. *Phys. status solidi C.* 3, 3577–3581. doi:10.1002/pssc.200672164

Zarif, F., Rauf, S., Khurshid, S., Muhammad, N., Hayat, A., Rahim, A., et al. (2020). Effect of pyridinium based ionic liquid on the sensing property of Ni0 nanoparticle for the colorimetric detection of hydrogen peroxide. *J. Mol. Struct.* 1219, 128620. doi:10.1016/j.molstruc.2020.128620

Zhang, L., Hai, X., Xia, C., Chen, X.-W., and Wang, J.-H. (2017). Growth of CuO nanoneedles on graphene quantum dots as peroxidase mimics for sensitive colorimetric detection of hydrogen peroxide and glucose. *Sensors Actuators B Chem.* 248, 374–384. doi:10.1016/j.snb.2017.04.011

Zhang, W., Ma, D., and Du, J. (2014). Prussian blue nanoparticles as peroxidase mimetics for sensitive colorimetric detection of hydrogen peroxide and glucose. *Talanta* 120, 362–367. doi:10.1016/j.talanta.2013.12.028

Zhang, W., Niu, X., Li, X., He, Y., Song, H., Peng, Y., et al. (2018). A smartphone-integrated ready-to-use paper-based sensor with mesoporous carbon-dispersed Pd nanoparticles as a highly active peroxidase mimic for H_2O_2 detection. *Sensors Actuators B Chem.* 265, 412–420. doi:10.1016/j.snb.2018.03.082

frontiers | Frontiers in Bioengineering and Biotechnology

TYPE Original Research
PUBLISHED 23 February 2024
DOI 10.3389/fbioe.2024.1310084

OPEN ACCESS

EDITED BY
Kang Cui,
University of Jinan, China

REVIEWED BY
Siwei Zhao,
University of Nebraska Medical Center, United States
Yixian Wang,
California State University, Los Angeles, United States

*CORRESPONDENCE
A. de la Escosura-Muñiz,
alfredo.escosura@uniovi.es

RECEIVED 09 October 2023
ACCEPTED 29 January 2024
PUBLISHED 23 February 2024

CITATION
Toyos-Rodríguez C, Valero-Calvo D, Iglesias-Mayor A and de la Escosura-Muñiz A (2024), Effect of nanoporous membranes thickness in electrochemical biosensing performance: application for the detection of a wound infection biomarker.
Front. Bioeng. Biotechnol. 12:1310084.
doi: 10.3389/fbioe.2024.1310084

Effect of nanoporous membranes thickness in electrochemical biosensing performance: application for the detection of a wound infection biomarker

C. Toyos-Rodríguez[1,2], D. Valero-Calvo[1,2], A. Iglesias-Mayor[1,2] and A. de la Escosura-Muñiz[1,2]*

[1]NanoBioAnalysis Group, Department of Physical and Analytical Chemistry, University of Oviedo, Oviedo, Spain, [2]Biotechnology Institute of Asturias, University of Oviedo, Oviedo, Spain

Introduction: Nanoporous alumina membranes present a honeycomb-like structure characterized by two main parameters involved in their performance in electrochemical immunosening: pore diameter and pore thickness. Although this first one has been deeply studied, the effect of pore thickness in electrochemical-based nanopore immunosensors has been less taken into consideration.

Methods: In this work, the influence of the thickness of nanoporous membranes in the steric blockage is studied for the first time, through the formation of an immunocomplex in their inner walls. Finally, the optimal nanoporous membranes were applied to the detection of catalase, an enzyme related with chronic wound infection and healing.

Results: Nanoporous alumina membranes with a fixed pore diameter (60 nm) and variable pore thicknesses (40, 60, 100 μm) have been constructed and evaluated as immunosensing platform for protein detection. Our results show that membranes with a thickness of 40 μm provide a higher sensitivity and lower limit-of-detection (LOD) compared to thicker membranes. This performance is even improved when compared to commercial membranes (with 20 nm pore diameter and 60 μm pore thickness), when applied for human IgG as model analyte. A label-free immunosensor using a monoclonal antibody against anti-catalase was also constructed, allowing the detection of catalase in the range of 50–500 ng/mL and with a LOD of 1.5 ng/mL. The viability of the constructed sensor in real samples was also tested by spiking artificial wound infection solutions, providing recovery values of 110% and 118%.

Discussion: The results obtained in this work evidence the key relevance of the nanochannel thickness in the biosensing performance. Such findings will illuminate nanoporous membrane biosensing research, considering thickness as a relevant parameter in electrochemical-based nanoporous membrane sensors.

KEYWORDS

nanochannel, nanochannel thickness, catalase, wound infection, sensing

1 Introduction

The raising spread of rapidly evolving illnesses (Baker et al., 2022), as well as the overcrowd of primary care centers (Sartini et al., 2022), have demonstrated the need for rapid and reliable diagnostic tools for a proper healthcare management (Bernabé-Ortiz et al., 2021). With the 50% of illnesses detected nowadays being diagnosed in purpose-built centralized laboratories (Luppa et al., 2011), the need of faster alternatives is mandatory. Traditional techniques as polymerase chain reaction (PCR) or enzyme-linked immunosorbent assay (ELISA) (Sokolenko and Imyanitov, 2018), cell culture (Opota et al., 2015), and mass spectrometry (Unlu and Abusoglu, 2022) are precise, robust and, in most cases, automated techniques, but they still lack from the decentralization and cost-effectivity demanded for a point-of-care clinical diagnosis.

Biosensing devices constitute suitable alternatives in this sense, with highly diverse materials and formulations (Campuzano and Pingarrón, 2023) that allow the detection of nucleic acids as desoxyribonucleic acid (DNA) and ribonucleic acid (RNA) or protein biomarkers. From the biosensing strategies available, nanoporous materials constitute a robust alternative, proof-of-which are commercial examples as the DNA/RNA sequencing MinION technology, based on this sensing principle (Wang et al., 2021).

Nanopore sensing relies on the monitoring of current fluctuations between two chambers filled with an electrolyte solution through a nanopore inserted inside an insulating membrane (Xue et al., 2020). The passage of an analyte through the pore reduces the current recorded in a specific signature, associated to the size, charge or sequence of the target molecule.

Nanopore sensing was initially developed making use of single protein pores (Bayley and Cremer, 2001) although the stability and size limitations of this technology, soon prompted the advancement of solid-state alternatives (Dekker, 2007) with nanopore sizes between 100 nm and 1 nm (Liu et al., 2023) and variable non-permeable materials.

All these membrane-based sensors rely on resistive pulse as sensing principle. However, the monitoring of current changes through these means has disadvantages, as the need to minimize signal-to-noise effects or the difficulty of multiplexing (Xue et al., 2020).

The combination of nanoporous membranes with alternative sensing strategies, as optical sensing (Spitzberg et al., 2019), field-effect transistors, quantum tunnelling (Ren et al., 2017) or electrochemistry (Ito and Nathani, 2022) is then a promising alternative.

In combination with electrochemistry, solid-state membranes, and more particularly nanoporous alumina membranes have been deeply used for sensing applications (de la Escosura-Muñiz and Merkoçi, 2012). This type of membranes stands out due to their ease of functionalization, large surface area, stability, and filtering properties. Nanoporous alumina membranes have a homogenous and self-ordered nanoporous structure, formed by the voltage mediated anodization of aluminium at an acidic pH, which forms a honeycomb-like structure characterized by their pore diameter and pore thickness.

Several works have previously studied the effect of this first dimension in detail (Van Den Hout et al., 2010). However, the effect of pore thickness in the analytical performance of an electrochemical-based nanopore sensor is still less known. Nanopore thickness has been previously considered in biological nanopores (Xue et al., 2020), were a reduction of the length of this dimension has been correlated with an increase in the sensitivity achieved. In solid-state membranes, thickness has been also identified as a critical factor for resistive pulse recording, as both signal (current intensity) and resolution (associated with the actual sensing region inside the nanopore) are inversely proportional to this dimension.

In this context, this work has evaluated for the first time the effect of nanoporous alumina membrane thickness in a sensing device relying in electrochemical detection. Membranes with a fixed pore diameter (60 nm) and variable pore thicknesses (40, 60, 100 µm) have been constructed through a two-step anodization process. Commercially available membranes with a diameter of 20 nm and a thickness of 60 µm have been also evaluated for comparison purposes. The analytical characteristics of these membranes have been compared developing a model immunosensor for the detection of human immunoglobulin G (HIgG) as model analyte. The principle of the developed sensor is based on the immobilization inside nanoporous alumina membranes of an antibody against HIgG. In the presence of this molecule, an immunocomplex is formed inside the channel, which hinders the diffusion of the redox indicator ferrocyanide ($[Fe(CN)_6]^{4-}$) through the nanochannel, changing the electrochemical signal recorded.

Optimal nanoporous membranes have been applied to the detection of a chronic wound infection biomarker as a proof-of-concept. Chronic wounds are a prevalent healthcare challenge in aging populations, affecting 1%–2% population in developed countries (Clinton and Carter, 2015). A major complication in the normal healing process of a wound is infection, that delays wound bed recovery and, if unattended, increases the risk of sepsis. A fast and accurate identification of an infection is then mandatory to stop bacteria colonization by providing a suitable antibiotic treatment. However, current identification techniques are based on first instance on visual signs of infection (Siddiqui and Bernstein, 2010) (i.e., redness, swelling, increased temperature of the wound bed, etc.) and as confirmation, gold-standard culture techniques. The long time required for these techniques to provide a result leads to the unrestrained administration of antibiotic treatments, what aggravates the appearance of multi-drug resistant microorganisms (Miethke et al., 2021; Inda-Díaz et al., 2023). The substitution of these approaches by point-of-care analytical tools, as the one proposed in this work, are desirable to tackle infection in a cost-effective, fast, and accurate manner.

Catalase, a hydrogen peroxidase enzyme that has been stablished as biomarker of several pathologies, including oxidative stress or chronic wound infection (Clemente et al., 2020), has been selected as target analyte. Catalase is produced by certain bacteria, including *Pseudomonas aeruginosa*, a prevalent microorganism present in chronic wounds, as well as Enterobacteriaceae or *Staphylococcus* among others (Chester and Moskowitz, 1987; Shin et al., 2008). But catalase can be also produced by the human body, and it has been related with the healing state of a wound (Rasik and Shukla, 2001), constituting a dual infection and healing biomarker. This relation has prompted the incorporation of catalase or catalase-like

nanozymes (Wang et al., 2023; Xu et al., 2023) as components of wound dressing materials, pointing out the relevance of this biomolecule in wound management.

2 Experiments

2.1 Materials

High purity aluminum discs (Al 99.999%, Goodfellow, United Kingdom), (3-aminopropyl) triethoxysilane (APTES), catalase from human erythrocytes, monoclonal anti-catalase antibody, N-(3-Dimethylaminopropyl)-N′-ethylcarbodiimide hydrochloride (EDC), Human IgG >95% (HPLC grade), polyclonal anti-Human IgG antibody, N-Hydroxysulfosuccinimide sodium salt (sulfo-NHS), potassium ferrocyanide $K_4[Fe(CN)_6]$, (2-(N-morpholino) ethanesulfonic acid) (MES) and Tris (tris(hydroxymethyl) aminomethane)-HCl (Tris-HCl) were purchased from Sigma-Aldrich (Spain). All acids required for the anodization process were purchased from VWR International Eurolabs (Spain).

Unless otherwise stated, all buffer solutions were prepared in ultrapure water (18.2 MΩ cm @ 25°C) obtained from a Millipore Direct-Q® 3 UV purification system from Millipore Ibérica S.A (Spain).

Commercial Whatman® AnodiscTM filter membranes (13 mm diameter, 60 µm thickness, 20 nm pore) used as control were obtained from VWR International Eurolabs (Spain). As working electrode, indium tin oxide/poly(ethylene terephthalate) (ITO/PET) sheets (with a surface resistivity of 60 Ω/sq) were obtained from Sigma-Aldrich (Spain). Silver/silver chloride from CH Instruments, Inc. (United States) and platinum wire from Alfa Aesar (United States) were used as reference and counter electrode respectively.

2.2 Instruments

The surface functionalization of the obtained nanoporous alumina membrane was performed on a Savannah 100 thermal atomic layer deposition (ALD) reactor (Cambridge Nanotech, Waltham, MA, United States). Characterization of the membranes was performed through scanning electron microscopy (SEM) using a MEB JOEL-6100 (Japan) operated at 20 kV. Electrochemical measurements were performed inside a customized methacrylate electrochemical cell with a PalmSens 3 potentiostat (PalmSens BV, Netherlands) controlled by a smartphone via Bluetooth.

2.3 Nanoporous alumina membranes preparation and functionalization

Nanoporous alumina membranes were obtained following a previously published procedure (Cuevas et al., 2023). Briefly, a highly pure aluminum disk (composed of Al 99.999% with a size of 0.5 mm in thickness and 25 in diameter) was cleaned with isopropanol and ethanol for further electropolishing with a 25% perchloric acid in ethanol solution. The aluminum was then anodized following a two-step anodization process, using a 0.3 M oxalic acid solution as electrolyte, and applying an anodization voltage of 40 V. The first anodization step was applied for 24 h at 0°C-1°C. The anodization time was modified to adjust the thickness of the resulting membranes. After that, the resulting Al template was washed to remove the aluminum oxide layer with an acidic solution of chromium trioxide (CrO_3) and phosphoric acid (H_3PO_4) at 35°C for 24 h. A second anodization step was then performed also applying a 40 V potential and adjusting the time of the anodization step to obtain a nanoporous membrane thickness of ~40, 60 or 100 µm. The membrane surface was protected by depositing a layer of poly(methyl methacrylate) (PMMA). A last cleaning step was then performed using an aqueous mixture of hydrochloric acid (HCl) and copper (II) chloride ($CuCl_2$) to remove a 1 cm^2 area of remaining Al at the bottom layer. Then, a wet chemical etching was applied using an aqueous solution of H_3PO_4 5% at room temperature for 120 min to open the formed pores. Afterwards, the PMMA layer was dissolved in acetone, thus exposing the porous structure of the membrane. Finally, the pore diameter was adjusted by widening them through chemical etching in a 5% aqueous solution of H_3PO_4 at room temperature for 1 h.

The obtained nanoporous membranes were later functionalized using ALD by pulsing water vapor and APTES while heating the substrates at 150°C.

2.4 Antibody immobilization and HIgG detection using membranes with different thickness

After functionalizing the inner walls of the nanoporous alumina membranes with amine groups through ALD, 30 µL of a solution of 5 mM EDC/sulfo-NHS in MES pH 5, containing a concentration of 1,000 µg/mL (highly excess) of monoclonal anti-HIgG antibody was placed on top of the nanoporous membrane and left at room temperature for incubation for 2 h. The mechanism of antibody immobilization is schematized in Supplementary Figure S1. After this time, membranes were gently washed with Tris-HCl 10 mM pH 7.40 buffer to remove the non-immobilized antibodies. Nanopores blockage obtained after the antibody immobilization step was measured at this point for each modified membrane using a 10 mM $K_4[Fe(CN)_6]$ redox indicator solution in 10 mM Tris-HCl pH 9.0 solution (see Section 2.5). After this measurement, membranes were gently washed with Tris-HCl 10 mM pH 7.40 buffer and measured again without the addition of further redox indicator, confirming that there was no remaining solution inside the membrane. Then, 30 µL of solutions containing increasing concentrations of HIgG (100, 500 and 1,000 ng/mL) were placed on the membranes and left for incubation at room temperature during 1 h, following a previously optimized protocol for this analyte (de la Escosura-Muñiz and Merkoçi, 2010). After incubation, membranes were washed again and measured using a 10 mM $K_4[Fe(CN)_6]$ redox indicator solution in 10 mM Tris-HCl pH 9.0.

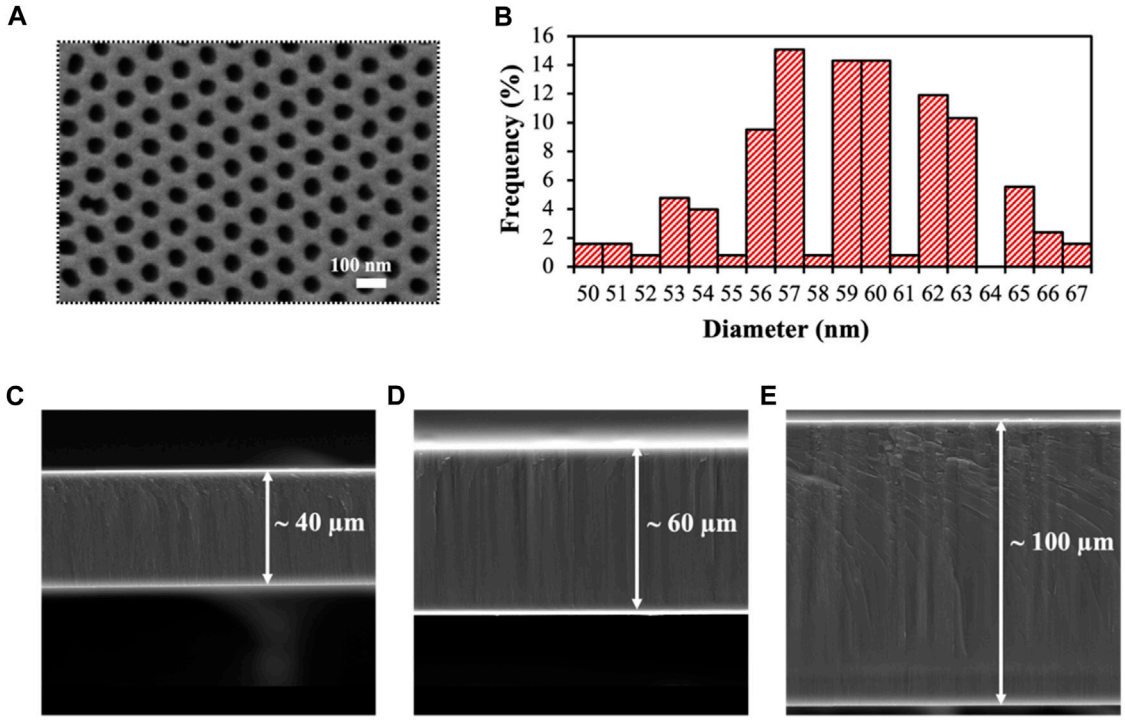

FIGURE 1
Characterization of the obtained nanoporous alumina membranes. **(A)**. SEM top-view of the self-obtained nanoporous membranes. **(B)**. Size distribution of the nanochannels diameter, showing an average size of 59 ± 4 nm. **(C, D)**. Cross-section of the self-produced nanoporous alumina membranes with thicknesses of 40 **(C)**, 60 **(D)** and 100 µm **(E)**.

This protocol was followed for the self-prepared membranes with a fixed pore diameter of ~60 nn and variable pore thicknesses (40, 60, 100 µm) and for the commercial ones with a pore diameter of 20 nm and a pore thickness of 60 µm.

2.5 Electrochemical measurements

ITO/PET electrodes were hydrolysed by immersion in a solution of H_2O:NH_3:H_2O_2 (17:3:1) for 20 min, followed by washing in acetone, isopropanol, and water and finally letting dry. Later, the modified electrodes were electrochemically characterized by cyclic voltammetry (CV) (scan range: −0.3 V to +0.8 V; step potential: 10 mV, scan rate: 50 mV/s) in 10 mM $K_4[Fe(CN)_6]$/0.1 M Tris-HCl at different pH values to confirm that the applied hydrophilization treatment did not affect conductivity.

For the electrochemical evaluation of the blocking/unblocking of the nanoporous membranes, APTES-modified membranes were collocated on top of the hydrophilized ITO/PET electrodes and fixed inside a methacrylate block with a hole defining an electrochemical cell of 500 µL. Membranes were maintained inside the cell during the immunocomplex formation steps (see Section 2.4.), performing washing steps with the appropriate buffer inside them. Measurements were performed using a 10 mM $K_4[Fe(CN)_6]$ red-ox indicator solution in 0.1M Tris-HCl (at the appropriate pH value in each case) and a three-electrode system (silver/silver chloride reference electrode, platinum wire counter electrode and ITO/PET working electrode). Differential pulse voltammetry (DPV) was used to evaluate the oxidation of $[Fe(CN)_6]^{4-}$ to $[Fe(CN)_6]^{3-}$, applying a pre-treatment at −0.1 V for 30 s and scanning between −0.1 V and +1.1 V (step potential: 10 mV, modulation amplitude: 50 mV, and scan rate: 33.5 mV/s). Measurements were carried out in triplicate using a single nanoporous membrane and ITO/PET electrode, both discarded after each measurement.

2.6 Catalase detection

For catalase enzyme detection, anti-catalase antibodies at a concentration of 50 µg/mL were immobilized in the inner walls of nanoporous alumina membranes following the same procedure as described in Section 2.4. The concentration of antibody was reduced in this case to improve the cost-effectivity of the sensor. First, the optimum pH used for measurement was evaluated, using buffer solutions of Tris-HCl 0.1M pH 7.0 and Tris-HCl 0.1 M pH 8.2, in an immunosensor containing a fixed catalase concentration of 500 ng/mL (added after anti-catalase antibody immobilization, as explained in Section 2.4). Control assays were performed in Tris-HCl 0.1 M pH 7.0 without catalase being added. For the quantification of catalase, increasing catalase concentrations ranging from 50 to 500 ng/mL were added to different membranes and measured using a measurement buffer solution of Tris-HCl 0.1 M pH 7.5, as optimum pH value.

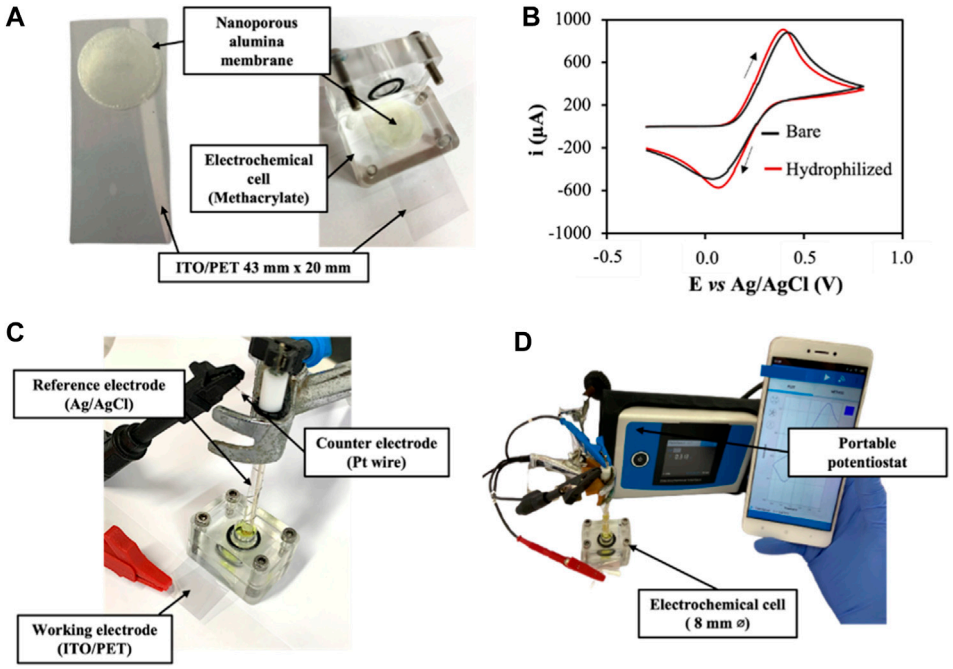

FIGURE 2
(A). Picture of the nanoporous membranes integrated on top of an hydrophilized ITO/PET electrode. **(B)**. Electrochemical characterization of bare ITO/PET electrodes and hydrophilized ITO/PET electrodes. Cyclic voltammograms recorded from −0.4 to +0.8 V (vs. Ag/AgCl) in $[Fe(CN)_6]^{4-}$/Tris-HCl 0.1M pH 7.2. Scan rate:50 mV/s; step potential: 10 mV. **(C)**. Picture of the electrochemical cell assembling. **(D)**. Picture of the complete set-up, including the portable potentiostat controlled by a smartphone.

2.7 Spike and recovery assay in artificial wound media

To evaluate the applicability of the method in a real scenario, a spike and recovery assay was performed in artificial wound media (Galliani et al., 2020), composed of sodium chloride (124 μM), sodium bicarbonate (36.8 μM), magnesium chloride (0.831 μM), calcium chloride (2.48 μM), glucose (5 μM), lactic acid (0.010 μM) and bovine albumin (0.150 μM). The pH of the solution was adjusted to 6.7. The artificial wound media was spiked with catalase at concentrations of 100 and 500 ng/mL. After incubation, membranes were gently washed with Tris-HCl 0.1 M pH 7.5 prior to measurement in a 10 mM $K_4[Fe(CN)_6]$ solution in the same buffer.

3 Results and discussion

3.1 Nanoporous membranes structural characterization and ITO/PET electrodes evaluation

Nanoporous alumina membranes with thicknesses of 40, 60 and 100 μm and a diameter size of around 60 nm were obtained following a two-step anodization process by modifying the time of the second anodization step. The rationale behind the selection of 40, 60 and 100 μm as pore thickness is based on the thickness of commercially available nanoporous alumina membranes (60 μm). This type of membranes have been extensively used for sensing purpose, with parameters such as the pore diameter been deeply optimized (de la Escosura-Muñiz and Merkoçi, 2010). However, due to the fixed thickness of these membranes, this parameter was to a lesser extent studied. A nanopore thickness equivalent to the commercially available one (60 μm) was compared in this work with a lower (40 μm) and a higher (100 μm) thickness value.

The obtained nanoporous alumina membranes were characterized, both top (Figure 1A) and cross-section (Figures 1C–E) by SEM. Membranes presented a homogeneous honeycomb-like structure of an average diameter size of 59 ± 4 nm for the 40 thickness membranes (Figure 1B), maintained for all the thicknesses tested (Supplementary Figure S2). The spherical shape of the obtained nanopores contrasts with the irregularities observed in commercial filtering alumina membranes (Supplementary Figure S3) with a nanopore diameter of 20 nm, making them more suitable for their use in biosensing. Commercial membranes of 20 nm diameter sized were selected in this case as control as the diameter size is the closest available to the membranes obtained in this case, being other commercial options of diameters of 100 and 200 nm.

To increase the integrability and portability of the developed sensor, membranes were incorporated on top of a hydrophilized ITO/PET electrode (Figure 2A). The effect of the hydrophilization pretreatment over the electrochemical behavior of the ITO/PET electrode was previously evaluated by recording cyclic voltammograms in $[Fe(CN)_6]^{4-}$/Tris-HCl 0.1 M pH 7.2, and comparing them with the obtained for an unmodified electrode (Figure 2B). No variation was observed neither in the anodic/cathodic peak potentials nor in the current peak intensity,

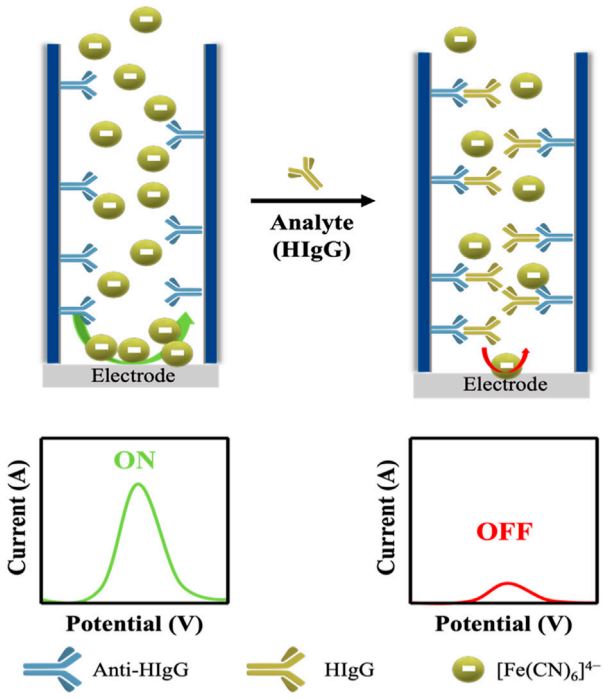

FIGURE 3
Schematic representation of the sensing principle for the immunosensor for the detection of HIgG. When anti-HIgG antibodies are immobilized inside the pore (left side), the passage of a redox indicator solution ($[Fe(CN)_6]^{4-}$) is slightly reduced, leaving the channel open, what leads to a high current recorded. In the presence of the target analyte, in this case HIgG, the capturing of this molecule inside the nanopore is associated to a decrease in the current recorded due to a closure of the channel.

confirming that the hydrophilization treatment applied did not affected the electrode performance. ITO/PET electrodes were selected over alternative electrode materials, as screen-printed carbon electrodes (SPCEs) as they are flexible and biocompatible materials that also increase the stability of the measurements (by being just the working electrode covered by the membrane) (Figure 2C), increasing the reproducibility of the system. The complete set-up is shown in Figure 2D, consisting on the anchoring of the nanoporous alumina membrane and the ITO/PET electrode inside a methacrylate chamber, that clamps both pieces without generating noticeable air gaps.

3.2 Evaluation of membrane thickness effect in the nanochannel blockage produced by the immunocomplex

To evaluate how the thickness of the nanoporous membranes affects the sensitivity of the (bio)analytical platform developed, an immunosensor for the detection of HIgG was constructed through the immobilization of anti-HIgG antibodies in the inner walls of the nanochannels (Figure 3). The principle of the developed platform is based on the specific capturing of HIgG inside the nanochannels, what blocks the passage of the red-ox indicator $[Fe(CN)_6]^{4-}$ to the electrode, reducing the voltammetric signal associated to the oxidation of this molecule.

HIgG has already been detected using commercially available nanoporous alumina membranes (de la Escosura-Muñiz and Merkoçi, 2010). In such work, the authors observed that the diameter of nanoporous membranes affected the blockage, being able to detect lower concentrations of HIgG with membranes of 20 nm of pore diameter than with those of 200 nm. However, the effect of membranes thickness has been hardly studied in these solid-state membranes.

Membranes with three different nanochannel thicknesses (40, 60 and 100 μm) and an average pore diameter of 60 nm have been fabricated and evaluated. The performance of these membranes has been compared to those of commercial membranes with 60 μm thickness and 20 nm diameter size. Since commercial diameters of 60 nm, highly desirable for an accurate comparison are not available, we selected those of 20 nm since this small size is what offers a better sensitivity (de la Escosura-Muñiz and Merkoçi, 2010). Membranes were tested for HIgG at concentrations 100, 500 and 1,000 μg/mL.

To simplify and standardize the results, the degree of blockage in the investigations reported in the following sections has been defined as the index of HIgG current blockage in percentage (Eq. (1)):

$$\text{Index of HIgG Current Blockage } (\Delta I_{HIgG})\ (\%) = \left(\frac{I_0 \text{ antibody modified membranes- } I_{HIgG} \text{ immunocomplex}}{I_0 \text{ antibody modified membranes}}\right) x\ 100 \quad (1)$$

where I correspond to the peak current value of the voltammetric oxidation of the redox indicator used.

The mentioned index was calculated for each membrane by measuring the current just after the antibody immobilization step (corresponding to I_0 antibody-modified membranes) and after the formation of the immunocomplex (I_{HIgG} immunocomplex). This strategy, compared to the use of individual membranes for each step (Toyos-Rodríguez et al., 2023), increases the reproducibility of the method while facilitates manipulation, what increases the potential of the sensor for point-of-care applications.

Measurements were performed at a pH of 9.0, at which both anti-HIgG antibody and HIgG were expected to be negatively charged (Tang et al., 2021). The equal charge of the redox indicator $[Fe(CN)_6]^{4-}$ and the biomolecules inside the channel leads to the appearance of a repulsion effect that hinders the passage of the redox indicator, increasing the electrostatic blockage of the electrochemical signal obtained. This variable has been previously reported as a relevant factor in electrochemical-based nanopore sensors (Wang et al., 2010).

Apart from the electrostatic blockage owing to the charges inside the nanopore, steric effects, associated with the dimensions of the nanopore, contribute to the global blockage obtained. In particular, the influence of the membranes thicknesses in the steric blockage applied for the detection of HIgG is studied in this work for the first time.

As shown in Figure 4A, the analytical signal, corresponding to the oxidation of $[Fe(CN)_6]^{4-}$ to $[Fe(CN)_6]^{3-}$, for a fixed amount of HIgG (100 μg/mL) decreases with the membrane thickness. This behavior suggests that for the thinner membranes all the antibodies are bound to antigens, leaving a narrow path for the redox indicator

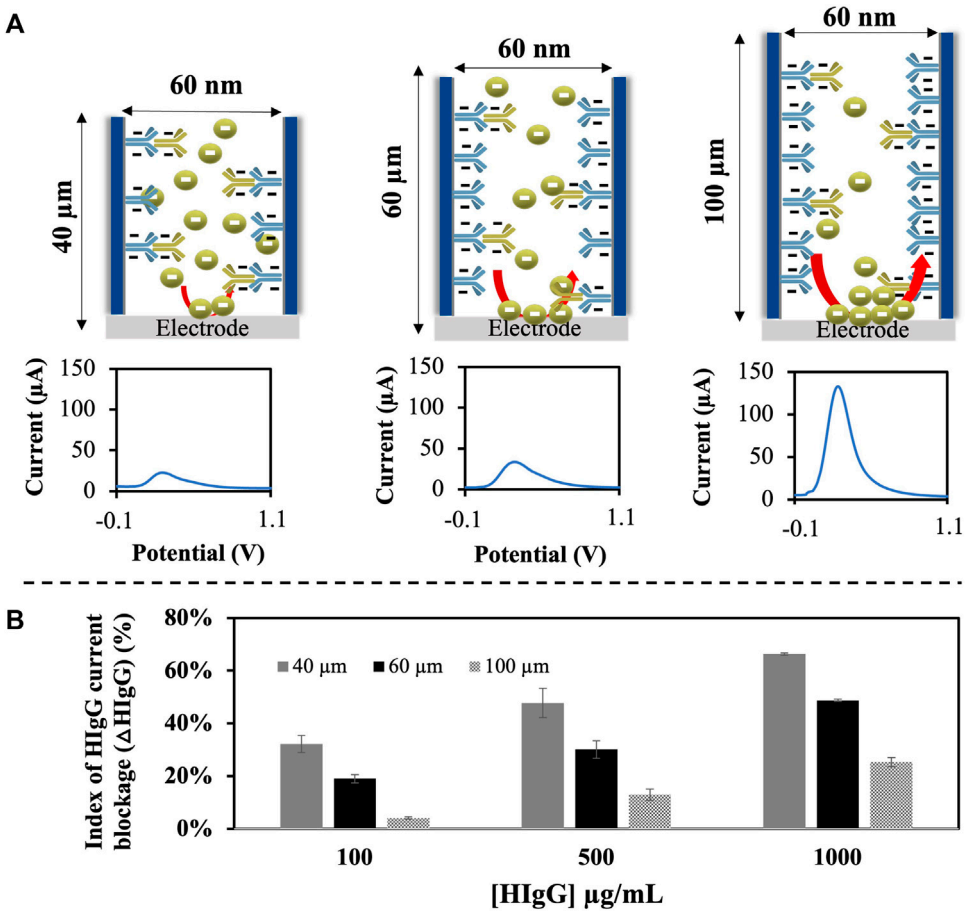

FIGURE 4
Study of the effect of membrane thickness in the sensitivity of an HIgG immunosensor. **(A)**. Schematic representation of the different membranes used with increasing thickness and different diameters, together with representative voltammograms obtained with differential pulse voltammetry (DPV) for each case at a HIgG concentration of 100 µg/mL. **(B)**. Results obtained represented as the mean and SD of the index of HIgG current blockage (ΔHIgG) (%) per each concentration studied. ΔHIgG was calculated considering the voltammetric signal, associated to the oxidation of $[Fe(CN)_6]^{4-}$ to $[Fe(CN)_6]^{3-}$ recorded through DPV with a pre-treatment at −0.1 V for 30 s and, a scan range of −0.1 V to +1.1 V (step potential: 10 mV, modulation amplitude: 50 mV, and scan rate: 33.5 mV/s).

TABLE 1 Analytical characteristics obtained or the detection of human IgG (HIgG) using nanoporous alumina membranes with different thicknesses.

Preparation	Thickness (µm)	Diameter size (nm)	Slope (ΔHIgG (%))	LOD (µg/mL)	r
Self-prepared	40	~60	0.0379	24.2	0.999
	60	~60	0.0332	158.8	0.997
	100	~60	0.0236	62.5	0.999
Commercial	60	~20	0.0373	152.8	0.997

ions diffusion. However, as the thickness increases, more antibodies are free leading to a wider space for the ions passage.

This behavior was also evaluated for different concentrations of HIgG, giving the results in terms of index of current blockage (Figure 4B). As can be observed, values of 32% are reached for membranes with a thickness of 40 µm for the lowest HIgG concentration tested (100 µg/mL) compared to a 4% in membranes with a 100 µm thickness. These results point out that the reduction of the nanoporous membrane thickness is directly related with the blockage obtained and hence the performance of sensors developed using this material as platform. In other words, for the thinner membranes lower amounts of antigen are enough to block the nanochannel, leading to a better sensitivity. Moreover, in all cases a linear relationship between the index of current blockage and the concentration of HIgG is obtained. The analytical characteristics obtained with the self-prepared nanoporous alumina membranes with variable thicknesses are shown at Table 1. Commercial membranes with a pore diameter of 20 nm and a thickness of 60 µm were also evaluated for comparison purposes.

As summarized in Table 1, when the sensitivity and limit-of-detection (LOD) obtained with each membrane were evaluated, results showed that membranes with a thickness of 40 μm provided a higher sensitivity (slope of 0.0379 ΔHIgG (%)) and lower LOD (calculated as three times the standard deviation of the intercepted divided by the slope) (24.2 μg/mL HIgG) compared to the analytical results provided with thicker membranes. For membranes with a thickness of 100 μm, the LOD obtained was lower than for those of 60 μm, even though they presented the lowest sensitivity.

For the commercial membranes used as a control with a diameter of 20 nm, a LOD more than 6 times higher than for self-prepared 40 μm membranes (152.8 μg/mL) was obtained, evidencing the better performance of our membranes and the key relevance of the nanochannel thickness.

Although the number of concentrations tested is reduced and a more representative HIgG calibration curve would be required to extract more accurate conclusions, results point out that controlling the thickness is also of paramount importance to improve the sensitivity of immunosensors and reduce de minimum quantity that can be differentiated through electrochemical recording.

Although the lowest LOD was achieved with the lower thickness 40 μm membranes, the obtained for 100 μm probed to be better than the one obtained for 60 μm. However, the sensitivity obtained in this second case is much lower, what also correlates with the index of current blockage achieved with these membranes (Figure 4). We believed that thickness of the membranes affects two aspects of the sensor that are directly related with the LOD achieved: 1) the physical space for antibody immobilization and 2) the distance between the upper side of the nanochannel and the electrode.

For the first one, the increase in the thickness also increases the number of antibodies that can be immobilized on the inner side of the nanochannel for a fixed excess concentration of antibody. In this sense, for nanoporous membranes with 100 μm thickness, a higher proportion of antibodies might be immobilized inside the nanochannel, facilitating the captured of the analyte of interest avoiding any steric impedance. However, the reduced thickness of 40 and 60 μm membranes also decreases the antibody immobilization rate that can be achieved. But although this aspect can increase steric hindrance, reducing antibody-antigen interaction, it also means that a lower protein concentration can completely block the nanochannel. This is probably a reason why the LOD is lower for 40 μm membranes, where a compromised situation between minimum protein concentration required for blocking and steric impedance is reached.

Additionally, a second factor, the distance between the upper side of a nanochannel and the electrode, also plays a role in the relation between thickness and LOD. Regarding this one, the larger the distance, the longer it takes to reach the electrode, introducing diffusion effects that can also alter the sensitivity and hence the LOD achieved.

3.3 Catalase wound infection biomarker detection

The optimal 40 μm-thickness nanoporous membranes were applied for the development of an immunosensor for the detection of catalase. Catalase is an important heme-containing enzyme that catalyzes the dismutation of hydrogen peroxide (H_2O_2) into O_2 and H_2O (Kurahashi and Fujii, 2015). Together with other enzymes as superoxide dismutase or peroxidase, catalase is implicated in wound healing, being downregulated in this process.

Catalase is also produced by most aerobic bacteria to neutralize the bactericidal effect of H_2O_2 (Dunnill et al., 2017). The identification of this enzyme is an easy way to determine the presence of infection inside a wound.

Considering the sizes of both catalase (~240 kDa) (Pakhomova et al., 2009) and of the anti-catalase antibody (~150 kDa) (Chiu et al., 2019), the detection of such enzyme is feasible using membranes containing nanopores of 60 nm.

Monoclonal anti-catalase antibodies were immobilized in the inner walls of the nanoporous membranes through carbodiimide chemistry. Although the exact isoelectric point (pI) of this antibody was not determined, mouse IgG present a pI in the range between 6.4 and 8.0 (Danielsson et al., 1988). Regarding human catalase from erythrocytes (UniProt Code P04040), the analyte of interest, it presents a theoretical pI of 6.9, thus a pH higher than this value would be desirable to maximize the blockage obtained. Moreover, catalase, as every enzyme, has an optimum pH range in between it maintains native conformation of the active site. For catalase, it is hypothesized that this value ranges between pH 6 and 8.

Considering this information, the pH of the measurement solution used for catalase detection was first optimized to maximize the electrostatic blockage obtained. Redox indicator solutions with pH values of 6.9 and 7.5 were tested for a catalase concentration of 500 ng/mL. At this pH range, the anti-catalase antibodies are positively charged (pH below their pI), what should favor the passage of the negatively charged red-ox indicator ions to the electrode. However, the introduction of negative charges inside the nanochannel should have an electrostatic repulsion effect over the $[Fe(CN)_6]^{4-}$ redox indicator, what would lead in a decrease in the voltammetric signal recorded.

Data has been normalized in terms of the index catalase current blockage as stated in Eq. (2):

$$\text{Index of Catalase Current Blockage}$$
$$(\Delta I_{Cat})\ (\%) = \left(\frac{I_0 \text{ anti-Cat antibody modified membrane} - I \text{ Cat immunoassay}}{I_0 \text{ anti-Cat antibody modified membrane}} \right) x\ 100. \quad (2)$$

According to the scheme depicted in Figure 5A, at a pH of 6.9, catalase enzyme is not charged, as this pH value almost corresponds with the pI of this molecule. As shown in Figure 5B, under these conditions, a current blockage of only 13% is obtained. However, at a pH 7.5, a high increase of ~3 times in the index blockage (35%) is recorded, what agrees with the fact that at this pH value, catalase enzyme is negatively charged, exerting a high electrostatic hindrance inside the nanochannel. This difference observed points out the utility of this methodology not just for biomolecules detection/quantification but also for the estimation of their pI.

After the optimization of the measurement pH, catalase was determined using a $[Fe(CN)_6]^{4-}$ solution in Tris-HCl at a pH 7.5 as buffer solution. A logarithmic relationship between the index of catalase current blockage and the concentration of this biomolecule was observed (Figure 5C). The LOD (calculated as three times the standard deviation of the intercepted divided by the slope) obtained

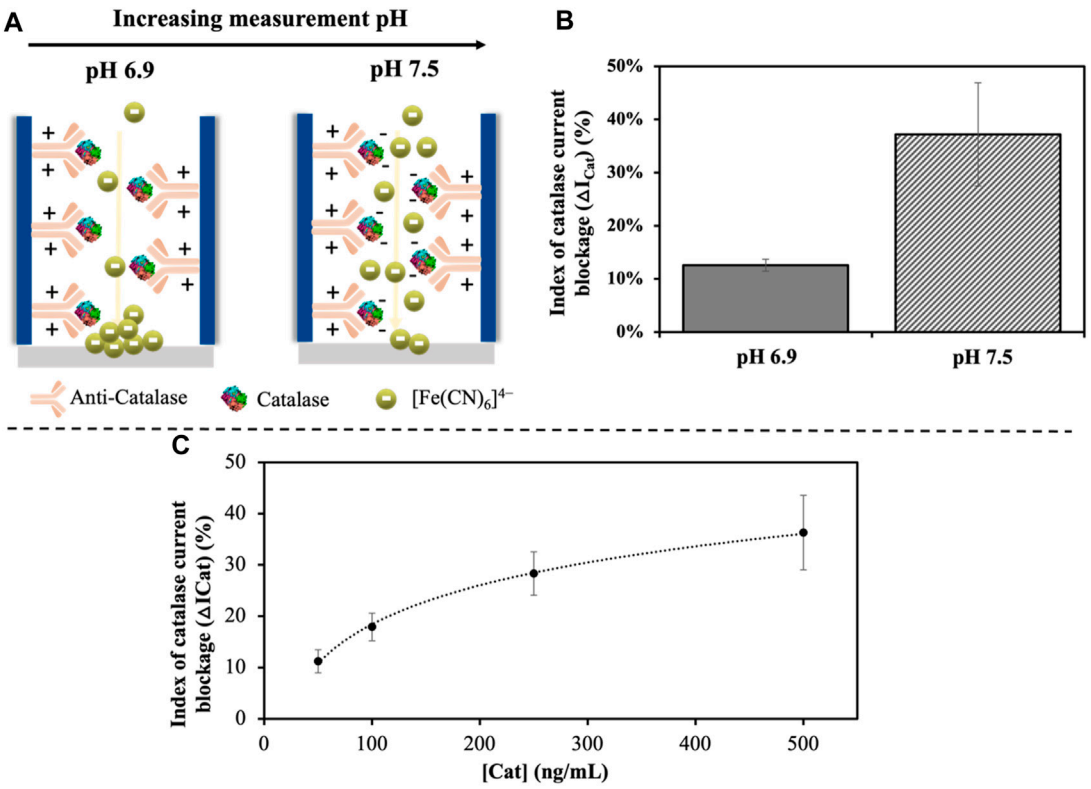

FIGURE 5
Effect of the pH used for measurement **(A)**. Representation of the electrostatic profile of the catalase immunocomplex at varying pH and how it affects the diffusion of the $[Fe(CN)_6]^{4-}$ red-ox indicator ions through the channel. **(B)**. Effect of the pH on the index of catalase current blockage (as defined in Eq. 2) represented by the average ±SD (n = 3). **(C)**. Effect of the catalase concentration on the index of catalase current blockage in the range of 50–500 ng/mL, showing a logarithmic relation.

TABLE 2 Spike and recovery assay data in artificial wound media for catalase concentrations of 100 and 500 ng/mL.

Sample	Spiked catalase concentration (ng/mL)	Index of catalase current blockage in buffer (%)	Index of catalase current blockage in artificial wound fluid (%)	Recovery (%)
Artificial wound fluid	100	17.9	21.2	118
	500	36.3	39.9	110

was of 1.5 ng/mL for a linear range of 50–500 ng/mL with a correlation coefficient (r) of 0.998, adjusted to Eq. (3):

$$\text{Peak current}\ (\mu A) = 25.241 \log[\text{Catalase}]\,(\text{ng/mL}) - 32.081 \quad (3)$$

The sensor developed showed a relevant performance, with a good reproducibility (relative standard deviation (RSD) of 12% (n = 3)), and a limit of quantification (LOQ) (calculated as ten-time the standard deviation of the intercept by the slope) of 3.8 ng/mL, which is equivalent to 0.19 U/mL (~50.000 U/mg protein). This value is in accordance with the provided by alternative techniques as the stablished spectrophotometric method of Aebi (Aebi, 1984). However, this methodology presents major drawbacks as the high concentration of H_2O_2 that needs to be added for the catalytic reaction to be recorded (30 mM), which can alter the activity of catalase, and the low specificity of the optical detection (at 240 nm) in biological samples (Farman and Hadwan, 2021).

The versatility of this methodology allows the detection of catalase not just as a wound management biomarker, but also as antioxidant in relation to other pathologies.

3.4 Spike and recovery in artificial wound fluid

The performance of the developed sensor was evaluated in an artificial wound fluid solution that mimics the composition of wound fluids in which catalase can be present (Galliani et al., 2020). By spiking an artificial wound fluid with two catalase concentrations, 100 and 500 ng/mL, the selectivity of the methodology was evaluated. The analytical signals obtained were in accordance with the ones provided in buffer solution, obtaining quantitative recoveries of 118% and 110%, respectively (Table 2). These confirms the suitability of the developed method for the

detection of catalase in wound fluids, which is expected due to the low filtering properties that nanoporous alumina membranes have.

4 Conclusion

The effect of the thickness of nanoporous alumina membranes in the sensitivity of a sensor developed using this material as sensing platform has been stated in this work. To probe this, an immunosensor based on the determination of the blockage that HIgG produces to the diffusion of the red-ox indicator $[Fe(CN)_6]^{4-}$ was developed. In previous works, the diameter of the nanochannels used was optimized and studied, observing that the reduction of this parameter not always favours the performance of the sensor. In this occasion, the contribution of the thickness of the nanochannel to the steric blockage was evaluated for an electrochemical-based nanoporous sensor. This work confirms that reducing this parameter increases the sensitivity while improves the LOD achieved. Our hypothesis points out that for the thinner membranes all the antibodies are bound to antigens, leaving a narrow path for the redox indicator ions diffusion. This means that lower amounts of antigen are enough to block the nanochannel, leading to a better sensitivity. However, as the thickness increases, more antibodies are free leading to a wider space for the ions passage, what is traduced in a worst sensitivity.

The reduction of the thickness to a value of 40 μm provides 6 times lower LOD than thicker commercially available nanoporous membranes (60 μm) with smaller diameter (20 nm instead of 60 nm). Overall, our work confirms that nanoporous alumina membrane thickness is as important as pore diameter and should be also considered in the use of these membranes as sensing platforms.

The optimized nanoporous membranes were applied for the detection of catalase, being able to detect this enzyme in artificial wound fluids, without sample pre-treatment, showing a low LOD. The feasibility, low cost and integrability of our system make it an ideal strategy for the rapid monitoring of not just wound infection, but also wound healing in just a few hours.

Data availability statement

The raw data supporting the conclusion of this article will be made available by the authors, without undue reservation.

Ethics statement

Written informed consent was obtained from the individual(s) for the publication of any potentially identifiable images or data included in this article.

Author contributions

CT-R: Conceptualization, Formal Analysis, Investigation, Methodology, Writing–original draft. DV-C: Writing–review and editing, Investigation. AI-M: Investigation, Writing–review and editing. AdlE: Writing–review and editing, Conceptualization, Data curation, Funding acquisition, Supervision.

Funding

The author(s) declare financial support was received for the research, authorship, and/or publication of this article. This work has been supported by the MCI-21-PID2020-115204RBI00 and RED2022-134120-T projects from Spanish Ministry of Science and Innovation (MICINN), and the SV-PA-21-AYUD/2021/51323 project from the Asturias Regional Government.

Acknowledgments

CT-R and DV-C thank the MICINN for the award of FPI Grants (PRE2018-084953 and PRE2021-097567, respectively). Authors would also like to acknowledge the technical support provided by Servicios Científico-Técnicos de la Universidad de Oviedo.

Conflict of interest

The authors declare that the research was conducted in the absence of any commercial or financial relationships that could be construed as a potential conflict of interest.

The author(s) declared that they were an editorial board member of Frontiers, at the time of submission. This had no impact on the peer review process and the final decision.

Publisher's note

Supplementary material

The Supplementary Material for this article can be found online at: https://www.frontiersin.org/articles/10.3389/fbioe.2024.1310084/full#supplementary-material

References

Aebi, H. (1984). "[13] catalase *in vitro*," in *Methods in enzymology* (Germany: Elsevier), 121–126. doi:10.1016/S0076-6879(84)05016-3

Baker, R. E., Mahmud, A. S., Miller, I. F., Rajeev, M., Rasambainarivo, F., Rice, B. L., et al. (2022). Infectious disease in an era of global change. *Nat. Rev. Microbiol.* 20, 193–205. doi:10.1038/s41579-021-00639-z

Bayley, H., and Cremer, P. S. (2001). Stochastic sensors inspired by biology. *Nature* 413, 226–230. doi:10.1038/35093038

Bernabé-Ortiz, A., Zafra-Tanaka, J. H., Moscoso-Porras, M., Sampath, R., Vetter, B., Miranda, J. J., et al. (2021). Diagnostics and monitoring tools for noncommunicable diseases: a missing component in the global response. *Glob. Health* 17, 26. doi:10.1186/s12992-021-00676-6

Campuzano, S., and Pingarrón, J. M. (2023). Electrochemical affinity biosensors: pervasive devices with exciting alliances and horizons ahead. *ACS Sens. acssensors* 8, 3276–3293. doi:10.1021/acssensors.3c01172

Chester, B., and Moskowitz, L. B. (1987). Rapid catalase supplemental test for identification of members of the family Enterobacteriaceae. *J. Clin. Microbiol.* 25, 439–441. doi:10.1128/jcm.25.2.439-441.1987

Chiu, M. L., Goulet, D. R., Teplyakov, A., and Gilliland, G. L. (2019). Antibody structure and function: the basis for engineering therapeutics. *Antibodies* 8, 55. doi:10.3390/antib8040055

Clemente, A., Alba-Patiño, A., Rojo-Molinero, E., Russell, S. M., Borges, M., Oliver, A., et al. (2020). Rapid detection of *Pseudomonas aeruginosa* biofilms via enzymatic liquefaction of respiratory samples. *ACS Sens.* 5, 3956–3963. doi:10.1021/acssensors.0c01618

Clinton, A., and Carter, T. (2015). Chronic wound biofilms: pathogenesis and potential therapies. *Lab. Med.* 46, 277–284. doi:10.1309/LMBNSWKUI4JPN7SO

Cuevas, A. L., Vega, V., Domínguez, A., González, A. S., Prida, V. M., and Benavente, J. (2023). Optical characterization of ALD-coated nanoporous alumina structures: effect of sample geometry or coated layer material. *Micromachines* 14, 839. doi:10.3390/mi14040839

Danielsson, Å., Ljunglöf, A., and Lindblom, H. (1988). One-step purification of monoclonal IgG antibodies from mouse ascites. *J. Immunol. Methods* 115, 79–88. doi:10.1016/0022-1759(88)90312-2

Dekker, C. (2007). Solid-state nanopores. *Nat. Nanotechnol.* 2, 209–215. doi:10.1038/nnano.2007.27

de la Escosura-Muñiz, A., and Merkoçi, A. (2010). Label-free voltammetric immunosensor using a nanoporous membrane based platform. *Electrochem. Commun.* 12, 859–863. doi:10.1016/j.elecom.2010.04.007

de la Escosura-Muñiz, A., and Merkoçi, A. (2012). Nanochannels preparation and application in biosensing. *ACS Nano* 6, 7556–7583. doi:10.1021/nn301368z

Dunnill, C., Patton, T., Brennan, J., Barrett, J., Dryden, M., Cooke, J., et al. (2017). Reactive oxygen species (ROS) and wound healing: the functional role of ROS and emerging ROS-modulating technologies for augmentation of the healing process. *Int. Wound J.* 14, 89–96. doi:10.1111/iwj.12557

Farman, A. A., and Hadwan, M. H. (2021). Simple kinetic method for assessing catalase activity in biological samples. *MethodsX* 8, 101434. doi:10.1016/j.mex.2021.101434

Galliani, M., Diacci, C., Berto, M., Sensi, M., Beni, V., Berggren, M., et al. (2020). Flexible printed organic electrochemical transistors for the detection of uric acid in artificial wound exudate. *Adv. Mat. Interfaces* 7, 2001218. doi:10.1002/admi.202001218

Inda-Díaz, J. S., Lund, D., Parras-Moltó, M., Johnning, A., Bengtsson-Palme, J., and Kristiansson, E. (2023). Latent antibiotic resistance genes are abundant, diverse, and mobile in human, animal, and environmental microbiomes. *Microbiome* 11, 44. doi:10.1186/s40168-023-01479-0

Ito, T., and Nathani, A. (2022). Electrochemical sensing at nanoporous film-coated electrodes. *Electrochem. Sci. Adv.* 2, e2100126. doi:10.1002/elsa.202100126

Kurahashi, T., and Fujii, J. (2015). Roles of antioxidative enzymes in wound healing. *J. Dev. Biol.* 3, 57–70. doi:10.3390/jdb3020057

Liu, H., Zhou, Q., Wang, W., Fang, F., and Zhang, J. (2023). Solid-state nanopore array: manufacturing and applications. *Small* 19, 2205680. doi:10.1002/smll.202205680

Luppa, P. B., Müller, C., Schlichtiger, A., and Schlebusch, H. (2011). Point-of-care testing (POCT): current techniques and future perspectives. *Trac. Trends Anal. Chem.* 30, 887–898. doi:10.1016/j.trac.2011.01.019

Miethke, M., Pieroni, M., Weber, T., Brönstrup, M., Hammann, P., Halby, L., et al. (2021). Towards the sustainable discovery and development of new antibiotics. *Nat. Rev. Chem.* 5, 726–749. doi:10.1038/s41570-021-00313-1

Opota, O., Croxatto, A., Prod'hom, G., and Greub, G. (2015). Blood culture-based diagnosis of bacteraemia: state of the art. *Clin. Microbiol. Infect.* 21, 313–322. doi:10.1016/j.cmi.2015.01.003

Pakhomova, S., Gao, B., Boeglin, W. E., Brash, A. R., and Newcomer, M. E. (2009). The structure and peroxidase activity of a 33-kDa catalase-related protein from *Mycobacterium avium* ssp. paratuberculosis: crystal Structure of MAP_2744c. *Protein Sci.* 18, 2559–2568. doi:10.1002/pro.265

Rasik, A. M., and Shukla, A. (2001). Antioxidant status in delayed healing type of wounds: delayed healing wounds and antioxidants. *Int. J. Exp. Pathol.* 81, 257–263. doi:10.1046/j.1365-2613.2000.00158.x

Ren, R., Zhang, Y., Nadappuram, B. P., Akpinar, B., Klenerman, D., Ivanov, A. P., et al. (2017). Nanopore extended field-effect transistor for selective single-molecule biosensing. *Nat. Commun.* 8, 586. doi:10.1038/s41467-017-00549-w

Sartini, M., Carbone, A., Demartini, A., Giribone, L., Oliva, M., Spagnolo, A. M., et al. (2022). Overcrowding in emergency department: causes, consequences, and solutions—a narrative review. *Healthcare* 10, 1625. doi:10.3390/healthcare10091625

Shin, D.-H., Choi, Y.-S., and Cho, Y.-H. (2008). Unusual properties of catalase A (KatA) of *Pseudomonas aeruginosa* PA14 are associated with its biofilm peroxide resistance. *J. Bacteriol.* 190, 2663–2670. doi:10.1128/JB.01580-07

Siddiqui, A. R., and Bernstein, J. M. (2010). Chronic wound infection: facts and controversies. *Clin. Dermatol.* 28, 519–526. doi:10.1016/j.clindermatol.2010.03.009

Sokolenko, A. P., and Imyanitov, E. N. (2018). Molecular diagnostics in clinical oncology. *Front. Mol. Biosci.* 5, 76. doi:10.3389/fmolb.2018.00076

Spitzberg, J. D., Zrehen, A., Van Kooten, X. F., and Meller, A. (2019). Plasmonic-nanopore biosensors for superior single-molecule detection. *Adv. Mat.* 31, 1900422. doi:10.1002/adma.201900422

Tang, Y., Cain, P., Anguiano, V., Shih, J. J., Chai, Q., and Feng, Y. (2021). Impact of IgG subclass on molecular properties of monoclonal antibodies. *mAbs* 13, 1993768. doi:10.1080/19420862.2021.1993768

Toyos-Rodríguez, C., García-Alonso, F. J., and de la Escosura-Muñiz, A. (2023). Towards the maximization of nanochannels blockage through antibody-antigen charge control: application for the detection of an Alzheimer's disease biomarker. *Sens. Actuators B Chem.* 380, 133394. doi:10.1016/j.snb.2023.133394

Unlu, A., and Abusoglu, S. (2022). Clinical laboratory use of liquid chromatography mass spectrometry. *Turk. J. Biochem.* 47, 548–556. doi:10.1515/tjb-2021-0259

Van Den Hout, M., Hall, A. R., Wu, M. Y., Zandbergen, H. W., Dekker, C., and Dekker, N. H. (2010). Controlling nanopore size, shape and stability. *Nanotechnology* 21, 115304. doi:10.1088/0957-4484/21/11/115304

Wang, S., Zhang, Y., Sun, F., Xi, K., Sun, Z., Zheng, X., et al. (2023). Catalase-like nanozymes combined with hydrogel to facilitate wound healing by improving the microenvironment of diabetic ulcers. *Mat. Des.* 225, 111557. doi:10.1016/j.matdes.2022.111557

Wang, Y., Zhao, Y., Bollas, A., Wang, Y., and Au, K. F. (2021). Nanopore sequencing technology, bioinformatics and applications. *Nat. Biotechnol.* 39, 1348–1365. doi:10.1038/s41587-021-01108-x

Wang, Z.-M., Wang, W., Coombs, N., Soheilnia, N., and Ozin, G. A. (2010). Graphene Oxide–Periodic mesoporous silica sandwich nanocomposites with vertically oriented channels. *ACS Nano* 4, 7437–7450. doi:10.1021/nn102618n

Xu, S., Du, C., Zhang, M., Wang, R., Feng, W., Wang, C., et al. (2023). Electroactive and antibacterial wound dressings based on Ti3C2Tx MXene/poly(ε-caprolactone)/gelatin coaxial electrospun nanofibrous membranes. *Nano Res.* 16, 9672–9687. doi:10.1007/s12274-023-5527-z

Xue, L., Yamazaki, H., Ren, R., Wanunu, M., Ivanov, A. P., and Edel, J. B. (2020). Solid-state nanopore sensors. *Nat. Rev. Mat.* 5, 931–951. doi:10.1038/s41578-020-0229-6

frontiers | Frontiers in Bioengineering and Biotechnology

TYPE Review
PUBLISHED 13 March 2024
DOI 10.3389/fbioe.2024.1361469

OPEN ACCESS

EDITED BY
Yizhong Huang,
Nanyang Technological University, Singapore

REVIEWED BY
Abdellatif Ait Lahcen,
Cornell University, United States
Elsa Materon,
University of São Paulo, São Carlos, Brazil

*CORRESPONDENCE
Resmond L. Reaño,
rlreano@up.edu.ph

RECEIVED 26 December 2023
ACCEPTED 15 February 2024
PUBLISHED 13 March 2024

CITATION
Reaño RL and Escobar EC (2024), A review of antibody, aptamer, and nanomaterials synergistic systems for an amplified electrochemical signal.
Front. Bioeng. Biotechnol. 12:1361469.
doi: 10.3389/fbioe.2024.1361469

A review of antibody, aptamer, and nanomaterials synergistic systems for an amplified electrochemical signal

Resmond L. Reaño* and Erwin C. Escobar

Department of Engineering Science, College of Engineering and Agro-industrial Technology, University of the Philippines Los Baños, Los Baños, Philippines

The synergy between biomolecules with inorganic nanomaterials and nanoparticles has been investigated over the past years, primarily to improve biomarker reception, generate signals, and amplify the signals generated. In this paper, several articles on aptamer-based and antibody-based electrochemical biosensors that target antigens were examined. Among the key characteristics identified were the electrochemical platform development, which includes the usage of nanomaterials as electroactive or electrocatalytic labels, crosslinking of the biological agent with inorganic compounds, and electrode coating to provide an electronic source and support efficient electron transfer. A single approach using labeled or unlabeled biological receptors has become advantageous due to its simple architecture and more straightforward application method. However, the dual system approach allows the incorporation of more nanomaterials to boost the signal and add more features to the electrochemical system. The dual system approach uses a capture and reporter probe in a competitive or sandwich detection format. The reporter probe is often labeled by an electroactive or electrocatalytic compound or immobilized in a nanocarrier, resulting in an increase in measured peak current in proportion to the target's concentration. The reported limit of detection and linear range for each platform is presented to assess its efficiency. Generally, the dual system aptasensor showed higher sensitivity, stability, and reproducibility than the immunosensor in comparable settings. The aptasensor showed promising results for the development of point-of-care type applications.

KEYWORDS

dual system approach, sandwich format, monoclonal antibody, electrochemical aptasensor, nanocarrier

1 Introduction

Biosensor offers advantages such as rapid, more straightforward sample processing and implementation and cost-effective, sensitive, and stable detection method (Wei et al., 2018). It can be utilized in various fields, such as medicine, the food and packaging industry, agriculture, and environmental monitoring (Jafari et al., 2019). The biosensor's analytical sensitivity and selectivity rely heavily on a stable, strong, and specific binding between the molecular recognition element—the bioreceptor, and the target biomarker (Kondzior and Grabowska, 2020). Antibodies have become a popular candidate for biosensor development owing to their high affinity and specificity to their target biomolecule. Antibody-based Enzyme-Linked Immuno-Sorbent Assay (ELISA), the gold standard for all immunoassays is

still popular and is used worldwide in different fields of application, particularly in clinical diagnostics. With the advancements in analytical and bioanalytical chemistry, the incorporation of antibodies directly to the signal transducer's surface gave birth to a combined immunoassay and biosensor technology termed immunosensor (Jafari et al., 2019; Popov et al., 2021).

An immunosensor is a biosensor that uses antibody (Ab), either polyclonal (pAb) or monoclonal (mAb), as a capture and signaling element. Such antibody forms a stable immunocomplex with the antigen (Ag), generating a measurable signal. In contrast with an immunosensor, in an immunoassay, the signal recognition takes place elsewhere (Mollarasouli et al., 2019; Shen et al., 2020). Among the limitations of using antibodies are difficulty in chemical modification, high cost of production, and low stability at high temperatures (Wei et al., 2018). Aptamer-based electrochemical biosensors were developed to overcome these limitations.

Aptamers gained research interest since it was revealed in 1990 as a potential rival to antibodies in terms of its diverse application due to its ability to form 2D and 3D shapes that help them to recognize and bind to their cognate target with high affinity and specificity (Jayasena, 1999). Aptamers are short single-stranded nucleic acids (can be DNA or RNA) that are selected from a set of random DNA or RNA library and synthesized *in vitro* using a method called Systematic Evolution of Ligands by Exponential Enrichment (SELEX) (Sypabekova et al., 2017). Aptamers are stable in complex environments and highly resistant to denaturation and degradation when modified and optimized appropriately. A biosensor that uses an aptamer as a molecular recognition element or bioreceptor is called an aptasensor (Bezerra et al., 2019; Anand et al., 2021; Bhardwaj and Kumar Sharma, 2022; McKeague et al., 2022).

Several transduction techniques can be used for biosensor development, which includes optical, chemiluminescent, electrochemiluminescent, colorimetric, fluorometric, piezoelectric, and electrochemical. Most of these techniques are complex, time-consuming, and require sample pre-treatment and personnel training to perform the procedure. Electrochemical techniques received much attention due to their high sensitivity and selectivity, simple design, and rapid detection without requiring expensive and complex equipment. Electrochemical techniques are easily integrated into the biosensor, and the resulting device can be miniaturized, making the electrochemical biosensor highly applicable for point-of-care testing (Marques et al., 2014; Zhong et al., 2020). Electrochemical biosensors can be operated using low-voltage disposable batteries. It can also obtain its power source from other electronic devices such as cell phones, tablets, laptops, and computers when accompanied by a computer application. Electrochemical biosensors can detect multiple analytes simultaneously (multiplexing) (Arkan et al., 2015). In such biosensors, antibodies and aptamers can be utilized as bioreceptors, often immobilized on the electrode surface using appropriate chemistry. Stable Ab-Ag or Ap-Ag complex formation generates electrical signals, such as changes in electrode potential, current, or capacitance (Shen et al., 2020). Furthermore, aptamers offer an additional advantage over antibodies as, unlike the latter, aptamers can undergo a target-induced structural change. When labeled with a redox molecule, this structural change can be quantified proportionately to the analyte concentration (Das et al., 2019).

The key challenges to improving the electrochemical biosensor's performance include signal amplification and electrode stability. The combination of biological and inorganic nanomaterials has been explored, including labeling of bioreceptors, using various bio-linking techniques, and incorporating electronic sources. A dual system has become a popular technique that allows the incorporation of more nanomaterials into the platform, resulting in a more flexible biosensor application.

This review aimed to obtain insight into the answers to the following research questions: 1) What strategies are used to enhance the electrochemical signal and lower the limit of detection? 2) What techniques are used to incorporate the biological and inorganic nanomaterials into the electrode assembly? 3) What is the impact of using a dual system approach in electrochemical signal amplification? The reviewed articles in this paper encompass single systems with unlabeled bioreceptors to more complex dual systems decorated with various electronic nanomaterials.

In this review paper, a biosensor refers to an electrochemical immunosensor or aptasensor, while a bioreceptor pertains to either an antibody or an aptamer. This review paper focuses on the recent application of aptamer and antibody as bioreceptors in a single system and dual systems composed of aptamer-aptamer (or complementary DNA), antibody-secondary antibody, and antibody-aptamer in developing electrochemical biosensors. Articles on electrochemical biosensor development against various protein biomarkers reported from 2012 to 2022 were considered, thoroughly studied, analyzed, and presented in this review.

2 Electrochemical signal amplification strategies

Typically, an electrochemical biosensor comprises an electrode with an interface architecture where the biological event occurs. This interaction includes the specific binding of the analyte to the bioreceptor, producing an electrochemical signal. In the transducer, this signal is detected and converted to an electronic signal and is sent to a computer for processing. Computer software converts the electronic signal into a meaningful physical quantity presented to the human operator through an interface. This technique's advantages are simplicity, rapidity, cost-effectiveness, and high sensitivity. Electrochemical biosensors are easy to miniaturize, are independent of sample turbidity, and are compatible with novel microfabrication techniques. Since an electronic signal is produced directly after an electrochemical reaction occurs, expensive signal transduction equipment is not required (Hayat and Marty, 2014).

Due to the advent of screen-printing technology, miniaturized electrodes have become more feasible. Carbon paste electrodes are prepared using paraffin or mineral oil, which can be printed on a screen. Nanoparticles can also be incorporated into the mixture while preparing the paste electrode. Recently, paper-based biosensors have become a viable choice for electrode fabrication since they are readily available, inexpensive, disposable, and biocompatible. Due to its simple fabrication method, it is a strong candidate for point-of-care (POC) applications. The paper electrode has been used to develop electrochemical immunosensors

(Fan et al., 2019) and aptasensors (Wei et al., 2018). The techniques used include wax printing, plasma treatment, UV photolithography, screen printing, and laser treatment (Fan et al., 2019).

The change in electrochemical signal from the protein-protein interaction on the electrode's surface is usually low and often requires a signal amplification method. Nanomaterials were used either 1) to modify the electrode's surface by coating or by labeling the immobilized bioreceptor and 2) to introduce the electroactive or electrocatalytic nanomaterials into the system as a secondary probe (Johari-Ahar et al., 2015).

2.1 Electrochemical techniques

Electrochemical techniques measure the response of an electrochemical cell containing an electrolyte upon the application of electric current by the conductive electrodes immersed in that electrolyte (Doménech-Carbó et al., 2015). The applied electric current results in the loss (oxidation) or gain (reduction) of electrons of a given material in the electrolyte or embedded into the electrode. These redox reactions provide information such as concentration, kinetics, reaction mechanism, and other behaviors of a species in a solution (Naresh and Lee, 2021). This information, obtained as an electrochemical signal, is translated into meaningful values, which are used to evaluate the performance of an electrochemical biosensor.

Electrochemical techniques can be classified as amperometry, potentiometry, and coulometry. Amperometry measures the current in response to applying a constant or pulsed potential (Costa et al., 2022). Voltammetry, a subclass of amperometry, is the most applied technique in diagnostics and environmental analysis, particularly cyclic voltammetry (CV), differential pulse voltammetry (DPV), and square wave voltammetry (SWV), because of its simplicity and speed (Magar et al., 2021). Voltammetry consists of the records of current measured using a working electrode as a function of the potential difference between the working electrode and reference electrode. Typically, a third electrode, the counter electrode, minimizes the current passing through the working electrode (Doménech-Carbó et al., 2015).

In a reversible system, more intense signals are obtained using SWV, increasing the sensitivity compared to other voltammetric techniques. SWV is more rapid and sensitive than DPV due to the absence of interference caused by the background current (Costa et al., 2022).

Potentiometry is based on the Nernst equation, which relates the potential produced by the galvanic cell to the concentration of the electroactive species. However, this is only valid under equilibrium or thermodynamic conditions. (Westbroek, 2005).

Coulometry measures the total charge or the number of coulombs spent as an analyte is exhaustively converted from one oxidation state to another at the working electrode. This is an absolute process wherein the current passed is measured to calculate the number of electrons passed (Houssin et al., 2021). Coulometry was an analytical technique popular in the twentieth century and is now finding applications in miniaturized systems.

An emerging electroanalytical method in biosensor applications is electrochemical impedance spectroscopy (EIS), which is used for characterizing electrodes and performing impedimetric analysis (Doménech-Carbó et al., 2015). In EIS, the sinusoidal response (current or voltage) is monitored as an equilibrium or steady electrochemical system undergoes perturbation via the application of a sinusoidal signal (AC voltage or AC current, respectively) at a varied range of frequencies (Lazanas and Prodromidis, 2023).

In an electrochemical immunosensor, EIS and SWV are the most popular techniques used due to their high sensitivity, with the limit of detection obtained at the picomolar level and over a wide dynamic range. SWV was determined to be rapid, efficient, cost-effective, and inexpensive when applied to label-free electrochemical immunosensors (Liu et al., 2010).

Aside from the electrochemical techniques used, the electrode type contributes to the sensitivity and selectivity of an electrochemical biosensor. Electrodes are usually based on carbon and noble metals, with carbon-based electrodes being more prevalent in biological research due to their high sensitivity and other benefits. Noble metals offer advantages in developing inexpensive multiplexed electrochemical sensors (Zachek et al., 2008). Carbon and gold-based electrodes have become popular due to their high conductivity, biocompatibility, and stability, which are crucial for biosensor development. Recent studies include hybrid electrode systems that take advantage of the benefits of various materials.

2.2 Electrode's surface modification with nanomaterials

The electrode's surface is modified with nanomaterials to increase the surface area and create a more favorable environment, leading to excellent biocompatibility, higher conductivity, and stability (Wei et al., 2018). Selecting appropriate nanomaterials is critical to improving the performance of an electrochemical biosensor (Jafari et al., 2019). Recent research focuses on modifying the electrode's surface with nanomaterials to promote electron transfer, signal amplification, and improvement of low-end detection limit (Freitas et al., 2019). Several studies showed that signal amplification can be achieved using nanomaterials such as graphene (G), quantum dots (QD), and metal nanoparticles (MNP) (Valipour and Roushani, 2017). Gold nanoparticles (AuNP) are often used to coat the electrode of the aptasensor due to the ease of immobilizing thiolated aptamers (Popov et al., 2021).

AuNP is a metallic nanoparticle with a high specific surface area, good biocompatibility, and high surface-free energy. It can also bond with the amino functional group ($-NH_2$) and thiol group (–SH) (Wei et al., 2018). AuNP can be used either as the electrode or integrated into carbon-based electrodes. It is often prepared by citrate reduction of chloroauric acid in aqueous solution using sodium citrate (Arkan et al., 2015). AuNP is used to immobilize biological substances due to its physicochemical properties. Thiolated biomolecules are quickly immobilized on AuNP's surface. Reports showed that protein immobilization on AuNP helps preserve the activity of the biomolecule. AuNP can help maintain the immunoactivity of the antibodies. Aside from that, AuNPs are highly conductive, facilitating direct electron transfer between redox species and bulk electrode materials, which is ideal for electrochemical sensing (Gasparotto et al., 2017).

Silver, platinum, and palladium nanoparticles can also be used to improve the sensitivity and performance of electrochemical biosensors. The advantages of these nanoparticles include strong adsorption ability, simplicity of the preparation process, cost-effective manufacturing process, high conductivity, and large specific surface area (Valipour and Roushani, 2017).

Carbon-based nanomaterials are used in various applications, such as detecting biomolecules, proteins, and nucleic acids (Raouafi et al., 2019). Graphene is one of the most promising carbon-based nanomaterials in designing electrochemical biosensors (Wei et al., 2018; Karaca and Acaralı, 2023). Graphene oxide (GO) has unique characteristics such as large surface area, good water dispersibility, facile surface modification, and photoluminescence (Zhu et al., 2015). GO can readily adsorb aptamers on its surface and is often combined with MNP for firmer protein immobilization. Carboxylic acid functionalized GO can be used to immobilize aminated aptamer via covalent bonding (Johari-Ahar et al., 2015).

Quantum dots are semiconductors used successfully to amplify faint sensing signals. QD capped with organic linkers can boost the signal generated from electrochemical measurements (Johari-Ahar et al., 2015). Among the novel nanomaterials are graphene quantum dots (GQD), which are inexpensive, have high aqueous dispersibility, are ultra-small, and can be modified with a functional group. GQD exhibits a redox behavior by applying electrochemical techniques (Srivastava et al., 2018; Jafari et al., 2019; Kansara et al., 2022). GQD is superior to other semiconductor QDs in terms of low cytotoxicity, biocompatibility, ease of production, chemical inertness, and resistance to photobleaching. GQD can be thiolated to promote the immobilization of metal nanoparticles. Thiolated GQD also forms stable colloidal suspensions in various solvents, including ethanol and dimethylformamide. The water solubility of thiolated GQD is also lower than that of oxidized GQD (Valipour and Roushani, 2017). Chitosan (CH) is used to avoid restacking of GQD and provides a stable film or matrix for immobilizing the biomolecule (Srivastava et al., 2018). Carbon quantum dots or carbon dots (CD), <10 nm fluorescent nanoparticles, are a new addition to the carbon nanomaterial family. GQD and CD have been commonly used for biosensors, bioimaging, and targeted drug delivery research for cancer theranostics (Jana and Dev, 2022).

Nanozymes are nanomaterials with properties like enzymes and are known to have advantages such as low production cost, ease of mass production, and robustness. Iron oxide nanoparticles (IONP), other metal oxides, and metal-organic framework (MOF) have been discovered to possess intrinsic enzyme-like activity similar to horseradish peroxidase (HRP) (Sun et al., 2019). A MOF is a porous crystalline material that has gained popularity due to its stable and tunable pore sizes and high surface area. MOF inherits the advantages of its parent material, thus significantly boosting its application. Nanohybrid electrocatalysis can be performed by combining MOF and bimetallic nanoparticles carrying the bioreceptors (Sun et al., 2019). Covalent organic framework (COF) belongs to the highly porous materials synthesized for water treatment, energy, gas storage, and biosensing applications (Altaf et al., 2021).

Zhong et al. (2020) used ferrocene nanoparticles, an organometallic compound, as the electrochemical signal indicator that passes through the carbon nanotube, acting as the conductive layer. This study used a surface-confined setup with a label-free protein as the receptor. This study demonstrates the use of nanoparticles to resolve the problem with low sensitivity without labeling the protein while also providing a reagent-less approach.

Functionalized metal nanoparticles such as iron oxide (Fe_3O_4) have been used in biosensing systems due to their biocompatibility, signal amplification, and ability to form covalent bonds with antibodies via their functional group (Emami et al., 2014). Magnetic IONP was used to immobilize antibodies efficiently to detect human epidermal growth factor receptor 2 (HER2) (Emami et al., 2014; Shamsipur et al., 2018). Polyethylene glycol (PEG) has been used as an antibody linker to MNP. PEG provides enough space to allow more antibodies to bind with the MNP, thus creating a more effective combination with the target (Emami et al., 2014). MNP is easy to collect, wash, and handle using magnets or magnetic bars. IONP has been utilized as a magnetic core of a bio-conjugated nanoparticle and is often coated with trimethoxy-silane compounds for biomolecule conjugation (Marques et al., 2014). Zinc oxide (ZnO) has been utilized in biosensor platforms due to its high isoelectric point (IEP~9.5). Due to its semiconductor properties, ZnO provides an effective channel for electron transport during redox. AuNP can be synthesized directly into ZnO and Zn-based MOF matrix (Gasparotto et al., 2017).

2.3 Labeling and detection format

Three types of detection formats are commonly used to facilitate biomarker detection. The simplest is the direct type, wherein the biomarker attaches to the bioreceptor immobilized on the electrode's surface. This method is more straightforward, easy to implement, quick, and desirable for miniaturized sensors (Emami et al., 2014).

In a label-free approach (Figure 1), the attachment of the biomarker to the electrode's surface hinders the electron transfer and decreases signal intensity. The probe can be labeled (Figure 2) to produce an electrochemical signal, promoting either signal conduction (signal-on) or reduction (signal-off) (Zhong et al., 2020). A redox indicator, such as methylene blue and ferrocene/ferrocyanide redox couple—which is sensitive to the protein charge and surface blocking, can be used (Salimian et al., 2017; Zhong et al., 2020).

Immunolabeling refers to labeling antibodies or antigens to catalyze complex formation and improve biosensor sensitivity (Shen et al., 2020). Two types of labels are commonly used: 1) an electroactive label or 2) an electrocatalytic label, such as an enzyme that catalyzes the production of an electroactive product (Kondzior and Grabowska, 2020). Standard labels comprise nanomaterials or nanoparticles, enzymes, radioisotopes, luciferin, and electronic dense substances (Shen et al., 2020). Among the most valuable labels are enzymes, such as horseradish peroxidase (HRP), glucose oxidase (GOD), alkaline phosphatase (ALP), or electroactive molecules such as ferrocene, ferrocyanide, methylene blue (MB), platinum and cadmium quantum dots (QDs), and other nanoparticles. Table 1 shows that antibodies are often labeled with horseradish peroxidase (HRP) or alkaline phosphatase (AP), assuming the exact mechanism as the commonly known ELISA technique.

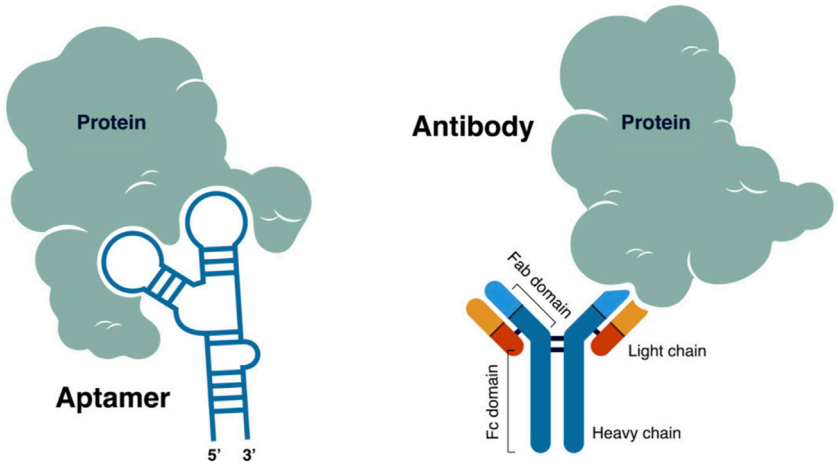

FIGURE 1
Label-free approach—the interaction between the biomarker and the biological receptor decreases the electrochemical signal.

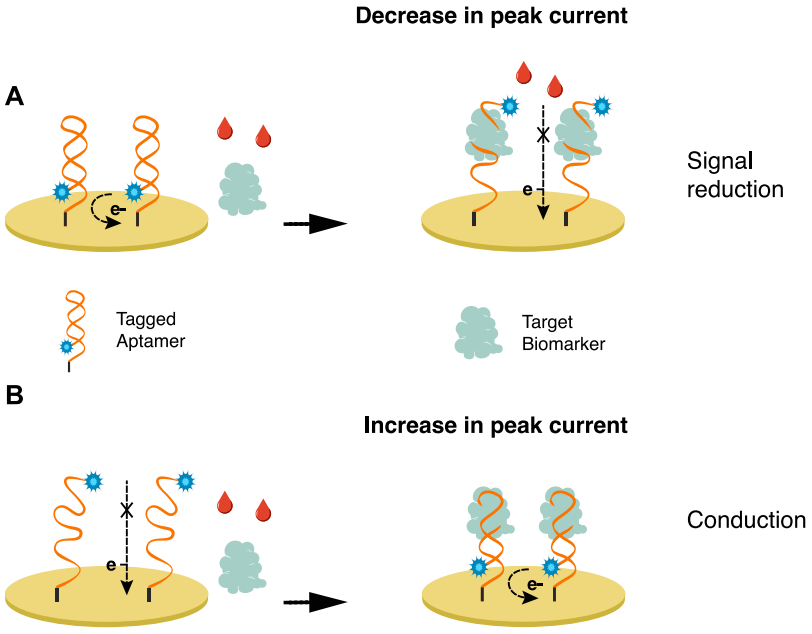

FIGURE 2
Bioreceptors are tagged with an electroactive label wherein the interaction with the biomarker either promotes **(A)** signal reduction or **(B)** conduction.

The dual system approach uses a labeled secondary probe, also called the reporter probe. Two formats are usually employed utilizing this approach, the competitive and sandwich format, providing a higher sensitivity than the direct approach (Popov et al., 2021). In a competitive format illustrated in Figure 3, a labeled secondary probe is released upon the interaction of the biomarker with the primary or capture probe. In an aptasensor, methylene blue (MB) is intercalated with the complementary DNA aptamer (cDNA) sequence due to its high affinity with guanine. The aptamer and biomarker complex formation releases MB-cDNA, decreasing the redox probe's electrochemical signal (Raouafi et al., 2019). Other nanomaterials, such as cadmium sulfide (CdS) and silver nanoparticles (AgNP), can be attached to a secondary probe, producing a stripping signal proportional to the concentration of biomarkers. Although the process is highly sensitive, its requirements of sample pre-treatment, separation, and purification of the secondary probe have limited its application (Emami et al., 2014). The redox electric signal of MB was significantly improved by using pure carbon-based electrodes, rather than the combination of graphene and gold electrodes, due to faster electron conduction velocity on the former setup (Duan et al., 2021).

TABLE 1 Labeled and dual system approaches to lowering the limit of detection (LOD).

Aptamer/ antibody and nanomaterial synergy	Electrochemical indicator or reporter probe	Electrochemical technique	Target biomarker	Sample	Performance	References
Single-labeled or unlabeled aptamer or antibody						
Aptamer-SH/AuNP/ SPCE	None	DPV	PSA	Clinical human serum	LOD: 0.077 pg/mL LR: 0.001–200 ng/mL	Hassani et al. (2020)
Aptamer-SH/AuNP/ THI[a]/rGO/SPCE	None	DPV	PSA	Clinical human serum	LOD: 10 pg/mL LR: 0.05–200 ng/mL	Wei et al. (2018)
Aptamer-NH_2/GQD-CoPc[b]/GCE	None	EIS, DPV	PSA	PSA solution in PBS and with BSA, glucose, and L-cysteine	LOD: 0.018 ng/mL LR: 0.034–0.057 ng/mL	Nxele and Nyokong (2021)
Aptamer-NH_2/CH-GQD@AuNR/SPCE	None	CV, DPV, EIS	PSA	Spiked human serum	For CV LOD: 0.14 ng/mL Sensitivity: 3.7 μA ng/mL For DPV LOD: 0.14 ng/mL Sensitivity: 2.5 μA ng/mL For EIS LOD: 0.14 ng/mL Sensitivity: 35 kΩ ng/mL	Srivastava et al. (2018)
mAb/CH-GQD@AuNR/ SPCE	None				For CV LOD: 0.14 ng/mL Sensitivity: 4.6 μA ng/mL For DPV LOD: 0.14 ng/mL Sensitivity: 2.39 μA ng/mL For EIS LOD: 0.14 ng/mL Sensitivity: 25.6 kΩ ng/mL	
Aptamer-NH_2/MPA[c]/ AuNP@Gold E	None	EIS	HER2	PBS solution	LOD: 5 ng/mL LR: 10^{-5}–10^{2} ng/mL	Chun et al. (2013)
Aptamer-NH_2/ SNGQD[d]@AuNP/GCE	None	EIS	HER2	Spiked human serum (1: 500 dilution)	LOD: 0.0489 ng/mL	Centane and Nyokong (2022)
Aptamer-NH_2/CoP-BNF/GCE					LOD: 0.0259 ng/mL	
Aptamer/SNGQD@ AuNP/CoP-BNF[e]/GCE					LOD: 0.0112 ng/mL	
Ab/SNGQD@ AuNP/GCE					LOD: 0.1072 ng/mL	
Ab/CoP-BNF/GCE					LOD: 0.0454 ng/mL	
Ab/SNGQD@AuNP/ CoP-BNF/GCE					LOD: 0.0327 ng/mL	
Ab/rGO-Au/GCE	None	SWV, EIS	PSA	Spiked human serum samples	SWV LOD: 2 pg/mL	Assari et al. (2019)

(Continued on following page)

TABLE 1 (*Continued*) Labeled and dual system approaches to lowering the limit of detection (LOD).

Aptamer/ antibody and nanomaterial synergy	Electrochemical indicator or reporter probe	Electrochemical technique	Target biomarker	Sample	Performance	References
					LR: 25–55 fg/mL and 1–36 ng/mL	
					EIS	
					LOD: 60 pg/mL	
					LR: 1.8 pg/mL –41 ng/mL	
Ab/AuNP@ZnO nanorod/SPGE	None	CV	CA125	PBS as support electrolyte	LOD: 2.5 ng/μL	Gasparotto et al. (2017)
Ab/Streptavidin/MOF-808@CNT/GCE	None	DPV	CA125	Tested on patient serum samples	LOD: 0.5 pg/mL	Biswas et al. (2021)
					LR: 0.001–0.1 and 0.1–30 ng/mL	
Ab/AuNP/THI/rGO/ SPCE	None	DPV	CA125	Quality control serum samples	LOD: 0.01 U/mL	Fan et al. (2019)
					LR: 0.1 U/mL to 200 U/mL	
Ab/AgNP@GQD/GCE	None	DPV	CA125	Riboflavin solution	LLOQ: 0.01 U/mL	Jafari et al. (2019)
					LR: 0.01–400 U/mL	
Ab/MPA-AuNP@SiO_2-CdSe QD/Gold E	$K_3Fe(CN)_6$ is used as an indicator	CV, EIS	CA125	Spiked human serum	LOD: 0.0016 U/mL	Johari-Ahar et al. (2015)
					LR: 0–0.1 U/mL	
Ab/R1[f]/SPGE	A quinone-based compound in R1	DPV	CEA	Spiked human serum sample	LOD: 0.33 ng/mL	Pavithra et al. (2018)
					LR: 1.0–100 ng/mL	
Aptamer/PEG[g]-Gold E	MB and $K_3Fe(CN)_6$ is used as indicator	CV	HER2	Buffer and 1% human serum	LOD: 1 pM	Salimian et al. (2017)
					LR: 1 pM–10 nM	
Ab/AuNP/HDT[h]/ AuNP@MW-CILE[i]	$K_3Fe(CN)_6$ is used as an indicator	EIS	HER2	Human serum	LOD: 7.4 ng/mL	Arkan et al. (2015)
					LR: 10–100 ng/mL	
Ab/Fc-PEI/SWNT/ITO[j]	Fc is used as an indicator attached to ITO	DPV	HER2	Human serum (diluted 20 times)	LOD: 0.220 ng/mL	Zhong et al. (2020)
					LR: 1.0–200 ng/mL	
Ab-bioconjugate[k]/Cys/ MPA/AuNP/Gold E	IONP core	CV, DPV, EIS	HER2	Human serum samples	LOD: 0.995 pg/mL	Emami et al. (2014)
					Sensitivity: 5.921 μA mL/ng	
					LR: 0.01–10 ng/mL and 10–100 ng/mL	
MB-Aptamer/PLLF[l]/ SPCE	MB from labeled 1° aptamer	DPV	HER2	Human serum (after albumin depletion)	LOD: 3 ng/mL	Bezerra et al. (2019)
					LR: 10–60 ng/mL	
MB-Aptamer-SH/Gold E	MB from labeled 1° aptamer	DPV	PSA	Human samples	LOD: 50 pg/mL (0.050 ng/mL)	Sattarahmady et al. (2017)
					LR: 0.125–128 ng/mL	
Dual Antibody–Secondary antibody system						
pAb_1/SPCE(passive Ab immobilization)	pAb_2-Biotin/ Streptavidin-HRP	CV	HER2	Tested on human serum samples	LOD: 4 ng/mL	Tallapragada et al. (2017)
	TMB is used as a substrate (*sandwich format*)				LOQ: 5 ng/mL	
					LR: 5–20 and 20–200 ng/mL	

(Continued on following page)

TABLE 1 (*Continued*) Labeled and dual system approaches to lowering the limit of detection (LOD).

Aptamer/ antibody and nanomaterial synergy	Electrochemical indicator or reporter probe	Electrochemical technique	Target biomarker	Sample	Performance	References
mAb_1/SPCE	mAb_2-Biotin/S-AP^m	LSV	HER2	Human serum samples	LOD: 4.4 ng/mL	Marques et al. (2014)
	3-indoxyl phosphate and silver ions were used as substrate (sandwich format)					
Ab_1/AuNP/MWCNT-SPCE	Ab_2-Biotin/S-AP	LSV	HER2-ECD	Human spiked serum	LOD: 0.16 ng/mL	Freitas et al. (2019)
Ab_1/SPCE*	3-indoxyl phosphate and silver ions were used as substrate (*sandwich format*)				LOD*:8.5 ng/mL	
Nb/SPCE (EDC/NHS coupling)	HRP-Nb	CV	HER2	Cell lysate spiked with HER2	LOD: 1 µg/mL	Patris et al. (2014)
	(H_2O_2 and hydroquinone were used as substrate) (*sandwich format*)				LOQ: 4.4 µg/mL	
pAb/IONP@MWCNT-COOH/GCE	HRP-mAb	DPV	PSA	Human serum samples	LOD: 0.39 pg/mL	Shamsazar et al. (2021)
	$H_2O_2 \rightarrow H_2O$				LR: 2.5 pg/mL–100 ng/mL	
	$HRP_{(red)} \rightarrow HRP_{(ox)}$ (*sandwich format*)					
Biotin-mAb/streptavidin/ABA^n/nano-TiO_2-CPE	THI/HRP-pAb (*sandwich format*)	CV	PSA	PSA solutions	LOD: 200 pg/mL	Biniaz et al. (2017)
				Human serum samples	LR: 0.10–5.0 ng/mL and 5.0–100 ng/mL	
Ab_1/CA15-3/rGO-NH_2/SPE	HRP-Ab_2	DPV	Anti-CA15-3	Human serum samples	LOD: 0.0001 ng/mL	Patil et al. (2022)
Dual aptamer system						
MB-Aptamer-NH_2/GO-CO_2H/SPCE (MB is intercalated)	cDNA-NH_2 (*competitive format*)	CV, DPV	PSA	PBS Solution	LOD: 0.064 pg/mL	Raouafi et al. (2019)
				Validated in spiked human blood serum	LR: 1 pg/mL–100 ng/mL	
$Aptamer_1$-SH/GNF^o@SPCE	Aptamer-probe A duplex	DPV	CA125	Spiked biological samples	LOD: 5.0 pg/mL	Chen et al. (2019)
$Aptamer_1$–hairpin-like structure	MB-$Aptamer_2$ in solution				LR: 0.05–50 ng/mL	
	Target binds to duplex, releasing probe A. Probe A opens $Aptamer_1$, MB-$Aptamer_2$ attaches to $Aptamer_1$.(*indirect format*)					
Aptamer-NH/TTCA^p/AuNP@SPCE	Hydrazine-Phosphate-Aptamer (*sandwich format*)	CA	cTnI	Human serum (male AB plasma)	LOD: 24 pg/mL	Jo et al. (2017)
					DR: 0.024–2.4 ng/mL	
Aptamer/NTH/SPGE	(NP1) Aptamer/Cu@Au/Fe_3O_4@UiO	DPV	cTnI	Human serum sample	LOD: 16 pg/mL	Sun et al. (2019)
	(NP2) cDNA/Au@Cu (*sandwich format*)				LR: 0.05–100 ng/mL	
$Aptamer_{1-2}$-NH/MPA-AuNP/3DGH^q-GCE (*duplex system*)	$Aptamer_3$/AuNP/HGN^r	DPV	CEA	Clinical serum samples	LOD: 11.2 pg/mL	Shekari et al. (2021)
	$Aptamer_4$/AuNP/Fc/Graphene		CA15-3		LOD: 0.112 U/mL	

(Continued on following page)

TABLE 1 (*Continued*) Labeled and dual system approaches to lowering the limit of detection (LOD).

Aptamer/ antibody and nanomaterial synergy	Electrochemical indicator or reporter probe	Electrochemical technique	Target biomarker	Sample	Performance	References
Dual antibody-aptamer system						
mAb/poly-DPB[a](AuNP)/GCE	Hyd-Aptamer-SH/AuNP	CV, SWV	HER2	25-fold diluted human serum	LOD: 0.037 pg/mL LR: 0.1 pg/mL–10 ng/mL	Zhu et al. (2013)
Ab/Gold E	Aptamer-Au-Cysteamine conjugate	EIS, CV, and DPV	Tau-381	Human serum	LOD: 0.42 pM LR: 0.5–100 pM	Shui et al. (2018)
Aptamer-Biotin/ Streptavidin-MB	Ab/AuNP	ASDPV[t]	EGFR[u]	Human serum	LOD: 50 ng/mL LR: 1–40 ng/mL	Ilkhani et al. (2015)

[a]THI–Thionine.
[b]GQD-CoPc–Graphene quantum dots–Co phthalocyanine.
[c]MPA–Mercaptopropionic acid.
[d]SNGQD–Sulfur-nitrogen doped graphene quantum dots.
[e]CoP-BNF–Cobalt porphyrin binuclear framework.
[f]R1–lawsone + 2-mercaptoethylamine.
[g]PEG–polyethylene glycol.
[h]HDT–1,6-hexanedithiol.
[i]MW-CILE–multi-walled carbon nanotube–ionic liquid electrode in PVC tube.
[j]Fc-PEI, Ferrocene in polyethylene imine; SWNT, single walled carbon nanotube; ITO, indium-tin oxide electrode.
[k]Ab-bioconjugate–IONP/3-amino-propyltrimethoxysilane (APTMS)/PEG/thiol-antibody.
[l]PLLF–poly-L-Lysine film.
[m]S-AP–streptavidin-alkaline phosphatase.
[n]ABA–4-amino benzoic acid, CPE–carbon paste electrode.
[o]GNF–gold nanoflower.
[p]TTCA–5,2':5′2″-terthiophene-3′-carboxylic acid.
[q]3DGH–three-dimensional graphene hydrogel.
[r]HGN, Hemin-graphene hybrid nanosheets.
[s]DPB–2,5-bis(2-thienyl)-1H-pyrrole-1-(p-benzoic acid).
[t]ASDPV, Anodic stripping differential pulse voltammetry.
[u]EGFR, Epidermal growth factor receptor.

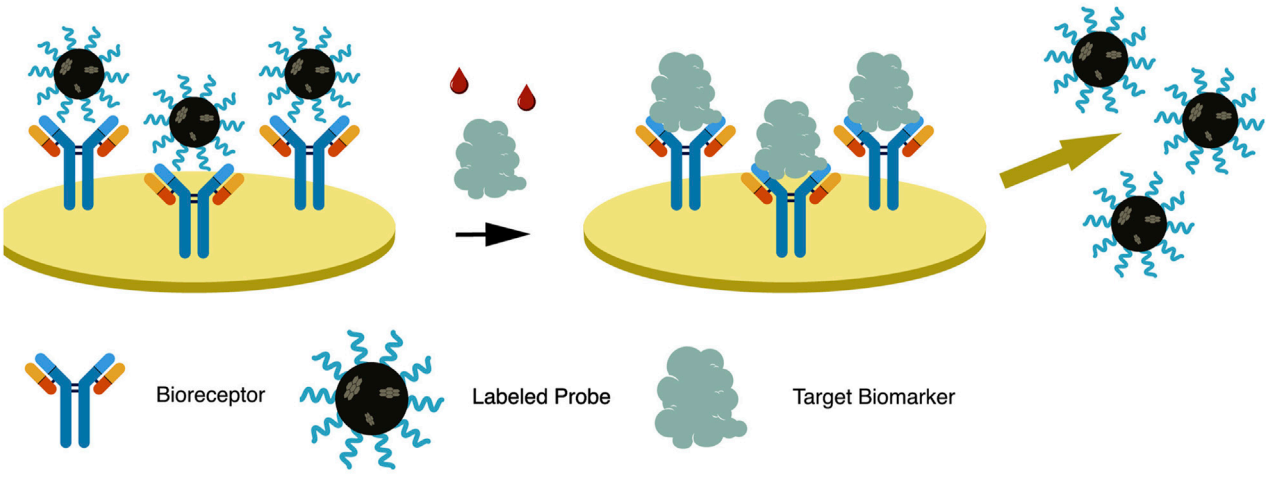

FIGURE 3
In a dual system approach—competitive format, a labeled reporter probe is released upon bioreceptor-biomarker interaction, resulting in signal generation.

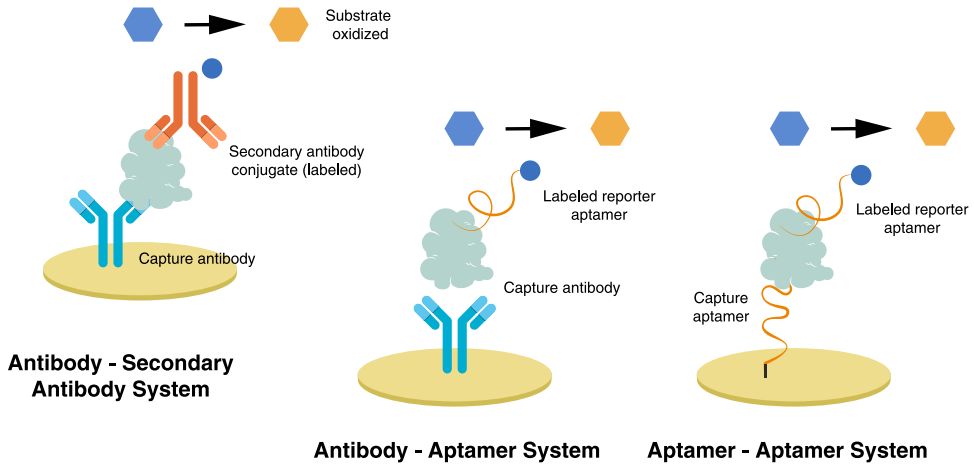

FIGURE 4
In a dual system approach—sandwich format, a capture probe is immobilized on the electrode while a labeled reporter probe attaches, thereby sandwiching the trapped biomarker.

The sandwich format in an electrochemical biosensor is a labeled method wherein an enzyme, usually HRP, is attached to a secondary probe. A primary or capture probe is used to capture the biomarker, sandwiched between the capture and enzyme-labeled secondary probe. HRP reduction catalyzes the oxidation of hydrogen peroxide, resulting in a measurable electrochemical signal (Emami et al., 2014). Among its downsides, solution-phase probe labeling may lower detection efficiency due to the diffusion limit. It may also cause contamination, especially for repetitive detections. This complicated operation of such probes is not ideal for integrated and miniaturized biosensor construction (Zhong et al., 2020). The dual system approach is illustrated in Figure 4 and is further discussed in the succeeding chapter.

3 Antibody, aptamer, and nanomaterial synergistic systems

The antibody, aptamer, or target antigen can be immobilized on the electrode depending on the detection approach. Proper immobilization technique will support the formation of the bioreceptor-biomarker complex on the electrode's surface and induce signal generation. The immobilization technique must not hamper the biological activity of the bioreceptor toward the target. More importantly, it should maximize the exposure of the binding sites to the target analyte. The density of the bioreceptor should be optimized since it may hinder the binding of the target biomarker (Sharafeldin et al., 2019; Popov et al., 2021).

Different protein immobilization methods are grouped as those forming covalent bonds or non-covalent interactions with the electrode. Passive adsorption is the simplest method of protein immobilization to the electrode's surface, using non-covalent interactions, adopted from the immobilization of antigen or antibody to ELISA microtiter plates. The main disadvantage of this method is the bioreceptors are oriented randomly on the surface, which may affect their binding capability and result in low sensitivity. Moreover, there is a massive chance of desorption during sample application and washing due to weak bonds sacrificing the reproducibility of the sensor. Bioreceptors may also undergo conformational changes, which decrease bioreactivity over time. Despite these limitations, this method is commonly used, particularly in antigen immobilization, due to its simplicity and high binding capacity (Sharafeldin et al., 2019; Popov et al., 2021). Tallapragada et al. (2017) directly immobilized antibodies on screen-printed carbon electrodes (SPCE) via passive adsorption.

Covalent linking via amine coupling is the classical and most practical technique that can be used to immobilize proteins on the electrodes' surface. In this process, carboxyl groups must be first deposited on the surface of the electrode, which is then activated using 1:1 N-ethyl-N'-(3-(dimethylamino) propyl) carbodiimide/N-hydroxysuccinimide (EDC/NHS) (Patris et al., 2014). The electrode's surface must develop a functional group, such as a carboxyl group (COOH), to support the linker and protein. The carboxyl group can be introduced by immersing the gold electrode or nanoparticles in an ethanol solution containing 1,6-hexanedithiol (HDT) and $LiClO_4$ (Arkan et al., 2015). Mercaptopropionic acid (MPA) can also be deposited on polished gold electrodes (Chun et al., 2013), while the carbon electrode can develop COOH on its surface using sulfuric acid (H_2SO_4) and applying voltage (Patris et al., 2014).

Antibodies naturally possess an amine group ($-NH_2$) that participates in amine coupling, while aptamers can be synthesized with amine on its 5′-end. Both bioreceptors can then be immobilized on EDC/NHS-treated surfaces, as demonstrated by Chun et al. (2013) and Nxele and Nyokong (2021). Antibodies were immobilized on rGO treated with EDC/NHS to develop a novel graphite paper-based bioelectrode (Özcan and Sezgintürk, 2022). The antigens can be immobilized in amine-functionalized rGO (Patil et al., 2022) for antibody or aptamer testing. Lysine was used to immobilize RNA aptamers into SPCE by creating a poly-L-lysine film (PLLF) layer (Bezerra et al., 2019).

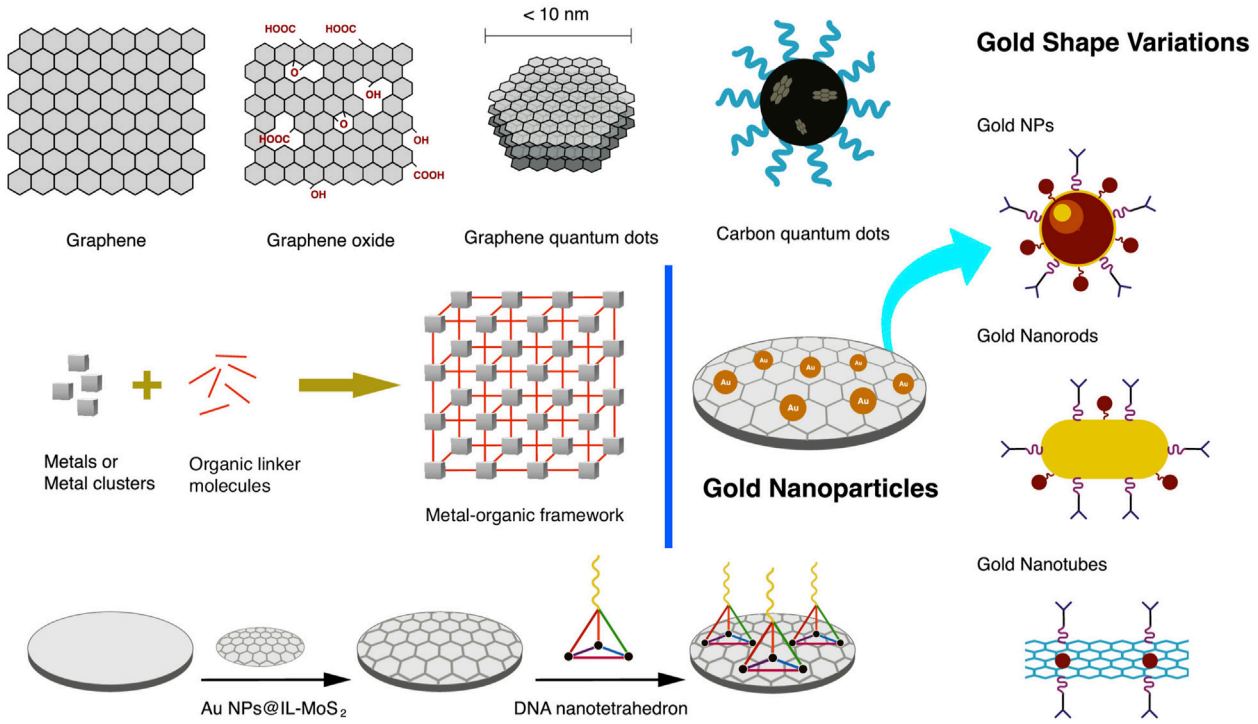

FIGURE 5
Nanomaterials are used in coating the electrode's surface primarily to increase the surface area, anchor bio-linkers and bioreceptors, and promote electron transfer, signal amplification, and improvement of the low-end detection limit. Such nanomaterials include graphene, graphene oxide, quantum dots, metal nanoparticles, and metal-organic framework.

Aside from the incorporation of an amine group, thiolation is commonly used to directly immobilize aptamers on gold electrodes or gold nanoparticles deposited on SPCE, as demonstrated in several studies (Salimian et al., 2017; Sattarahmady et al., 2017; Wei et al., 2018; Hassani et al., 2020). The thiol group can be easily incorporated into aptamers during their chemical synthesis. Various techniques are employed for antibodies, either taking advantage of the present functional group or incorporating a new one into the antibody. Marques et al. (2014) used SPCE nanostructured with AuNP to immobilize the capture antibody via chemisorption, while Ravalli et al. (2015) developed Au nanostructured graphite screen-printed electrode (SPE) to immobilize terminal cysteine-modified affibody. The labeled biomolecules are used while attached to AuNP as an electrochemical support. In a study, gold nanocubes were used to immobilize an HRP-labeled antibody (Shen et al., 2020).

Incorporating AuNP into carbon-based electrodes has been a typical study in electrochemistry. AuNP has been embodied in various forms of carbon-based electrodes, from simple GCE and SPE to specially modified carbon-based electrodes. Arkan et al. (2015) used electrodeposition to grow AuNP on the surface of multi-walled carbon nanotubes in a carbon ionic liquid electrode. A paste electrode of AuNP is deposited on a multiwall carbon nanotube mixed with graphite powder. The resulting paste is tightly packed into a PVC tube with an ID of 2.0 mm, with a copper wire introduced at the other end to provide electrical contact. AuNP was used with QD, which also helped amplify faint signals from a biosensor (Johari-Ahar et al., 2015). Gold nanorods (AuNR) combined with GQD showed enhanced and new functional properties due to their cooperative interaction (Srivastava et al., 2018). AuNP shape variations are depicted in Figure 5.

Self-assembled monolayers (SAM) are formed through the spontaneous reaction of thiols with solid metal surfaces such as gold, silver, and copper. The thiolated biomolecules can arrange themselves in a well-ordered and close-packed monolayer on the gold electrode surface. Impedance measurements can be performed to characterize SAM in the absence or presence of redox species in solution (Lasia, 2014).

Random accumulation and aggregation of the bioreceptor on the electrode's surface can impede the binding of target proteins. Immobilization techniques have been developed and improved to ensure the precise assembly and density of the biorecognition element on the electrode's surface. Coating the electrode's surface with nanomaterials provides support to anchor a variety of biological receptors and expand the application of the biosensor. At the same time, surface coating improves the sensitivity of the electrochemical biosensor by adding an electronic source.

AuNPs offer advantages such as biocompatibility, large efficient surface area, electrocatalytic properties, and high conductivity. Coating a glassy carbon electrode (GCE) with AuNP enhances the electron transfer rate and reduces the limit of detection. Reduced GO can also be decorated with AuNP to improve performance by reducing its tendency to aggregate upon chemical modification (Jafari et al., 2019). The catalytic activity of AuNP depends on its particle size. In the study of Wei et al.

(2018), an average of 15 nm particle size was used to immobilize thiolated aptamers and improve the electrocatalytic activity provided by the electrode.

Graphene oxide (GO) is a graphene derivative with a 2D-nanostructure single atomic layered material with a significant amount of sp^3 C-O bonds on its surface. The electrochemical reduction of GO to reduced GO includes eliminating oxygen, which boosts its electronic conductivity (Assari et al., 2019). Reduced graphene oxide (rGO) has high biocompatibility and conductivity, which is favorable for improving electrochemical signals. Moreover, rGO also introduces nanoporous structures to the electrode's surface, resulting in a high specific surface area that can accommodate more electroactive nanomaterials and deliver a higher electrochemical response. The application of rGO in developing ultrasensitive graphite paper-based immunosensors was reported (Özcan and Sezgintürk, 2022).

Carboxyl functionalized multi-walled carbon nanotubes (MWCNT-COOH) have shown extraordinary mechanical, electrical, and thermal properties and are applied in electrochemical biosensors. The dispersion and attachment of MWCNT on the electrode are essential for more stable biomolecule attachment and electron transfer (Shamsazar et al., 2021). Incorporating iron oxide nanoparticles helps form a uniform and ordered nanocomposite layer. Due to its magnetic properties, the nanocomposite attaches tightly to the electrode (Wang et al., 2018).

Biological macromolecules can also be used as linkers to optimize the bioreceptor's assembly. In a study by Sun et al. (2019), DNA nano-tetrahedron (NTH) anchors aptamers for its precise orientation and density. DNA NTH structure is assembled from four single-stranded nucleic acids and is firmly and homogeneously attached to the electrode's surface. DNA NTH increases the bioreceptor's accessibility and recognition efficiency, thereby improving the sensitivity of the electrochemical device (Sun et al., 2019).

Upon bioreceptor immobilization, surface blocking is implemented before the assay to avoid the detrimental effects of non-specific binding (Salimian et al., 2017). Common reagents for blocking include ethanolamine for EDC/NHS treated surfaces, non-fat milk, and bovine serum albumin (BSA) (Patris et al., 2014). Others employ the formation of antifouling ternary self-assembled monolayers or use antifouling polyethylene-glycol (PEG) blocking (Salimian et al., 2017).

4 The impact of dual system approaches to lowering the limit of detection

The electrocatalytic activity depends on the type of electrode used. Electrodes are modified with graphene oxides, metal oxides, and metal nanoparticles to increase the electrocatalytic activity while providing a platform for bioreceptor immobilization. On the other hand, the probe can be labeled to induce the redox reaction or boost the signal generation.

A single system uses one biorecognition element, an aptamer or antibody immobilized on the electrode's surface, while the analyte is detected directly. The changes in the electrochemical measurement of a single system rely heavily on the interference caused by the immobilization of the bioreceptor and the capture of usually nonconductive biological targets. In this case, the peak current decreases in proportion to the concentration of the target analyte. Despite its setback of low peak current, most research employs this process due to its simplicity, ease of implementation, cheaper platform development, and direct measurement approach. The issue of low electronic signal generation can be circumvented by modifying the electrode or labeling the probe. For example, thionine (THI) can be attached to the electrode and used as a redox mediator to increase the electrochemical signal of an unlabeled single-system setup (Wei et al., 2018). Several studies that use a single system with labeled and unlabeled probes are presented in Table 1.

A dual system combines an antibody and a secondary antibody, two or more aptamers, and a complementary DNA aptamer, or antibodies and aptamers, in a biosensor. The main objective is to create a bio-nanocomposite that attaches to the captured target and introduces an electroactive or electrocatalytic material. A bio-nanocomposite composed of several nanomaterials often performs better than a single nanomaterial in a biosensor. The dual system is executed in two formats: the competitive format, wherein the target biomolecule displaces the secondary probe upon binding, or a sandwich format, wherein the nanocarrier of the redox catalyst attaches to the captured target. Both approaches use a capture probe immobilized on the electrode's surface. Several articles that used a dual system approach are presented in Table 1.

4.1 Antibody–secondary antibody system

Sandwich-type immunoassay has been employed in most antibody-based detection, such as ELISA. This mechanism has been adopted in developing sandwich-type immunosensors, wherein the primary or capture antibody is immobilized on the electrode, and a secondary antibody attaches to and sandwiches with the target protein. The secondary antibody is tagged with an enzyme that will induce the redox reaction.

A secondary antibody tagged with HRP was used in a sandwich-type immunosensor for prostate-specific antigen (PSA) and HER2 detection. Electrocatalysis of hydrogen peroxide (H_2O_2) is aided by HRP, leading to higher peak current and sensitivity for PSA detection. IONP plays a vital role in redox reactions with HRP and electron exchange with the electrode (Shamsazar et al., 2021). Biniaz et al. (2017) used a biotinylated monoclonal antibody as the capture probe, while HRP and thionine-tagged polyclonal antibody was used to promote the electrocatalytic degradation of H_2O_2 (Biniaz et al., 2017). Other substrates used with HRP are hydroquinone/H_2O_2 (Patris et al., 2014) and 1,3,5-trimethylbenzene (TMB) (Tallapragada et al., 2017).

Other formats include a capture primary antibody and a biotinylated secondary antibody with high specificity to the isotype of the primary antibody. Streptavidin, a protein with a high affinity to biotin, is conjugated with HRP or alkaline phosphatase (AP), both electrocatalytic enzymes. With AP, p-nitrophenyl phosphate (pNPP) is used as a substrate that is hydrolyzed rapidly to p-nitrophenol and inorganic phosphate. AP is also used to oxidize metallic silver deposited enzymatically via 3-indoxyl phosphate (3-IP) and silver ion mixture (Marques et al., 2014; Freitas et al., 2019).

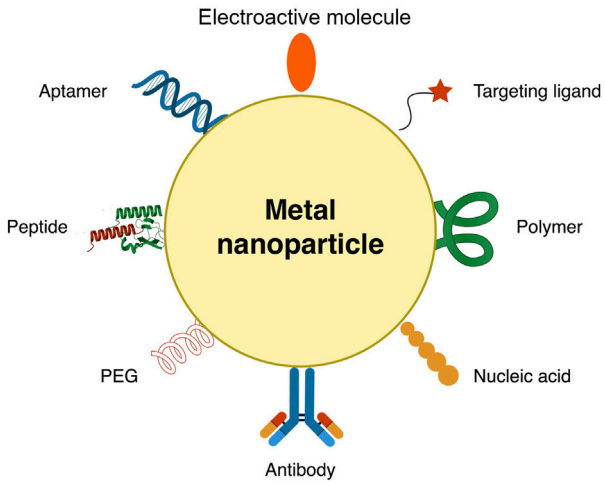

FIGURE 6
Metallic nanocarrier decorated with nanomaterials to enhance signal generation and lower limit of detection.

4.2 Aptamer–secondary/complementary aptamer

In a study conducted by Sun et al. (2019), Zr(IV)-based MOF known as UiO-66 was used as a shell over the IONP to form the novel magnetic MOF (MMOF IONP@UiO-66), while bimetallic nanoparticle Au@Cu was employed as a linker of the aptamer to MMOF. The capture aptamer was immobilized on a screen-printed gold electrode (SPGE) using NTH as a linker. The target is then captured by the aptamer on SPGE and sandwiched by aptamer/IONP@UiO-66. Complementary DNA attached to Au@Cu nanoparticles binds to the aptamer on IONP@UiO-66. The combination of Au@Cu and UiO-66 improves the electrocatalytic performance of IONP and amplifies the electrochemical signal while serving as nanocarriers of two types of aptamers. The increase in captured target is proportional to the amount of the nanocarriers, thus resulting in an increase in peak current by the chemical reaction: $O_2 + 2H_2Q \rightarrow 2Q + 2H_2O$ and $Q + 2H^+ + 2e^- \rightarrow H_2Q$, where H_2Q is hydroquinone, and Q is benzoquinone (Sun et al., 2019). Figure 6 depicts the nanocarrier and the common nanomaterials embedded in a metallic nanocarrier.

SPCE is coated with graphene oxide–carboxylic acid (GO-COOH) via drop-casting to immobilize aminated aptamers. A complimentary DNA (cDNA) aptamer is conjugated to the attached aminated aptamer, while methylene blue (MB) is intercalated between the aptamer and cDNA. This dual aptamer approach uses the competitive format, wherein binding the analyte will release the MB trapped between the anti-PSA aptamer-cDNA conjugate. The release of MB will increase the redox electric signal, producing a higher peak current (Raouafi et al., 2019).

4.3 Antibody–aptamer system

In this process, the antibody is used as a bioreceptor and an aptamer with an electrocatalytic label or incorporated in a nanocarrier (Figure 6) serves as a recognition element. Ilkhani et al. (2015) used an aptamer immobilized on magnetic beads as a capture probe for detecting the epidermal growth factor receptor (EGFR). Using magnetic beads allows an easier way of separating antigens captured by the aptamer. The antibody was conjugated to AuNP, which sandwiches the captured antigen—the increase in antigen concentration results in an increase in peak current (Ilkhani et al., 2015).

Self-assembled 2,5-*bis*(2-thienyl)-1H-pyrrole-1-(*p*-benzoic acid) or DBP and AuNP was deposited on the surface of GCE via electro-polymerization. Monoclonal anti-HER2 antibody was then immobilized to the poly-DBP@AuNP via amine coupling. In this sandwich format, the hydrazine-tagged aptamer in AuNP attaches to the captured HER2. Electrochemical measurement was performed in silver nitrate solution, wherein silver ion was reduced to silver metal by hydrazine attached to the aptamer and AuNP as a catalyst. A gradual increase in peak current was observed as the target concentration increased. As a downside, this process resulted in the deposition of reduced silver metals into the electrode (Zhu et al., 2013).

4.4 Comparison of LOD obtained using various detection approaches

The limit of detection (LOD) and the linear range (LR) are often used to determine the sensitivity of a biosensor. Other categories could also be examined, such as biosensor stability during implementation and storage, reproducibility, cost per analysis, and sustainability of materials used. The proposed electrochemical platform and methodology resulting in the lowest LOD based on the articles reviewed are presented in Table 2. For PSA detection, a dual aptamer system with a competitive format using MB intercalated between the capture aptamer and the complementary DNA aptamer showed the lowest LOD of 0.064 pg/mL with a dynamic LR of 0.001–100 ng/mL (Raouafi et al., 2019). Aptamers labeled with MB showed lower LOD than unlabeled aptamers, while electrochemical aptasensors performed better than immunosensors. Aptamer tagged with MB and directly immobilized on the gold electrode is the most straightforward setup, resulting in a LOD of 50 pg/mL (Sattarahmady et al., 2017).

For cardiac troponin I (cTnI), a 16 pg/mL LOD was obtained using a multiple aptamer system, wherein one aptamer is utilized as a capture probe and two others as reporter probes, with one attached to an electrocatalytic nanocarrier. The lowest LOD (0.037 pg/mL) for HER2 detection was obtained using a dual antibody-aptamer system with a monoclonal antibody as the capture probe. The aptamer reporter probe and an electroactive label, hydrazine, were immobilized in AuNP as a nanocarrier (Zhu et al., 2013). Nanobodies applied in a dual-system immunosensor showed the highest LOD in this review, equal to 1 μg/mL (Patris et al., 2014).

In the same study, an electrochemical aptasensor performed better than an immunosensor in LOD for HER2 detection. In this case, aminated aptamers and antibodies were immobilized in separate electrodes. The results also showed the superiority of AuNP in improving the biosensor's sensitivity (Centane and Nyokong, 2022). Srivastava et al. (2018) performed a comparative

TABLE 2 Cancer protein biomarker normal and infection levels and lowest reported LOD.

Biomarker	Cancer	Normal level	Infection level	Lowest reported LOD	Biosensor description
Prostate-specific antigen (PSA)	Prostate cancer	<4 ng/mL (Assari et al., 2019; Raouafi et al., 2019; Nxele and Nyokong, 2021) <20 ng/mL (Padmavathi et al., 2017)	4–10 ng/mL (Raouafi et al., 2019)	0.064 pg/mL (Raouafi et al., 2019)	Dual aptamer system, MB as indicator, competitive format, DPV
Cardiac troponin I (cTnI)	Acute myocardial infarction (AMI)		5–50 ng/mL (Sun et al., 2019)	16 pg/mL (Sun et al., 2019)	Dual aptamer system, one capture and two reporter probes on nanocarrier, sandwich format, DPV
Human epidermal growth factor receptor 2 (HER2 or ErbB2)	Breast cancer	<1% positive stain (Padmavathi et al., 2017) 2–15 ng/mL (Bezerra et al., 2019)	15–75 ng/mL (Chun et al., 2013; Bezerra et al., 2019)	0.037 pg/mL (Zhu et al., 2013)	Dual antibody-aptamer system, hydrazine label, sandwich format, SWV
Carbohydrate antigen (CA125)	Ovarian cancer (also in lung cancer, endometrial cancer, and breast cancer)	<35 U/mL (Fan et al., 2019)		0.0016 U/mL (Johari-Ahar et al., 2015)	A single antibody on quantum dots on a gold electrode, $K_3Fe(CN)_6$ as an indicator
				0.5 pg/mL (Biswas et al., 2021)	A single antibody, ZnO nanorod, Gold electrode
Cancer antigen (CA15-3)	Metastatic breast cancer	<45 U/mL (Padmavathi et al., 2017)		0.112 U/mL (Shekari et al., 2021)	Dual aptamer system, reporter probe on nanocarrier, sandwich format, DPV
Carcinoembryonic antigen (CEA)	Breast, colorectal, and lung cancer	<5 ng/mL (cut-off range 2.5–40 ng/mL) (Padmavathi et al., 2017)	10 ng/mL	11.2 pg/mL (Shekari et al., 2021)	Dual aptamer system, reporter probe on nanocarrier, sandwich format, DPV

study of aptasensor vs. immunosensor using GQD and gold nanorod-modified screen-printed electrodes for PSA detection. Both setups showed comparable results with an LOD of 0.14 ng/mL (Srivastava et al., 2018). In both cases, the aptasensor outperforms the immunosensor in simplicity, cost-effectiveness, stability, and regeneration (Srivastava et al., 2018; Centane and Nyokong, 2022).

Monoclonal antibodies on cadmium selenide QD, AuNP-SiO_2, and gold electrodes modified with MPA showed the lowest LOD of 0.0016 U/mL for CA125 detection using EIS. This ultra-sensitive electrochemical technique measures changes in electrical resistance (Johari-Ahar et al., 2015). The carbon-based electrodes with Ab on AuNP with reduced GO and AgNP with graphene QD showed a similar LOD of 0.01 u/mL measured using DPV (Fan et al., 2019; Jafari et al., 2019).

Most of the reviewed articles used DPV as an electrochemical technique. EIS showed lower LOD in a single system than DPV (Nxele and Nyokong, 2021), while SWV is more sensitive than EIS (Assari et al., 2019). Gold electrodes or the application of AuNP have exhibited lower LOD and better stability than carbon-based electrodes. Electrochemical immunosensors with sandwich format outperform single system immunosensors using an antibody as a capture element and rely on a change in resistance only. In a sandwich format, a secondary antibody labeled with biotin is used. HRP-streptavidin or ALP-streptavidin binds to biotin, which serves as an enzyme that catalyzes the substrate reduction process. This reaction produces a higher change in the electrochemical signal. Incorporation of IONP significantly decreases the LOD of the immunosensor (Shamsazar et al., 2021). A dual system using two or more aptamers, a complementary aptamer, and an antibody-aptamer system showed the lowest reported LOD for each antigen.

Table 2 shows the limit of detection of the biosensors reviewed in this article compared to the biomarkers' average body level and infection level. Dual systems have shown detection limits lower than the infection level, indicating the high possibility of translating the research methodology into commercially viable product design.

4.5 Point-of-care testing adoption

Point-of-care testing (PoCT) continues to attract technology developers to produce clinically helpful PoCT devices. The critical characteristics of PoCT should match its users' clinical and individual needs (Korte et al., 2020). Among the crucial factors described by Garg et al. (2023) that affect the translation of research output to PoCT are listed in Table 3.

The materials used in the biosensor assembly and the transduction method dramatically affect the PoCT cost. A whole gold or glassy carbon electrode is expensive and thus must be reusable to lower the testing cost. Due to this, single-use paper-based electrode modified with AuNP or other nanomaterials have gained valuable interest in PoCT due to its simplicity, low cost, stability, and ease of disposal. Electrochemical methods, such as DPV, SWV, and EIS, have been used as a readout method in PoCT. Electrochemical techniques can provide a higher sensitivity and accuracy than the usual colorimetric PoCT. However, this would require a more expensive electronic readout device that can be purchased once.

TABLE 3 Comparison of the key characteristics of the commercially available Point-of-care test (PoCT) with the selected biosensor.

Biomarker	Brief description of technology	Limit of detection	Assay time	Sample/ Test sample	Storage stability	Cost
PSA	Dual aptamer system, competitive format, DPV (Raouafi et al., 2019)	0.064 pg/mL	30 min detection time using DPV	Spiked human blood serum	stability of 98% over 2 weeks, results are reproducible over 8–10 months	Electrochemical transducer machine (one-time fee) and modified screen-printed carbon electrode (consumables)
	Lateral flow chromatographic immunoassay, semi-quantitative, cassette/strip (CTK Biotech, CA, United States)	4 ng/mL	15 min	Whole blood, serum, or plasma	1.4 months (for most immunosensors)	0.30–0.40 USD/kit (local price)
CEA	Dual aptamer system, sandwich format, DPV (Shekari et al., 2021)	11.2 pg/mL	>30 min detection time using DPV	Clinical serum samples	91% stability after 3 days of storage at 4°C, satisfactory reproducibility	Electrochemical transducer machine (one-time fee) and modified screen-printed carbon electrode (consumables)
	Immunochromatographic rapid test, quantitative, cassette (Quadratech Diagnostics, Eastbourne, United Kingdom)	5 ng/mL	5–15 min	Whole blood, serum, or plasma	Store at 4°C–30°C Shelf-life: 2 years	0.30–0.40 USD/kit (local price)

The obtained LR and LoD in all articles presented in this review are clinically relevant and highly competitive with the existing and commercially available PoCT devices. Before adoption, the proposed PoCT technology must be clinically tested. The type of sample, its volume, and collection techniques are essential considerations. Most of the current research tested the technology on spiked human blood samples.

PoCT should be accomplished within around 20 min to allow for a test and subsequent discussion of results performed within the same clinical session. Most electrochemical techniques require at least 30 min to allow ample time for sample incubation. However, this does not include the time to obtain, collect, and pre-process samples (Garg et al., 2023).

The most common PoCT is the lateral flow immunosensor, which is inexpensive and has storage stability of up to 2 years. Aptamers are more stable and affordable than antibodies and thus could improve the stability of the PoCT. However, due to the high cost of the construction materials for electrochemical biosensors, maximizing the reusability and regenerability of the product could significantly help lower its price. Table 3 presents that the electrochemical dual system aptasensor is stable at 4°C–30°C storage conditions with satisfactory reproducibility.

New opportunities in electrochemical PoCT device development have emerged in view of the developments in microfluidics, multiplexing, and machine learning. Simultaneous detection of various analytes can be achieved by using multiple aptamers in one platform. Meanwhile, integrating microfluidics into electrochemical biosensors is motivated by several perceived potential benefits such as portability, real-time monitoring, efficient sampling process, and precise detection of analyte/s, even with complex samples. This integration involves 1) the design of the microfluidic device via microfabrication techniques (e.g., soft lithography, laser ablation, or 3D printing) to include channels, chambers, and necessary features for sample introduction, mixing, flow control, delivery to the electrochemical sensor, and sample exit; 2) incorporation of electrodes onto the microfluidic chip; 3) immobilization of recognition elements onto the electrodes within the microfluidic channels; 4) provision of microfluidic structures that ensure uniform exposure of the analyte to the recognition elements on the electrochemical sensor; and 5) integrating the microfluidic-electrochemical biosensor with external systems, such as microcontrollers or data analysis software for enhanced automation, control, and data processing.

5 Conclusion and perspective

Incorporating nanomaterials into electrochemical biosensors has successfully improved the analytical sensitivity of the biosensor, thus allowing the detection of trace amounts of analytes relevant to clinical diagnostics. Inherent to using biological receptors are low electrical signals generated, which were overcome by labeling with ferrocene, methylene blue, and iron oxide nanoparticles or embedding the proteins in electrodes coated with metal nanoparticles, graphene oxide, and quantum dots. The bioreceptors are immobilized using organic linkers and nanoparticles with proper orientation via self-assembly, and the density can be controlled.

Aptamers pose a considerable advantage over antibodies since the former can be easily synthesized and functionalized with a label, a linker, or both. The incorporation of linkers to aptamers makes it more flexible when it comes to its immobilization and electrode development. Notable differences include the aptamer being highly efficient even as a capture element alone while using labeled complementary aptamers in a competitive or sandwich format showed the best potential.

The dual system improves the assembly of the capture probe on the surface of the electrode, regardless of whether it is carbon or gold-based. A dual system also helps increase electrocatalytic activity during measurement. The abundance of electrocatalysts on the electrode's surface increases the peak current, thus amplifying the signal generated.

The secondary antibody, aptamer, or complementary DNA can be attached to a nanocarrier that possesses electrocatalytic properties. For the electrochemical immunosensor, the application of the secondary antibody in a sandwich format, patterned from the standard ELISA technique, significantly increased the immunosensor's sensitivity.

The impact of using aptamers over antibodies and applying nanomaterials on the sensor's life cycle should be examined. For developing a high-quality aptamer-based biosensor, a pragmatic approach could be using an electrochemical surface during the SELEX process. Translating the dual system electrochemical aptasensor to a PoCT device requires increasing the speed of the assay time, improving the storage stability and reusability, and performing construction materials analysis for lower assay cost.

Author contributions

RR: Conceptualization, Funding acquisition, Writing–original draft. EE: Conceptualization, Writing–review and editing.

Funding

The authors declare financial support was received for the research, authorship, and/or publication of this article. Open Access funding is provided by the Department of Science and Technology—Philippine Council for Health Research and Development.

Acknowledgments

Ms. Halyanna M. Luis created all the artworks in this manuscript.

Conflict of interest

The authors declare that the research was conducted in the absence of any commercial or financial relationships that could be construed as a potential conflict of interest.

Publisher's note

References

Altaf, A., Baig, N., Sohail, M., Sher, M., Ul-Hamid, A., and Altaf, M. (2021). Covalent organic frameworks: advances in synthesis and applications. *Mater Today Commun.* 28, 102612. doi:10.1016/j.mtcomm.2021.102612

Anand, A., Chatterjee, B., Dhiman, A., Goel, R., Khan, E., Malhotra, A., et al. (2021). Complex target SELEX-based identification of DNA aptamers against Bungarus caeruleus venom for the detection of envenomation using a paper-based device. *Biosens. Bioelectron.* 193, 113523. doi:10.1016/j.bios.2021.113523

Arkan, E., Saber, R., Karimi, Z., and Shamsipur, M. (2015). A novel antibody–antigen based impedimetric immunosensor for low level detection of HER2 in serum samples of breast cancer patients via modification of a gold nanoparticles decorated multiwall carbon nanotube-ionic liquid electrode. *Anal. Chim. Acta* 874, 66–74. doi:10.1016/j.aca.2015.03.022

Assari, P., Rafati, A. A., Feizollahi, A., and Asadpour Joghani, R. (2019). An electrochemical immunosensor for the prostate specific antigen based on the use of reduced graphene oxide decorated with gold nanoparticles. *Microchim. Acta* 186, 484. doi:10.1007/s00604-019-3565-8

Bezerra, G., Córdula, C., Campos, D., Nascimento, G., Oliveira, N., Seabra, M. A., et al. (2019). Electrochemical aptasensor for the detection of HER2 in human serum to assist in the diagnosis of early stage breast cancer. *Anal. Bioanal. Chem.* 411, 6667–6676. doi:10.1007/s00216-019-02040-5

Bhardwaj, T., and Kumar Sharma, T. (2022). Aptasensors for full body health checkup. *Biosens. Bioelectron. X* 11, 100199. doi:10.1016/j.biosx.2022.100199

Biniaz, Z., Mostafavi, A., Shamspur, T., Torkzadeh-Mahani, M., and Mohamadi, M. (2017). Electrochemical sandwich immunoassay for the prostate specific antigen using a polyclonal antibody conjugated to thionine and horseradish peroxidase. *Microchim. Acta* 184, 2731–2738. doi:10.1007/s00604-017-2284-2

Biswas, S., Lan, Q., Xie, Y., Sun, X., and Wang, Y. (2021). Label-free electrochemical immunosensor for ultrasensitive detection of carbohydrate antigen 125 based on antibody-immobilized biocompatible MOF-808/CNT. *ACS Appl. Mater Interfaces* 13, 3295–3302. doi:10.1021/acsami.0c14946

Centane, S., and Nyokong, T. (2022). Aptamer versus antibody as probes for the impedimetric biosensor for human epidermal growth factor receptor. *J. Inorg. Biochem.* 230, 111764. doi:10.1016/j.jinorgbio.2022.111764

Chen, J., Hu, W., Wei, J., Yu, F., Wu, L., Wang, C., et al. (2019). An electrochemical aptasensing platform for carbohydrate antigen 125 based on the use of flower-like gold nanostructures and target-triggered strand displacement amplification. *Microchim. Acta* 186, 388. doi:10.1007/s00604-019-3497-3

Chun, L., Kim, S.-E., Cho, M., Choe, W., Nam, J., Lee, D. W., et al. (2013). Electrochemical detection of HER2 using single stranded DNA aptamer modified gold nanoparticles electrode. *Sens. Actuators B Chem.* 186, 446–450. doi:10.1016/j.snb.2013.06.046

Costa, N. G., Antunes, J. C., Paleo, A. J., and Rocha, A. M. (2022). A review on flexible electrochemical biosensors to monitor alcohol in sweat. *Biosens. (Basel)* 12, 252. doi:10.3390/bios12040252

Das, R., Dhiman, A., Mishra, S. K., Haldar, S., Sharma, N., Bansal, A., et al. (2019). Structural switching electrochemical DNA aptasensor for the rapid diagnosis of tuberculous meningitis. *Int. J. Nanomedicine* 14, 2103–2113. doi:10.2147/IJN.S189127

Doménech-Carbó, A., Machado de Carvalho, L., Martini, M., Valencia, D. P., and Cebrián-Torrejón, G. (2015). "Electrochemical monitoring of the pharmacological activity of natural products," in *Studies in natural products chemistry* (Elsevier), 59–84. doi:10.1016/B978-0-444-63473-3.00003-4

Duan, R., Fang, X., and Wang, D. (2021). A methylene blue assisted electrochemical sensor for determination of drug resistance of *Escherichia coli*. *Front. Chem.* 9, 689735. doi:10.3389/fchem.2021.689735

Emami, M., Shamsipur, M., Saber, R., and Irajirad, R. (2014). An electrochemical immunosensor for detection of a breast cancer biomarker based on antiHER2–iron oxide nanoparticle bioconjugates. *Analyst* 139, 2858–2866. doi:10.1039/C4AN00183D

Fan, Y., Shi, S., Ma, J., and Guo, Y. (2019). A paper-based electrochemical immunosensor with reduced graphene oxide/thionine/gold nanoparticles nanocomposites modification for the detection of cancer antigen 125. *Biosens. Bioelectron.* 135, 1–7. doi:10.1016/j.bios.2019.03.063

Freitas, M., Nouws, H. P. A., and Delerue-Matos, C. (2019). Electrochemical sensing platforms for HER2-ECD breast cancer biomarker detection. *Electroanalysis* 31, 121–128. doi:10.1002/elan.201800537

Garg, S., Sachdeva, A., Peeters, M., and McClements, J. (2023). Point-of-Care prostate specific antigen testing: examining translational progress toward clinical implementation. *ACS Sens.* 8, 3643–3658. doi:10.1021/acssensors.3c01402

Gasparotto, G., Costa, J. P. C., Costa, P. I., Zaghete, M. A., and Mazon, T. (2017). Electrochemical immunosensor based on ZnO nanorods-Au nanoparticles nanohybrids for ovarian cancer antigen CA-125 detection. *Mater. Sci. Eng. C* 76, 1240–1247. doi:10.1016/j.msec.2017.02.031

Hassani, S., Salek Maghsoudi, A., Rezaei Akmal, M., Rahmani, S. R., Sarihi, P., Ganjali, M. R., et al. (2020). A sensitive aptamer-based biosensor for electrochemical quantification of PSA as a specific diagnostic marker of prostate cancer. *J. Pharm. Pharm. Sci.* 23, 243–258. doi:10.18433/jpps31171

Hayat, A., and Marty, J. L. (2014). Aptamer based electrochemical sensors for emerging environmental pollutants. *Front. Chem.* 2, 41. doi:10.3389/fchem.2014.00041

Houssin, T., Bridle, H., and Senez, V. (2021). "Electrochemical detection," in *Waterborne pathogens* (Elsevier), 147–187. doi:10.1016/B978-0-444-64319-3.00006-X

Ilkhani, H., Sarparast, M., Noori, A., Zahra Bathaie, S., and Mousavi, M. F. (2015). Electrochemical aptamer/antibody based sandwich immunosensor for the detection of EGFR, a cancer biomarker, using gold nanoparticles as a signaling probe. *Biosens. Bioelectron.* 74, 491–497. doi:10.1016/j.bios.2015.06.063

Jafari, M., Hasanzadeh, M., Solhi, E., Hassanpour, S., Shadjou, N., Mokhtarzadeh, A., et al. (2019). Ultrasensitive bioassay of epitope of Mucin-16 protein (CA 125) in human plasma samples using a novel immunoassay based on silver conductive nano-ink: a new platform in early stage diagnosis of ovarian cancer and efficient management. *Int. J. Biol. Macromol.* 126, 1255–1265. doi:10.1016/j.ijbiomac.2019.01.009

Jana, P., and Dev, A. (2022). Carbon quantum dots: a promising nanocarrier for bioimaging and drug delivery in cancer. *Mater Today Commun.* 32, 104068. doi:10.1016/j.mtcomm.2022.104068

Jayasena, S. D. (1999). Aptamers: an emerging class of molecules that rival antibodies in diagnostics. *Clin. Chem.* 45, 1628–1650. doi:10.1093/clinchem/45.9.1628

Jo, H., Her, J., Lee, H., Shim, Y.-B., and Ban, C. (2017). Highly sensitive amperometric detection of cardiac troponin I using sandwich aptamers and screen-printed carbon electrodes. *Talanta* 165, 442–448. doi:10.1016/j.talanta.2016.12.091

Johari-Ahar, M., Rashidi, M. R., Barar, J., Aghaie, M., Mohammadnejad, D., Ramazani, A., et al. (2015). An ultra-sensitive impedimetric immunosensor for detection of the serum oncomarker CA-125 in ovarian cancer patients. *Nanoscale* 7, 3768–3779. doi:10.1039/C4NR06687A

Kansara, V., Shukla, R., Flora, S. J. S., Bahadur, P., and Tiwari, S. (2022). Graphene quantum dots: synthesis, optical properties and navigational applications against cancer. *Mater Today Commun.* 31, 103359. doi:10.1016/j.mtcomm.2022.103359

Karaca, E., and Acaralı, N. (2023). Application of graphene and its derivatives in medicine: a review. *Mater Today Commun.* 37, 107054. doi:10.1016/j.mtcomm.2023.107054

Kondzior, M., and Grabowska, I. (2020). Antibody-electroactive probe conjugates based electrochemical immunosensors. *Sensors* 20, 2014. doi:10.3390/s20072014

Korte, B. J., Rompalo, A., Manabe, Y. C., and Gaydos, C. A. (2020). Overcoming challenges with the adoption of point-of-care testing. *Point Care J. Near-Patient Test. Technol.* 19, 77–83. doi:10.1097/POC.0000000000000209

Lasia, A. (2014). "Self-assembled monolayers, biological membranes, and biosensors," in *Electrochemical impedance spectroscopy and its applications* (New York, NY: Springer), 263–270. doi:10.1007/978-1-4614-8933-7_12

Lazanas, A.Ch., and Prodromidis, M. I. (2023). Electrochemical impedance Spectroscopy—A tutorial. *ACS Meas. Sci. Au* 3, 162–193. doi:10.1021/acsmeasuresciau.2c00070

Liu, X., Duckworth, P. A., and Wong, D. K. Y. (2010). Square wave voltammetry versus electrochemical impedance spectroscopy as a rapid detection technique at electrochemical immunosensors. *Biosens. Bioelectron.* 25, 1467–1473. doi:10.1016/j.bios.2009.10.047

Magar, H. S., Hassan, R. Y. A., and Mulchandani, A. (2021). Electrochemical impedance spectroscopy (EIS): principles, construction, and biosensing applications. *Sensors* 21, 6578. doi:10.3390/s21196578

Marques, R. C. B., Viswanathan, S., Nouws, H. P. A., Delerue-Matos, C., and González-García, M. B. (2014). Electrochemical immunosensor for the analysis of the breast cancer biomarker HER2 ECD. *Talanta* 129, 594–599. doi:10.1016/j.talanta.2014.06.035

McKeague, M., Calzada, V., Cerchia, L., DeRosa, M., Heemstra, J. M., Janjic, N., et al. (2022). The minimum aptamer publication standards (MAPS guidelines) for *de novo* aptamer selection. *Aptamer* 6, 10–18.

Mollarasouli, F., Kurbanoglu, S., and Ozkan, S. A. (2019). The role of electrochemical immunosensors in clinical analysis. *Biosens. (Basel)* 9, 86. doi:10.3390/bios9030086

Naresh, V., and Lee, N. (2021). A review on biosensors and recent development of nanostructured materials-enabled biosensors. *Sensors* 21, 1109. doi:10.3390/s21041109

Nxele, S. R., and Nyokong, T. (2021). The electrochemical detection of prostate specific antigen on glassy carbon electrode modified with combinations of graphene quantum dots, cobalt phthalocyanine and an aptamer. *J. Inorg. Biochem.* 221, 111462. doi:10.1016/j.jinorgbio.2021.111462

Özcan, B., and Sezgintürk, M. K. (2022). Fabrication of an ultrasensitive and single-use graphite paper based immunosensor for Neuropeptide Y detection: a promising biosensing system for early detection of childhood obesity. *Mater Today Commun.* 33, 104797. doi:10.1016/j.mtcomm.2022.104797

Padmavathi, G., Bordoloi, D., Banik, K., and Kunnumakkara, A. B. (2017). "Cancer biomarkers: important tools for cancer diagnosis and prognosis," in *Next generation point-of-care biomedical sensors technologies for cancer diagnosis* (Singapore: Springer Singapore), 1–29. doi:10.1007/978-981-10-4726-8_1

Patil, S. M., Karade, V. C., Kim, J. H., Chougale, A. D., and Patil, P. B. (2022). Electrochemical immunosensor to detect breast cancer marker CA 15-3 antibody. *Mater Today Commun.* 33, 104856. doi:10.1016/j.mtcomm.2022.104856

Patris, S., de Pauw, P., Vandeput, M., Huet, J., van Antwerpen, P., Muyldermans, S., et al. (2014). Nanoimmunoassay onto a screen printed electrode for HER2 breast cancer biomarker determination. *Talanta* 130, 164–170. doi:10.1016/j.talanta.2014.06.069

Pavithra, M., Muruganand, S., and Parthiban, C. (2018). Development of novel paper based electrochemical immunosensor with self-made gold nanoparticle ink and quinone derivate for highly sensitive carcinoembryonic antigen. *Sens. Actuators B Chem.* 257, 496–503. doi:10.1016/j.snb.2017.10.177

Popov, A., Brasiunas, B., Kausaite-Minkstimiene, A., and Ramanaviciene, A. (2021). Metal nanoparticle and quantum dot tags for signal amplification in electrochemical immunosensors for biomarker detection. *Chemosensors* 9, 85. doi:10.3390/chemosensors9040085

Raouafi, A., Sánchez, A., Raouafi, N., and Villalonga, R. (2019). Electrochemical aptamer-based bioplatform for ultrasensitive detection of prostate specific antigen. *Sens. Actuators B Chem.* 297, 126762. doi:10.1016/j.snb.2019.126762

Ravalli, A., da Rocha, C. G., Yamanaka, H., and Marrazza, G. (2015). A label-free electrochemical affisensor for cancer marker detection: the case of HER2. *Bioelectrochemistry* 106, 268–275. doi:10.1016/j.bioelechem.2015.07.010

Salimian, R., Kékedy-Nagy, L., and Ferapontova, E. E. (2017). Specific picomolar detection of a breast cancer biomarker HER-2/neu protein in serum: electrocatalytically amplified electroanalysis by the aptamer/PEG-modified electrode. *ChemElectroChem* 4, 872–879. doi:10.1002/celc.201700025

Sattarahmady, N., Rahi, A., and Heli, H. (2017). A signal-on built in-marker electrochemical aptasensor for human prostate-specific antigen based on a hairbrush-like gold nanostructure. *Sci. Rep.* 7, 11238. doi:10.1038/s41598-017-11680-5

Shamsazar, A., Asadi, A., Seifzadeh, D., and Mahdavi, M. (2021). A novel and highly sensitive sandwich-type immunosensor for prostate-specific antigen detection based on MWCNTs-Fe3O4 nanocomposite. *Sens. Actuators B Chem.* 346, 130459. doi:10.1016/j.snb.2021.130459

Shamsipur, M., Emami, M., Farzin, L., and Saber, R. (2018). A sandwich-type electrochemical immunosensor based on *in situ* silver deposition for determination of serum level of HER2 in breast cancer patients. *Biosens. Bioelectron.* 103, 54–61. doi:10.1016/j.bios.2017.12.022

Sharafeldin, M., McCaffrey, K., and Rusling, J. F. (2019). Influence of antibody immobilization strategy on carbon electrode immunoarrays. *Analyst* 144, 5108–5116. doi:10.1039/C9AN01093A

Shekari, Z., Zare, H. R., and Falahati, A. (2021). Dual assaying of breast cancer biomarkers by using a sandwich–type electrochemical aptasensor based on a gold nanoparticles–3D graphene hydrogel nanocomposite and redox probes labeled aptamers. *Sens. Actuators B Chem.* 332, 129515. doi:10.1016/j.snb.2021.129515

Shen, C., Wang, L., Zhang, H., Liu, S., and Jiang, J. (2020). An electrochemical sandwich immunosensor based on signal amplification technique for the determination of alpha-fetoprotein. *Front. Chem.* 8, 589560. doi:10.3389/fchem.2020.589560

Shui, B., Tao, D., Cheng, J., Mei, Y., Jaffrezic-Renault, N., and Guo, Z. (2018). A novel electrochemical aptamer–antibody sandwich assay for the detection of tau-381 in human serum. *Analyst* 143, 3549–3554. doi:10.1039/C8AN00527C

Srivastava, M., Nirala, N. R., Srivastava, S. K., and Prakash, R. (2018). A comparative study of aptasensor vs immunosensor for label-free PSA cancer detection on GQDs-AuNRs modified screen-printed electrodes. *Sci. Rep.* 8, 1923. doi:10.1038/s41598-018-19733-z

Sun, D., Luo, Z., Lu, J., Zhang, S., Che, T., Chen, Z., et al. (2019). Electrochemical dual-aptamer-based biosensor for nonenzymatic detection of cardiac troponin I by nanohybrid electrocatalysts labeling combined with DNA nanotetrahedron structure. *Biosens. Bioelectron.* 134, 49–56. doi:10.1016/j.bios.2019.03.049

Sypabekova, M., Bekmurzayeva, A., Wang, R., Li, Y., Nogues, C., and Kanayeva, D. (2017). Selection, characterization, and application of DNA aptamers for detection of *Mycobacterium tuberculosis* secreted protein MPT64. *Tuberculosis* 104, 70–78. doi:10.1016/j.tube.2017.03.004

Tallapragada, S. D., Layek, K., Mukherjee, R., Mistry, K. K., and Ghosh, M. (2017). Development of screen-printed electrode based immunosensor for the detection of HER2 antigen in human serum samples. *Bioelectrochemistry* 118, 25–30. doi:10.1016/j.bioelechem.2017.06.009

Valipour, A., and Roushani, M. (2017). Using silver nanoparticle and thiol graphene quantum dots nanocomposite as a substratum to load antibody for detection of hepatitis C virus core antigen: electrochemical oxidation of riboflavin was used as redox probe. *Biosens. Bioelectron.* 89, 946–951. doi:10.1016/j.bios.2016.09.086

Wang, J., Cao, Z., Yang, F., Wang, S., and Zhong, H. (2018). Enhancement of catalytic performance by regulating the surface properties of Fe3O4 composites. *J. Taiwan Inst. Chem. Eng.* 93, 350–362. doi:10.1016/j.jtice.2018.07.043

Wei, B., Mao, K., Liu, N., Zhang, M., and Yang, Z. (2018). Graphene nanocomposites modified electrochemical aptamer sensor for rapid and highly sensitive detection of prostate specific antigen. *Biosens. Bioelectron.* 121, 41–46. doi:10.1016/j.bios.2018.08.067

Westbroek, P. (2005). "Electrochemical methods," in *Analytical electrochemistry in textiles* (Elsevier), 37–69. doi:10.1533/9781845690878.1.37

Zachek, M. K., Hermans, A., Wightman, R. M., and McCarty, G. S. (2008). Electrochemical dopamine detection: comparing gold and carbon fiber microelectrodes using background subtracted fast scan cyclic voltammetry. *J. Electroanal. Chem.* 614, 113–120. doi:10.1016/j.jelechem.2007.11.007

Zhong, H., Zhao, C., Chen, J., Chen, M., Luo, T., Tang, W., et al. (2020). Electrochemical immunosensor with surface-confined probe for sensitive and reagentless detection of breast cancer biomarker. *RSC Adv.* 10, 22291–22296. doi:10.1039/D0RA01192D

Zhu, Y., Cai, Y., Xu, L., Zheng, L., Wang, L., Qi, B., et al. (2015). Building an aptamer/graphene oxide FRET biosensor for one-step detection of bisphenol A. *ACS Appl. Mater Interfaces* 7, 7492–7496. doi:10.1021/acsami.5b00199

Zhu, Y., Chandra, P., and Shim, Y.-B. (2013). Ultrasensitive and selective electrochemical diagnosis of breast cancer based on a hydrazine–Au nanoparticle–aptamer bioconjugate. *Anal. Chem.* 85, 1058–1064. doi:10.1021/ac302923k

Frontiers in
Bioengineering and Biotechnology

Accelerates the development of therapies, devices, and technologies to improve our lives

A multidisciplinary journal that accelerates the development of biological therapies, devices, processes and technologies to improve our lives by bridging the gap between discoveries and their application.

Discover the latest Research Topics

See more →

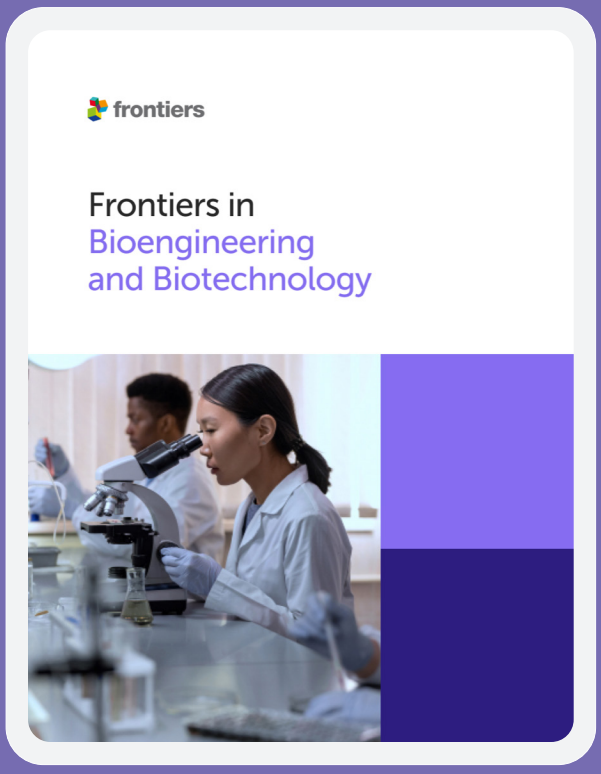

Frontiers

Avenue du Tribunal-Fédéral 34
1005 Lausanne, Switzerland
frontiersin.org

Contact us

+41 (0)21 510 17 00
frontiersin.org/about/contact